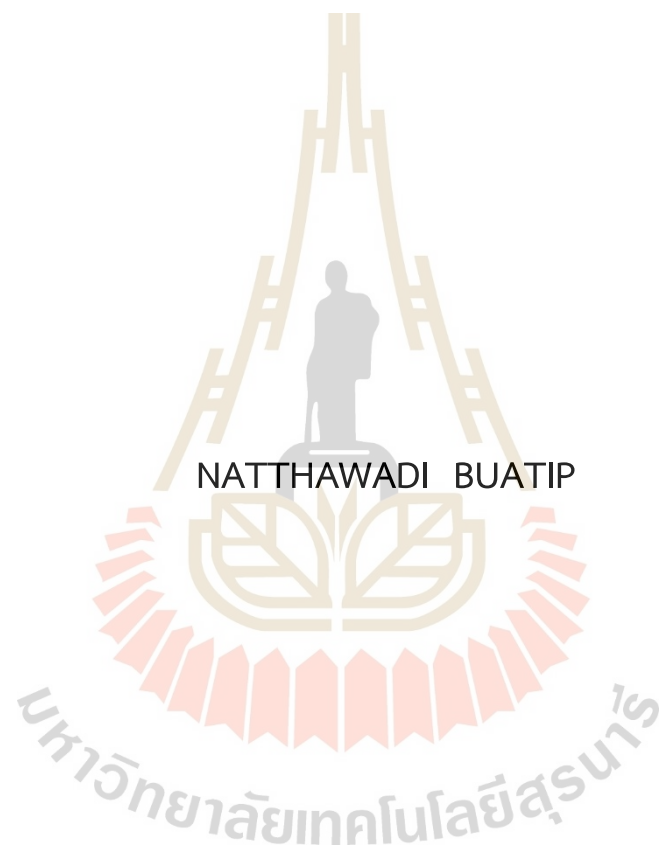


LEAD FREE PIEZO-TRIBOELECTRIC HYBRID
FOR ENERGY HARVESTING APPLICATION



A Thesis Submitted in Partial Fulfillment of the Requirements for the
Degree of Doctor of Philosophy in Materials Engineering
Suranaree University of Technology
Academic Year 2022

เพียโซอิเล็กทริกปลอดสารตะกั่ว – ไทโรโบอิเล็กทริก ชนิดไฮบริด
สำหรับประยุกต์ใช้ในการเก็บเกี่ยวพลังงาน



นางสาวณัฐวดี บัวดี

วิทยานิพนธ์นี้เป็นส่วนหนึ่งของการศึกษาตามหลักสูตรปริญญาวิศวกรรมศาสตรดุษฎีบัณฑิต
สาขาวิชาวิศวกรรมวัสดุ
มหาวิทยาลัยเทคโนโลยีสุรนารี
ปีการศึกษา 2565

LEAD FREE PIEZO-TRIBOELECTRIC HYBRID
FOR ENERGY HARVESTING APPLICATION

Suranaree University of Technology has approved this thesis submitted in partial fulfillment of the requirements for the Degree of Doctor of Philosophy

Thesis Examining Committee



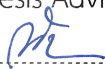
(Dr. Somchai Tancharakorn)

Chairperson



(Assoc. Prof. Dr. Soodkhet Pojprapai)

Member (Thesis Advisor)



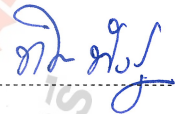
(Dr. Pattanaphong Janphaung)

Member (Thesis Co-advisor)



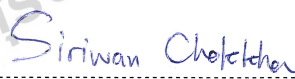
(Asst. Prof. Dr. Wipawee Usaha)

Member



(Asst. Prof. Dr. Thipwan Fangsuwannarak)

Member



(Asst. Prof. Dr. Siriwan Chokkha)

Member



(Assoc. Prof. Dr. Chaiwat Ruksakulpiwat)

Member



(Assoc. Prof. Dr. Pornsiri Jongkol)

Dean of Institute of Engineering



(Assoc. Prof. Dr. Chatchai Jothityangkoon)
Vice Rector for Academic Affairs and
Quality Assurance

ณัฐวดี บัวตึบ : เพียโซอิเล็กทริกปลอดสารตะกั่ว – ไทโรโบอิเล็กทริก ชนิดไฮบริด
สำหรับประยุกต์ใช้ในการเก็บเกี่ยวพลังงาน (LEAD FREE PIEZO-TRIBOELECTRIC
HYBRID FOR ENERGY HARVESTING APPLICATION) อาจารย์ที่ปรึกษา :
รองศาสตราจารย์ ดร. สุตเขตต์ พจน์ประไพ, 160 หน้า.

คำสำคัญ: แบบเรียมแคลเซียมเซอร์โคเนตไททานเนต/วัสดุเพียโซอิเล็กทริกปลอดสารตะกั่ว/วัสดุคอม
โพสิตเพียโซอิเล็กทริก/เพียโซอิเล็กทริก-ไทรโบอิเล็กทริกชนิดไฮบริด/การเก็บเกี่ยว
พลังงาน

งานวิจัยนี้มุ่งเน้นไปที่การสังเคราะห์และการประดิษฐ์ วัสดุเพียโซอิเล็กทริกเซรามิกและ
วัสดุเพียโซอิเล็กทริกคอมโพสิตที่ปลอดสารตะกั่ว เพื่อสร้างอุปกรณ์สำหรับเก็บเกี่ยวพลังงานจาก
พลังงานกลเป็นพลังงานไฟฟ้าด้วยเพียโซอิเล็กทริก-ไทรโบอิเล็กทริก ชนิดไฮบริด (Piezo-
Trieboelectric hybrid) สำหรับประยุกต์ใช้ในการเก็บเกี่ยวพลังงานภายใต้แรงบีบอัดทางกล

ในครั้งแรก วิทยานิพนธ์นี้ได้ศึกษาการสังเคราะห์และการสร้างวัสดุเพียโซอิเล็กทริกเซรามิก
โดยสารแบบเรียมแคลเซียมเซอร์โคเนตไททานเนต (BCZT) ซึ่งเป็นวัสดุเฟอร์โรอิเล็กทริกที่ปลอดสาร
ตะกั่ว และมีสมบัติเพียโซอิเล็กทริกที่สามารถแปลงพลังงานกลเป็นพลังงานไฟฟ้าได้ จาก
ปรากฏการณ์เพียโซอิเล็กทริกทางตรง (piezoelectric direct effect) งานวิจัยนี้ได้ทำการศึกษา
เปรียบเทียบระหว่างการเผาผนึกด้วยปฏิกิริยาสถานะของแข็งแบบดั้งเดิม (Conventional sintering;
CS) และการเผาผนึกด้วยปฏิกิริยา (Reactive sintering; RS) ซึ่งผลแสดงให้เห็นว่าวัสดุเพียโซอิเล็ก
ทริกเซรามิก BCZT จากการเผาผนึกโดยทั้งสองเทคนิคที่อุณหภูมิ 1540 °C เป็นเวลา 2 ชั่วโมงแสดง
สมบัติทางไฟฟ้าและเพียโซอิเล็กทริกที่เหมาะสมที่สุด ถึงแม้ว่าเซรามิก RS-BCZT จะมีกระบวนการ
ผลิตที่ง่ายและประหยัดกว่าเซรามิก CS-BCZT แต่สมบัติทางไฟฟ้าของเซรามิกนั้นยังไม่เพียงพอ
สำหรับการนำมาประยุกต์ใช้งานในการเก็บเกี่ยวพลังงาน เพื่อปรับปรุงสมบัติการเก็บเกี่ยวพลังงาน
ของวัสดุเพียโซอิเล็กทริกเซรามิก BCZT การศึกษาครั้งนี้จึงได้ทำการสังเคราะห์และผลิตเซรามิก BCZT
โดยใช้ปฏิกิริยาสถานะของแข็ง (Solid state reaction; SSR) และการอัดขึ้นรูปโดยให้ความดันทุก
ทิศทางแบบเย็น (Cold isostatic pressing; CIP) ก่อนการเผาผนึก จากกระบวนการดังกล่าวเซรามิก
BCZT แสดงค่าสัมประสิทธิ์ทางเพียโซอิเล็กทริก (d_{33} , g_{33}) ที่ดี ซึ่งเป็นคุณสมบัติพิเศษทางเพียโซ
อิเล็กทริกและทางไฟฟ้าของวัสดุสำหรับเก็บเกี่ยวพลังงาน นอกจากนี้ประสิทธิภาพในการเก็บเกี่ยว
พลังงานของวัสดุเซรามิก BCZT ได้ถูกศึกษาทดลองภายใต้เงื่อนไขของการบีบอัด (compressive
loads) ที่แตกต่างกัน อย่างไรก็ตาม วัสดุเซรามิกเป็นวัสดุที่เปราะและแตกหักง่ายภายใต้แรงกระทำ
เชิงกล ด้วยเหตุนี้ งานวิจัยนี้จึงได้ประดิษฐ์วัสดุเพียโซอิเล็กทริกคอมโพสิต BCZT/MCNTs/PDMS ใน
รูปแบบโครงสร้าง 0-3 เพื่อกำจัดข้อจำกัดนี้ และทำการประดิษฐ์วัสดุเพียโซอิเล็กทริก-ไทรโบอิเล็ก

ทริก ชนิดไฮบริด ที่สร้างจากวัสดุเพียโซอิเล็กทริกคอมโพสิต โดยปรากฏการณ์ไพโรอิเล็กทริกคือการสร้างพลังงานไฟฟ้าด้วยการเหนี่ยวนำไฟฟ้าสถิตและการเกิดไฟฟ้าสถิต ซึ่งจากการศึกษาอิทธิพลของอัตราส่วนน้ำหนักของอนุภาค BCZT แสดงให้เห็นว่าการเพิ่มเปอร์เซ็นต์โดยน้ำหนักของอนุภาค BCZT จะช่วยเพิ่มประสิทธิภาพทางไฟฟ้าได้ โดยคอมโพสิตที่มีอนุภาค BCZT ในอัตราส่วน 50 เปอร์เซ็นต์ โดยน้ำหนักแสดงผลลัพธ์ทางไฟฟ้าที่ดีที่สุด

จากผลการศึกษาในครั้งนี้แสดงให้เห็นว่า วัสดุเพียโซอิเล็กทริก-ไพโรอิเล็กทริก ชนิดไฮบริด ที่ใช้วัสดุเพียโซอิเล็กทริกคอมโพสิต BCZT/MCNTs/PDMS แสดงประสิทธิภาพในการแปลงพลังงานกลเป็นพลังงานไฟฟ้าและมีความทนทานต่อแรงเชิงกลที่ดีขึ้น เมื่อเปรียบเทียบกับวัสดุเซรามิกเพียโซอิเล็กทริก BCZT ซึ่งอาจเป็นทางเลือกที่มีความเป็นไปได้สำหรับการประยุกต์ใช้งานด้านการเก็บเกี่ยวพลังงานภายใต้แรงบีบอัดสูงและการโหลดเชิงกลซ้ำๆได้



สาขาวิชา วิศวกรรมเซรามิก

ปีการศึกษา 2565

ลายมือชื่อนักศึกษา

ลายมือชื่ออาจารย์ที่ปรึกษา

ลายมือชื่ออาจารย์ที่ปรึกษารวม

NATTHAWADI BUATIP : LEAD FREE PIEZO-TRIBOELECTRIC HYBRID FOR
ENERGY HARVESTING APPLICATION. THESIS ADVISOR : ASSOC. PROF.
SOODKHET POJPRAPAI, Ph.D., 160 PP.

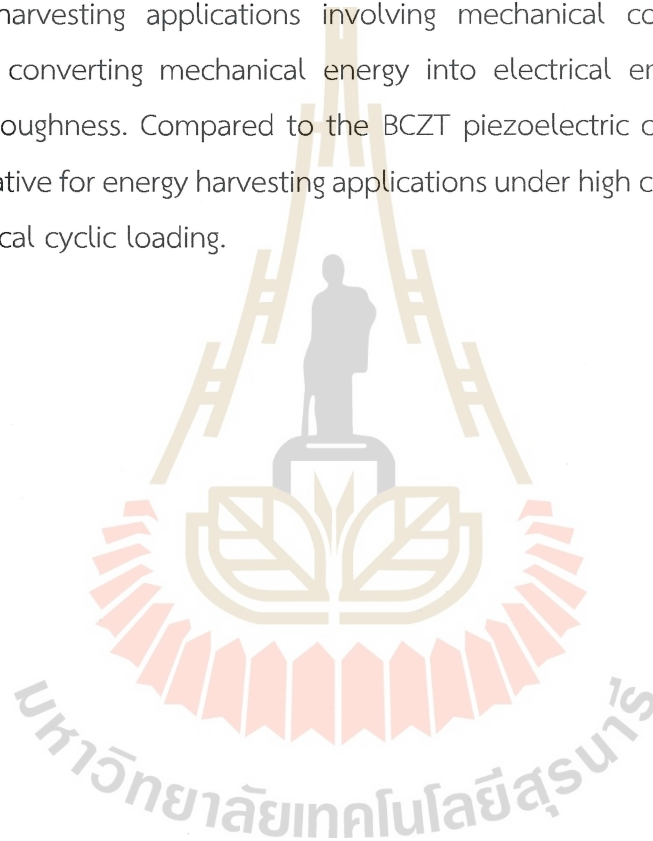
Keyword: BCZT/lead-free piezoelectric/piezoelectric composite/piezo-triboelectric
hybrid/energy harvesting

This research focuses on the synthesis and fabrication of lead-free piezoelectric ceramics and piezoelectric composites. The objective is to develop a device that can harvest electrical energy from mechanical energy using a piezoelectric-triboelectric hybrid mechanism (referred to as a "Piezo-Triboelectric Hybrid") specifically designed for energy harvesting applications involving compression forces.

The first part of this thesis examines the synthesis and fabrication of piezoelectric ceramic with barium calcium zirconate titanate (BCZT) as a lead-free ferroelectric material. BCZT exhibits piezoelectric properties that allow for the conversion of mechanical energy to electrical energy through the direct piezoelectric effect. In this research, a comparative study was conducted, comparing conventional solid-state reaction sintering (CS) with reactive sintering (RS) techniques. The findings indicate that BCZT ceramics sintered at 1540 °C for 2 hts using either CS or RS demonstrated optimum electrical and piezoelectric properties. However, while RS-BCZT ceramics offer a simpler and more cost-effective manufacturing process compared to CS-BCZT ceramics, their electrical properties are insufficient for energy harvesting applications. To enhance the energy harvesting capabilities of BCZT ceramics, this study employed solid-state reaction (SSR) method and cold isostatic pressing (CIP) prior to sintering. The BCZT ceramics exhibited favorable piezoelectric coefficients (d_{33} , g_{33}), which are critical properties for energy harvesting. Additionally, the energy harvesting efficiency of BCZT ceramics was experimentally investigated under various compressive loads. However, due to the brittleness of ceramics under mechanical stress, this research also involved the fabrication of a piezoelectric composite material, BCZT/MCNTs/PDMS, in a 0-3 structure to overcome this limitation. Furthermore, a piezo-triboelectric hybrid was developed using the piezoelectric composite, as the triboelectric effect enables the generation of electrical energy

through electrostatic induction and static electricity. The study also explored the influence of the weight ratio of BCZT particles on electrical efficiency, revealing that an increased weight percentage of BCZT particles led to improved electrical performance. Specifically, the composite containing 50 wt% of BCZT particles exhibited the most favorable electrical results.

The findings of this study demonstrate that the piezo-triboelectric hybrid based on the BCZT/MCNTs/PDMS piezoelectric composite is a promising lead-free alternative for energy harvesting applications involving mechanical compression. It shows efficiency in converting mechanical energy into electrical energy and has better mechanical toughness. Compared to the BCZT piezoelectric ceramic, it could be a viable alternative for energy harvesting applications under high compressive load force and mechanical cyclic loading.



School of Ceramic Engineering
Academic Year 2022

Student's Signature.....
Advisor's Signature.....
Co-advisor's Signature.....

ACKNOWLEDGEMENT

I would like to express my heartfelt gratitude to everyone who has contributed to the completion of this dissertation. Without their assistance, I would not have been able to achieve this milestone.

First and foremost, I extend my sincere thanks to the National Research Council of Thailand (NRCT), Thailand Research Fund (TRF), Synchrotron Light Research Institute (SLRI), and Public Organization Thailand for their generous financial support through the Royal Golden Jubilee Ph.D. program scholarship (Grant No. PHD/0233/2558), which made this research possible.

I am deeply grateful to my supervisor, Associate Professor Dr. Soodkhet Pojprapai, for his invaluable guidance, support, and opportunities that have enriched my learning experiences. I am also grateful to my co-supervisor, Dr. Pattanaphong Janphuang, for his assistance and support throughout my research. I am also indebted to my co-author, Dr. Dhanunjaya Munthala, for his insightful guidance and advice.

I would also like to express my gratitude to the members of my thesis committee, Assistant Professor Dr. Wipawee Usaha, Assistant Professor Dr. Thipwan Fangsuwannarak, Assistant Professor Dr. Siriwan Chokkha, and Associate Professor Dr. Chaiwat Ruksakulpiwat, as well as external committee member Dr. Somchai Tancharakorn, for their valuable feedback, suggestions, and constructive criticism.

Furthermore, I would like to extend my appreciation to Professor Dr. Roger Whatmore for recommending me to Dr. Chaoying Wang at the International Institute for Nanocomposites (IINM), WMG, University of Warwick, and to Professor Dr. Chris Bowen at Department of Mechanical Engineering, University of Bath, for allowing me to be a visiting research student in their groups and laboratories in the United Kingdom. I am also thankful to the Synchrotron Light Research Institute (SLRI), BL8: X-ray Absorption Spectroscopy (XAS), BL1.2W: X-ray Imaging and X-ray Tomographic Microtomography (XTM), and BL6a: Deep X-ray Lithography (DXL), School of Ceramic Engineering, Suranaree University of Technology, and all their staff, scientists, and technicians for their support and assistance throughout my research.

I would like to express my heartfelt gratitude to my beloved family for their unwavering love, understanding, and support throughout my academic journey. I dedicate this Ph.D. thesis to my dear parents, Mr. Boonlern and Mrs. Sriwan Buatip, as well as to Mr. Jessada, Mrs. Lumnao, and Mr. Jutarop Reungyos, for their constant care, trust, encouragement, and support.

I would also like to express my appreciation to my best friend, Dr. Penphitcha Amonpattaratkit, for her encouragement and advice during my Ph.D. studies, and to my co-workers, brothers, and sisters at the Research Unit of Dr. Soodkhet Projprapai for our excellent collaboration and work relationship.

Finally, I am immensely grateful for the challenges and difficulties that I encountered during my Ph.D. studies. They have taught me valuable life skills, including patience, collaboration, forgiveness, and persistence, which have enabled me to become a better researcher and person.

Natthawadi Buatip

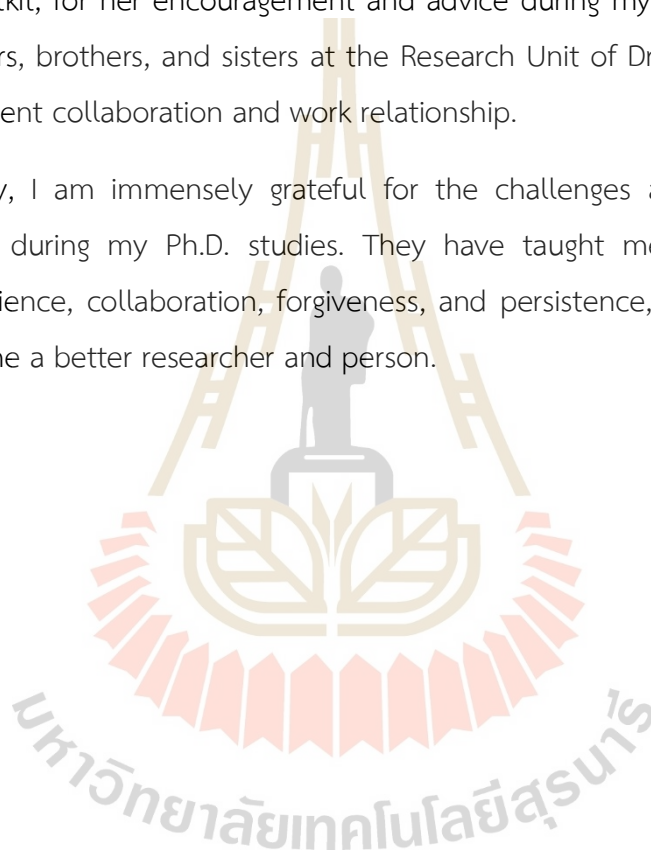


TABLE OF CONTENTS

	Page
ABSTRACT (THAI).....	I
ABSTRACT (ENGLISH).....	III
ACKNOWLEDGEMENT.....	V
TABLE OF CONTENTS.....	VII
LIST OF TABLES.....	XI
LIST OF FIGURES.....	XII
LIST OF ABBREVIATIONS.....	XVIII
CHAPTER	
1 INTRODUCTION.....	1
1.1 Rationale and Background.....	1
1.2 Research Objectives.....	3
1.3 Hypotheses.....	4
1.4 Scope of Thesis.....	5
1.5 Usefulness of the Research.....	6
1.6 Outline of Thesis.....	7
1.7 References.....	9
2 LITERATURE REVIEWS.....	12
2.1 Lead-free piezoelectric.....	12
2.1.1 Piezoelectric ceramics.....	12
2.1.2 BCZT Lead-free piezoelectric ceramic.....	15
2.1.3 Direct piezoelectric effect.....	17
2.1.4 Theory and principle of piezoelectric energy harvesting.....	21
2.1.5 Application of piezoelectric ceramics for energy harvesting ..	26
2.2 Piezoelectric ceramic-polymer composites.....	29
2.2.1 Piezoelectric composites.....	29

TABLE OF CONTENTS (Continued)

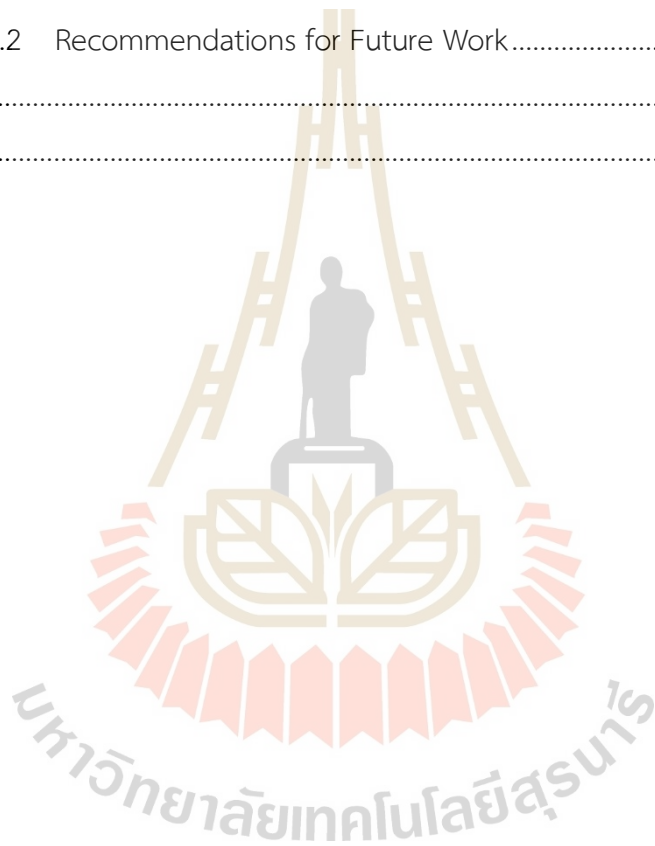
	Page
2.2.2 Theoretical model for 0-3 piezoelectric composite.....	34
2.2.3 Applications of piezoelectric composites for energy harvesting.....	37
2.3 Piezoelectric-triboelectric hybrid	38
2.3.1 Piezoelectric-triboelectric hybrid materials	38
2.3.2 Theoretical and principle of piezoelectric-triboelectric hybrid.....	42
2.3.3 Application of piezoelectric-triboelectric hybrid for energy harvesting.....	46
2.4 References	48
3 A COMPARISON BETWEEN CONVENTIONAL AND REACTIVE SINTERING TECHNIQUES FOR BCZT CERAMIC FABRICATION.....	58
3.1 Introduction.....	58
3.2 Experimental procedure	59
3.2.1 Sample Preparation	59
3.2.2 Characterization.....	61
3.3 Results and Discussion.....	62
3.3.1 XRD Results.....	62
3.3.2 SEM Results.....	65
3.3.3 Densities Results.....	67
3.3.4 Electrical Properties Results.....	67
3.3.5 XANES Results.....	71
3.4 Chapter Summary	75
3.5 References	76
4 THE ENERGY HARVESTING PERFORMANCE OF BCZT PIEZOELECTRIC CERAMICS UNDER LOW FREQUENCY.....	80

TABLE OF CONTENTS (Continued)

	Page
4.1 Introduction.....	80
4.2 Experimental Procedure	80
4.3 Results and Discussion.....	84
4.3.1 BCZT ceramics characterization	84
4.3.2 Energy harvesting under various compressive loads	89
4.3.3 Stored voltage and energy density in capacitors	96
4.4 Chapter Summary	98
4.5 References	99
5 PIEZO-TRIBOELECTRIC NANOGENERATOR BASED ON BCZT/MCNTs/PDMS COMPOSITE FOR COMPRESSIVE ENERGY HARVESTING	102
5.1 Introduction.....	102
5.2 Experimental Procedure	103
5.2.1 Materials.....	103
5.2.2 Synthesis of BCZT microparticles	103
5.2.3 Preparation of the piezoelectric composites.....	103
5.2.4 Fabrication of the piezo-triboelectric nanogenerator (P-TENG) device.....	105
5.2.5 Piezoelectric composites characterization	105
5.3 Results and Discussion	109
5.3.1 Physical and chemical properties of the piezoelectric composites.....	109
5.3.2 Mechanical properties of the piezoelectric composites.....	114
5.3.3 Electrical properties of the piezoelectric composites.....	117
5.3.4 Dielectric properties of the piezoelectric composites	119
5.3.5 Electrical output performance of P-TENG devices.....	121
5.4 Chapter Summary	129

TABLE OF CONTENTS (Continued)

	Page
5.5 References	130
6 CONCLUSION AND FUTURE PERSPECTIVES.....	134
6.1 General Conclusions	134
6.2 Recommendations for Future Work.....	139
APPENDIX	141
BIOGRAPHY.....	160



LIST OF TABLES

Table	Page
2.1 Piezoelectric properties of BCZT ceramics compare with other piezoelectric materials.....	25
2.2 Comparison of the output performance of flexible lead-free piezoelectric energy harvesters.....	32
2.3 Comparison of the output performance of piezo-triboelectric hybrid energy harvesters.....	41
3.1 The differences between RS and CS techniques.....	60
3.2 Electrical properties of BCZT ceramics sintered at 1540 °C for 2, 3 and 4 hrs by CS, and RS technique.....	71
3.3 The area under the corresponding peaks at the PEFS of XANES Ti K-edge of BCZT ceramics sintered at 1540 °C for 2, 3 and 4 hrs by CS and RS techniques.....	73
3.4 Edge position of Ti K-edge and Zr L ₃ -edge of BCZT ceramics sintered at 1540 °C for 2, 3 and 4 hrs by CS and RS techniques and reference samples.....	73
4.1 Piezoelectric properties of BCZT ceramics compared with other piezoelectric materials.....	89
4.2 Comparison of piezoelectric energy harvesters in terms of output performance.....	95

LIST OF FIGURES

Figure		Page
2.1	Relationship between the curie temperature (T_c) and the piezoelectric constant (d_{33}) of piezoelectric ceramics with various crystal structures (inset shows schematics of the perovskite, tungsten bronze, bismuth layer, and perovskite layer structures). (ZHOU, CHEN, & DONG, 2018)	14
2.2	Perovskite structure in pseudo-cube shape (ABO_3). For lead-free piezoelectric ceramics, the typical cations are $A = Ba^{2+}, Ca^{2+}, Bi^{3+}, Na^+K^+$; $B = Ti^{4+}, Zr^{4+}, Nb^{5+}$; and $X = O^{2-}$. (Villafuerte-Castrejón et al., 2016)	14
2.3	Relationship between the piezoelectric coefficient and the depolarization temperature of KNN-based, BCZT, BNT-based, BNT-based Incipient Piezoelectric, and PZT. (Rödel et al., 2015)	15
2.4	Relation of $d \cdot g$ in a function of depolarization temperature for KNN-based, BCZT, BNT-based, BNT-based Incipient Piezoelectric, and PZT. (Rödel et al., 2015)	15
2.5	System $BaTiO_3$ - $BaZrO_3$ - $CaTiO_3$ ternary diagram and the piezoelectric constant (d_{33}) values. (Villafuerte-Castrejón et al., 2016)	17
2.6	Direct piezoelectric effect. (J.-H. Lee et al., 2016)	18
2.7	Reference axis for piezoelectric constant notations.	19
2.8	Piezoelectric working operation in (a) d_{33} (transverse mode) and (b) d_{31} (longitudinal mode). (Covaci & Gontean, 2020).....	20
2.9	The piezoelectric constants of a ferroelectric material poled in three directions are shown. (a) depicts the d_{33} and d_{31} effects, while (b) depicts the d_{15} effect.....	21
2.10	The frequency range for various mechanical energy sources. (Maamer, Boughamoura, El-Bab, Francis, & Tounsi, 2019).....	26

LIST OF FIGURES (Continued)

Figure	Page
2.11	Example of a piezoelectric energy harvesters (PEHs) model. (Covaci & Gontean, 2020)..... 27
2.12	Typical application of piezoelectric energy harvesters in cantilever configuration. (Z. Yang et al., 2018)..... 28
2.13	Various piezoelectric energy harvesting applications for different locations on the human body. (Y. Liu et al., 2021) 28
2.14	Classification of two-phase composites with respect to connectivity. (K. Uchino, 2017) 29
2.15	Schematic of piezoelectric composites with several connectivity types for sensor and actuator applications. (Akdogan, Allahverdi, & Safari, 2005) 30
2.16	Banno's modified cubes model of a unit cell layout for a 0-3 composite. The overall structure (A) and the size-dependent unit cell structure (B). (Kenji Uchino, 2017b)..... 35
2.17	Piezoelectric composite made of carbon black, polymer, and piezoceramic for damping vibration. (K. Uchino, 2017) 36
2.18	Flexible piezoelectric devices are taken into consideration in terms of prospective energy sources for energy harvesting (left side) and the potential to use this energy for sensing and excitation (right side). (Dagdeviren et al., 2016)..... 38
2.19	Trieboelectric series (J. W. Lee, Ye, & Baik, 2017)..... 39
2.20	The four fundamental modes of triboelectric nanogenerators (TENGs): (a) vertical contact separation mode, (b) in-plane contact-sliding mode, (c) single-electrode mode, and (d) freestanding triboelectric-layer mode. (Z. L. Wang, 2014) 40
2.21	Trieboelectric effect of Vertical contact-separation mode. (J.-H. Lee et al., 2016)..... 42

LIST OF FIGURES (Continued)

Figure		Page
2.22	The diagram compares the mechanism's action of TENGs (a) and PENGs (b). (Chen et al., 2020; Han, Chen, Yu, & Zhang, 2015)	44
2.23	The three charge distribution schemes are for the PENGs-TENGs hybrid structure (E is an electric charge, and D is a dielectric material). (Chen et al., 2020; Han et al., 2015)	45
2.24	Self-powered PENGs/TENGs device applications in biomedical engineering and advanced technology. (Karan et al., 2020).....	47
3.1	Schematic diagram of the comparison of conventional (CS) and reactive (RS) sintering techniques for lead-free BCZT ferroelectric ceramics.....	62
3.2	XRD patterns of BCZT ceramics: (a, b) CS and (c, d) RS.....	63
3.3	Fraction of orthorhombic phase of BCZT ceramics were sintered at 1540 °C for 2, 3 and 4 hrs by CS and RS.....	65
3.4	SEM micrograph of surface of BCZT ceramics were sintered at 1540 °C for 2, 3 and 4 hrs by CS (a) and RS (b).	66
3.5	<i>P-E</i> hysteresis loops of BCZT ceramics were sintered by CS and RS at 1540 °C for 2, 3 and 4 hrs at frequencies 50 Hz under an electric filed ± 10 kV/cm.....	68
3.6	Temperature dependent dielectric constant (ϵ_r) and dielectric loss ($\tan \delta$) at 100 Hz of BCZT ceramics prepared by CS and RS techniques.....	69
3.7	Physical properties (a, b, c) and piezoelectric properties (d, e, f) of BCZT ceramics at 1540 °C by different sintering techniques (CS and RS) and dwelling times.	70
3.8	Normalized XANES spectra of BCZT ceramics prepared by CS and RS : (a) Ti <i>K</i> -edge spectra and (b) Zr <i>L</i> ₃ -edge spectra.....	72

LIST OF FIGURES (Continued)

Figure		Page
4.1	(a) The BCZT energy harvester structure and (b) the pneumatic actuator machine to apply the compressive load, and energy harvesting system to measure the output performance of BCZT ceramics ; (c) the diagram of a testing circuit with load resistance.....	83
4.2	(a) XRD patterns and (b) a fraction of rhombohedral/tetragonal phase of BCZT ceramics.....	85
4.3	(a) SEM surface micrograph and (b) the average grain size of a sintered BCZT ceramics.....	86
4.4	(a) <i>P-E</i> and (b) <i>S-E</i> loops of BCZT ceramics (unpoled) at 50 Hz frequency under ± 20 kV/cm electric field.....	87
4.5	The output performance of BCZT ceramics at a range of resistance from 100 k Ω - 20 M Ω under compressive load 50 N at 0.3 Hz of frequency : (a) DC voltage and DC current, and (b) Power.....	90
4.6	The physical and electrical properties of BCZT ceramics across 1 M Ω resistance under compressive loads 50 N, 100 N, 150 N, and 200 N at 0.3 Hz of frequency : (a) stress and dielectric displacement, (b) the output performance on DC voltage and DC current, (c) power and energy....	92
4.7	Output performance and reliability of BCZT ceramic energy harvester across 1 M Ω of resistance, at compressive load 200 N and 0.3 Hz of frequency : (a) Power, (b) DC current, and (c) DC voltage.	94
4.8	(a) Stored voltage and (b) energy density of BCZT ceramics at different capacitances. (The number of compressive cyclic mechanical loads are 900 cycles).....	97
5.1	The fabrication procedure of the piezoelectric composite (BCZT/MCNTs/PDMS).....	104

LIST OF FIGURES (Continued)

Figure	Page
5.2	(a) Energy harvesting test machine and (b) schematic of triboelectric nanogenerator-based piezoelectric composite (P-TENG device)..... 108
5.3	Phase structure of the piezoelectric composite : XRD patterns of (a) BCZT particles, (b) MCNTs/PDMS composite, the piezoelectric composites at different weight ratios of BCZT (c) 40 wt% BCZT, (d) 50 wt% BCZT, and (e) 60 wt% BCZT. 110
5.4	Physical properties of the piezoelectric composite : FE-SEM micrographs of (a) BCZT particles, (b) BCZT particle size distribution, (c) pure MCNTs, and (d) high-resolution images of MCNTs. 111
5.5	Physical properties of the piezoelectric composite : (a-d) Cross-sectional optical microscope images and (e-h) cross-sectional FE-SEM micrographs of the piezoelectric composites at different weight ratios of BCZT. 112
5.6	Chemical properties of the piezoelectric composite : FXI images of cross-sectional piezoelectric composites at different weight ratios of BCZT ; (a) regular image, (b) Ba element mapping, (c) Ti element mapping, and (d) Ca element mapping..... 113
5.7	Physical properties of the piezoelectric composite : SR-XTM images of the piezoelectric composites at different weight ratios of BCZT ; (a) 40 wt% BCZT, (b) 50 wt% BCZT, and (c) 60 wt% BCZT..... 114
5.8	Mechanical properties of the piezoelectric composites : Dynamic behavior of composites with different BCZT particles weight ratios on storage modulus (E') and $\tan \delta$ versus temperature at (a) 1 Hz and (b) 10 Hz measured by DMTA method using a heating rate of 5 °C/min. and (c) the glass transition temperature (T_g), (d) the storage modulus (E') and loss modulus (E'') at room temperature for 1 Hz and 10 Hz..... 116

LIST OF FIGURES (Continued)

Figure		Page
5.9	(a) Electrical conductivity and resistivity, (b) density and crosslink density of the piezoelectric composites at different weight ratios of BCZT.	118
5.10	Electrical properties of the piezoelectric composites : (a) ac conductivity, (b) phase angle, (c) relative permittivity, and (d) $\tan \delta$ as a function of frequency, at different weight ratios of BCZT. (unpoled).....	120
5.11	Stepwise operation mechanism of P-TENG device : (a) initial state, (b) contacting, (c) pressing, and (d) releasing and separating for the energy harvesting investigation.....	122
5.12	Electrical output performance of the P-TENG device (various weight ratios of BCZT) : (a) output voltage, (b) output current, (c) average maximum output voltage, (d) average maximum output current, and (e) peak to peak output power at R 10 k Ω . The devices are operated under 500 N compressive mechanical load and \sim 1 Hz frequency.....	124
5.13	Schematic of the piezoelectric composites : microstructure diagram with various weight ratios of BCZT : (a-d) unpoled samples and (e-h) poled samples.....	125
5.14	Electrical output performance of P-TENG device (50 wt% BCZT) : (a) block diagram of conventional diode bridge rectifier (AC to DC) and charging circuit diagram, the DC output voltage, output current, and output power of various load resistances under compressive loading 500 N at frequency 1 Hz (b) and 3 Hz (c), (d) and (e) charge ability into capacitors.	127
5.15	Electrical output performance of P-TENG device (50 wt% BCZT) : Stability test of DC output, (a) output voltage, (b) output current, and (c) output power under 6900 compressive loading cycles.	128

LIST OF ABBREVIATIONS

BCZT	=	Barium calcium zirconate titanate
CNTs	=	Carbon nanotubes
MCNTs	=	Multi-walled carbon nanotubes
PDMS	=	Polydimethylsiloxane
CS	=	Conventional sintering technique
RS	=	Reactive sintering technique
SSR	=	Solid state reaction method
CIP	=	Cold isostatic pressing
MPB	=	Morphotropic phase boundary
PEHs	=	Piezoelectric energy harvesting
PENGs	=	Piezoelectric nanogenerators
TENGs	=	Triboelectric nanogenerators
P-TENGs	=	Piezo-triboelectric hybrid materials
SEM	=	Scanning electron microscope
XRD	=	X-ray diffraction
XAS	=	X-ray absorption spectroscopy
OM	=	Optical microscope
FE-SEM	=	Field emission scanning electron microscopy
DMTA	=	Dynamic mechanical thermal analysis
LCR	=	Inductance, capacitance, resistance
XANES	=	X-ray absorption near edge structure
PEFS	=	Pre-edge fine structure
FXI	=	Full field X-ray imaging

LIST OF ABBREVIATIONS (Continued)

SR-XTM	=	Synchrotron radiation X-ray tomographic microscopy
AC	=	Alternating current
DC	=	Direct current
I_{sc}	=	Short circuit current
V_{oc}	=	Open circuit voltage



CHAPTER 1

INTRODUCTION

1.1 Rationale and Background

In recent times, mobile and wearable electronic devices have become an integral part of daily life, with most of them being powered by small-sized batteries. However, the battery capacity of such devices is limited and requires frequent recharging, which can be an inconvenience for users. To address this issue, the concept of energy harvesting technology has emerged, where self-power systems based on nanogenerators are utilized to extend battery life (Harb, 2011; Liu, Fu, Sun, Lee, & Yeatman, 2021; Liu, Zhong, Lee, Lee, & Lin, 2018). Energy harvesters convert mechanical energy from human body motion, such as walking, breathing, and movement, into electricity, thereby eliminating the need for external charging sources (Houng, Sarah, Parasuraman, Khan, & Elamvazuthi, 2014; Kuang, Ruan, Chew, & Zhu, 2017; Proto, Penhaker, Conforto, & Schmid, 2017; Zhou, Al-Furjan, Zou, & Liu, 2018). In this thesis, the author studied energy harvesting based on the hybrid of piezoelectric and triboelectric effects. Piezoelectric materials, which can convert kinetic energy into electric energy, are utilized in this study to harvest electricity from stress/strain through the piezoelectric direct effect. Piezoelectric materials with excellent performance, such as PZT, PZN-PT, and PMN-PT, are currently used for energy harvesters due to their high piezoelectric charge coefficient (d_{ij}), piezoelectric voltage coefficient (g_{ij}) and figure of merit ($d \cdot g$) (Yang, Zhou, Zu, & Inman, 2018). However, the presence of lead in these materials makes them toxic to humans and the environment. In recent years, research has focused on developing lead-free alternatives using non-toxic materials (Rödel et al., 2015; Villafuerte-Castrejón et al., 2016). One such material is barium calcium zirconate titanate ((Ba,Ca)(Zr,Ti)O₃, BCZT), which exhibits good piezoelectric properties and can replace PZT (Rödel et al., 2015; Villafuerte-Castrejón et al., 2016). Various methods, including solid-state reaction and sol-gel (Pichini method), have been used to synthesize BCZT (Villafuerte-Castrejón et al., 2016). However, these methods are

time-consuming and energy intensive. Therefore, in this study, the author synthesized BCZT using conventional solid-state reaction and reactive sintering methods, which was simpler, required less energy, and took less time than other methods. BCZT is typically constructed as a ceramic material that is prone to breakage under high impact force or heavy loads, rendering it unsuitable for use in energy harvesters designed to collect energy from mechanical loads and vibration environments. Composite materials, such as PVDF, epoxy, silicone rubber, rubber, polyurethane, and polydimethylsiloxane (PDMS), have been proposed as alternatives to overcome this limitation. Among these, PDMS stands out as a promising choice due to its durability, non-toxicity, biocompatibility, non-flammability, and ease of fabrication, as documented in previous studies (Akdogan, Allahverdi, & Safari, 2005; Dagdeviren et al., 2016; Kwi-Il, Kyu, Jungho, Geon-Tae, & Jae, 2013; Park, Jeong, Kim, & Lee, 2016; Uchino, 2017). However, flexible composites are known to have lower output performance compared to bulk and MEMS piezoelectric materials due to their lower packing density (Kang, Jung, Kang, & Yoon, 2016). To compensate for this limitation, the triboelectric effect can be employed to generate additional energy. Since its discovery in 2012, the triboelectric effect has been recognized as a promising means of generating electrical energy by electrostatic induction and triboelectrification (Z. L. Wang, 2014). Its simple structure and high output voltage make it an attractive candidate for integration with the BCZT/MCNTs/PDMS composite to enhance the electrical output for self-powered nano-micro systems.

Recently, there has been an active research focus on enhancing output performance from mechanical energy by using piezo-triboelectric hybrid systems. Examples of such systems include P(VDF-TrFE) – PDMS:MWCNT (X. Wang et al., 2016), BaTiO₃:PDMS-Cu (Suo et al., 2016) BaTiO₃:PDMS:MCNTs-Al (Xue et al., 2015). These studies have demonstrated that the output power of hybrid systems exhibits superior performance compared to that of piezoelectric and triboelectric output alone, thus opening up the possibility of lead-free piezo-triboelectric hybrids for energy harvesting applications. However, despite these findings, there is currently a lack of knowledge regarding the fabrication and investigation of piezo-triboelectric hybrid energy harvesting based on the composite of BCZT/MCNTs/PDMS piezoelectric materials.

Therefore, this thesis aims to address this gap by studying the fabrication and investigation of the energy harvesting properties of these materials for potential application.

1.2 Research Objectives

The critical goals of this dissertation are summarized as follows:

1.2.1 To synthesize and fabricate BCZT bulk ceramic using the solid-state reaction and sintering technique, and to characterize its physical, dielectric, piezoelectric, electrical properties, and energy harvesting performance under compressive loads and mechanical cyclic loading,

1.2.2 To fabricate a 0-3 structure of BCZT/MCNTs/PDMS composite and investigate the effect of the BCZT weight percentage ratios on the physical, mechanical, dielectric, and electrical properties of the composite,

1.2.3 To fabricate a piezo-triboelectric hybrid device based on BCZT /MCNTs/PDMS composite and investigate the effect of the BCZT weight percentage ratios on enhancing the electrical output performance of the hybrid device. This will be achieved by investigating the energy harvesting performance under compressive load force and mechanical cyclic loading of the device for potential energy harvesting applications.

1.3 Hypotheses

The objective of this dissertation is to enhance the energy harvesting potential of lead-free piezoelectric by utilizing piezo-triboelectric hybridization. The following hypotheses are proposed to achieve this aim:

1.3.1 By employing a suitable sintering technique, the piezoelectric properties of BCZT ceramic could be improved, which could influence the phase, grain size, density, dielectric, piezoelectric, and electrical properties of the material. The improvement of piezoelectric properties for energy harvesting purposes can be gauged by assessing the piezoelectric charge coefficient (d_{33}) and piezoelectric voltage coefficient (g_{33}).

1.3.2 The physical, mechanical, dielectric, electrical properties, and electrical output performance of BCZT/MCNTs/PDMS composites, used for energy harvesting applications, could be affected by the weight percentage ratios of BCZT particles present in them.

1.3.3 The energy harvesting performance of BCZT/MCNTs/PDMS piezoelectric composite could be further enhanced by utilizing piezo-triboelectric hybridization. Additionally, it could provide better mechanical endurance under compressive loading when compared to BCZT piezoelectric ceramic.

1.4 Scope of Thesis

The scope of this thesis pertains to the fabrication and evaluation of the energy harvesting performance of various materials, including BCZT ceramic, BCZT /MCNTs /PDMS composite, and piezo-triboelectric hybridization based on BCZT/MCNTs/PDMS composite. The specific objectives of this research are outlined as follows:

1.4.1 To improve the fabrication process and achieve a high piezoelectric coefficient ($d_{33} \sim 350\text{--}650$ pC/N, $g_{33} \sim 12\text{--}20$ (10^{-3} Vm/N) for BCZT bulk piezoelectric ceramic using solid-state reaction and sintering techniques,

1.4.2 To enhance the mechanical endurance of energy harvesting materials subjected to a load force greater than 300 newtons by developing a flexible composite with a 0-3 structure of BCZT/MCNTs/PDMS composite. The study will also examine the impact of BCZT weight percentage ratios on the physical, mechanical, dielectric, and electrical properties of the piezoelectric composite,

1.4.3 To optimize the energy harvesting performance by constructing a piezo-triboelectric hybrid based on BCZT/MCNTs/PDMS composite. The research will investigate the influence of the BCZT weight percentage ratios on the energy harvesting performance of these devices under compressive loading force and frequency, as well as study impedance matching via external load resistance. Additionally, the devices will be tested for mechanical endurance under compressive loading.

1.5 Usefulness of the Research

This research aims to achieve the following objectives by outlining its significance:

1.5.1 To understand the fabrication process of lead-free BCZT piezoelectric ceramics and investigate their physical, dielectric, piezoelectric, and electrical properties for potential energy harvesting applications,

1.5.2 To comprehend the fabrication processing of piezoelectric ceramic-polymer composites based on BCZT/MCNTs/PDMS and examine the effect of BCZT weight percentage ratios on physical, mechanical, dielectric, and electrical properties of the piezoelectric composites,

1.5.3 To build the prototype of an energy harvester based on the piezo-triboelectric hybridization using BCZT/MCNTs/PDMS materials,

1.5.4 To provide a guideline for improving the energy harvesting output performance of piezo-triboelectric hybridization devices based on BCZT/MCNTs/PDMS materials under compressive cyclic loading and frequency, as well as their potential applications.

1.6 Outline of Thesis

The remaining portions of this thesis are organized as follows:

Chapter 2 provides the background and basic knowledge of lead-free piezoelectric ceramic, piezoelectric-polymer composite, and piezo-triboelectric hybrid materials, as well as their theoretical underpinnings and practical uses for energy harvesting. Additionally, reviews of previous research on lead-free piezoelectric ceramic, piezoelectric composite, and piezo-triboelectric hybrid devices based on perovskite piezoelectric (lead-free) and polymer (polydimethylsiloxane; PDMS) composite on energy harvesting output performance are presented.

Chapter 3 describes experiments conducted to investigate the effectiveness of conventional sintering (CS) and reactive sintering (RS) methods on the phase, microstructure, piezoelectric, dielectric, and ferroelectric properties of barium calcium zirconate titanate (BCZT) ceramics. In both CS and RS techniques, X-ray Diffraction (XRD) was used to identify the BCZT ceramics' phase and structure. Furthermore, Scanning Electron Microscopy (SEM) was employed to study the surface morphology and grain size variations for different dwell times. Additionally, Pre-edge fine structure (PEFS) and X-Ray absorption near edge spectroscopy (XANES) were used to elucidate the variation and oxidation state of Ti and Zr in BCZT ceramics.

Chapter 4 demonstrates the use of $\text{Ba}_{0.85}\text{Ca}_{0.15}\text{Zr}_{0.1}\text{Ti}_{0.9}\text{O}_3$ (BCZT) piezoceramics for ultra-low frequency energy harvesting. The design and output performance of the BCZT energy harvester is presented. BCZT ceramics were fabricated using the solid-state reactive sintering (SSRS) method and the cold isostatic compressive (CIP) technique. This chapter investigates the ceramic phase and microstructure, dielectric properties, ferroelectric properties, piezoelectric properties, electrical output performance under various compressive loads, stored voltage and energy density in capacitors, and reliability of BCZT ceramics.

Chapter 5 introduces a piezo-triboelectric nanogenerator (P-TENG) that can convert mechanical energy into electrical energy in compressive mode at low frequencies. An arch-shaped P-TENG device based on BCZT/MCNTs/PDMS composite

with various weight percentages of BCZT fillers was prepared and utilized for energy harvesting. The chapter investigated the physical, mechanical, electrical, and dielectric properties of composites. Furthermore, the optimal condition of the P-TENG device was studied for electrical output performance, including the output voltage, output current, output power, impedance matching via various load resistances, charge ability into capacitors, and stability tests under vertical compressive loads and frequency.

Finally, Chapter 6 provides the summary of all the conclusions reached in this thesis, along with recommendations for further research.



1.7 References

- Akdogan, E. K., Allahverdi, M., & Safari, A. (2005). Piezoelectric composites for sensor and actuator applications. *IEEE Transactions on Ultrasonics, Ferroelectrics, and Frequency Control*, 52(5), 746-775. doi:10.1109/TUFFC.2005.1503962
- Covaci, C., & Gontean, A. (2020). Piezoelectric Energy Harvesting Solutions: A Review. *Sensors*, 20(12), 3512. Retrieved from <https://www.mdpi.com/1424-8220/20/12/3512>
- Dagdeviren, C., Joe, P., Tuzman, O. L., Park, K.-I., Lee, K. J., Shi, Y., Rogers, J. A. (2016). Recent progress in flexible and stretchable piezoelectric devices for mechanical energy harvesting, sensing and actuation. *Extreme Mechanics Letters*, 9, 269-281. doi:<https://doi.org/10.1016/j.eml.2016.05.015>
- Harb, A. (2011). Energy harvesting: State-of-the-art. *Renewable Energy*, 36(10), 2641-2654. doi:<https://doi.org/10.1016/j.renene.2010.06.014>
- Houng, H. O. C., Sarah, S., Parasuraman, S., Khan, M. K. A. A., & Elamvazuthi, I. (2014). Energy Harvesting from Human Locomotion: Gait Analysis, Design and State of Art. *Procedia Computer Science*, 42, 327-335. doi:<https://doi.org/10.1016/j.procs.2014.11.070>
- Kang, M.-G., Jung, W.-S., Kang, C.-Y., & Yoon, S.-J. (2016). Recent Progress on PZT Based Piezoelectric Energy Harvesting Technologies. *Actuators*, 5(1), 5. Retrieved from <http://www.mdpi.com/2076-0825/5/1/5>
- Kuang, Y., Ruan, T., Chew, Z. J., & Zhu, M. (2017). Energy harvesting during human walking to power a wireless sensor node. *Sensors and Actuators A: Physical*, 254, 69-77. doi:<https://doi.org/10.1016/j.sna.2016.11.035>
- Kwi-Il, P., Kyu, J. C., Jungho, R., Geon-Tae, H., & Jae, L. K. (2013). Flexible and Large-Area Nanocomposite Generators Based on Lead Zirconate Titanate Particles and Carbon Nanotubes. *Advanced Energy Materials*, 3(12), 1539-1544. doi:[doi:10.1002/aenm.201300458](https://doi.org/10.1002/aenm.201300458)

- Liu, H., Fu, H., Sun, L., Lee, C., & Yeatman, E. M. (2021). Hybrid energy harvesting technology: From materials, structural design, system integration to applications. *Renewable and Sustainable Energy Reviews*, 137, 110473. doi: <https://doi.org/10.1016/j.rser.2020.110473>
- Liu, H., Zhong, J., Lee, C., Lee, S.-W., & Lin, L. (2018). A comprehensive review on piezoelectric energy harvesting technology: Materials, mechanisms, and applications. *Applied Physics Reviews*, 5(4), 041306. doi:10.1063/1.5074184
- Park, K.-I., Jeong, C. K., Kim, N. K., & Lee, K. J. (2016). Stretchable piezoelectric nanocomposite generator. *Nano Convergence*, 3(1), 12. doi:10.1186/s40580-016-0072-z
- Priya, S., Song, H. C., Zhou, Y., Varghese, R. P., Chopra, A., Kim, S.-G., Polcawich, R. (2017). A Review on Piezoelectric Energy Harvesting: Materials, Methods, and Circuits. *Energy Harvesting and Systems*, 4, 3 - 39.
- Proto, A., Penhaker, M., Conforto, S., & Schmid, M. (2017). Nanogenerators for Human Body Energy Harvesting. *Trends in Biotechnology*, 35(7), 610-624. doi: <https://doi.org/10.1016/j.tibtech.2017.04.005>
- Rödel, J., Webber, K. G., Dittmer, R., Jo, W., Kimura, M., & Damjanovic, D. (2015). Transferring lead-free piezoelectric ceramics into application. *Journal of the European Ceramic Society*, 35(6), 1659-1681. doi:<https://doi.org/10.1016/j.jeurceramsoc.2014.12.013>
- Suo, G., Yu, Y., Zhang, Z., Wang, S., Zhao, P., Li, J., & Wang, X. (2016). Piezoelectric and Triboelectric Dual Effects in Mechanical-Energy Harvesting Using BaTiO₃/Polydimethylsiloxane Composite Film. *ACS Applied Materials & Interfaces*, 8(50), 34335-34341. doi:10.1021/acsami.6b11108
- Uchino, K. (2017). Chapter 9 - Piezoelectric Composite Materials. In *Advanced Piezoelectric Materials (Second Edition)* (pp. 353-382): Woodhead Publishing.

- Villafuerte-Castrejón, M., Morán, E., Reyes-Montero, A., Vivar-Ocampo, R., Peña-Jiménez, J.-A., Rea-López, S.-O., & Pardo, L. (2016). Towards Lead-Free Piezoceramics: Facing a Synthesis Challenge. *Materials*, 9(1), 21. doi:<https://doi.org/10.3390/ma9010021>
- Wang, X., Yang, B., Liu, J., Zhu, Y., Yang, C., & He, Q. (2016). A flexible triboelectric-piezoelectric hybrid nanogenerator based on P(VDF-TrFE) nanofibers and PDMS/MWCNT for wearable devices. *Scientific Reports*, 6, 36409. doi:10.1038/srep36409
- Wang, Z. L. (2014). Triboelectric nanogenerators as new energy technology and self-powered sensors - Principles, problems and perspectives. *Faraday Discussions*, 176(0), 447-458. doi:10.1039/C4FD00159A
- Xue, C., Li, J., Zhang, Q., Zhang, Z., Hai, Z., Gao, L., Sun, D. (2015). A Novel Arch-Shape Nanogenerator Based on Piezoelectric and Triboelectric Mechanism for Mechanical Energy Harvesting. *Nanomaterials*, 5(1), 36. Retrieved from <http://www.mdpi.com/2079-4991/5/1/36>
- Yang, Z., Zhou, S., Zu, J., & Inman, D. (2018). High-Performance Piezoelectric Energy Harvesters and Their Applications. *Joule*, 2(4), 642-697. doi:<https://doi.org/10.1016/j.joule.2018.03.011>
- Zhou, M., Al-Furjan, M. S. H., Zou, J., & Liu, W. (2018). A review on heat and mechanical energy harvesting from human – Principles, prototypes and perspectives. *Renewable and Sustainable Energy Reviews*, 82, 3582-3609. doi:<https://doi.org/10.1016/j.rser.2017.10.102>

CHAPTER 2

LITERATURE REVIEWS

This chapter is structured into three distinct sections. First, Section 2.1 provides the background on lead-free piezoelectric ceramics, BCZT piezoelectric ceramic, the theory and principle of piezoelectric effect related to energy harvesting, and their applications. The second part focuses on the fundamentals of piezoceramic-polymer composites, the theoretical model of 0-3 piezoelectric composites, and their applications in Section 2.2. The last part discusses the basic principles of triboelectricity, piezo-triboelectric hybrid materials, the trends in piezoelectric-triboelectric hybrids, and their applications in Section 2.3.

2.1 Lead-free piezoelectric

2.1.1 Piezoelectric ceramics

Piezoelectric effects refer to the phenomenon exhibited by certain materials whereby they are capable of transforming mechanical energy into electrical (called direct piezoelectric effect) and conversely, electrical energy into mechanical energy (called converse piezoelectric effect). Based on their crystal structures, the most extensively investigated piezoelectric ceramics can be classified into four groups: (1) perovskite, such as PbZrTiO_3 , $(\text{K}_{0.5}\text{Na}_{0.5})\text{NbO}_3$ (KNN), $(\text{Bi}_{0.5}\text{Na}_{0.5})\text{TiO}_3$ (BNT), and BaTiO_3 , (2) bronze-tungsten, such as PbNb_2O_6 , (3) bismuth layer, such as $\text{Bi}_4\text{Ti}_3\text{O}_{12}$ and $\text{PbBi}_2\text{Nb}_2\text{O}_9$, and (4) perovskite layer, such as $\text{Sr}_2\text{Nb}_2\text{O}_7$ and $\text{Ca}_2\text{Nb}_2\text{O}_7$. Figure 2.1 shows the various crystal structures of piezoelectric materials and their properties on the curie temperature (T_c) and the piezoelectric constant (d_{33}). Among the perovskite-structured piezoelectric materials, $\text{Pb}(\text{Zr},\text{Ti})\text{O}_3$ (PZT), PMN-PT, and PZT-PT are the most extensively studied because of their high-performance in piezoelectric, electrical, and electromechanical properties. (Caliò et al., 2014; Khan, Abas, Kim, & Oh, 2016; Kenji Uchino, 2017a; Z. Yang, Zhou, Zu, & Inman, 2018; Z. Yang & Zu, 2016). Piezoelectric materials have also been employed in self-powered technologies where electrical

power can be harvested from mechanical vibrations. The vibration sources could be building and bridge oscillations, human motion, or vehicle vibrations, among others. Such self-powered devices have a wide range of applications, including tire condition monitors, pacemakers, and energy-harvesting shoes (Covaci & Gontean, 2020; Kuang, Ruan, Chew, & Zhu, 2017; Proto, Penhaker, Conforto, & Schmid, 2017; Z. Yang et al., 2018). However, lead-based piezoelectric ceramics are not considered suitable options because the lead (Pb) element is toxic to both health and the environment. Therefore, many research groups have been trying to develop lead-free piezoelectric materials that could potentially replace lead-based ones (Hong et al., 2016; Panda & Sahoo, 2015; Rödel et al., 2015; Villafuerte-Castrejón et al., 2016). It is widely known that lead-free piezoelectric materials with a perovskite structure exhibit high piezoelectric capabilities due to the structure's ability to enable spontaneous polarization rotations along three-dimensional orientations (Du et al., 2008; SHUKAI, 2012; Sluka, Tagantsev, Damjanovic, Gureev, & Setter, 2012). As a result, lead-free piezoelectric materials with a perovskite structure and their applications are of significant interest in the field of materials science and engineering (Villafuerte-Castrejón et al., 2016). The general perovskite unit cell structure (ABO_3) of lead-free piezoelectric ceramics has a pseudo-cubic shape, as illustrated in Figure 2.2. Among the lead-free piezoelectric materials, some of the most highly promising ones include $BaTiO_3$ (BT), $Ba_{1-x}Ca_xTi_{1-y}Zr_yO_3$ (BCZT), $(Bi_{0.5}Na_{0.5})TiO_3$ (BNT-based), and $(K_{0.5}Na_{0.5})NbO_3$ (KNN-based). Figure 2.3 and Figure 2.4 shows a comparison of the properties of these materials with PZT (Rödel et al., 2015; Villafuerte-Castrejón et al., 2016). Barium calcium zirconate titanate ($(Ba,Ca)(Zr,Ti)O_3$ (BCZT) ceramic exhibits excellent piezoelectric charge coefficient (d_{33}^*) and figure of merit ($d \cdot g$) values, which are equivalent to those of PZT and greater than those of KNN and BNT-based ceramics (Rödel et al., 2015). These values represent the efficiency of these materials in converting mechanical energy to electrical energy (Kang, Jung, Kang, & Yoon, 2016; Li, Xu, Liu, & Gao, 2018). A review of the BCZT lead-free piezoelectric ceramics and perovskite-structured piezoelectric materials is provided in the section 2.1.2.

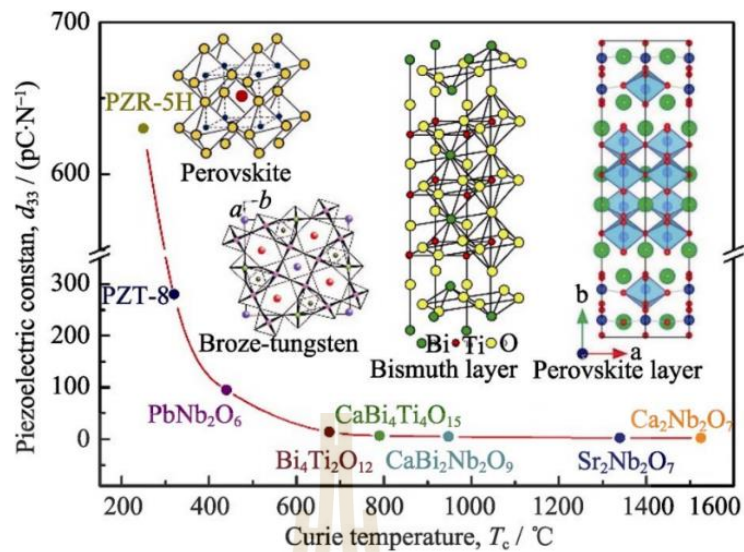


Figure 2.1 Relationship between the curie temperature (T_c) and the piezoelectric constant (d_{33}) of piezoelectric ceramics with various crystal structures (inset shows schematics of the perovskite, tungsten bronze, bismuth layer, and perovskite layer structures). (ZHOU, CHEN, & DONG, 2018)



Figure 2.2 Perovskite structure in pseudo-cube shape (ABO_3). For lead-free piezoelectric ceramics, the typical cations are $A = Ba^{2+}, Ca^{2+}, Bi^{3+}, Na^+K^+$; $B = Ti^{4+}, Zr^{4+},$ and Nb^{5+} ; and $X = O^{2-}$. (Villafuerte-Castrejón et al., 2016)

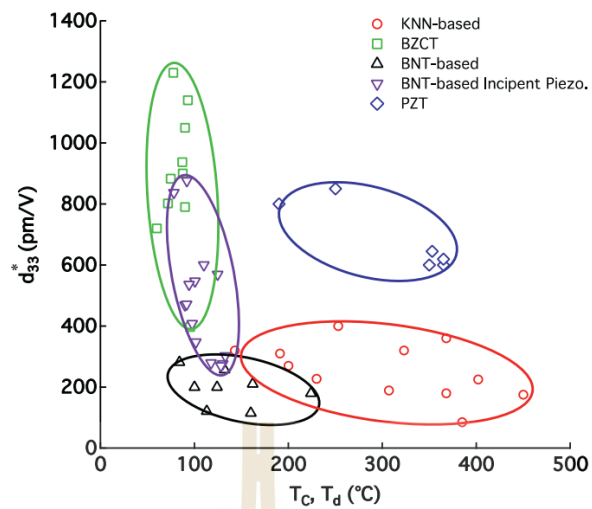


Figure 2.3 Relationship between the piezoelectric coefficient and the depolarization temperature of KNN-based, BCZT, BNT-based, BNT-based Incipient Piezoelectric, and PZT. (Rödel et al., 2015)

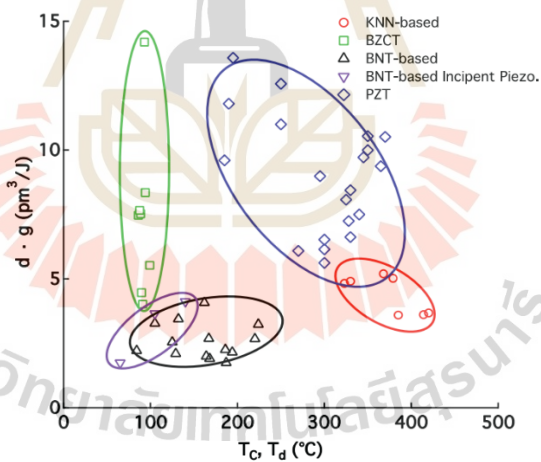


Figure 2.4 Relation of $d \cdot g$ in a function of depolarization temperature for KNN-based, BCZT, BNT-based, BNT-based Incipient Piezoelectric, and PZT. (Rödel et al., 2015)

2.1.2 BCZT Lead-free piezoelectric ceramic

Barium calcium zirconate titanate (BCZT) piezoelectric ceramics have a high piezoelectric coefficient (d_{33}^*) and Figure of Merit (FOM) ($d \cdot g$) equivalent to PZT ceramics as shown in Figure 2.3 and Figure 2.4 (Rödel et al., 2015). The BCZT ceramics

have an ABO_3 perovskite structure, as illustrated in Figure 2.2 (Villafuerte-Castrejón et al., 2016). Many researchers reported that BCZT ceramics were fabricated from $BaTiO_3$ -based solid solutions with various A-site and B-site dopants that were utilized to improve the piezoelectric and dielectric properties. For example, the Ca^{2+} and Zr^{4+} doped $BaTiO_3$ exhibits $Ba_{1-x}Ca_xTi_{1-y}Zr_yO_3$ ceramics with high piezoelectric constant ($d_{33} = 620$ pC/N) of a certain stoichiometry of BCZT (i.e. $Ba_{0.85}Ca_{0.15}Ti_{0.90}Zr_{0.10}O_3$) (W. Liu & Ren, 2009). From the ternary system diagram of $BaTiO_3$ - $BaZrO_3$ - $CaTiO_3$, it is found that the excellent piezoelectric constant (d_{33}) around 328–637 pC/N belongs to $0.5Ba(Ti_{0.80}Zr_{0.20})O_3$ - $0.5(Ba_{0.70}Ca_{0.30})TiO_3$, as shown in Figure 2.5 (Villafuerte-Castrejón et al., 2016). Additionally, Pan Wang et al. (P. Wang, Li, & Lu, 2011) reported that $(Ba_{0.85}Ca_{0.15})(Ti_{0.9}Zr_{0.1})O_3$ (BCZT) exhibited d_{33} of 650 pC/N through the optimization of calcining and sintering temperature, as well as dwelling time. Moreover, Tian et al. (Tian, Wei, Chao, Liu, & Yang, 2013) reported on the phase transition behavior and piezoelectric properties of $(Ba_{1-x}Ca_x)(Zr_{0.1}Ti_{0.9})O_3$ and $(Ba_{0.85}Ca_{0.15})(Zr_yTi_{1-y})O_3$ ceramics. They found that $(Ba_{0.85}Ca_{0.15})(Ti_{0.9}Zr_{0.1})O_3$ ceramic exhibited d_{33} of 572 pC/N, with the MPB region close to tetragonal phase side. Furthermore, $(Ba_{100-15}Ca_{15})(Ti_{100-9.5}Zr_{9.5})O_3$ ($BC_{15}TZ_{9.5}$) piezoelectric ceramic showed d_{33} of 458 pC/N and d_{33}^* of 740 pm/V (Y. Zhang et al., 2014). Several research articles showed several methods for BCZT ceramics fabrication including the solid-state reactive (SSR), hydrothermal, Pechini, and sol-gel techniques (Villafuerte-Castrejón et al., 2016). It is known that different synthesis processes and preparation environments can impact physical, chemical, and electrical properties. For example, SSR-produced BCZT ceramics have outstanding piezoelectric coefficients (d_{33}) of 140–620 pC/N (Villafuerte-Castrejón et al., 2016), which are higher than those produced by other techniques and equal to PZT ($d_{33} = 225$ –593 pC/N) (Z. Yang et al., 2018). Therefore, the recipe for $(Ba_{0.85}Ca_{0.15})(Ti_{0.9}Zr_{0.1})O_3$ piezoelectric ceramics fabricated and synthesized using a solid-state reaction method could be used for piezoelectric energy harvesting applications due to its high piezoelectric properties compared to PZT (Rödel et al., 2015; Villafuerte-Castrejón et al., 2016).

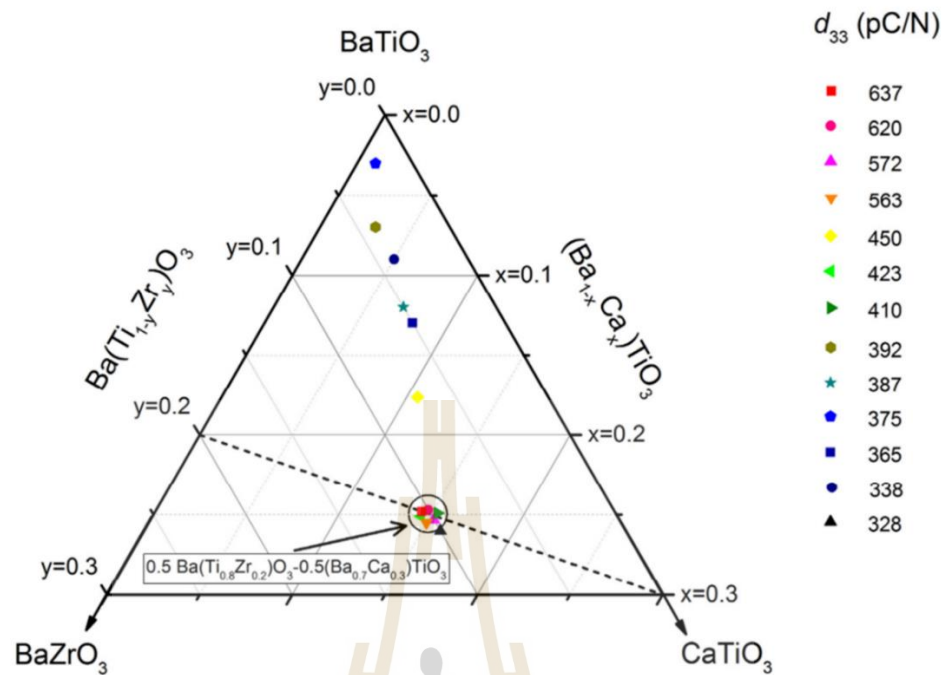


Figure 2.5 System BaTiO_3 - BaZrO_3 - CaTiO_3 ternary diagram and the piezoelectric constant (d_{33}) values. (Villafuerte-Castrejón et al., 2016)

2.1.3 Direct piezoelectric effect

The concept of piezoelectric energy harvesting is based on the direct piezoelectric effect, which involves converting mechanical energy into electrical energy. This effect is generated when piezoelectric materials are subjected to a mechanical force, which generates electrical surface charges, as illustrated in Figure 2.6 (J.-H. Lee et al., 2016). By creating a piezoelectric device with top and bottom electrodes, the piezoelectric materials can be used for various applications, including sensors, self-power generators, and electric energy harvesters, when an external force is applied. This process is inspired by the need to harness energy from various universal sources, such as vibration, body motion, acoustic noise, airflow, among others, through efficient energy conversion using piezoelectric materials.

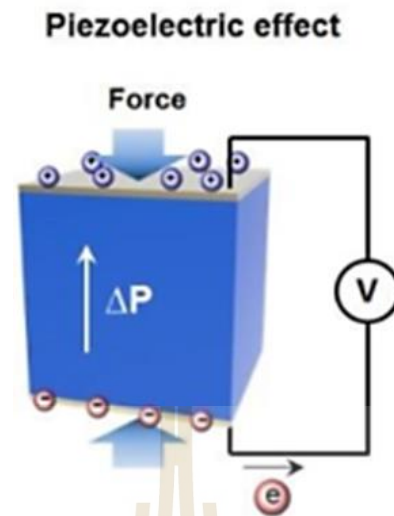


Figure 2.6 Direct piezoelectric effect. (J.-H. Lee et al., 2016)

To apply the direct piezoelectric effect for energy harvesting, it is necessary to have a fundamental understanding of the two subscript notations in the piezoelectric constant (d_{ij}). This concept can also be extended to other piezoelectric parameters, such as g_{ij} and ϵ_{ij} . The subscript notations "i" and "j" in the piezoelectric constant (d_{ij}) represent the direction of the piezoelectric properties. Specifically, the first subscript "i" denotes the direction of the electric field (E) or the displacement of the dielectric (D), while the second subscript "j" represents the direction of the mechanical stress (σ) or strain (S). The axes of reference for piezoelectric constant notation are illustrated in Figure 2.7. The subscripts 1 and 2 represent orthogonal axes that are perpendicular to the poling axis, denoted by the subscript 3. Furthermore, the subscripts 4, 5, and 6 refer to the shear stress or strain direction that is perpendicular to axes 1, 2, and 3, respectively.

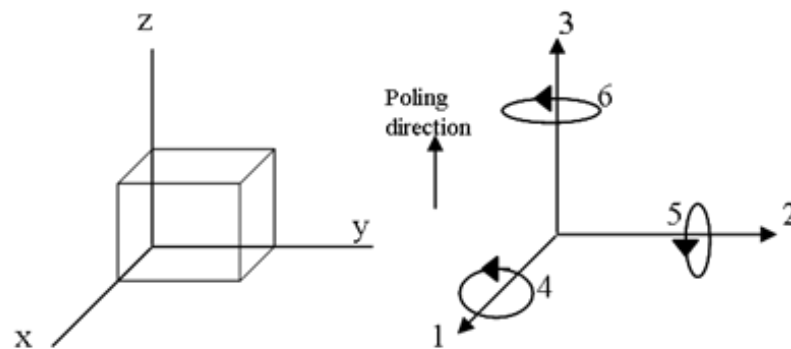


Figure 2.7 Reference axis for piezoelectric constant notations.

For instance, the piezoelectric constant (d_{ij}) expressed as d_{33} indicates that an electric field is applied parallel to the poling axis, resulting in deformation (strain). The first subscript "3" specifies the direction of the electric field or dielectric displacement (3-axis), and the second subscript "3" represents the mechanical deformation (strain) that occurs in the same direction as the 3-axis, which is commonly referred to as the d_{33} -effect. If the electric field induces transverse strain along the 1-axis or 2-axis when the poling direction is in the 3-axis, the d_{ij} constant can be expressed as d_{31} , which is called the d_{31} -effect. Figure 2.8 illustrates the two primary operation modes of the piezoelectric energy harvester: (1) d_{31} and (2) d_{33} effects. In d_{31} , the "3" represents a polarization direction that is perpendicular to the direction of applied stress represented by the "1" direction. This is the common operating mode used for cantilever beam-based piezoelectric energy harvesters. In d_{33} , the applied stress is parallel to the polarization direction represented by the "3" direction. Both d_{31} and d_{33} operation modes, the electrode surfaces are perpendicular to the polarization direction, while the electric field is parallel to the polarization. (Covaci & Gontean, 2020; Z. Yang et al., 2018).

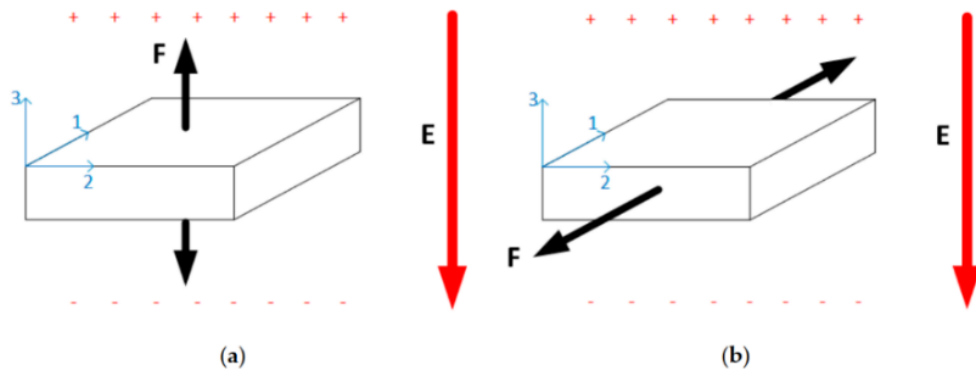


Figure 2.8 Piezoelectric working operation in (a) d_{33} (transverse mode) and (b) d_{31} (longitudinal mode). (Covaci & Gontean, 2020)

When an electric field is applied perpendicular to the poling direction or parallel to the 2-axis or 1-axis, it can cause shear strains on the plane that is normal to the 4 or 5-axis. In such cases, the d constant is commonly referred to as the d_{15} -effect or d_{24} -effect. Having high d constants is desirable for transducer applications (Shields, 1966). Figure 2.9 illustrates the diagrams of the d_{33} -effect, d_{31} -effect, and d_{15} -effect.

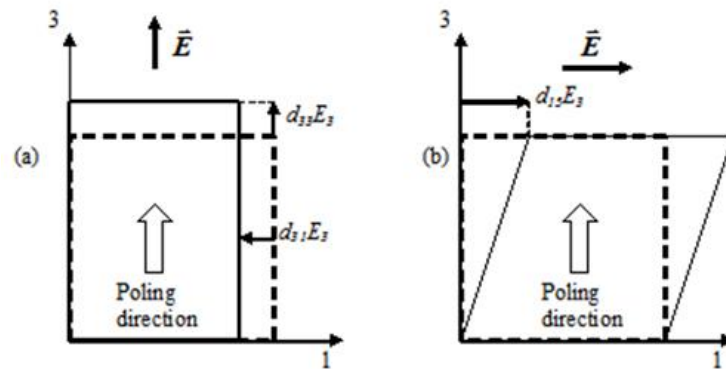


Figure 2.9 The piezoelectric constants of a ferroelectric material poled in three directions are shown. (a) depicts the d_{33} and d_{31} effects, while (b) depicts the d_{15} effect.

2.1.4 Theory and principle of piezoelectric energy harvesting

Polarization domains in piezoelectric materials change when mechanical stress (or strain) is applied to the materials. This causes a change in the polarization charge density, which can be represented by the ratio of surface charges to electrode area. Equation (2.1) states that the polarization charge density caused by electrical movement is proportional to the applied mechanical stress (J.-H. Lee et al., 2016).

$$\rho = d\sigma \quad (2.1)$$

where ρ is polarization charge density

d is piezoelectric coefficient

σ is applied stress

Then the charge density results in an electric field and electric potential, as shown in equation (2.2). (J.-H. Lee et al., 2016)

$$\nabla \cdot E = \frac{r}{\epsilon} \quad (2.2)$$

where $\nabla \cdot E$ is divergence of the electric field

r is charge density

ϵ is permittivity

The direct piezoelectric effect phenomenon is the basis for piezoelectric energy harvesting (PEHs) and is governed by the composite of equation (2.3), which connects the mechanical domain of stress (T) and strain (S) to the electric domain of electric field (E) and charge density (D): (Z. Yang et al., 2018)

$$\begin{bmatrix} \text{Converse} \\ \text{Direct} \end{bmatrix} = \begin{bmatrix} S \\ D \end{bmatrix} = \begin{bmatrix} s^E & d^t \\ d & \varepsilon^T \end{bmatrix} \begin{bmatrix} T \\ E \end{bmatrix} \quad (2.3)$$

where s^E is the compliance under a constant electrical field

ε^T is the dielectric permittivity under a constant stress

d and d^t are the matrices for direct and converse piezoelectric effects (d^t is the transpose of d)

To compare piezoelectric devices with electrical phenomena, one can consider them as parallel plate capacitors with surface area (S) and thickness (t), which, when subjected to stress (σ), generate charge (Q) and voltage (V). Equation (2.4) determines the total converted electric energy (U) as a function of σ , and it can be written as (Z. Yang et al., 2018)

$$U = \frac{1}{2} QV = \frac{1}{2} (d \times \sigma \times S) \cdot (g \times \sigma \times t) = \frac{1}{2} d \times g \times \sigma^2 \times Volume \quad (2.4)$$

Here, d and g are piezoelectric charge and piezoelectric voltage constants, respectively, which are determined by the specific operating mode of the piezoelectric material. Simplified equation (2.4) predicts that materials with high $d \times g$ values exhibit high-power density when directly subjected to stress.

Piezoelectric materials, consisting of dense polycrystalline and single crystalline ceramics, have been studied for their remarkable properties. The piezoelectric charge constant (d), piezoelectric voltage constant (g), electromechanical coupling factor (k), mechanical quality factor (Q_m), Figures of Merit (FOM), and the factors of piezoelectric materials that describe the properties of energy harvesting are shown below. (Kang et al., 2016; Uchino, 2018)

1. Piezoelectric strain (pm/V) and Charge constant (pC/N) (Kang et al., 2016)

$$\sigma = d_{ij}E \quad (2.5)$$

where d_{ij} is piezoelectric strain and charge constant, σ and E are stress and external electric field.

2. Piezoelectric voltage constant (Vm/N) (Kang et al., 2016)

$$E = g_{ij}\sigma \quad (2.6)$$

where g_{ij} is piezoelectric voltage constant, E is the electric field, σ is stress

3. Electromechanical coupling factor (Kang et al., 2016)

$$k^2 = \left(\frac{\text{Stored mechanical energy}}{\text{Input electrical energy}} \right) \quad (2.7)$$

$$k^2 = \left(\frac{\text{Stored electrical energy}}{\text{Input mechanical energy}} \right) \quad (2.8)$$

The input electrical energy is $\left(\frac{1}{2}\right) \epsilon_0 \epsilon_r E^2$ per unit volume and stored mechanical energy per unit volume under zero external stress is given by $\frac{\frac{1}{2}\sigma^2}{\sigma} = \frac{\left(\frac{1}{2}\right)(dE)^2}{\sigma}$. Therefore, k^2 can be calculated from

$$k^2 = \left[\frac{\left(\frac{1}{2}\right)(d_{ij}E)^2}{\sigma} \right] = \frac{d_{ij}^2}{\epsilon_0 \epsilon_r \sigma} \quad (2.9)$$

where σ is stress

4. Mechanical quality factor (Kang et al., 2016)

$$Q_m = \frac{\omega_0}{2\Delta\omega} \quad (2.10)$$

where ω_0 is resonance frequency

5. Permittivity (Li et al., 2018)

$$\varepsilon_r = \frac{Ct}{\varepsilon_0 A} \quad (2.11)$$

where C is the measured capacitance, t is the thickness of the workpiece, ε_0 is dielectric constant in a vacuum, A is the cross-sectional area of the plate conductor.

6. Piezoelectric constant (d)

$$d_{ij} = \frac{\int_0^t I dt}{F} \quad (2.12)$$

where d_{ij} is piezoelectric constant (pC/N), I is electric current (pC), F is the force used to press (N)

7. Piezoelectric voltage constant (g) (Li et al., 2018)

$$g_{ij} = \frac{d_{ij}}{\varepsilon_r \varepsilon_0} \quad (2.13)$$

where d_{ij} is piezoelectric constant (pC/N), ε_r is relative dielectric constant, ε_0 is dielectric constant in a vacuum

8. Figure of merit (FOM) (Li et al., 2018)

$$FOM(\text{pm}^2/\text{N}) = d_{ij} \times g_{ij} = \frac{(d_{ij})^2}{\varepsilon_r \varepsilon_0} \quad (2.14)$$

where d_{ij} is piezoelectric constant (pC/N), g_{ij} is piezoelectric voltage constant (10^{-3}VmN^{-1}), (i is polarization direction, j is loading direction stress/strain).

Therefore, the above equations require the d and g values for utilizing piezoelectric materials in energy harvesting. As shown in Table 2.1, the d_{33} and g_{33} values of PZT demonstrate higher piezoelectric properties than those of BaTiO₃. Lead-free piezoelectric materials such as (Ba, Ca) (Zr, Ti) O₃ show properties that compete with PZT. Thus, BCZT is an interesting lead-free piezoelectric material for energy harvesting, representing PZT.

Table 2.1 Piezoelectric properties of BCZT ceramics compare with other piezoelectric materials.

Materials/Properties	(Ba,Ca) (Zr,Ti)O ₃	BaTiO ₃	PZT-4	PZT-5A	PZT-5H	PZT-8
d_{33} (pC/N)	546	149	289	374	593	225
g_{33} (10 ⁻³ Vm/N)	15.3	14.1	26.1	24.8	19.7	25.4
k_{33}, k_p	0.65	0.48	0.7	0.71	0.75	0.64
Mechanical Q_M		300	500	75	65	1,000
Dielectric loss			0.4 %		2 %	0.4 %
Curie temperature (°C)	94	115	328	365	193	300
FOM ($d_{33} * g_{33}$) (10 ⁻¹⁵ m ² /N)	8,354	2,100	7,543	9,275	11,682	5,715
Ref.	(Rödel et al., 2015)	Z. Yang et al., 2018(Z. Yang et al., 2018)				

According to the resonance power formula shown in equation (2.15), the power density of the harvested mechanical energy P_{res} , is influenced by the frequency and magnitude of the motion (Mitcheson, Green, Yeatman, & Holmes, 2004).

$$P_{res} = 4\pi^3 m f_{res}^3 y Z_{max} \quad (2.15)$$

where m is the inertial mass, f_{res} is the resonance frequency, y is the amplitude of vibration of the housing, and Z_{max} is the maximum displacement. Figure 2.10 depicts the general operating frequency level for various mechanical energy sources.

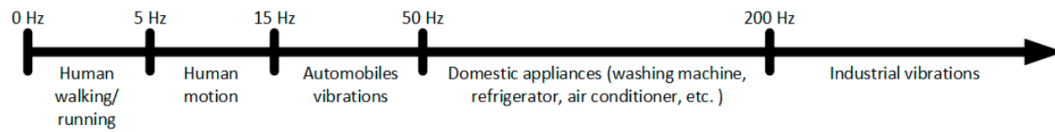


Figure 2.10 The frequency range for various mechanical energy sources. (Maamer, Boughamoura, El-Bab, Francis, & Tounsi, 2019)

2.1.5 Application of piezoelectric ceramics for energy harvesting

Recently, significant developments have been made in the field of piezoelectric energy harvesters (PEHs), with the introduction of innovative methods and unique structures. These energy harvesters can be classified into several types, including bulk type, microelectronic systems (MEMS), and flexible energy harvesters (Kang et al., 2016; Li et al., 2018; Z. Yang et al., 2018). The choice of piezoelectric materials for an energy harvester depends not only on its properties and function in the application sector but also on other parameters, such as design flexibility, frequency range of operation, and scope of usage (Priya et al., 2017). An example of a piezoelectric energy harvester model, based on piezoelectric ceramic, is shown in Figure 2.11 (Covaci & Gontean, 2020). These harvesters have been used in various energy harvesting systems that harness mechanical vibrations, such as building and bridge oscillations, human motion, vehicle vibration, tire condition monitoring, pacemakers, and power shoes, is shown in Figure 2.12 (Z. Yang et al., 2018).

Figure 2.13 shows the numerous uses of piezoelectric energy harvesting for various sites on the human body (Y. Liu et al., 2021). Piezoelectric energy storage technology can be used in self-powered or battery-less devices that operate with little power in microwatts to milliwatts (μW - mW). It can be applied in many applications, such as power sources for portable systems, wireless sensors, health monitoring, and self-powered wearables. Piezoelectric ceramics are extensively employed in various applications owing to their exceptional piezoelectric coefficients. However, their susceptibility to fracture under stress and loads limits their practical use. Researchers have explored flexible piezoelectric materials based on nano- and micro-structures and thin films to address this challenge. These materials offer superior mechanical

properties and high durability under extreme loads, overcoming the limitations of conventional piezoelectric ceramics.

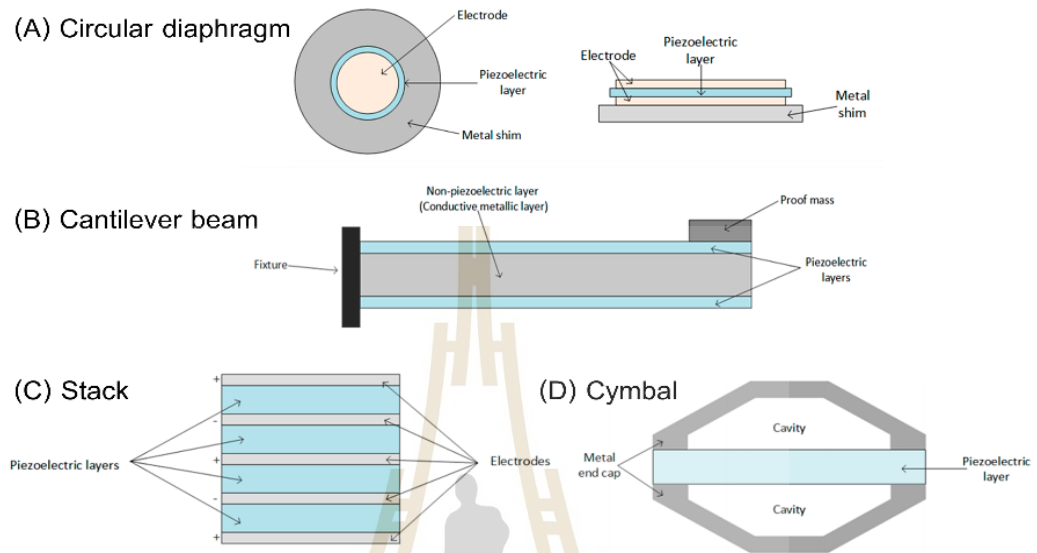


Figure 2.11 Example of a piezoelectric energy harvesters (PEHs) model. (Covaci & Gontean, 2020)

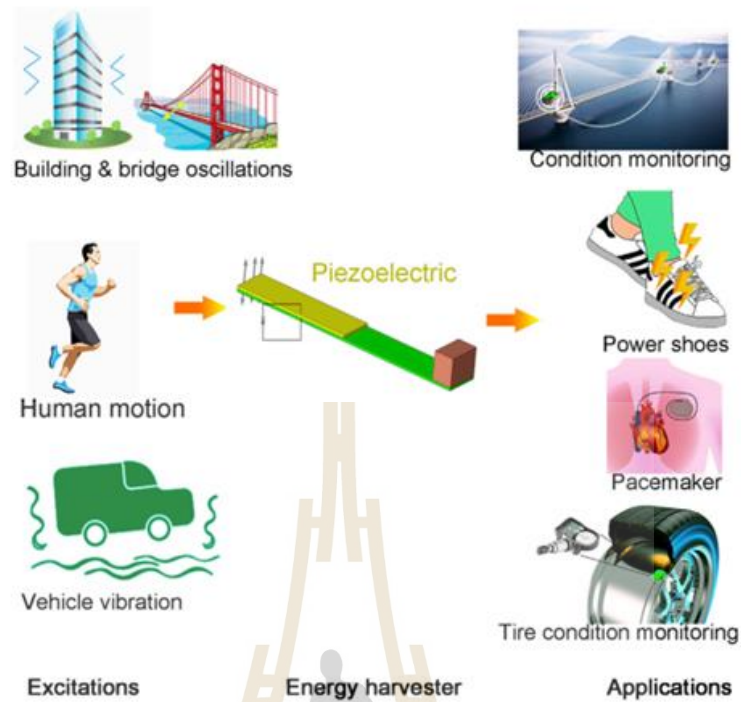


Figure 2.12 Typical application of piezoelectric energy harvesters in cantilever configuration. (Z. Yang et al., 2018)

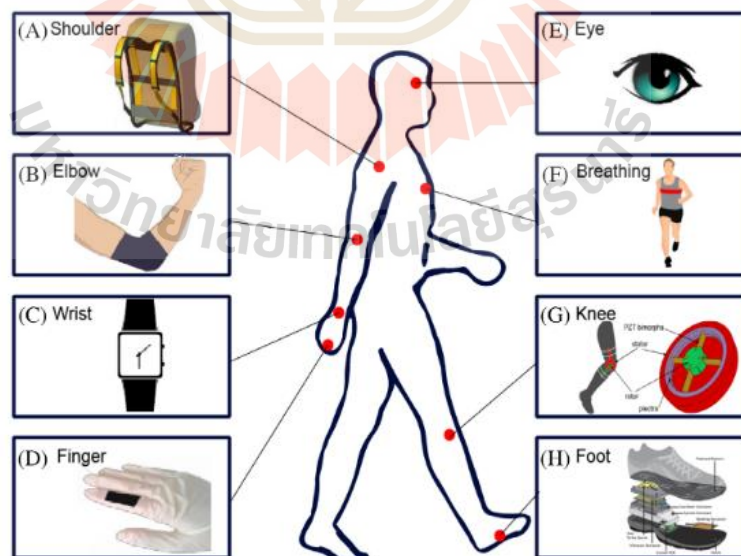


Figure 2.13 Various piezoelectric energy harvesting applications for different locations on the human body. (Y. Liu et al., 2021)

2.2 Piezoelectric ceramic-polymer composites

2.2.1 Piezoelectric composites

Developing flexible piezoelectric composite materials can further expand their application scope, as the flexible structure can harvest energy under loads and vibrations more effectively (Dagdeviren et al., 2016). These materials can be utilized in a wide range of energy harvesting applications. For example, polymer composites can be combined with piezo-ceramic materials to create piezo-composites that consist of a piezoelectric ceramic and a polymer property. The geometry of a two-phase composite can be classified based on the connection of each phase, which can be one-, two-, or three-dimensional. There are 10 structures, represented by 0-0, 0-1, 0-2, 0-3, 1-1, 1-2, 1-3, 2-2, 2-3, and 3-3 (K. Uchino, 2017) as shown in Figure 2.14. The first digit (1, 2, or 3) denotes the number of directions in which the active phase is self-connected, while the second digit (1, 2, or 3) indicates the number of directions in which the passive phase is self-connected. If either digit is "0", this indicates that the material is in the form of particles (K. Uchino, 2017).

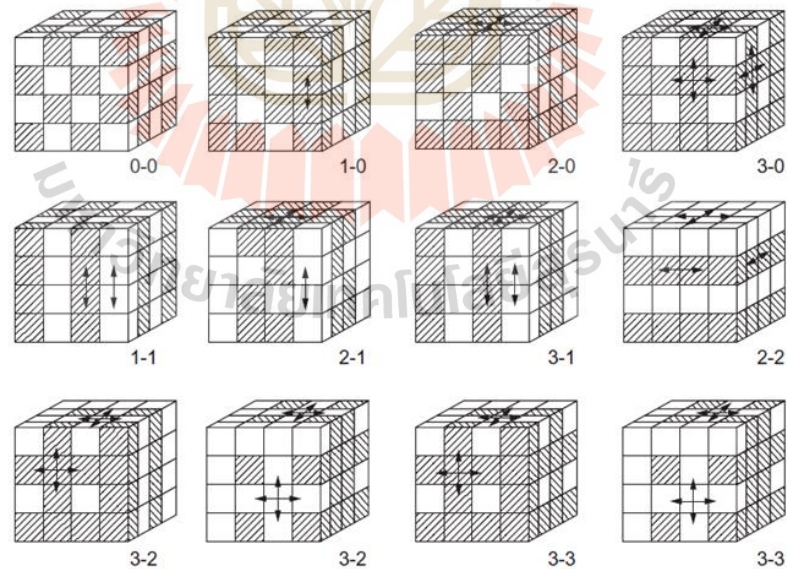


Figure 2.14 Classification of two-phase composites with respect to connectivity. (K. Uchino, 2017)

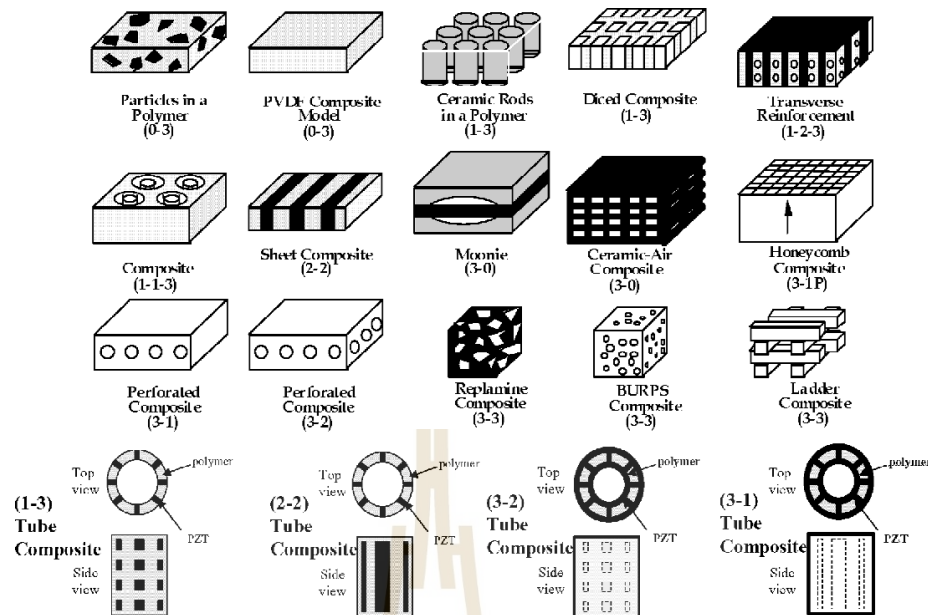


Figure 2.15 Schematic of piezoelectric composites with several connectivity types for sensor and actuator applications. (Akdogan, Allahverdi, & Safari, 2005)

Piezoelectric composites have been studied extensively for various applications, and they come in different connectivity types as shown in Figure 2.15. The first reported piezo-ceramic/polymer composite with the 0-3 type was in 1972 by T. Kitayama *et al.* (K. Uchino, 2017). Since then, research on piezoelectric composites has continued to evolve. In 2010, perovskite structures of PZT, PMN-PT, and BaTiO_3 ceramics were used in thin film-based piezo-composites, which had high energy conversion efficiency and generated higher power density than other perovskite structures. Piezoelectric nanocomposites have also been found to have good mechanical hardness and can induce high output performance. In particular, the 0-3 and 1-3 piezoelectric ceramic/polymer-matrix nanocomposites are widely applied and extensively researched (Kothari, Kumar, Kumar, Vaish, & Chauhan, 2016; Thi et al., 2010; K. Uchino, 2017; Kenji Uchino, 2017b). The flexible piezoelectric composites have many advantages, such as flexibility and durability under large strain and high applied load force (Dagdeviren et al., 2016; Kang et al., 2016). Recent research has focused on composites between piezoelectric ceramics (nano-micro particles) and polymer matrices, such as Polyvinylidene fluoride (PVDF), Polyurethane, Cellulose, Polyamides,

Polyurea, Epoxy resin, Silicone rubber, Rubber, or Polydimethylsiloxane (PDMS) (Jaafar & Salleh, 2015; Jain, J, Sharma, Jain, & P.N, 2015; Khaliq et al., 2017; Mishra, Unnikrishnan, Nayak, & Mohanty, 2019; Park, Jeong, Kim, & Lee, 2016a). Furthermore, flexible piezoelectric energy harvesting devices using PZT-based flexible materials, including nanotubes, nanorods, nanowires, nanofibers, nanocomposites, thin films, etc., have been presented and studied. By comparing the power output of each device, the energy harvesting effect of flexible piezo-composites (PZT/Polymer) is expressed in nanowatts to milliwatts (Kang et al., 2016).

In addition, a number of studies have explored the use of piezo-ceramic/polymer composites to create energy harvesters with low energy consumption. PDMS, an elastomer with silicone based, is an excellent choice for the composite matrix due to its durability, non-toxic and non-flammable nature, biocompatibility, and ease of fabrication (Danish, Bin, Xiaochao, Hao, & Meifang, 2017). Perovskite piezo-ceramic/polymer composites (with 0-3 connectivity) blended with PDMS can be cast onto a flexible plastic substrate at low temperatures, making it a cost-effective and straightforward manufacturing process (Dagdeviren et al., 2016; Park, Jeong, Kim, & Lee, 2016b). An overview of the latest advancements in lead-free piezo-ceramic/PDMS composites for creating bio-eco-compatible and flexible energy harvesters based on piezoelectric ceramics are summarized in Table 2.2.

Table 2.2 Comparison of the output performance of flexible lead-free piezoelectric energy harvesters.

Material/Structure	Filler micro-structure	Output voltage	Output current/ current density	Output power/ power density	Ref.
NaNbO ₃ /PDMS	nanowire	3.2 V	72 nA	0.2 μW	(Jung et al., 2011)
BaTiO ₃ /PDMS	nanotube	5.5 V	350 nA	1.9 μW	(Lin et al., 2012)
BaTiO ₃ /MW-CNT/PDMS	round shape	3.2 V	350 nA	1.1 μW	(Kwi-Il et al., 2012)
LiNbO ₃ /PDMS	nanowire	0.46 V	9.11 nA	4.2 nW	(Yun et al., 2014)
ZnSnO ₃ /PDMS	nano cube	20 V	1 μA/cm ²	20 μW/cm ²	(Young et al., 2014)
BaTiO ₃ /PDMS	nanowire	7 V	360 nA	2.5 μW	(Park et al., 2014)
KNLN-Cu rods/PDMS	particles	12 V	1.2 μA	14.4 μW	(Kyu, Kwi-Il, Jungho, Geon-Tae, & Jae, 2014)
Na _{0.47} K _{0.47} Li _{0.06} NbO ₃ /PDMS	microcube	48 V	0.43 μA/cm ²	20.6 μW/cm ²	(Gupta, Kim, & Kumar, 2016)
0.5(Ba _{0.7} Ca _{0.3})TiO ₃ -0.5Ba(Zr _{0.2} Ti _{0.8})O ₃ (BCTZ)/PDMS/Ag NWs	nanoparticle	15 V	0.8 μA	12 μW	(Baek et al., 2016)

Table 2.2 Comparison of the output performance of flexible lead-free piezoelectric energy harvesters. (Continued)

Material/Structure	Filler micro-structure	Output voltage	Output current/ current density	Output power/ power density	Ref.
$(\text{Na}_{0.83}\text{K}_{0.17})_{0.5}\text{Bi}_{0.5}\text{TiO}_3$ (BNT-BKT)/PDMS	nanowire	3.5 V	280 nA	1 μW	(Q. Yang et al., 2016)
BTO/PDMS	nanoparticle	60 V	1 μA	60 μW	(Bojing et al., 2016)
KNbO_3 /PDMS	nanofiber	16 V	230 nA	3.7 μW	(Ganeshkumar, Cheah, Xu, Kim, & Zhao, 2017)
$(\text{Ba}_{0.85}\text{Ca}_{0.15})(\text{Ti}_{0.9}\text{Zr}_{0.1})\text{O}_3$ (BCZT)/PDMS/MWCNTs	nanowire	0.8 V	8 nA	6.4 nW	(Jin et al., 2017)
$0.5\text{Ba}(\text{Zr}_{0.2}\text{Ti}_{0.8})\text{O}_3$ - $0.5(\text{Ba}_{0.7}\text{Ca}_{0.3})\text{TiO}_3$ /PDMS	nanoparticle	0.6 V	7.5 nA	4.5 nW	(Kou et al., 2017)
$(\text{Ba}_{0.85}\text{Ca}_{0.15})(\text{Ti}_{0.9}\text{Zr}_{0.1})\text{O}_3$ (BCZT)/PDMS	nanowire	2.2 V	90 nA	0.2 μW	(H. H. Fan, Jin, Wang, Hwang, & Zhang, 2017)
$(\text{Ba}_{0.85}\text{Ca}_{0.15})(\text{Ti}_{0.9}\text{Zr}_{0.1})\text{O}_3$ (BCZT)/PDMS	nanowire	9 V	85 nA	0.8 μW	(Jin et al., 2018)

According to Table 2.2, the majority of research in this area has focused on the nanoscale of piezoelectric generators. However, flexible piezoelectric energy harvesters have gained attention due to their suitability for use in environments with random vibrations, such as wind, water flow, and human motion (Kang et al., 2016; Park et al., 2016b). Devices that operate in such environments often have limited battery capacity and may be located in difficult-to-access areas, making it challenging to replace the battery when it runs out. In such cases, piezoelectric composites or piezoelectric nanogenerators (PENGs) that can be self-powered are highly advantageous as they can extend the device's lifetime without requiring battery replacement.

2.2.2 Theoretical model for 0-3 piezoelectric composite

The 0-3 composite, which is the subject of most active research, is typically composed of piezoelectric ceramic powders dispersed in a polymer matrix. These composites can be produced in large quantities due to their simple fabrication and shape customization. Banno proposed a modified cubes model for the 0-3 composite, which accounts for the anisotropic distribution of cubes in the x, y, and z dimensions. Figure 2.16 illustrates the unit cell of this model for a uniaxially anisotropic situation, where l, m, and n are integers representing the number of cubes in each direction. The model is considered uniaxially anisotropic when l=m=1 and n≠1, indicating that the dimensions of the cubes are the same in the x and y directions, but different in the z direction. This leads to the following formulas, as derived by (Kenji Uchino, 2017b)

$$\varepsilon_{33}^* = \frac{[a^2(a + (1 - a)n)^2 \varepsilon_{33}^l \varepsilon_{33}^n]}{[a^l \varepsilon_{33} + (1 - a)n^l \varepsilon_{33}]} + [(1 - a^2)/(a + (1 - a)n)]^n \varepsilon_{33} \quad (2.16)$$

$$d_{33}^* = \frac{d_{33}^l [a^3(a + (1 - a)n)]}{[a + (1 - a)n(\varepsilon_{33}^l / \varepsilon_{33}^n)]} \frac{1}{[(1 - a)n/(a + (1 - a)n) + a^3]} \quad (2.17)$$

$$d_{31}^* = \frac{{}^I d_{31} [a^2(a + (1 - a)n)]}{[a + (1 - a)n({}^I \varepsilon_{33} / {}^{II} \varepsilon_{33})]} \quad (2.18)$$

$$a/[1 - a(a + (1 - a)n)^{1/2} + a^3]$$

Given by is the volume fraction of Phase 1 (I).

$${}^I V = a^3 / (a + (1 - a)n) \quad (2.19)$$

A value of n , where $0 < n < 1$, typically indicates a denser configuration in the z direction than in the x or y directions. In contrast, when $n = 1$, the model corresponds to the cube model of phase 1 (I) and phase 2 (II).

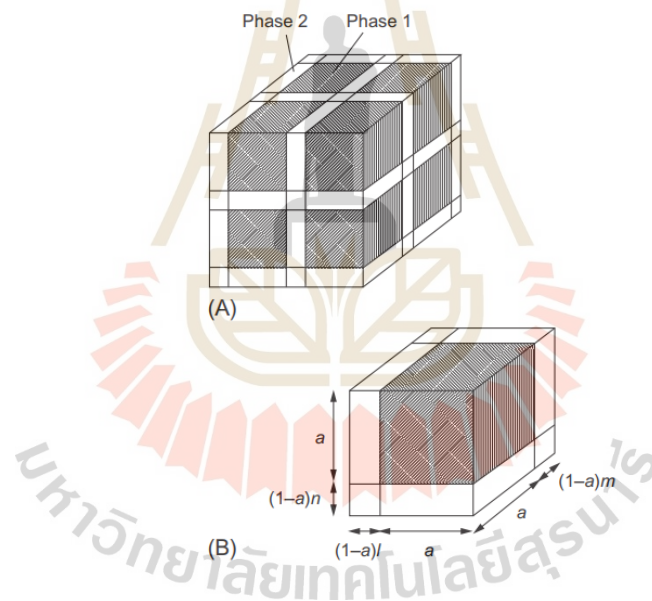


Figure 2.16 Banno's modified cubes model of a unit cell layout for a 0-3 composite. The overall structure (A) and the size-dependent unit cell structure (B). (Kenji Uchino, 2017b)

The composite density (ρ_t) is calculated as follows equation (2.20) (Chan, Zhang, Ng, & Choy, 2000; Choi et al., 2013):

$$\rho_t = \phi\rho_c + (1 - \phi)\rho_p \quad (2.20)$$

where ϕ is ceramic volume percent, ρ_c is ceramic density, ρ_p is polymer density

Ceramics have limitations in their ability to be combined with mechanical systems due to their brittle nature. Therefore, the development of flexible composites is more practical for applications requiring higher durability. For instance, adding specific amounts of carbon black to a composite made of a polymer and piezoceramic powder can enhance the electrical conductivity of the composite by using 0-3 connectivity of carbon black, as illustrated in Figure 2.17 (Suzuki et al., 1991).

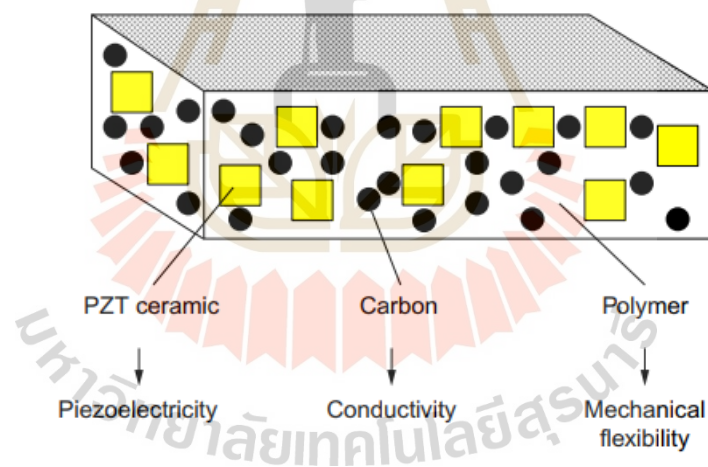


Figure 2.17 Piezoelectric composite made of carbon black, polymer, and piezoceramic for damping vibration. (K. Uchino, 2017)

2.2.3 Applications of piezoelectric composites for energy harvesting

Due to their small size, lightweight, thinness, and flexibility, piezoelectric composites are capable of enduring heavy loads. Moreover, they can generate energy in the range of nanowatts to microwatts (nW- μ W), making them suitable for use in piezoelectric nanogenerators (Briscoe & Dunn, 2015). Piezoelectric nanogenerators (PENGs) have laid the foundation for a wide range of applications, including mechanical energy harvesters (MEHs) in vibrating environments, biomedical applications, protection technology, nano electrical equipment, micro-electrical devices (MEMS), personal electronic devices, and human movement (Siddiqui et al., 2015; Siddiqui et al., 2016). For instance, as shown in Figure 2.18, Canan Dagdeviren et al. (Dagdeviren et al., 2016) developed flexible piezoelectric devices that can collect, sense, and convert mechanical energy into electrical energy. Despite their advantages as flexible energy harvesters, piezoelectric composites also exhibit certain limitations that constrain their performance. One significant drawback of these composites is their relatively low power density, which results in a limited ability to convert mechanical energy into electrical energy. Consequently, their utility in high-power applications is restricted. Additionally, piezoelectric composites have a narrow bandwidth, which hinders their efficiency in capturing mechanical energy across a limited frequency range. This limits their suitability for applications where mechanical vibration frequency is unpredictable or widely varied. Moreover, piezoelectric composites can be sensitive to changes in temperature and humidity, which can adversely impact their electrical output and reliability, restricting their performance and durability in harsh environments. To address these limitations, a potential solution is using a piezoelectric-triboelectric hybrid energy harvester that combines the piezoelectric effect with the triboelectric effect. This technology leverages the contact and separation of two materials with different triboelectric properties to generate electrical energy.

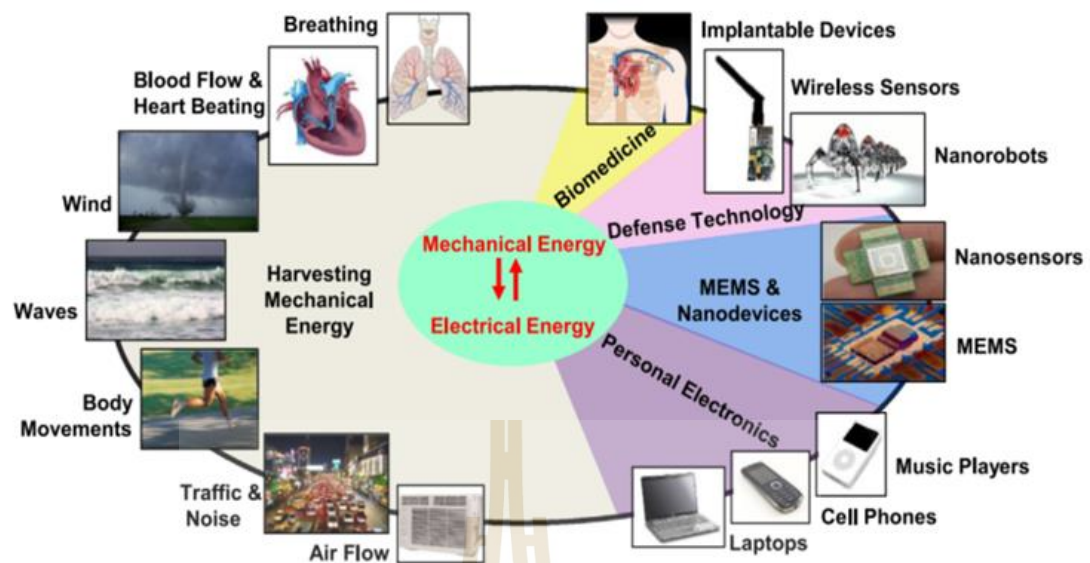


Figure 2.18 Flexible piezoelectric devices are taken into consideration in terms of prospective energy sources for energy harvesting (left side) and the potential to use this energy for sensing and excitation (right side). (Dagdeviren et al., 2016)

2.3 Piezoelectric-triboelectric hybrid

2.3.1 Piezoelectric-triboelectric hybrid materials

In 2012, Zhong Lin Wang et al. from Georgia Tech pioneered the study of triboelectric nanogenerators (TENGs) (F.-R. Fan, Tian, & Lin Wang, 2012). They discovered a modern way to convert mechanical energy into electrical energy using the principles of electrostatic induction and triboelectrification, making TENGs a promising candidate for energy harvesting devices. The device operates on the principle of electrostatics between two materials with different electrical potentials, generating positive and negative charges through collision or friction. The different triboelectric charges (+/-) of various materials are listed in Figure 2.19.

Positive 	Polyurethane foam	(continued)	 Negative
	Etylcellulose	Polyester (Dacron)	
	Sorbothane	Polyisobutylene	
	Polyamide 6-6	Polyuretane flexible sponge	
	Hair, oily skin	Polyethylene Terephthalate (PET)	
	Wool, Knitted	Polyvinyl butyral	
	Silk, woven	Polychlorobutadiene	
	Aluminum	Natural rubber	
	Paper	Polyacrilonitrile	
	Cotton, woven	Polystyrene	
	Steel	Polyimide	
	Wood	Neoprene	
	Hard rubber	Polyehylene	
	Nickel, copper	Polypropylene	
	Sulfur	Polyimide (Kapton)	
	Brass, silver	Polyvinyl chloride (PVC)	
	Acetate, Rayon	Latex (natural) rubber	
	Polymethyl methacrylate (Lucite)	Santoprene rubber	
	Polyvinyl alcohol	Polydimethylsiloxane (PDMS)	
	(continued)	Polytetrafluoroethylene (Teflon)	

Figure 2.19 Triboelectric series (J. W. Lee, Ye, & Baik, 2017)

Moreover, TENGs have a simple structure, are cost-effective and easy to fabricate, while delivering high output power and being environmentally friendly. The triboelectric effect can occur in four modes: (1) vertical contact separation, (2) in-plane contact-sliding, (3) single-electrode, and (4) freestanding triboelectric-layer (Z. L. Wang, 2014) as shown in Figure 2.20.

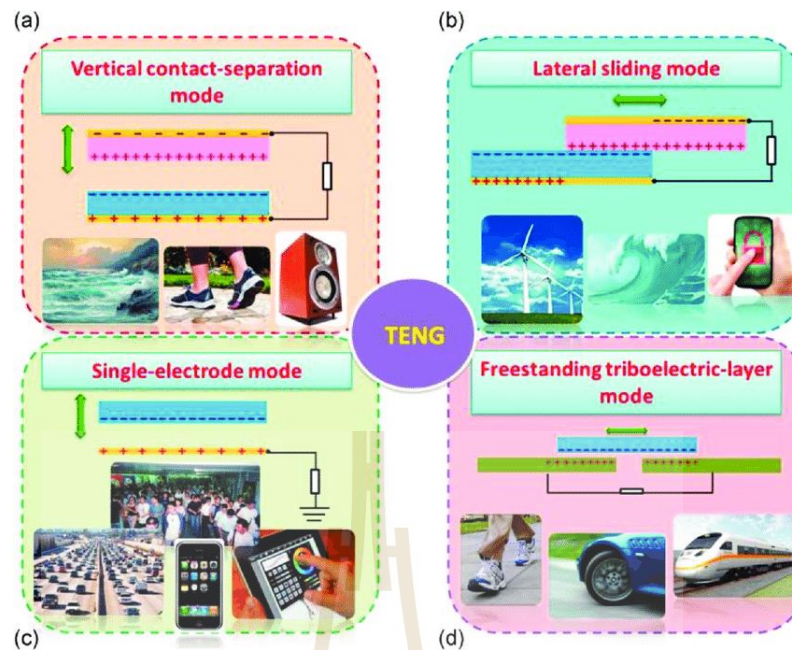


Figure 2.20 The four fundamental modes of triboelectric nanogenerators (TENGs) : (a) vertical contact separation mode, (b) in-plane contact-sliding mode, (c) single-electrode mode, and (d) freestanding triboelectric-layer mode. (Z. L. Wang, 2014)

The contact-separation mode is the fundamental mechanism of TENGs, which generates electron movement by the contact and separation of two dissimilar materials, such as polymer and metal (Z. L. Wang, Chen, & Lin, 2015; X.-S. Zhang et al., 2018). This mode has found widespread applications in energy harvesting from a variety of activities, including walking, finger typing, engine vibration, and biomedical systems (Z. L. Wang et al., 2015). Recent research on piezo-triboelectric hybrid energy harvesting based on lead-free piezoelectric composites has shown promising results in enhancing output power. Table 2.3 provides a list of piezo-triboelectric hybrids for energy harvesting based on lead-free piezoelectric/PDMS composites.

Table 2.3 Comparison of the output performance of piezo-triboelectric hybrid energy harvesters.

Piezoelectric composite material	Triboelectric material/ electrode	Output voltage	Output current/ current density	Output power/ power density	Ref.
ZnSnO ₃ /PDMS (nanocube)	Al/ Al-PET	400 V	28 μ A	11.2 mW	(G. Wang et al., 2015)
ZnSnO ₃ /PDMS/MCNTs (nanoparticle)	Al foil	40 V	0.4 μ A	16 μ W	(Md Mehebab, Sujoy Kumar, Ayesha, & Dipankar, 2015)
BaTiO ₃ /PDMS/MCNTs	Al foil and arch-shape ITO/PET	22 V	9 μ A	198 μ W	(Xue et al., 2015)
BaTiO ₃ /PDMS (nanoparticle)	Cu/IOT-PET	13.5 V	17.2 μ A/cm ²	232.2 μ W/cm ³	(Suo et al., 2016)
BaTiO ₃ /PDMS (post-poling)	Al	375 V	6 μ A	2.25 mW	(Danish et al., 2017)

According to Table 2.3, piezo-triboelectric hybrids demonstrate higher output performance than flexible piezoelectric composites. Earlier research has identified surface charge density as a key factor that influences the performance of TENGs (Z. L. Wang, 2014). Results from recent studies show that hybrid materials offer superior electrical energy harvesting power compared to using only triboelectric or single piezoelectric materials. The present study focuses on the enhancement of energy harvesting using lead-free piezo-triboelectric hybrids.

2.3.2 Theoretical and principle of piezoelectric-triboelectric hybrid

The triboelectric effect, also known as the contact electrification effect, is a phenomenon whereby electrical charge accumulates on the surface of a material after contact with dissimilar materials through friction, resulting in a charge transfer between the two materials. These accumulated charges persist as electrostatic charges on their respective surfaces for an extended period of time. The difference in charge between the two materials creates an electrical potential that drives induced electrons to flow between the electrodes through the frequent contact and separation of the two materials (J.-H. Lee et al., 2016), as shown in Figure 2.21.

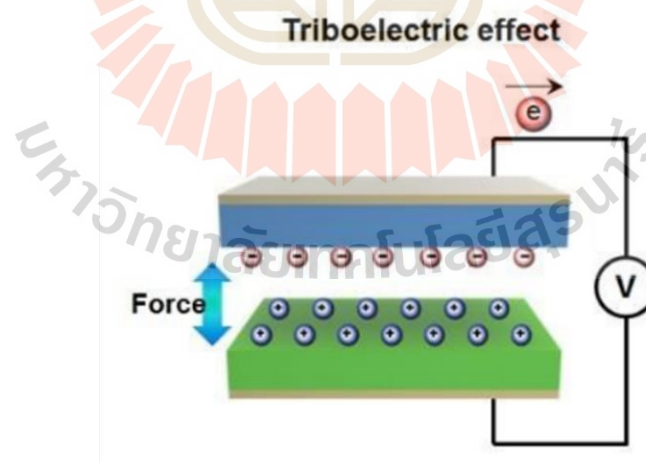


Figure 2.21 Triboelectric effect of Vertical contact-separation mode. (J.-H. Lee et al., 2016)

The generated electrical potential (V) of triboelectric system can be calculated by equation (2.21) (J.-H. Lee et al., 2016). The charges transferred to the surfaces of materials tend to remain there for extended periods. Electrostatically charged materials generate a potential difference that drives induced electrons between electrodes through periodic contact and separation. The value of voltage generated (V) is calculated using equation (2.21):

$$V = \frac{\rho d}{\epsilon_0} \quad (2.21)$$

where ρ is triboelectric charge density, ϵ_0 is vacuum permittivity, d is interlayer distance.

The current generated (I) by an external load can be given by equation (2.22). (J.-H. Lee et al., 2016)

$$I = C \frac{\partial V}{\partial t} + V \frac{\partial C}{\partial t} \quad (2.22)$$

where C is the capacitance of the system, V is the voltage across the two electrodes. Therefore, the triboelectric effect generates electrical energy through the accumulation of static charges resulting from contact and separation. Moreover, the mechanical movement or force that occurs during triboelectric system operation can be utilized to improve the efficiency of energy generation in piezoelectric systems.

The energy generated by a piezoelectric nanogenerator (PENG) is dependent on the piezoelectric properties of the materials used. The PENG works by applying stress to a piezoelectric material, which causes a change in the electric dipole moment within the crystal structure and creates a potential difference in the macro-scale. When electrodes are attached to the surface of the material, the resulting flow of electrons between them balances the internal polarization. In the case of a piezo-triboelectric hybrid system, the contact/separation mode of the triboelectric element applies compressive and tensile stress to the piezoelectric material, which creates an electrical potential in both modes of operation. (Chen, Ren, Han, Wan, & Zhang, 2020).

When the stress aligns with the polarization direction, the device operates in d_{33} -effect mode. The resulting piezoelectric charge (Q) can be calculated

using equation (2.23), while the piezoelectric potential under open-circuit conditions can be obtained through equation (2.24): (Chen et al., 2020)

$$Q_{PENG} = A\sigma d_{33} \quad (2.23)$$

$$V_{PENG} = T\sigma g_{33} \quad (2.24)$$

If the stress or strain is perpendicular to the polarization direction, the device operates in d_{31} -effect mode. Equations (2.25) and (2.26) can be used to calculate the resulting piezoelectric charge (Q) and output voltage, respectively: (Chen et al., 2020)

$$Q_{PENG} = A\sigma d_{31} \quad (2.25)$$

$$V_{PENG} = T\sigma g_{31} \quad (2.26)$$

where A is the area of the piezoelectric material,

σ is the stress/strain in the direction of the acting force,

d_{33} or d_{31} is the piezoelectric charge constant,

T is the thickness of the piezoelectric material,

g_{33} or g_{31} is piezoelectric voltage constant.

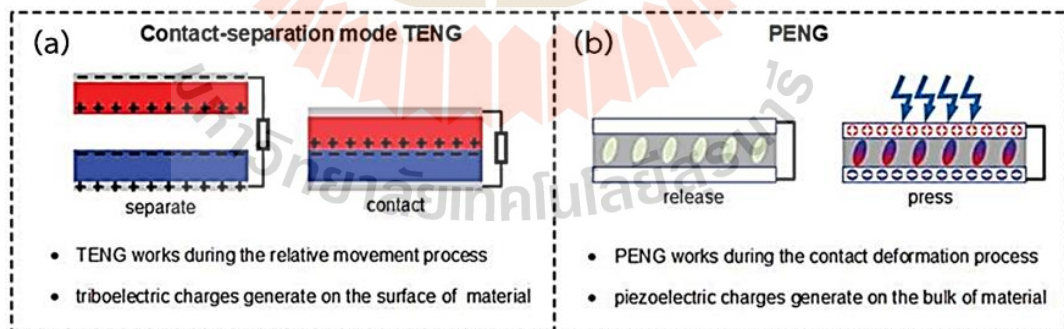


Figure 2.22 The diagram compares the mechanism's action of TENGs (a) and PENGs (b). (Chen et al., 2020; Han, Chen, Yu, & Zhang, 2015)

Figure 2.22 illustrates the comparison and coupling of triboelectric nanogenerators (TENGs) and piezoelectric nanogenerators (PENGs). The TENGs (Figure 2.22(a)) generates electrical output through surface functions, while the PENGs (Figure

2.22(b)) rely on the bulk material's response to contact deformation. Despite their different mechanisms, both TENGs and PENGs can convert mechanical energy into electricity, making them complementary. They can be combined into flexible structures to respond to multiple mechanical energy sources, such as vibration, compression, and bending. Moreover, the electrostatic induction effect yields high output voltage, low short-circuit current, and high matching impedance through charge distribution in all three general structures. Figure 2.23 illustrates the hybrid structure of PENGs-TENGs in the touch-press state (contact-press state), touch-release state (contact-release state) and split-release state (separate-release state).

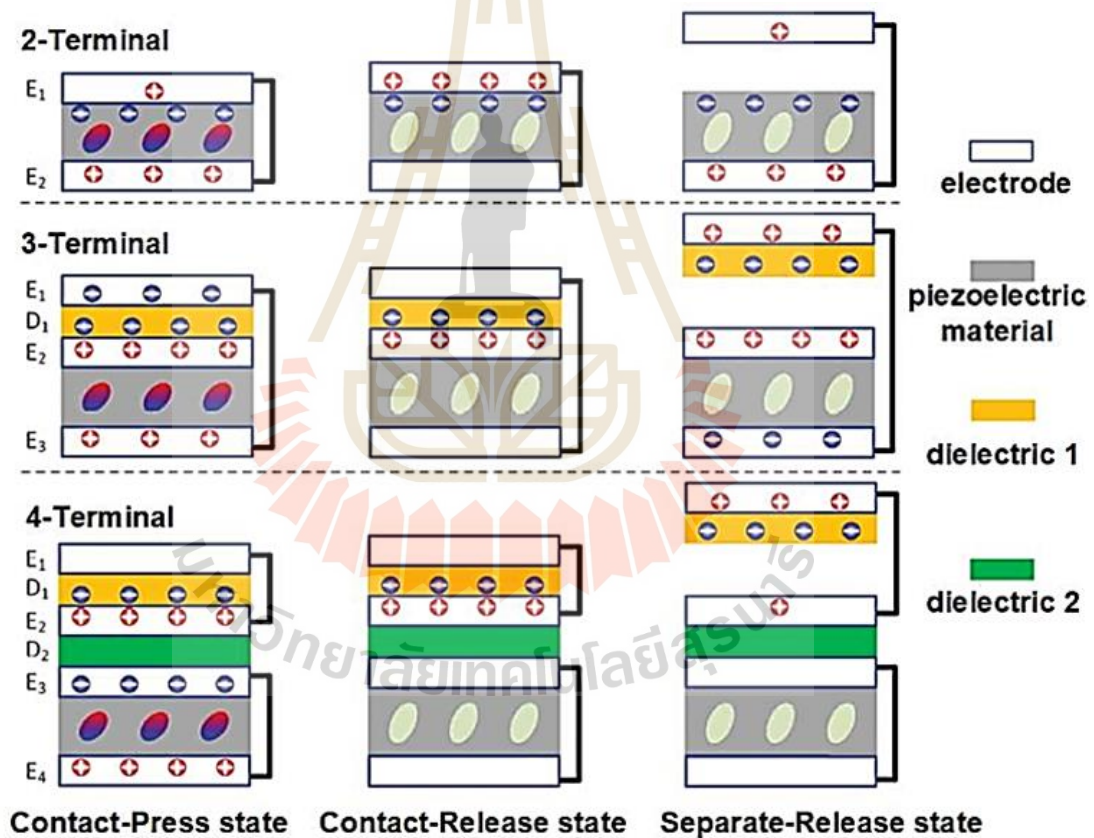


Figure 2.23 The three charge distribution schemes are for the PENGs-TENGs hybrid structure (E is an electric charge, and D is a dielectric material). (Chen et al., 2020; Han et al., 2015)

2.3.3 Application of piezoelectric-triboelectric hybrid for energy harvesting

To achieve better mechanical and electrical properties, researchers have studied hybrid piezoelectric and triboelectric composites, also known as piezo-triboelectric hybrid materials (P-TENGs). These materials offer higher output power, durability, and ease of fabrication, making them suitable for a wide range of applications, including sensors and self-powered devices that can operate in flexible conditions (Karan et al., 2020; J.-H. Lee et al., 2016). Such applications include wearables attached to human skin, mounted on robotic arms, used as soft actuators, and illuminating LED lamps (Pan et al., 2020). These generators can harvest mechanical energy from vibrating environments, such as body motion, wind, transportation-traffic, and acoustics, and convert it into renewable energy (Karan et al., 2020), Figure 2.24 illustrates some examples of these applications. Combining the piezoelectric and triboelectric effects, the piezoelectric-triboelectric hybrid captures mechanical energy efficiently across a wider frequency range and generates a higher power output than a piezoelectric composite alone. Additionally, its improved mechanical robustness and suitability for harsh environments make it applicable in various scenarios. Overall, the combination of these effects enables the hybrid energy harvester to offer superior performance compared to piezo-ceramic and piezo-polymer composite energy harvesters, including wider operating bandwidth and higher power density. Hence, piezo-triboelectric hybrid energy harvesters represent a promising area of research and development in energy harvesting.

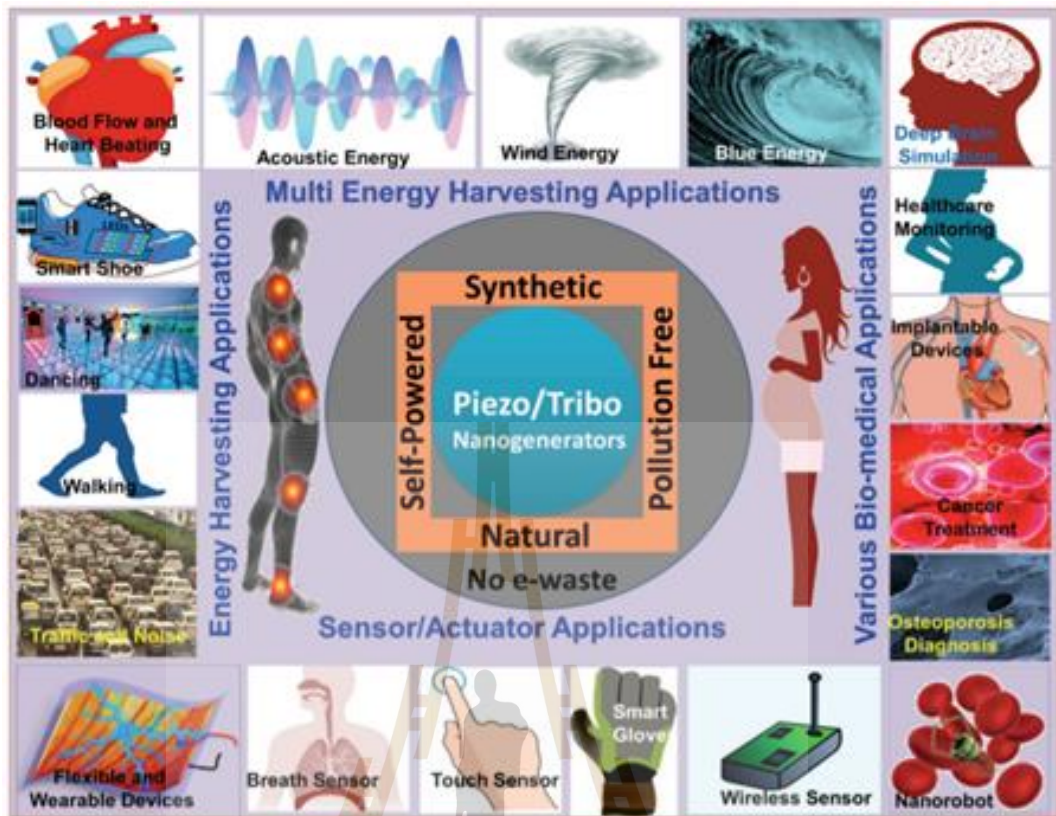


Figure 2.24 Self-powered PENGs/TENGs device applications in biomedical engineering and advanced technology. (Karan et al., 2020)

2.4 References

- Akdogan, E. K., Allahverdi, M., & Safari, A. (2005). Piezoelectric composites for sensor and actuator applications. *IEEE Transactions on Ultrasonics, Ferroelectrics and Frequency Control*, 52, 746-775.
- Baek, C., Yun, J. H., Wang, J. E., Jeong, C. K., Lee, K. J., Park, K.-I., & Kim, D. K. (2016). A flexible energy harvester based on a lead-free and piezoelectric BCTZ nanoparticle-polymer composite. *Nanoscale*, 8(40), 17632-17638. doi:10.1039/C6NR05784E
- Bojing, S., Qiang, Z., Wen, J., Ling, Y., Xinxin, W., Hong, L., Lin, W. Z. (2016). A Packaged Self-Powered System with Universal Connectors Based on Hybridized Nanogenerators. *Advanced Materials*, 28(5), 846-852. doi:10.1002/adma.201503356
- Briscoe, J., & Dunn, S. (2015). Piezoelectric nanogenerators – a review of nanostructured piezoelectric energy harvesters. *Nano Energy*, 14, 15-29. doi:org/10.1016/j.nanoen.2014.11.059
- Caliò, R., Rongala, U. B., Camboni, D., Milazzo, M., Stefanini, C., De Petris, G., & Oddo, C. M. (2014). Piezoelectric energy harvesting solutions. *Sensors*, 14(3), 4755-4790.
- Chan, H., Zhang, Q., Ng, W., & Choy, C. (2000). Dielectric permittivity of PCLT/PVDF-TRFE nanocomposites. *IEEE Transactions on Dielectrics and Electrical Insulation*, 7(2), 204-207.
- Chen, X., Ren, Z., Han, M., Wan, J., & Zhang, H. (2020). Hybrid energy cells based on triboelectric nanogenerator: From principle to system. *Nano Energy*, 75, 104980. doi:https://doi.org/10.1016/j.nanoen.2020.104980
- Choi, Y. J., Yoo, M.-J., Kang, H.-W., Lee, H.-G., Han, S. H., & Nahm, S. (2013). Dielectric and piezoelectric properties of ceramic-polymer composites with 0–3 connectivity type. *Journal of Electroceramics*, 30(1), 30-35. doi:10.1007/s10832-012-9706-7

- Covaci, C., & Gontean, A. (2020). Piezoelectric Energy Harvesting Solutions: A Review. *Sensors*, *20*(12), 3512. Retrieved from <https://www.mdpi.com/1424-8220/20/12/3512>
- Dagdeviren, C., Joe, P., Tuzman, O. L., Park, K.-I., Lee, K. J., Shi, Y., Rogers, J. A. (2016). Recent progress in flexible and stretchable piezoelectric devices for mechanical energy harvesting, sensing and actuation. *Extreme Mechanics Letters*, *9*, 269-281. doi:<https://doi.org/10.1016/j.eml.2016.05.015>
- Danish, A., Bin, Y., Xiaochao, D., Hao, Y., & Meifang, Z. (2017). Enhancement of output performance through post-poling technique on BaTiO₃ /PDMS-based triboelectric nanogenerator. *Nanotechnology*, *28*(7), 075203. doi:<https://doi.org/10.1088/1361-6528/aa52b7>
- Du, H., Zhou, W., Luo, F., Zhu, D., Qu, S., Li, Y., & Pei, Z. (2008). Design and electrical properties' investigation of (K 0.5 Na 0.5) NbO₃-BiMeO₃ lead-free piezoelectric ceramics. *Journal of Applied Physics*, *104*(3), 034104.
- Fan, F.-R., Tian, Z.-Q., & Lin Wang, Z. (2012). Flexible triboelectric generator. *Nano Energy*, *1*(2), 328-334. doi:<https://doi.org/10.1016/j.nanoen.2012.01.004>
- Fan, H. H., Jin, C. C., Wang, Y., Hwang, H. L., & Zhang, Y. F. (2017). Structural of BCTZ nanowires and high performance BCTZ-based nanogenerator for biomechanical energy harvesting. *Ceramics International*, *43*(8), 5875-5880. doi:<https://doi.org/10.1016/j.ceramint.2017.01.057>
- Ganeshkumar, R., Cheah, C. W., Xu, R., Kim, S.-G., & Zhao, R. (2017). A high output voltage flexible piezoelectric nanogenerator using porous lead-free KNbO₃ nanofibers. *Applied Physics Letters*, *111*(1), 013905. doi:10.1063/1.4992786
- Gupta, M. K., Kim, S.-W., & Kumar, B. (2016). Flexible High-Performance Lead-Free Na_{0.47}K_{0.47}Li_{0.06}NbO₃ Microcube-Structure-Based Piezoelectric Energy Harvester. *ACS Applied Materials & Interfaces*, *8*(3), 1766-1773. doi:10.1021/acsami.5b09485

- Han, M., Chen, X., Yu, B., & Zhang, H. (2015). Coupling of piezoelectric and triboelectric effects: from theoretical analysis to experimental verification. *Advanced Electronic Materials*, 1(10), 1500187.
- Hong, C.-H., Kim, H.-P., Choi, B.-Y., Han, H.-S., Son, J. S., Ahn, C. W., & Jo, W. (2016). Lead-free piezoceramics – Where to move on? *Journal of Materiomics*, 2(1), 1-24. doi:<https://doi.org/10.1016/j.jmat.2015.12.002>
- Jaafar, M. F. B., & Salleh, A. D. H. (2015). Performance of piezoelectric energy harvester (PEH) modification using silicon rubber.
- Jain, A., J. P., Sharma, A., Jain, A., & P.N, R. (2015). Dielectric and piezoelectric properties of PVDF/PZT composites: A review. *Polymer Engineering & Science*, 55. doi:10.1002/pen.24088
- Jin, C. C., Liu, X. C., Fan, H. H., Wang, Y., Hwang, H. L., Zhang, Y. F., & Wang, Q. (2017). Fabrication and structure of lead-free BCTZ-MWCNTs composite and its application in energy harvesting. *Ceramics International*, 43(17), 15886-15890. doi:<https://doi.org/10.1016/j.ceramint.2017.08.162>
- Jin, C. C., Liu, X. C., Liu, C. H., Wang, Y., Hwang, H. L., & Wang, Q. (2018). High-performance BCTZ nanowires-based energy harvesting device and self-powered bio-compatible flexion sensor. *Materials & Design*, 144, 55-63. doi:<https://doi.org/10.1016/j.matdes.2018.02.008>
- Jung, J. H., Lee, M., Hong, J. I., Ding, Y., Chen, C. Y., Chou, L. J., & Wang, Z. L. (2011). Lead-free NaNbO_3 nanowires for a high output piezoelectric nanogenerator. *ACS Nano*, 5(12), 10041-10046. doi:10.1021/nn2039033
- Kang, M.-G., Jung, W.-S., Kang, C.-Y., & Yoon, S.-J. (2016). Recent Progress on PZT Based Piezoelectric Energy Harvesting Technologies. *Actuators*, 5(1), 5. Retrieved from <http://www.mdpi.com/2076-0825/5/1/5>

- Karan, S. K., Maiti, S., Lee, J. H., Mishra, Y. K., Khatua, B. B., & Kim, J. K. (2020). Recent Advances in Self-Powered Tribo-/Piezoelectric Energy Harvesters: All-In-One Package for Future Smart Technologies. *Advanced Functional Materials*, 30(48), 2004446. doi:<https://doi.org/10.1002/adfm.202004446>
- Khaliq, J., Deutz, D. B., Frescas, J. A. C., Vollenberg, P., Hoeks, T., van der Zwaag, S., & Groen, P. (2017). Effect of the piezoelectric ceramic filler dielectric constant on the piezoelectric properties of PZT-epoxy composites. *Ceramics International*, 43(2), 2774-2779. doi:<https://doi.org/10.1016/j.ceramint.2016.11.108>
- Khan, A., Abas, Z., Kim, H. S., & Oh, I.-K. (2016). Piezoelectric thin films: an integrated review of transducers and energy harvesting. *Smart Materials and Structures*, 25(5), 053002.
- Kothari, A., Kumar, A., Kumar, R., Vaish, R., & Chauhan, V. S. (2016). A study on epoxy-based 1-3 piezoelectric composites using finite element method. *Polymer Composites*, 37(6), 1895-1905. doi:<https://doi.org/10.1002/pc.23368>
- Kou, Y., Kou, Z., Zhao, D., Wang, Z., Gao, G., & Chai, X. (2017). Fabrication of lead-free Ba(Zr_{0.2}Ti_{0.8})O₃-(Ba_{0.7}Ca_{0.3})TiO₃ nanoparticles and the application in flexible piezoelectric nanogenerator. *Ceramics International*, 43(6), 4803-4806. doi:<https://doi.org/10.1016/j.ceramint.2016.11.221>
- Kuang, Y., Ruan, T., Chew, Z. J., & Zhu, M. (2017). Energy harvesting during human walking to power a wireless sensor node. *Sensors and Actuators A: Physical*, 254, 69-77. doi:<https://doi.org/10.1016/j.sna.2016.11.035>
- Kwi-Il, P., Minbaek, L., Ying, L., San, M., Geon-Tae, H., Guang, Z., Jae, L. K. (2012). Flexible Nanocomposite Generator Made of BaTiO₃ Nanoparticles and Graphitic Carbons. *Advanced Materials*, 24(22), 2999-3004. doi:10.1002/adma.201200105
- Kyu, J. C., Kwi-Il, P., Jungho, R., Geon-Tae, H., & Jae, L. K. (2014). Large-Area and Flexible Lead-Free Nanocomposite Generator Using Alkaline Niobate Particles and Metal Nanorod Filler. *Advanced Functional Materials*, 24(18), 2620-2629. doi:10.1002/adfm.201303484

- Lee, J.-H., Kim, J., Kim, T. Y., Al Hossain, M. S., Kim, S.-W., & Kim, J. H. (2016). All-in-one energy harvesting and storage devices. *Journal of Materials Chemistry A*, 4(21), 7983-7999. doi:10.1039/C6TA01229A
- Lee, J. W., Ye, B. U., & Baik, J. M. (2017). Research Update: Recent progress in the development of effective dielectrics for high-output triboelectric nanogenerator. *APL Materials*, 5(7), 073802. doi:10.1063/1.4979306
- Li, L., Xu, J., Liu, J., & Gao, F. (2018). Recent progress on piezoelectric energy harvesting: structures and materials. *Advanced Composites and Hybrid Materials*, 1(3), 478-505. doi:10.1007/s42114-018-0046-1
- Lin, Z.-H., Yang, Y., Wu, J. M., Liu, Y., Zhang, F., & Wang, Z. L. (2012). BaTiO₃ Nanotubes-Based Flexible and Transparent Nanogenerators. *The Journal of Physical Chemistry Letters*, 3(23), 3599-3604. doi:10.1021/jz301805f
- Liu, W., & Ren, X. (2009). Large piezoelectric effect in Pb-free ceramics. *Physical review letters*, 103(25), 257602.
- Liu, Y., Khanbareh, H., Halim, M. A., Feeney, A., Zhang, X., Heidari, H., & Ghannam, R. (2021). Piezoelectric energy harvesting for self-powered wearable upper limb applications. *Nano Select*, 2(8), 1459-1479. doi:https://doi.org/10.1002/nano.202000242
- Maamer, B., Boughamoura, A., El-Bab, A. M. F., Francis, L. A., & Tounsi, F. (2019). A review on design improvements and techniques for mechanical energy harvesting using piezoelectric and electromagnetic schemes. *Energy Conversion and Management*, 199, 111973.
- Md Meheub, A., Sujoy Kumar, G., Ayesha, S., & Dipankar, M. (2015). Lead-free ZnSnO₃ /MWCNTs-based self-poled flexible hybrid nanogenerator for piezoelectric power generation. *Nanotechnology*, 26(16), 165403. Retrieved from <http://stacks.iop.org/0957-4484/26/i=16/a=165403>

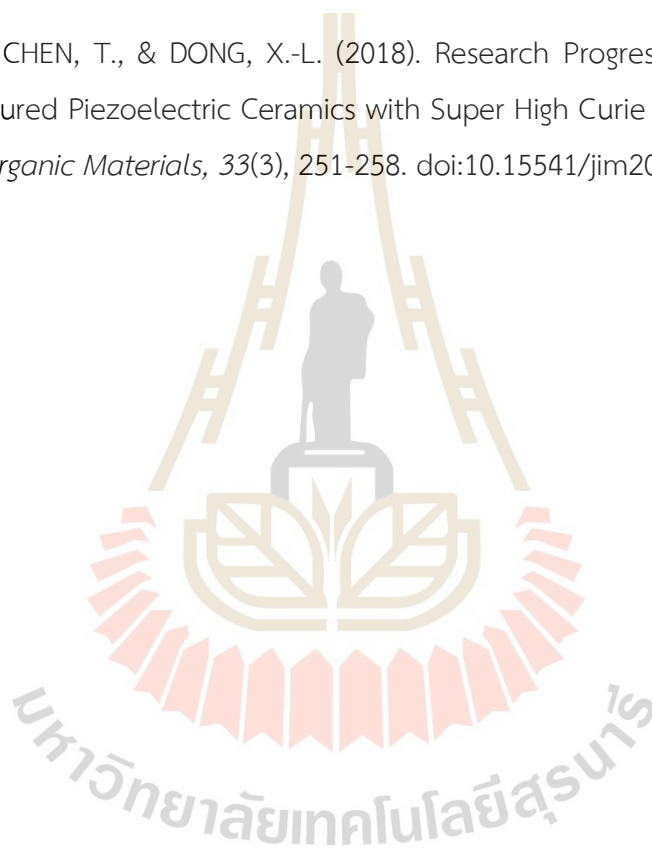
- Mishra, S., Unnikrishnan, L., Nayak, S. K., & Mohanty, S. (2019). Advances in Piezoelectric Polymer Composites for Energy Harvesting Applications: A Systematic Review. *Macromolecular Materials and Engineering*, 304(1), 1800463. doi:<https://doi.org/10.1002/mame.201800463>
- Mitcheson, P. D., Green, T. C., Yeatman, E. M., & Holmes, A. S. (2004). Architectures for vibration-driven micropower generators. *Journal of microelectromechanical systems*, 13(3), 429-440.
- Pan, M., Yuan, C., Liang, X., Zou, J., Zhang, Y., & Bowen, C. (2020). Triboelectric and Piezoelectric Nanogenerators for Future Soft Robots and Machines. *Isience*, 23, 101682. doi:10.1016/j.isci.2020.101682
- Panda, P. K., & Sahoo, B. (2015). PZT to Lead Free Piezo Ceramics: A Review. *Ferroelectrics*, 474(1), 128-143. doi:10.1080/00150193.2015.997146
- Park, K.-I., Bae, S. B., Yang, S. H., Lee, H. I., Lee, K., & Lee, S. J. (2014). Lead-free BaTiO₃ nanowires-based flexible nanocomposite generator. *Nanoscale*, 6(15), 8962-8968. doi:10.1039/C4NR02246G
- Park, K.-I., Jeong, C. K., Kim, N. K., & Lee, K. J. (2016a). Stretchable piezoelectric nanocomposite generator. *Nano Convergence*, 3(1), 1-12.
- Park, K.-I., Jeong, C. K., Kim, N. K., & Lee, K. J. (2016b). Stretchable piezoelectric nanocomposite generator. *Nano Convergence*, 3(1), 12. doi:10.1186/s40580-016-0072-z
- Priya, S., Song, H. C., Zhou, Y., Varghese, R. P., Chopra, A., Kim, S.-G., Polcawich, R. (2017). A Review on Piezoelectric Energy Harvesting: Materials, Methods, and Circuits. *Energy Harvesting and Systems*, 4, 3 - 39.
- Proto, A., Penhaker, M., Conforto, S., & Schmid, M. (2017). Nanogenerators for Human Body Energy Harvesting. *Trends in Biotechnology*, 35(7), 610-624. doi:<https://doi.org/10.1016/j.tibtech.2017.04.005>

- Rödel, J., Webber, K. G., Dittmer, R., Jo, W., Kimura, M., & Damjanovic, D. (2015). Transferring lead-free piezoelectric ceramics into application. *Journal of the European Ceramic Society*, 35(6), 1659-1681. doi:<https://doi.org/10.1016/j.jeurceramsoc.2014.12.013>
- SHUKAI, Y. (2012). TOWARDS HIGHER PERFORMANCE LEAD-FREE PIEZOELECTRIC CERAMICS-NEXT GENERATION (Ba, Ca)(Zr, Ti) O₃.
- Siddiqui, S., Kim, D.-I., Duy, L. T., Nguyen, M. T., Muhammad, S., Yoon, W.-S., & Lee, N.-E. (2015). High-performance flexible lead-free nanocomposite piezoelectric nanogenerator for biomechanical energy harvesting and storage. *Nano Energy*, 15, 177-185. doi:<https://doi.org/10.1016/j.nanoen.2015.04.030>
- Siddiqui, S., Kim, D.-I., Roh, E., Duy, L. T., Trung, T. Q., Nguyen, M. T., & Lee, N.-E. (2016). A durable and stable piezoelectric nanogenerator with nanocomposite nanofibers embedded in an elastomer under high loading for a self-powered sensor system. *Nano Energy*, 30, 434-442. doi:<https://doi.org/10.1016/j.nanoen.2016.10.034>
- Sluka, T., Tagantsev, A. K., Damjanovic, D., Gureev, M., & Setter, N. (2012). Enhanced electromechanical response of ferroelectrics due to charged domain walls. *Nature communications*, 3(1), 1-7.
- Suo, G., Yu, Y., Zhang, Z., Wang, S., Zhao, P., Li, J., & Wang, X. (2016). Piezoelectric and Triboelectric Dual Effects in Mechanical-Energy Harvesting Using BaTiO₃/Polydimethylsiloxane Composite Film. *ACS Applied Materials & Interfaces*, 8(50), 34335-34341. doi:10.1021/acsami.6b11108
- Suzuki, Y., Uchino, K., Gouda, H., Sumita, M., Newnham, R., & Ramachandran, A. (1991). Mechanical dampers using piezoelectric composites. *Journal of the Ceramic Society of Japan*, 99(1155), 1135-1137.

- Thi, M. P., Hladky-Hennion, A.-C., Khanh, H. L., Tran-Huu-Hue, L.-P., Lethiecq, M., & Levassort, F. (2010). Large area 0-3 and 1-3 piezoelectric composites based on single crystal PMN-PT for transducer applications. *Physics Procedia*, *3*(1), 897-904. doi:<https://doi.org/10.1016/j.phpro.2010.01.115>
- Tian, Y., Wei, L., Chao, X., Liu, Z., & Yang, Z. (2013). Phase Transition Behavior and Large Piezoelectricity Near the Morphotropic Phase Boundary of Lead-Free $(\text{Ba}_{0.85}\text{Ca}_{0.15})(\text{Zr}_{0.1}\text{Ti}_{0.9})\text{O}_3$ Ceramics. *Journal of the American Ceramic Society*, *96*(2), 496-502. doi:<https://doi.org/10.1111/jace.12049>
- Uchino, K. (2017). Chapter 9 - Piezoelectric Composite Materials. In *Advanced Piezoelectric Materials (Second Edition)* (pp. 353-382): Woodhead Publishing.
- Uchino, K. (2017a). The development of piezoelectric materials and the new perspective. In *Advanced Piezoelectric Materials* (pp. 1-92): Elsevier.
- Uchino, K. (2017b). Piezoelectric composite materials. In *Advanced Piezoelectric Materials* (pp. 353-382): Elsevier.
- Uchino, K. (2018). *Ferroelectric devices*: CRC press.
- Villafuerte-Castrejón, M., Morán, E., Reyes-Montero, A., Vivar-Ocampo, R., Peña-Jiménez, J.-A., Rea-López, S.-O., & Pardo, L. (2016). Towards Lead-Free Piezoceramics: Facing a Synthesis Challenge. *Materials*, *9*(1), 21. doi:<https://doi.org/10.3390/ma9010021>
- Wang, G., Xi, Y., Xuan, H., Liu, R., Chen, X., & Cheng, L. (2015). Hybrid nanogenerators based on triboelectrification of a dielectric composite made of lead-free ZnSnO_3 nanocubes. *Nano Energy*, *18*, 28-36. doi:<https://doi.org/10.1016/j.nanoen.2015.09.012>
- Wang, P., Li, Y., & Lu, Y. (2011). Enhanced piezoelectric properties of $(\text{Ba}_{0.85}\text{Ca}_{0.15})(\text{Ti}_{0.9}\text{Zr}_{0.1})\text{O}_3$ lead-free ceramics by optimizing calcination and sintering temperature. *Journal of the European Ceramic Society*, *31*(11), 2005-2012. doi:<https://doi.org/10.1016/j.jeurceramsoc.2011.04.023>

- Wang, Z. L. (2014). Triboelectric nanogenerators as new energy technology and self-powered sensors - Principles, problems and perspectives. *Faraday Discussions*, 176(0), 447-458. doi:10.1039/C4FD00159A
- Wang, Z. L., Chen, J., & Lin, L. (2015). Progress in triboelectric nanogenerators as a new energy technology and self-powered sensors. *Energy & Environmental Science*, 8(8), 2250-2282. doi:10.1039/C5EE01532D
- Xue, C., Li, J., Zhang, Q., Zhang, Z., Hai, Z., Gao, L., Sun, D. (2015). A Novel Arch-Shape Nanogenerator Based on Piezoelectric and Triboelectric Mechanism for Mechanical Energy Harvesting. *Nanomaterials*, 5(1), 36. Retrieved from <http://www.mdpi.com/2079-4991/5/1/36>
- Yang, Q., Wang, D., Zhang, M., Gao, T., Xue, H., Wang, Z., & Xiong, Z. (2016). Lead-free $(\text{Na}_{0.83}\text{K}_{0.17})_{0.5}\text{Bi}_{0.5}\text{TiO}_3$ nanofibers for wearable piezoelectric nanogenerators. *Journal of Alloys and Compounds*, 688, 1066-1071. doi:<https://doi.org/10.1016/j.jallcom.2016.07.131>
- Yang, Z., Zhou, S., Zu, J., & Inman, D. (2018). High-Performance Piezoelectric Energy Harvesters and Their Applications. *Joule*, 2(4), 642-697. doi:<https://doi.org/10.1016/j.joule.2018.03.011>
- Yang, Z., & Zu, J. (2016). Comparison of PZN-PT, PMN-PT single crystals and PZT ceramic for vibration energy harvesting. *Energy Conversion and Management*, 122, 321-329.
- Young, L. K., Dohwan, K., Ju-Hyuck, L., Yun, K. T., Kumar, G. M., & Sang-Woo, K. (2014). Unidirectional High-Power Generation via Stress-Induced Dipole Alignment from ZnSnO_3 Nanocubes/Polymer Hybrid Piezoelectric Nanogenerator. *Advanced Functional Materials*, 24(1), 37-43. doi:10.1002/adfm.201301379
- Yun, B. K., Park, Y. K., Lee, M., Lee, N., Jo, W., Lee, S., & Jung, J. H. (2014). Lead-free LiNbO_3 nanowire-based nanocomposite for piezoelectric power generation. *Nanoscale Research Letters*, 9(1), 4. doi:10.1186/1556-276x-9-4

- Zhang, X.-S., Han, M., Kim, B., Bao, J.-F., Brugger, J., & Zhang, H. (2018). All-in-one self-powered flexible microsystems based on triboelectric nanogenerators. *Nano Energy*, 47, 410-426. doi:<https://doi.org/10.1016/j.nanoen.2018.02.046>
- Zhang, Y., Glaum, J., Groh, C., Ehmke, M. C., Blendell, J. E., Bowman, K. J., & Hoffman, M. J. (2014). Correlation Between Piezoelectric Properties and Phase Coexistence in (Ba,Ca)(Ti,Zr)O₃ Ceramics. *American Ceramic Society*, 97(9), 2885-2889.
- ZHOU, Z.-Y., CHEN, T., & DONG, X.-L. (2018). Research Progress of Perovskite Layer Structured Piezoelectric Ceramics with Super High Curie Temperature. *Journal of Inorganic Materials*, 33(3), 251-258. doi:10.15541/jim20170265



CHAPTER 3

A COMPARISON BETWEEN CONVENTIONAL AND REACTIVE SINTERING TECHNIQUES FOR BCZT CERAMIC FABRICATION

3.1 Introduction

The BCZT piezoelectric ceramic can be produced using various methods, as discussed in chapter 1. Sintering and solid-state reaction methods are the main topics of discussion in this chapter. It is aware that the sintering process impacts the phase structure, grain size, density, dielectric, and piezoelectric properties of piezoelectric ceramic. Therefore, this chapter presents the comparison of the physical properties of BCZT ceramics fabricated by using conventional and reactive sintering methods.

Recently, many publications investigated BCZT ceramics prepared by solid-state reactive (SSR) technique (Wang, Li, & Lu, 2011; Wu, Xiao, Wu, Zhu, & Wang, 2011), hydrothermal technique (Liu, Pu, & Sun, 2014; Lu et al., 2017), and sol-gel technique (Bharathi & Varma, 2014; Praveen et al., 2015). It is well known that various synthesis techniques and different preparation conditions affect the physical, chemical and electrical properties of a material (Coondoo et al., 2018; Villafuerte-Castrejón et al., 2016). BCZT ceramics that are synthesized by SSR technique shown excellent piezoelectric coefficient (d_{33}) about 140–620 pC/N (Villafuerte-Castrejón et al., 2016) and this value is greater than or equal to the PZT ($d_{33} \sim 225\text{--}593$ pC/N) (Yang, Zhou, Zu, & Inman, 2018). BCZT ceramics prepared by a conventional sintering (CS) technique requires high calcination temperature ($\sim 1200\text{--}1350$ °C), high sintering temperature ($\sim 1300\text{--}1500$ °C) and long dwelling time ($\sim 2\text{--}6$ hrs) (Villafuerte-Castrejón et al., 2016).

On the other hand, reactive sintering (RS) technique is an optional method to fabricate the piezoelectric ceramics, in which the constituent phases react with each other and lead to the formation of new phase at high sintering temperature without need of calcination process (Loiu, 2015). The fabrication of many ferroelectric ceramics by using RS technique such as PZT (Kong & Ma, 2001), KNN (Farooq et al., 2016),

($K_{0.5}Bi_{0.5}$) TiO_3 - $BiFeO_3$ (Fisher et al., 2015) and $0.94Bi_{0.5}Na_{0.5}TiO_3$ - $0.06BaTiO_3$ (Kawashima & Suzuki, 2016) have been reported. The advantages of RS technique are its simple procedure to improve the density of ceramics, cost-effective, less preparation time, be able to avoid contamination during the re-grinding process and suitable for the preparation of electronic ceramic materials (Loiu, 2015). Wang et al. (Wang et al., 2011) reported that the specific composition of BCZT ($Ba_{0.85}Ca_{0.15}Zr_{0.1}Ti_{0.9}O_3$) ceramics can be achieved by sintered at 1540 °C for 2 hrs of dwelling time using CS method. Therefore, we would like to adopt the same composition and sintering condition to prepare the BCZT ceramics by RS technique and compare this result with the CS technique prepared ceramics to investigate the effect of various sintering dwell times.

In general, characterization techniques like Scanning Electron Microscope (SEM) and X-Ray Diffraction (XRD) methods are used to investigate microstructure and phase formation in ferroelectric materials (Bharathi & Varma, 2014). However, SEM and XRD cannot provide the information of oxidation state and electronic transitions in a material (Kempet, Marungsri, Yimnirun, Klysubun, & Pojprapai, 2013). In this experiment, the X-ray Absorption Spectroscopy (XAS) was employed to investigate the oxidation state, electronic transitions, neighboring atoms, coordination number and local structure of a material (Bootchanont et al., 2014; Kempet et al., 2013; Leitzke et al., 2018; Mastelaro et al., 2015; Ray et al., 2011).

This chapter aims to compare the microstructure, phase, electrical, ferroelectric, and piezoelectric properties of BCZT ceramics fabricated by RS and CS techniques. We believe that this study will be useful to understand the effect of sintering technique to prepare the BCZT ceramics.

3.2 Experimental procedure

3.2.1 Sample Preparation

The specific composition of BCZT ($Ba_{0.85}Ca_{0.15}Zr_{0.1}Ti_{0.9}O_3$) ceramics were fabricated by using both CS and RS sintering techniques. Commercially purchased $BaCO_3$ (99.0 %, Sigma Aldrich), $CaCO_3$ (99.0 %, Loba Chemie), ZrO_2 (99.5 %, Eleps) and TiO_2 (99.8 %, Aldrich) powders were used as an initial material. A 30.0951 g of $BaCO_3$

powder, 12.8965 g of TiO_2 powder, 2.6936 g of CaCO_3 and 2.2109 g of ZrO_2 powders were mixed by ball milling process in ethanol for 24 hrs. Then, the ball-milled powder dried at 120 °C for 24 hrs to remove the ethanol content. In RS technique, 0.5 g of compositionally mixed powders (without calcine) made into 1 cm diameter pellets by uniaxial press 1.25 ton. Then the pellets were sintered at 1540 °C for 2, 3 and 4 hrs of dwell time.

In CS technique, the compositionally mixed powders were dried and calcined at 1300 °C in an alumina crucible for 2 hrs (as mentioned condition by Wang *et al.* (Wang et al., 2011)), then re-grounded the calcined powders and made into 1 cm diameter pellets by uniaxial press 1.25 ton. After that, pellets were sintered at 1540 °C for 2, 3 and 4 hrs of dwell time. The heating and cooling rates of sintering and calcination processes were maintained at 5 °C/min. The key differences between RS and CS techniques that were used in this research are shown in Table 3.1.

Table 3.1 The differences between RS and CS techniques

Process/Method	RS	CS
Weighing substrate i.e., BaCO_3 , CaCO_3 , ZrO_2 , TiO_2	●	●
Mixing substrate of BCZT by ball mill in ethanol for 24 hrs	●	●
Drying mixed BCZT at 120 °C for 24 hrs in Oven	●	●
Calcining BCZT powder at 1300 °C for 2 hrs		●
Re-grinding BCZT calcined powder by ball mill in ethanol for 6 hrs		●
Drying calcined BCZT at 120 °C for 24 hrs in Oven		●
Dry Pressing BCZT powders into pellets (\varnothing ~10 mm, t ~2 mm)	●	●
Sintering at 1540 °C for 2, 3 and 4 hrs of dwell time	●	●

3.2.2 Characterization

BCZT ceramics prepared by both CS and RS method characterized by using X-Ray Diffractometer (XRD, Bruker Phaser DII). Dwell time driven surface morphology and grain size were measured using a Scanning Electron Microscope (SEM, JEOL JSM-6010LV). The average grain size was estimated by using ImageJ software.

Each pellet was polished on both sides and thinned down to 1 mm by using SiC paper (this process was done sequentially by decreasing the roughness of SiC paper). The density of the pellets was estimated by using Archimedes' principle (ASTM C 378–88) (Kireš, 2007).

Next, both faces of each pellet were coated with gold (Au) of thickness around 100 nm as a top and bottom electrode using radio frequency (RF) sputtering technique. The dielectric properties of pellets were measured at 100 Hz frequency by using aixPES piezoelectric evaluation system from aix-ACCT Systems GmbH, Aachen, Germany. Ferroelectric hysteresis loop (P - E) was measured by P - E hysteresis (TREK, Model 20/20C) at room temperature at 50 Hz of ± 10 kV/cm sinusoidal electric field.

Then, some of the ceramics were dipped in silicon oil bath (to avoid the high voltage spark) and poled under 2.0 kV/mm DC field for 30 min at room temperature. The piezoelectric constant (d_{33}) was measured from the poled ceramics by using d_{33} meter (International Ltd., APC-S5865).

In addition, XAS measurement was performed on BCZT ceramics at Beam Line 8 (BL-8), Siam Photon Laboratory, Synchrotron Light Research Institute (SLRI), Thailand. 1.2 GeV energetic electron beam and 60–150 mA beam current was utilized to get the energetic polarized X-ray beam. A double crystal monochromator (a pair of Ge (220) and InSb (111) crystals) was used to collect the fluorescent X-ray beam with energy steps of 0.2 eV. Ti K -edge (4966 eV) and Zr L_3 -edge (2223 eV) absorption spectra were recorded to analyze the structural parameters. Before the actual experiment, the photon energy was calibrated by measuring Ti and Zr foils absorption edges respectively. Finally, data was analyzed by using ATHENA program (Ravel & Newville, 2006) to extract the structural parameters. A schematic diagram of the experimental methods used in this investigation is shown in Figure 3.1.

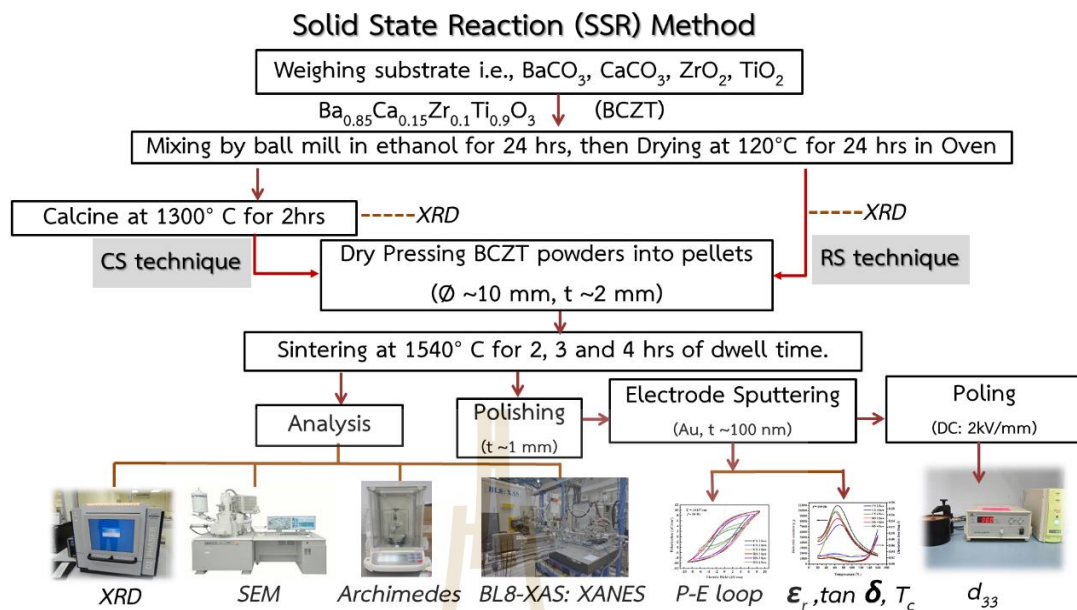


Figure 3.1 Schematic diagram of the comparison of conventional (CS) and reactive (RS) sintering techniques for lead-free BCZT ferroelectric ceramics.

3.3 Results and Discussion

3.3.1 XRD Results

XRD patterns of BCZT ceramics prepared by CS and RS techniques at 1540°C for 2, 3 and 4 hrs dwell time are shown in Figure 3.2. Here we have included XRD patterns of calcined and non-calcined powders as a reference. For all samples, XRD measurement was performed from 20° to 70° of 2θ . Figure 3.2 (a) and (b) represents the CS technique prepared samples and Figure 3.2 (c) and (d) represents the RS technique prepared samples. Initial observation suggests that the XRD pattern of both (RS and CS) techniques exhibit a pure perovskite structure without any secondary phase. This considers that Ca^{2+} diffuses into Ba^{2+} A-site and Zr^{4+} diffuses into Ti^{4+} at B-site, and Ca and Zr have completely diffused into the BaTiO_3 lattice (Buatip et al., 2018; Wang et al., 2011). All BCZT ceramics resemble mixture phase structures of tetragonal and orthorhombic. Even though prepared BCZT ceramics from either RS or CS technique exhibit the same phase, the CS-BCZT ceramics showed greater XRD peak intensities than RS-BCZT ceramics. This might be because a CS-BCZT pellet was

prepared from pure phase calcined BCZT powder before sintering. The XRD peak pattern at 44° – 46° of 2θ indicates multiple phase formation in the both of CS-BCZT and RS-BCZT ceramics.

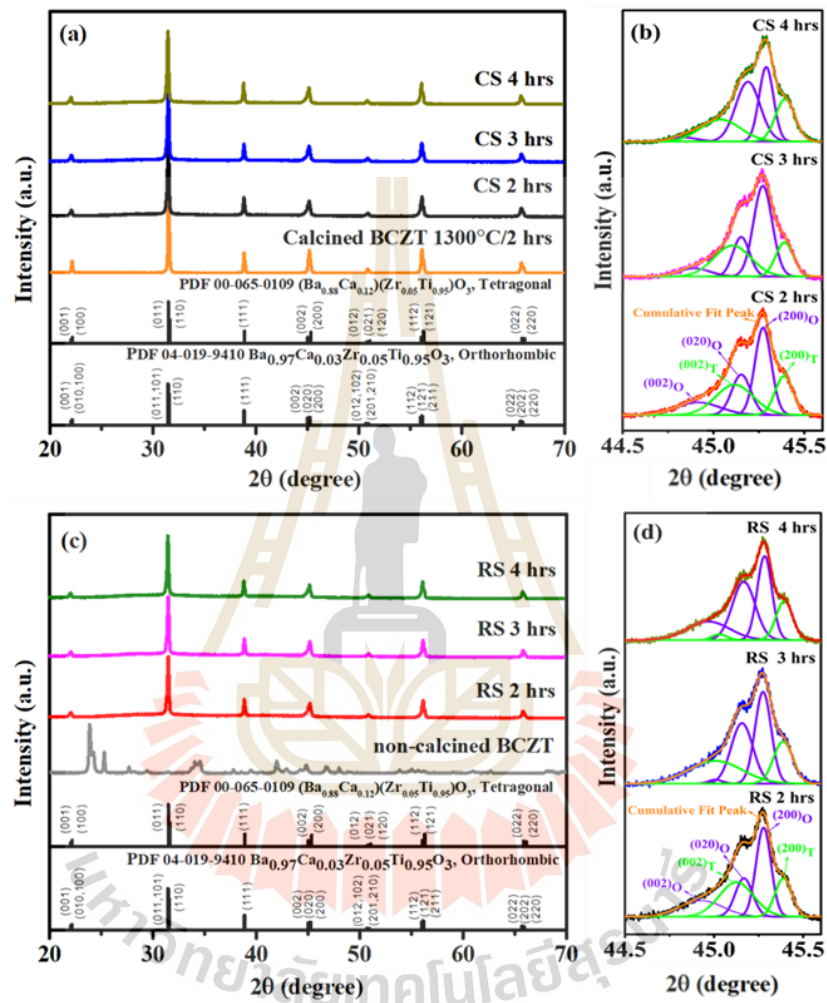


Figure 3.2 XRD patterns of BCZT ceramics: (a, b) CS and (c, d) RS.

The peak deconvolution is shown in Figure 3.2 (b) and (d). The deconvoluted peaks at 44.91°, 45.15° and 45.27° of 2θ belong to the orthorhombic phase of (002), (020) and (200) crystal planes, respectively. These peaks are well matched with the JCPDS file (PDF# 04-019-9410). Similarly, the peaks at 45.12° and 45.39° belong to the tetragonal phase of (002) and (200) crystal planes. The same tetragonal phase peaks are well-matched with the JCPDS file (PDF# 00-064-0109). These results obtained from CS and RS techniques prepared samples were the same. The mixture phase of orthorhombic and tetragonal peak intensities was studied with respect to the various sintering dwell times to understand the phase evaluation. A fraction of orthorhombic phase is calculated by applying Garvie and Nicholson (GARVIE & NICHOLSON, 1972) equation (3.1) as given below:

$$C_o = \frac{I_o(002) + I_o(020) + I_o(200)}{I_o(002) + I_t(002) + I_o(020) + I_o(200) + I_t(200)} \quad (3.1)$$

where ' C_o ' is the compositional weight of orthorhombic phase, ' I_o ' and ' I_t ' are integral areas of the orthorhombic and tetragonal phases (or intensities of corresponding peaks). The fraction of orthorhombic phase increased with an increase of dwell time. The calculated fractional orthorhombic phase with respect to dwell time in both (CS and RS) techniques are shown in Figure 3.3. An increase in the fraction of orthodromic phase was observed with increasing dwell time. However, fraction of orthogonality is less in RS technique compared to CS technique at 2, 3 hrs of dwell time and higher than CS technique at 4 hrs of dwell time. Along with that, tetragonality (c/a ratio) of BCZT samples (from both techniques) was calculated; it equals to 1.006, 1.006, 1.008 for CS and 1.006, 1.008, 1.008 for RS, at 2, 3 and 4 hrs of dwell time respectively (shown as Figure 3.7 (a)). These values are consistent with the standard XRD pattern of the tetragonal BCZT JCPDS file (PDF#00-064-0109) which is around 1.006.

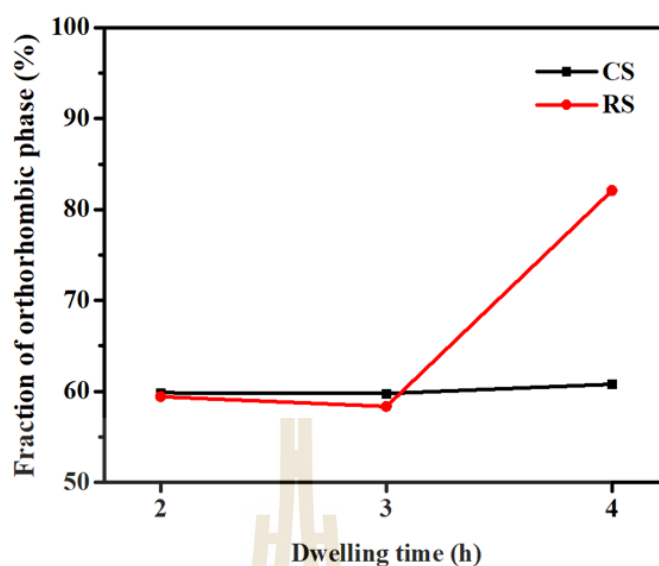


Figure 3.3 Fraction of orthorhombic phase of BCZT ceramics were sintered at 1540 °C for 2, 3 and 4 hrs by CS and RS.

3.3.2 SEM Results

SEM micrographs of BCZT ceramics prepared by RS and CS techniques are shown in Figure 3.4 (inset shows the corresponding histograms). RS-BCZT ceramics sintered within 2, 3 and 4 hrs dwell time possess the average grain size of $13.24 \pm 4.46 \mu\text{m}$, $7.82 \pm 2.38 \mu\text{m}$, and $12.56 \pm 6.58 \mu\text{m}$, respectively. By comparison with RS-BCZT, CS-BCZT ceramics exhibit $14.42 \pm 6.02 \mu\text{m}$, $11.84 \pm 4.20 \mu\text{m}$, and $12.38 \pm 4.04 \mu\text{m}$ for 2, 3 and 4 hrs of dwell time, respectively. In RS technique, average grain size decreased significantly for 3 hrs dwell time and increased further. Inhomogeneous grain size was observed for 4 hrs of dwell time. The decrease and increase in grain sizes could be because of strain/stress relaxation induced grain fragmentation and/or agglomeration (Cheng, Zhou, Du, Luo, & Zhu, 2013; Wu et al., 2011). CS-BCZT ceramics do not show many variations in their grain sizes. This can be taken account of the pre-calcination effect. Therefore, we can conclude that long dwell time can cause abnormal grain growth and inhomogeneous microstructure. The average grain size and relative density of BCZT ceramics fabricated from both sintering techniques are plotted in Figure 3.4 (a) and (b). The grain size of RS-BCZT ceramics is smaller than that of CS-BCZT ceramics, this could be because particles of non-calcined BCZT powder do

not aggregate as same as the calcined BCZT powder in the process of high-temperature sintering does. However, the density of RS-BCZT ceramics, 96–97 %, are comparable to the theoretical density.

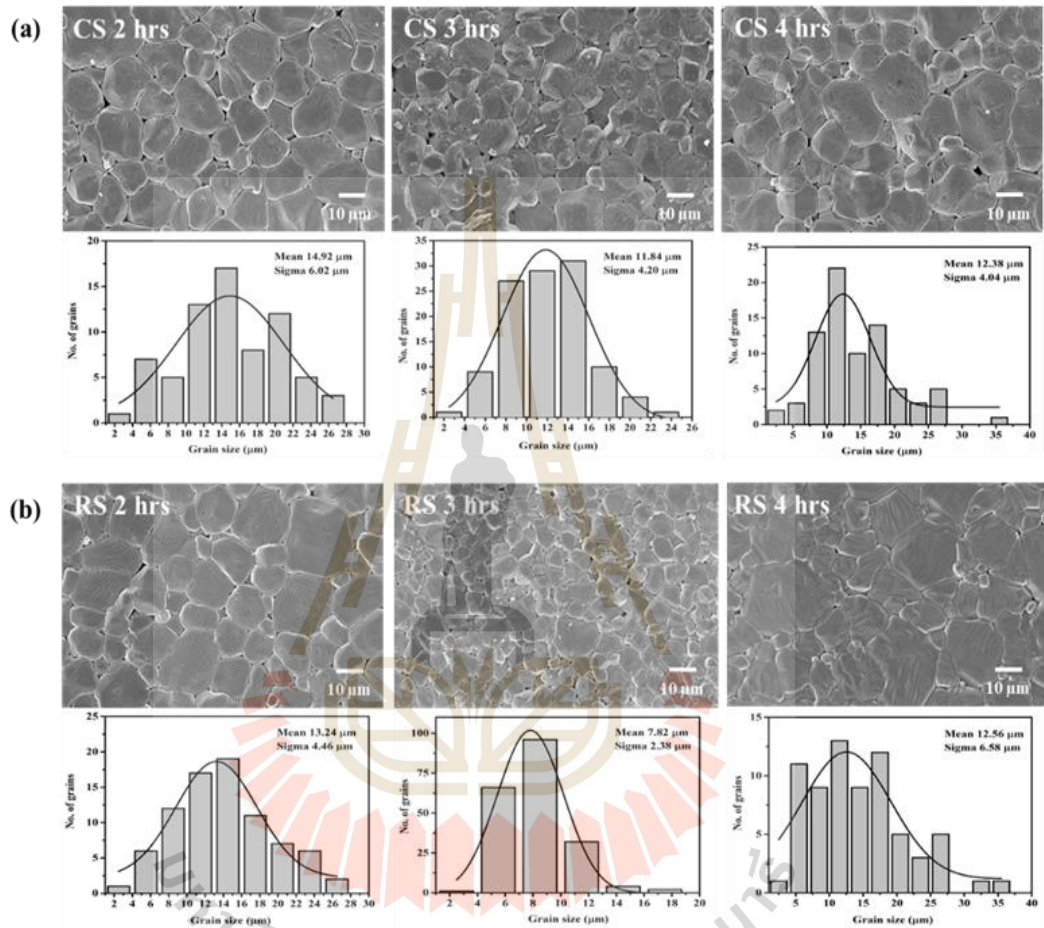


Figure 3.4 SEM micrograph of surface of BCZT ceramics were sintered at 1540 °C for 2, 3 and 4 hrs by CS (a) and RS (b).

3.3.3 Densities Results

At 2 hrs dwell time, RS-BCZT and CS-BCZT ceramic densities are equal. However, for the further increase of dwell time to 3 hrs and 4 hrs, RS-BCZT ceramics showed higher density than that of CS-BCZT ceramics. In overall comparison, RS-BCZT ceramics shown better densification similar to the densification of the PZT and KNN ferroelectric ceramics reported by L.B. Kong and J. Ma (Kong & Ma, 2001), and M. U. Farooq *et al.* (Farooq *et al.*, 2016). Moreover, all the RS-BCZT ceramics exhibited 24 % shrinkage ratio, which is higher than the CS-BCZT ceramic shrinkage ratio (9 %) under the same sintering condition. This is the effect of non-aggregation of BCZT powder with and without the calcination process.

3.3.4 Electrical Properties Results

The hysteresis loop of BCZT ceramics is shown in Figure 3.5. In overall, the ferroelectric properties (E_c , P_s , P_r) of BCZT ceramics slightly decreased with an increase of dwell time. The coercive fields (E_c), the saturation polarization (P_s) and the remnant polarization (P_r) values of RS-BCZT and CS-BCZT ceramics are tabulated in Table 3.1. The E_c of RS-BCZT ceramics decreased from 3.26 to 1.80 kV/cm with an increase of dwell time. On the other hand, E_c of CS-BCZT ceramics initially decreased but increased further with respect to increased dwell time. For saturation polarization, P_s , RS-BCZT ceramics decreased from 9.32 to 3.34 $\mu\text{C}/\text{cm}^2$, and CS-BCZT ceramics decreased from 9.68 to 5.31 $\mu\text{C}/\text{cm}^2$ with respect to the increase of dwell time. It can be seen clearly that in both techniques (CS and RS), P_s and P_r values decreased with an increase of dwell time. Similarly, for piezoelectric charge coefficient (d_{33}), the d_{33} value decreased with an increase of dwell time in both sintering techniques. The greatest d_{33} value of RS-BCZT and CS-BCZT ceramics is approximately 288 pC/N and 284 pC/N, respectively. These values belong to the samples sintered at 2 hrs dwell time.

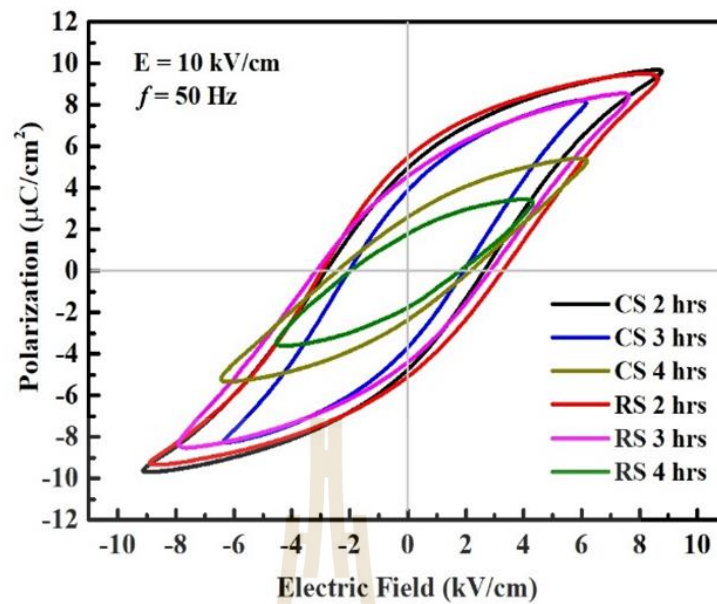


Figure 3.5 P - E hysteresis loops of BCZT ceramics were sintered by CS and RS at 1540 °C for 2, 3 and 4 hrs at frequencies 50 Hz under an electric field ± 10 kV/cm.

However, the piezoelectric charge constant (d_{33}) of both RS-BCZT and CS-BCZT ceramics are rather low comparing to the results from other studies (Coondoo et al., 2018; SHUKAI, 2012; Villafuerte-Castrejón et al., 2016; Wang et al., 2011), this is the consequence from inhomogeneous grain size and porosity inside the microstructure. It affects the domain orientation in the aligned electric field direction. In addition, the temperature dependent dielectric constant (ϵ_r) and dielectric loss ($\tan \delta$) of BCZT ceramics measured at 100 Hz frequency from 20 °C to 160 °C, are illustrated in Figure 3.6.

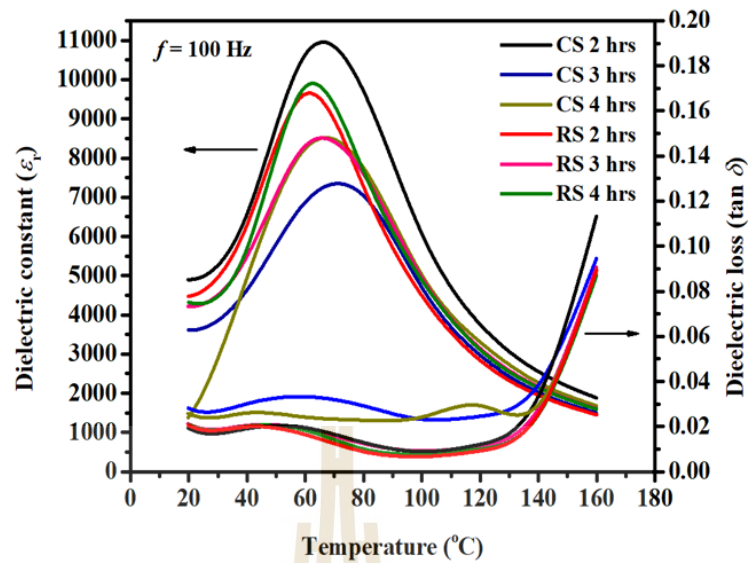


Figure 3.6 Temperature dependent dielectric constant (ϵ_r) and dielectric loss ($\tan \delta$) at 100 Hz of BCZT ceramics prepared by CS and RS techniques.

The BCZT ceramics transformed from tetragonal phase to cubic phase with increasing temperature. The Curie temperature (T_c) of RS-BCZT and CS-BCZT ceramics was noticed in the ranges of 63-67 °C and 67-73 °C, respectively. Similar kind of results was reported by M. Villafuerte-Castrejón *et al.* (Villafuerte-Castrejón *et al.*, 2016) ($T_c \approx 60-120$ °C). The T_c of RS-BCZT ceramics is slightly lower than that of CS-BCZT ceramics. It is believed that the inhomogeneous grain formation, domain wall motion, and internal stress/strain are responsible for the change in transition temperature (Buessem, Cross, & Goswami, 2006; Martirena & Burfoot, 1974). The relative maximum permittivity ($\epsilon_{r,max}$) of BCZT ceramics showed maximum value at 2 hrs of dwell time and these values are 9628 and 10610 respectively for RS and CS-BCZT. The noticed dielectric loss ($\tan \delta$) was approximately 0.02 and it is well below 2 % in both techniques. The polarization curves also give enough evidence that the leakage current density of both CS and RS samples is low.

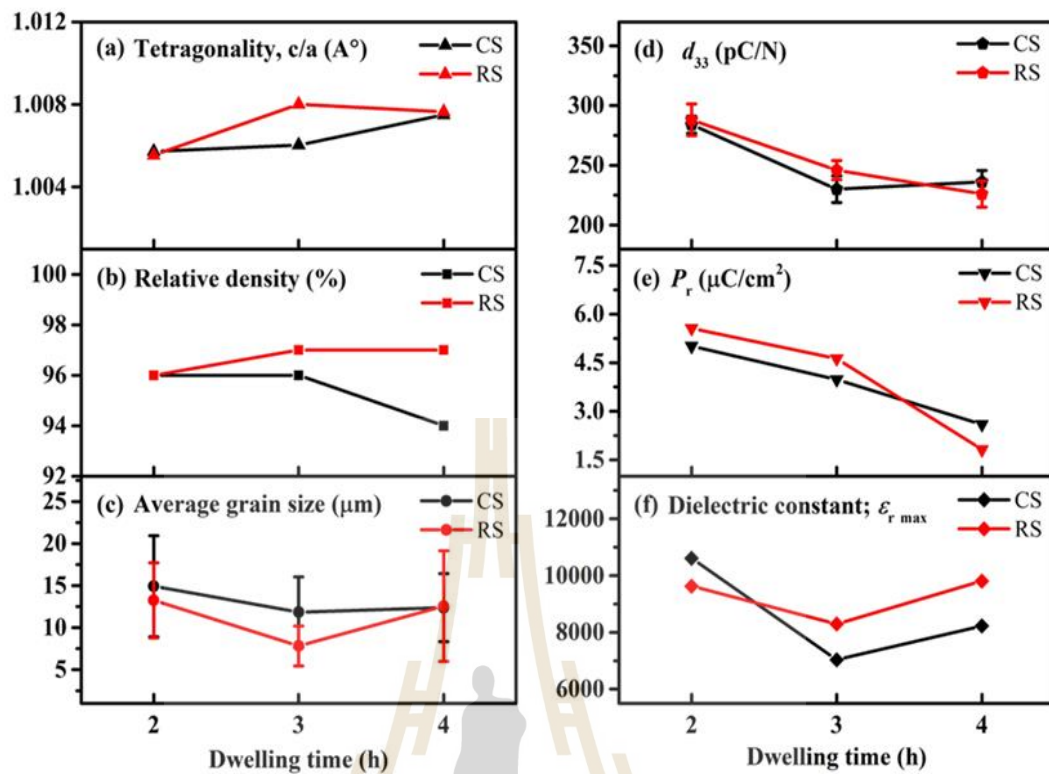


Figure 3.7 Physical properties (a, b, c) and piezoelectric properties (d, e, f) of BCZT ceramics at 1540 °C by different sintering techniques (CS and RS) and dwelling times.

Table 3.2 Electrical properties of BCZT ceramics sintered at 1540 °C for 2, 3 and 4 hrs by CS, and RS technique.

Sintering condition		Electrical properties					
Tech niques	Dwell time (hrs.)	$\epsilon_{r,max}$	$\tan \delta_{max}$	Saturation polarization; P_s ($\mu\text{C}/\text{cm}^2$)	Remanent polarization; P_r ($\mu\text{C}/\text{cm}^2$)	Coercive field; E_c (kV/cm)	d_{33} (pC/N)
CS	2	10610	0.02	9.68	5.01	2.53	284±6.97
	3	7035	0.03	8.13	3.98	1.91	230±11.09
	4	8232	0.09	5.31	2.60	2.11	236±9.65
RS	2	9628	0.02	9.32	5.56	3.26	288±13.27
	3	8295	0.02	8.54	4.63	2.80	246±8.02
	4	9807	0.02	3.34	1.82	1.80	226±10.93

3.3.5 XANES Results

Ti *K*-edge and Zr *L*₃-edge X-ray absorption spectra of BCZT ceramics prepared by CS and RS sintering techniques are shown in Figure 3.8. Figure 3.8(a) refers to the Ti *K*-edge XANES spectra and Figure 3.8(b) refers to the Zr *L*₃-edge XANES spectra, respectively. XANES spectra of Ti foil, Zr foil, Ti₂O₃, TiO₂ (Anatase) and ZrO₂ were used for reference purpose (shown in Figure 3.8(a) and (b)). The main absorption peak located at 4980 eV in XANES spectra (i.e. mainly due to Ti 1s to 4*p* dipole transitions) obtained from all sintering conditions is the same. A small hump at 4969 eV labeled as ‘A₁’ represents 1s to 3*d* quadrupolar transition. This peak is prominent in perovskite ferroelectric structures with a twisted TiO₆ octahedral site (Mastelaro et al., 2015; Ray et al., 2011; Vedrinskii, Kraizman, Novakovich, Demekhin, & Urazhdin, 1998). The second peak labeled as ‘A₂’ at 4970 eV is mainly related to the hybridization effect of 3*d* and 4*p* orbitals under the neighboring oxygen atoms. This peak also indirectly related to the Ti off-center distortion in TiO₆ octahedron perovskite ferroelectrics (Bootchanont et al., 2014; Mastelaro et al., 2015; Vedrinskii et al., 1998).

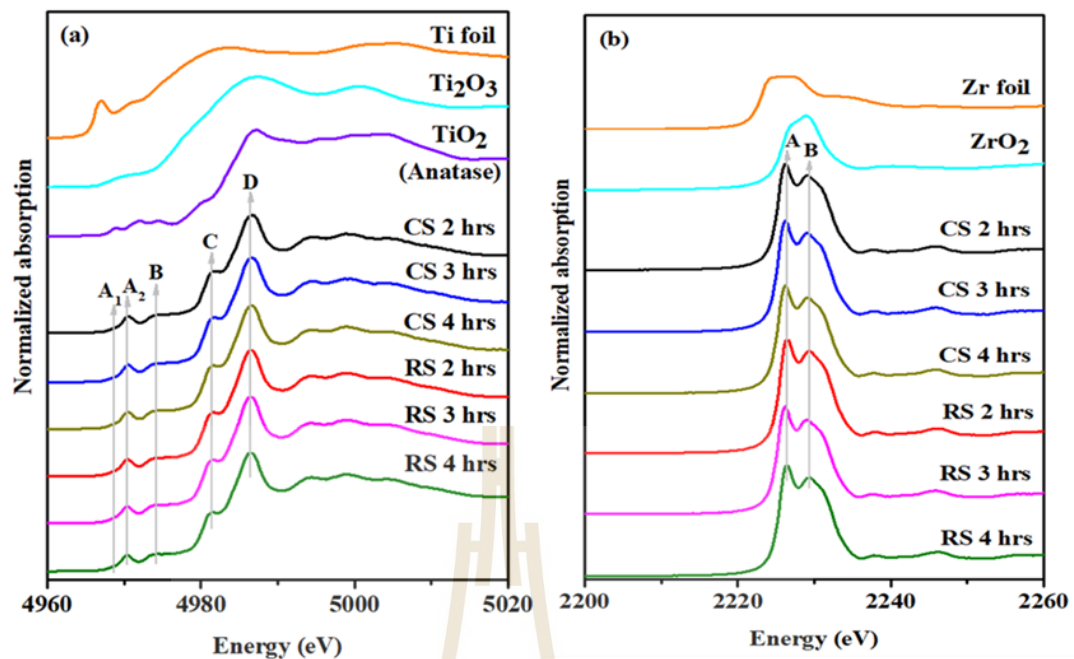


Figure 3.8 Normalized XANES spectra of BCZT ceramics prepared by CS and RS : (a) Ti K -edge spectra and (b) Zr L_3 -edge spectra.

The peak was deconvoluted into 'A₁' and 'A₂' and analyzed the variation of peak intensity with different sintering conditions (see Table 3.3). RS-BCZT ceramics exhibit an increase or decrease of the area under a corresponding peak at the PEFS more than CS-BCZT ceramics. The peak labeled as 'B' at 4974 eV related to the Ti 1s electron transition to unoccupied 3d states of the neighboring atom such Zr (Mastelaro et al., 2015; Ray et al., 2011; Vedrinskii et al., 1998). In addition, the features of peak labeled as 'C' and 'D' show the higher energies of 4981 eV and 4986 eV. This is also attributed to the ratio of Zr/Ti in the 3rd shell and the change in the local structure around main absorbed atom (Ti), respectively (Bootchanont et al., 2014). These results show that RS-BCZT ceramics in each dwell time exhibit the features of peaks labeled as A, B, C and D from XANES spectra which are comparable to CS-BCZT ceramics. The oxidation state of the Ti atoms was studied in each sintered BCZT ceramics, as well as compared with the three reference samples that are shown in Figure 3.8(a).

Table 3.3 The area under the corresponding peaks at the PEFS of XANES Ti K-edge of BCZT ceramics sintered at 1540 °C for 2, 3 and 4 hrs by CS and RS techniques.

Sample Name	Dwell time (hrs.)	Area under a corresponding peak at the PEFS (eV)				
		Peak A Total (A ₁ +A ₂)	Peak A ₁	%increase/ decrease (-)	Peak A ₂	%increase/ decrease (-)
CS-BCZT	2	0.21	0.03	-	0.18	-
	3	0.22	0.03	-19.44	0.19	3.69
	4	0.22	0.03	-10.37	0.19	4.68
RS-BCZT	2	0.21	0.04	-	0.17	-
	3	0.21	0.05	20.81	0.16	-5.94
	4	0.20	0.03	-34.53	0.17	8.31

Table 3.4 Edge position of Ti K-edge and Zr L₃-edge of BCZT ceramics sintered at 1540 °C for 2, 3 and 4 hrs by CS and RS techniques and reference samples.

Sample Name	Dwell time (hrs.)	Edge position (eV)	
		Ti K-edge (±0.3 eV)	Zr L ₃ -edge (±0.2 eV)
Ti foil	-	4966.0	-
Ti ₂ O ₃	-	4976.6	-
TiO ₂ (Anatase)	-	4979.2	-
Zr foil	-	-	2222.9
ZrO ₂	-	-	2225.9
CS-BCZT	2	4980.3	2225.3
CS-BCZT	3	4980.3	2225.4
CS-BCZT	4	4980.2	2225.3
RS-BCZT	2	4980.2	2225.3
RS-BCZT	3	4980.2	2225.4
RS-BCZT	4	4980.2	2225.4

Table 3.4 shows the Ti *K*-edge absorption positions of RS-BCZT, CS-BCZT and the reference samples. The pure Ti foil absorption edge position showed at 4966.1 eV which is related to Ti⁰ oxidation state. Ti *K*-edge position for Ti₂O₃ powder showed at 4976.6 eV which is related to the Ti³⁺ oxidation state and TiO₂ (Anatase) at 4979.2 eV related to Ti⁴⁺ oxidation state. These results are in agreement with the report done by Waychunas and Lin *et al.* (Lin, Mai, Chiu, Yang, & Chan, 2012; Waychunas, 1987). The absorption edge positions of RS-BCZT and CS-BCZT ceramics are at 4980 eV and these positions are very much close to the TiO₂ (Anatase) with Ti⁴⁺ oxidation state. This implies that BCZT ceramics prepared in both techniques were showed octahedrally coordinated TiO₆ structure and this coordination does not affect by various dwell times.

The Zr *L*₃-edge XAS spectra of BCZT ceramics prepared by CS and RS techniques at different dwell times are shown in Figure 3.8 (b). Two dominant peaks labeled as ‘A’ at 2226 eV and ‘B’ at 2229 eV are composed to the $2p \rightarrow e_g$ and $2p \rightarrow t_{2g}$ transitions, respectively. Zr foil *L*₃ absorption edge at 2222.9 eV correspond to the Zr⁰ oxidation state and ZrO₂ *L*₃ absorption edge at 2225.9 eV correspond to the Zr⁴⁺ oxidation state respectively. In our case, Zr *L*₃-edge of all BCZT ceramics showed at 2225 eV, which is very close to the Zr⁴⁺ oxidation state. The intensity ratio of peak ‘A’ to ‘B’ gives the information of the coordination number around Zr (i.e. absorbent atom) (Ikeno *et al.*, 2013). Peak A and B are originated from Zr 4*d* orbitals due to ligand field splitting effect into e_g and t_{2g} states within the ZrO₆ octahedral. This results are also consistent with the existing results in perovskite PZT system (Ray *et al.*) (Ray *et al.*, 2011). Similar kind of results in ferroelectric perovskite BCZT were reported by V.R. Mastelaro *et al.* (Mastelaro *et al.*, 2015) Ba(Ti,Zr)O₃ (Bootchanont *et al.*, 2014) and PZT compounds (Ray *et al.*, 2011).

3.4 Chapter Summary

In this chapter, the effect of CS and RS sintering techniques on the phase formation, microstructure, electrical properties, and oxidation state of BCZT ferroelectric ceramics have been studied in detail. The proposed composition of BCZT ($\text{Ba}_{0.85}\text{Ca}_{0.15}\text{Zr}_{0.1}\text{Ti}_{0.9}\text{O}_3$) was achieved by sintering at 1540 °C with different dwell times. All BCZT ceramics appear in a pure perovskite phase and mixture phase structures of tetragonal and orthorhombic. Both (CS and RS) BCZT ceramics prepared at 1540 °C for 2 hrs of dwell time exhibit optimal properties. RS-BCZT ceramic exhibits $13.24 \pm 4.46 \mu\text{m}$ of grain size, 96 % of relative density, 63 °C of T_c , $5.56 \mu\text{C}/\text{cm}^2$ of P_r , 3.26 kV/cm of E_c , 9628 of $\epsilon_{r,\text{max}}$, 0.02 of $\tan \delta$ and 288 pC/N of d_{33} . In CS-BCZT ceramic exhibits $14.42 \pm 6.02 \mu\text{m}$ of grain size, 96 % of relative density, 67 °C of T_c , $5.01 \mu\text{C}/\text{cm}^2$ of P_r , 2.53 kV/cm of E_c , 10610 of $\epsilon_{r,\text{max}}$, 0.02 of $\tan \delta$ and 284 pC/N of d_{33} . The Ti K -edge and Zr L_3 -edge XANES spectra resembles the 4+ oxidation state for Ti and Zr atoms of both (CS and RS) BCZT ceramics. Thus, the current study demonstrates that RS technique is a simple procedure and is more cost- and time- effective than CS method.

3.5 References

- Bharathi, P., & Varma, K. B. R. (2014). Grain and the concomitant ferroelectric domain size dependent physical properties of Ba_{0.85}Ca_{0.15}Zr_{0.1}Ti_{0.9}O₃ ceramics fabricated using powders derived from oxalate precursor route. *Journal of Applied Physics*, 116(16), 164107. doi:10.1063/1.4900494
- Bootchanont, A., Jutimoosik, J., Chandarak, S., Unruan, M., Kidkhunthod, P., Klysubun, W., Bhalla, A. (2014). Synchrotron X-ray absorption spectroscopy study of local structure transformation behavior in perovskite Ba(Ti,Zr)O₃ system. *Journal of Alloys and Compounds*, 616, 430-435.
doi:https://doi.org/10.1016/j.jallcom.2014.07.175
- Buatip, N., Promsawat, N., Pisitpipathsin, N., Namsar, O., Pawasri, P., Ounsung, K., Projprapai, S. (2018). Investigation on electrical properties of BCZT ferroelectric ceramics prepared at various sintering conditions. *Integrated Ferroelectrics*, 187(1), 45-52. doi:10.1080/10584587.2018.1445395
- Buessem, R., Cross, W. E., & Goswami, L. A. K. (2006). Phenomenological Theory of High Permittivity in Fine-Grained BaTiO₃. *Journal of the American Ceramic Society*, 49, 33-36. doi:10.1111/j.1151-2916.1966.tb13144.x
- Cheng, H.-l., Zhou, W.-c., Du, H.-l., Luo, F., & Zhu, D.-m. (2013). Effects of dwell time during sintering on electrical properties of 0.98(K_{0.5}Na_{0.5})NbO₃-0.02LaFeO₃ ceramics. *Transactions of Nonferrous Metals Society of China*, 23(10), 2984-2988. doi:https://doi.org/10.1016/S1003-6326(13)62824-1
- Coondoo, I., Panwar, N., Alikin, D., Bdikin, I., Islam, S. S., Turygin, A., Kholkin, A. L. (2018). A comparative study of structural and electrical properties in lead-free BCZT ceramics: Influence of the synthesis method. *Acta Materialia*, 155, 331-342. doi:https://doi.org/10.1016/j.actamat.2018.05.029
- Farooq, M. U., Fisher, J., Kim, J.-H., Kim, D., Shin, E.-C., Kim, Y.-H., Zhang, D. (2016). Reactive sintering of lead-free piezoelectric (K_{0.5}Na_{0.5})NbO₃ ceramics. *Journal of Ceramic Processing Research*, 17, 304-312.

- Fisher, J. G., Kim, M.-G., Kim, D., Cha, S.-J., Vu, H. V., Nguyen, D., Kim, M.-H. (2015). Reactive sintering of $(K_{0.5}Bi_{0.5})TiO_3$ - $BiFeO_3$ lead-free piezoelectric ceramics. *Journal of the Korean Physical Society*, 66(9), 1426-1438. doi:10.3938/jkps.66.1426
- GARVIE, R. C., & NICHOLSON, P. S. (1972). Phase Analysis in Zirconia Systems. *Journal of the American Ceramic Society*, 55(6), 303-305. doi:10.1111/j.1151-2916.1972.tb11290.x
- Ikeno, H., Krause, M., Höche, T., Patzig, C., Hu, Y., Gawronski, A., Rüssel, C. (2013). Variation of Zr-L2,3XANES in tetravalent zirconium oxides. *Journal of Physics: Condensed Matter*, 25(16), 165505. doi:10.1088/0953-8984/25/16/165505
- Kawashima, T., & Suzuki, Y. (2016). Reactive sintering and piezoelectric properties of $0.94Bi_{0.5}Na_{0.5}TiO_3$ - $0.06BaTiO_3$ ceramics with ZnO additive. *Journal of the Ceramic Society of Japan*, 124(9), 911-914. doi:10.2109/jcersj2.16051
- Kempet, W., Marungsri, B., Yimnirun, R., Klysubun, W., & Pojprapai, S. (2013). Investigation of the Unit Cell Distortion in PZT Ceramic via in-situ XAS Technique. *Ferroelectrics*, 453. doi:10.1080/00150193.2013.842138
- Kireš, M. (2007). Archimedes' principle in action. *Physics Education*, 42, 484-487. doi:10.1088/0031-9120/42/5/006
- Kong, L. B., & Ma, J. (2001). PZT ceramics formed directly from oxides via reactive sintering. *Materials Letters*, 51(2), 95-100. doi:https://doi.org/10.1016/S0167-577X(01)00272-5
- Leitzke, F., Fonseca, R., Goettlicher, J., Steininger, R., Jahn, S., Prescher, C., & Lagos, M. (2018). Ti K-edge XANES study on the coordination number and oxidation state of Titanium in pyroxene, olivine, armalcolite, ilmenite, and silicate glass during mare basalt petrogenesis. *Contributions to Mineralogy and Petrology*, 173. doi: 10.1007/s00410-018-1533-7

- Lin, K.-S., Mai, Y.-J., Chiu, S.-W., Yang, J.-H., & Chan, S. L. I. (2012). Synthesis and Characterization of Metal Hydride/Carbon Aerogel Composites for Hydrogen Storage. *Journal of Nanomaterials*, 2012, 9. doi:10.1155/2012/201584
- Liu, Y., Pu, Y., & Sun, Z. (2014). Enhanced relaxor ferroelectric behavior of BCZT lead-free ceramics prepared by hydrothermal method. *Materials Letters*, 137, 128-131. doi:https://doi.org/10.1016/j.matlet.2014.08.138
- Loiu, Y.-C. (2015). Reaction-Sintering Process for Preparing Electronic Ceramics. *Recent Patents on Materials Science*, 8(3), 225-238.
- Lu, X., Fang, B., Zhang, S., Yuan, N., Ding, J., Zhao, X., Luo, H. (2017). Decreasing sintering temperature for BCZT lead-free ceramics prepared via hydrothermal route. *Functional Materials Letters*, 10(04), 1750046. doi:10.1142/s17936 04717500461
- Martirena, H. T., & Burfoot, J. C. (1974). Grain-size effects on properties of some ferroelectric ceramics. *Journal of Physics C: Solid State Physics*, 7(17), 3182-3192. doi:10.1088/0022-3719/7/17/024
- Mastelaro, V. R., Favarim, H. R., Mesquita, A., Michalowicz, A., Moscovici, J., & Eiras, J. A. (2015). Local structure and hybridization states in Ba_{0.9}Ca_{0.1}Ti_{1-x}Zr_xO₃ ceramic compounds: Correlation with a normal or relaxor ferroelectric character. *Acta Materialia*, 84, 164-171. doi:https://doi.org/10.1016/j.actamat .2014.10.059
- Praveen, J. P., Karthik, T., James, A. R., Chandrakala, E., Asthana, S., & Das, D. (2015). Effect of poling process on piezoelectric properties of sol-gel derived BZT-BCT ceramics. *Journal of the European Ceramic Society*, 35(6), 1785-1798. doi:https://doi.org/10.1016/j.jeurceramsoc.2014.12.010
- Ravel, B., & Newville, M. (2006). Ravel, B. & Newville, M. *ATHENA and ARTEMIS: Interactive graphical data analysis using IFEFFIT. Phys. Scr.* 115, 1007-1010 (Vol. 2005).
- Ray, S. C., Hsueh, H. C., Wu, C. H., Pao, C. W., Asokan, K., Liu, M. T., Lee, J. F. (2011). Local atomic and electronic structures and ferroelectric properties of PbZr_{0.52}Ti_{0.48}O₃: An x-ray absorption study. *Applied Physics Letters*, 99(4), 042909. doi:10.1063/1.3607475

- SHUKAI, Y. (2012). TOWARDS HIGHER PERFORMANCE LEAD-FREE PIEZOELECTRIC CERAMICS—NEXT GENERATION (Ba, Ca)(Zr, Ti) O₃.
- Vedrinskii, R. V., Kraizman, V. L., Novakovich, A. A., Demekhin, P. V., & Urazhdin, S. V. (1998). Pre-edge fine structure of the 3d atom K x-ray absorption spectra and quantitative atomic structure determinations for ferroelectric perovskite structure crystals. *Journal of Physics: Condensed Matter*, *10*(42), 9561-9580. doi:10.1088/0953-8984/10/42/021
- Villafuerte-Castrejón, M., Morán, E., Reyes-Montero, A., Vivar-Ocampo, R., Peña-Jiménez, J.-A., Rea-López, S.-O., & Pardo, L. (2016). Towards Lead-Free Piezoceramics: Facing a Synthesis Challenge. *Materials*, *9*(1), 21. doi:https://doi.org/10.3390/ma9010021
- Wang, P., Li, Y., & Lu, Y. (2011). Enhanced piezoelectric properties of (Ba_{0.85}Ca_{0.15})(Ti_{0.9}Zr_{0.1})O₃ lead-free ceramics by optimizing calcination and sintering temperature. *Journal of the European Ceramic Society*, *31*(11), 2005-2012. doi:https://doi.org/10.1016/j.jeurceramsoc.2011.04.023
- Waychunas, G. (1987). Synchrotron radiation XANES spectroscopy of Ti in minerals: Effects of Ti bonding distances, Ti valence, and site geometry on absorption edge structure. *American Mineralogist*, *72*.
- Wu, J., Xiao, D., Wu, W., Zhu, J., & Wang, J. (2011). Effect of dwell time during sintering on piezoelectric properties of (Ba_{0.85}Ca_{0.15})(Ti_{0.90}Zr_{0.10})O₃ lead-free ceramics. *Journal of Alloys and Compounds*, *509*(41), L359-L361. doi:https://doi.org/10.1016/j.jallcom.2011.08.024
- Yang, Z., Zhou, S., Zu, J., & Inman, D. (2018). High-Performance Piezoelectric Energy Harvesters and Their Applications. *Joule*, *2*(4), 642-697. doi:https://doi.org/10.1016/j.joule.2018.03.011

CHAPTER 4

THE ENERGY HARVESTING PERFORMANCE OF BCZT PIEZOELECTRIC CERAMICS UNDER LOW FREQUENCY

4.1 Introduction

This chapter reports the energy harvesting performance of BCZT ceramics fabricated using the solid-state reactive sintering (SSRS) method. The cold isostatic pressing (CIP) technique was applied to improve the piezoelectric properties for energy harvesting applications. The phase and microstructure of the ceramics were investigated using X-ray diffraction (XRD) and scanning electron microscope (SEM), while dielectric, ferroelectric, and piezoelectric properties were characterized, including the piezoelectric constant (d_{33}), piezoelectric voltage constant (g_{33}), Figure of Merit (FOM), mechanical quality factor (Q_m), and the electromechanical coupling factor (k_p). The effect of compressive load on the energy harvesting output performance of the material was also presented.

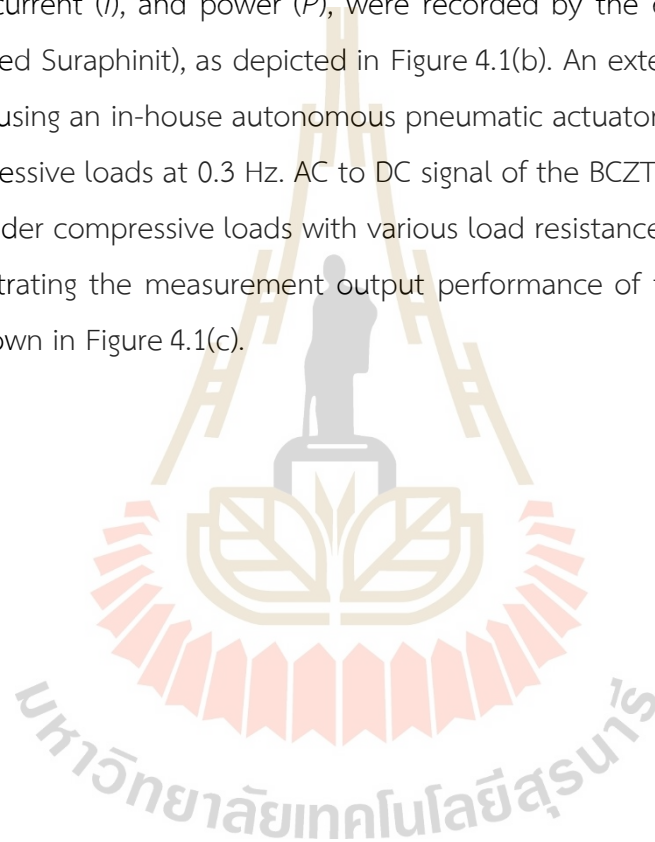
This chapter is divided into several sections. Section 4.2 describes the experimental procedure used in this study. Section 4.3 presents the results and discussion of the BCZT piezoelectric ceramic characterization and investigation, which includes section 4.3.1 on the phase, microstructure, electrical and piezoelectric properties of BCZT ceramic, section 4.3.2 on the energy harvesting performance of BCZT ceramic under various compressive loads, and section 4.3.3 on the charging ability to the stored voltage and energy density in various capacitors of BCZT ceramic. Finally, section 4.4 concludes the chapter.

4.2 Experimental Procedure

$Ba_{0.85}Ca_{0.15}Zr_{0.1}Ti_{0.9}O_3$ (BCZT) lead-free ferroelectric ceramics were synthesized via the conventional solid-state reaction technique (Wang, Li, & Lu, 2011). This study utilized commercially available powders of barium carbonate ($BaCO_3$, 99.0 %, Sigma

Aldrich), calcium carbonate (CaCO_3 , 99.9 %, Eleps), zirconium oxide (ZrO_2 , 99.5 %, Eleps), and titanium oxide (TiO_2 , 99.8 %, Aldrich chemistry) as starting materials. To produce a mixture of 50 g $\text{Ba}_{0.85}\text{Ca}_{0.15}\text{Zr}_{0.1}\text{Ti}_{0.9}\text{O}_3$, the initial powders of 37.6189 g BaCO_3 , 16.1206 g TiO_2 , 3.3670 g CaCO_3 , and 2.7636 g ZrO_2 were ball-milled for 24 hrs in ethanol, followed by drying at 120 °C for 24 hrs to remove residual ethanol. The powders were subsequently calcined in air at 1300 °C for 2 hrs, with heating and cooling rates of 5 °C/min. The calcined powders were then re-ball milled in ethanol for 6 hrs and dried at 120 °C for 24 hrs in an oven to remove any remaining ethanol content. Finally, the well-mixed $\text{BaCO}_3\text{-CaCO}_3\text{-ZrO}_2\text{-TiO}_2$ (BCZT) powder was pressed into $40 \times 20 \times 3 \text{ mm}^3$ pellets using a uniaxial press with 4 tons of pressure. The BCZT pellets, with a size of $40 \times 20 \times 3 \text{ mm}^3$, were re-pressed using cold isostatic pressing (CIP) at 300 MPa for 30 s before the sintering process. The sintering process was carried out at 1540 °C for 2 hrs in the air, with heating and cooling rate of 5 °C/min. Furthermore, the sintered BCZT ceramics, with a size of $30 \times 15 \times 2 \text{ mm}^3$, were thinned down from 2 mm to 1 mm using silicon carbide (SiC) grit papers. The calcined BCZT powder and sintered BCZT ceramics were characterized using an X-Ray Diffractometer (XRD, Bruker Phaser DII). The surface morphology and grain size were analyzed using a Scanning Electron Microscope (SEM, JEOL JSM-6010LV). The average grain size was estimated by using Image J software. Subsequently, fine polished BCZT ceramics were coated with silver (Ag) electrodes on both sides and annealed at 600 °C for 1 hr in the air, with a heating and cooling rate of 5 °C/min. The BCZT bulk was poled under 3.0 kV/mm of DC electric field for 30 minutes in a silicon oil bath (at room temperature) (Matsusada, AU-30*40 instrument). The piezoelectric constant (d_{33}) was measured from the poled ceramics using d_{33} meter (International Ltd., APC-S5865). Polarization versus electric field (P - E) and Strain versus electric field (S - E) hysteresis loops of BCZT were measured by P - E and S - E hysteresis (TREK, Model 20/20C) at room temperature under $\pm 15 \text{ kV/cm}$ electric field with 50 Hz frequency. The mechanical quality factor (Q_m) and the electromechanical coupling factor (k_p) were determined using an impedance analyzer (Keysight, E4990A). The piezoelectric voltage constant (g_{33}) can be calculated by d_{33}/ϵ^T , where $\epsilon^T = \epsilon_0 \cdot \epsilon_r$. The dielectric properties (ϵ_r and $\tan \delta$) were measured using a precision LCR meter (Keysight, E4980A) at room temperature.

To make a BCZT energy harvester, the poled BCZT ceramic was attached to a Cu substrate using conductive epoxy (EPO-TEK H20E, Electron Microscopy Sciences, Hatfield, PA) and aluminium (Al) tape as a top electrode. The sample was then soldered to positive and negative electrical wires as shown in Figure 4.1(a). Subsequently, the sample was placed on the sample holder of a pneumatic actuator machine, which was connected to a load resistance variable box, voltmeter and amp meter (Keysight, 34465A, Digital Multimeter). The energy harvesting signals, such as voltage (V), current (I), and power (P), were recorded by the custom-built software package (called Suraphinit), as depicted in Figure 4.1(b). An external mechanical load was applied using an in-house autonomous pneumatic actuator in the range of 50 to 200 N compressive loads at 0.3 Hz. AC to DC signal of the BCZT energy harvester was measured under compressive loads with various load resistances and capacitors. The diagram illustrating the measurement output performance of the energy harvesting system is shown in Figure 4.1(c).



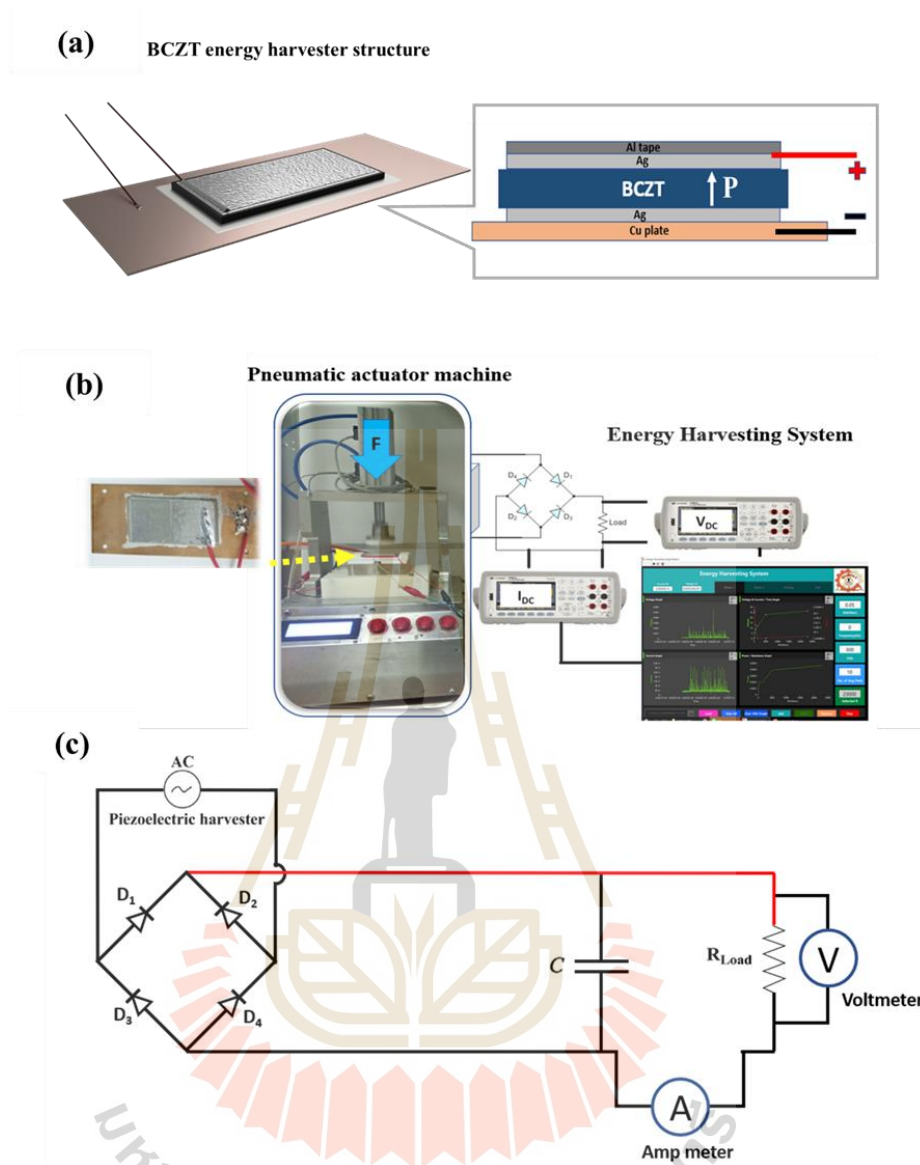


Figure 4.1 (a) The BCZT energy harvester structure and (b) the pneumatic actuator machine to apply the compressive load, and energy harvesting system to measure the output performance of BCZT ceramics ; (c) the diagram of a testing circuit with load resistance.

4.3 Results and Discussion

4.3.1 BCZT ceramics characterization

The conventional solid-state reaction technique with optimum sintering conditions referred from Wang *et al.* (Wang et al., 2011) was used to fabricate bulk BCZT ceramics. The relative density of BCZT ceramics was about 98-99 % (with an average bulk density of approximately 5.607 g/cm³), which is comparable to the theoretical density ($\rho_t \square 5.687$ g/cm³) (Wang et al., 2011). Figure 4.2(a) shows the XRD pattern of calcined BCZT powder (calcined at 1300 °C for 2 hrs) and sintered BCZT ceramics (sintered at 1540 °C for 2 hrs). The XRD patterns from 20° to 70° of 2 θ showed that BCZT powders and ceramics have a pure perovskite structure without other impurity phases. The specific peak at 44°– 46° of 2 θ represents the perovskite structure of the ceramics, and the exact peak deconvolution is shown in Figure 4.2(b). The deconvoluted peaks at 45.01° and 45.36° of 2 θ belong to the tetragonal phase of (002)_T and (200)_T crystal planes. Similarly, the deconvoluted peaks at 45.10° of 2 θ belong to the rhombohedral phase of the (202)_R crystal plane. The above-deconvoluted peaks are well-matched with the JCPDS file (PDF# 00-065-0109) for the tetragonal phase and the JCPDS file (PDF# 00-063-0612) for the rhombohedral phase. The Ba_{0.85}Ca_{0.15}Zr_{0.1}Ti_{0.9}O₃ ceramics possess the morphotropic phase boundary (MPB) structure, as evident from the XRD result. This phase structure analysis agrees with previous studies (Buatip et al., 2020; Munthala et al., 2020; Munthala et al., 2021).

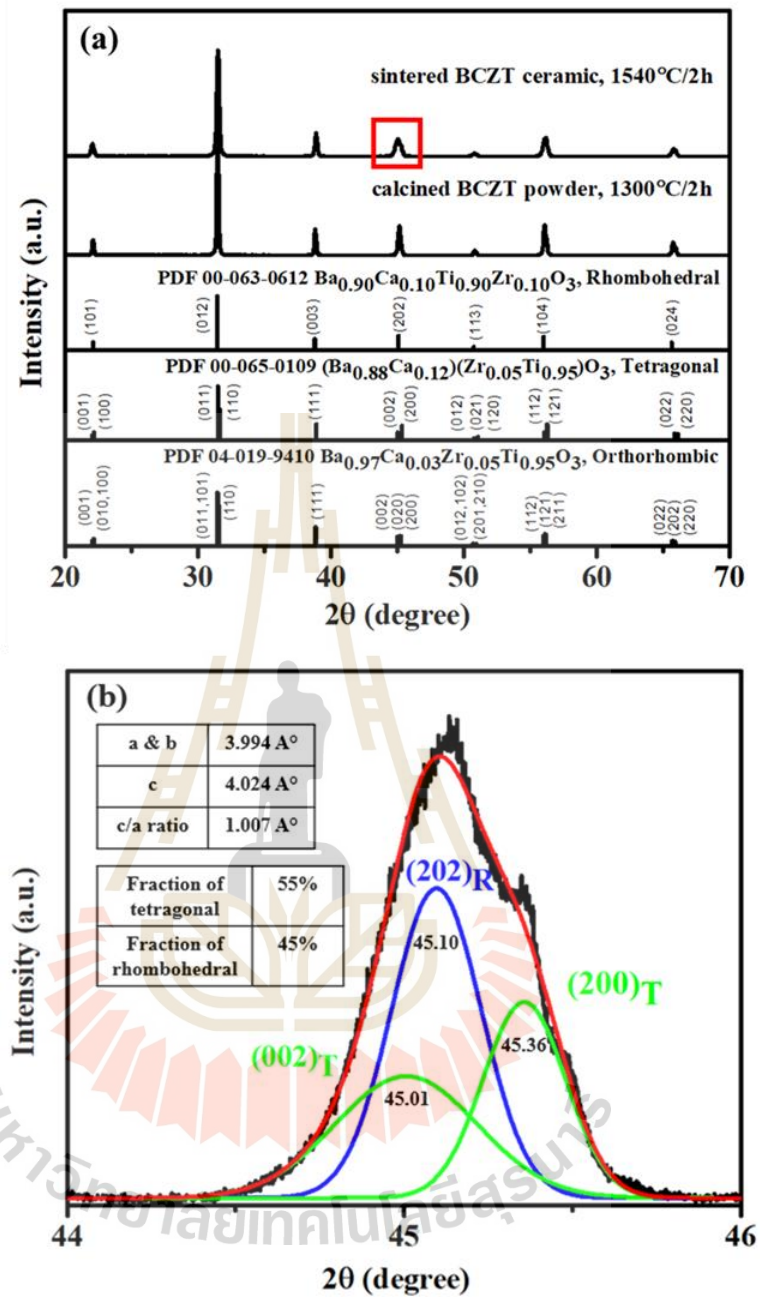


Figure 4.2 (a) XRD patterns and (b) a fraction of rhombohedral/tetragonal phase of BCZT ceramics.

The fraction of the tetragonal phase (C_T) from the compositional MPB structure can be estimated using the following Garvie and Nicholson equation (4.1) (GARVIE & NICHOLSON, 1972):

$$C_T = \frac{I_T(002) + I_T(200)}{I_T(002) + I_T(200) + I_R(202)} \quad (4.1)$$

where ' C_T ' is the compositional weight of the tetragonal phase, and ' I_T ' and ' I_R ' are crucial areas of the tetragonal and rhombohedral phases. The estimated tetragonal and rhombohedral phase fractions are 55 % and 45 %, respectively. The sintered BCZT ceramics demonstrate a calculated tetragonality (c/a ratio) of 1.007, with a corresponding tetragonality value of approximately 1.006 obtained from JCPDS file no. PDF#00-065-0109. Notably, the experimental value is found to be in significant agreement with the latter value, indicating the reliability of the calculation. The SEM surface micrograph and the average grain size histogram are shown in Figure 4.3. The surface has uniformly distributed grains, and the average grain size is $17.84 \pm 6.40 \mu\text{m}$ (as shown in Figure 4.3(a)).

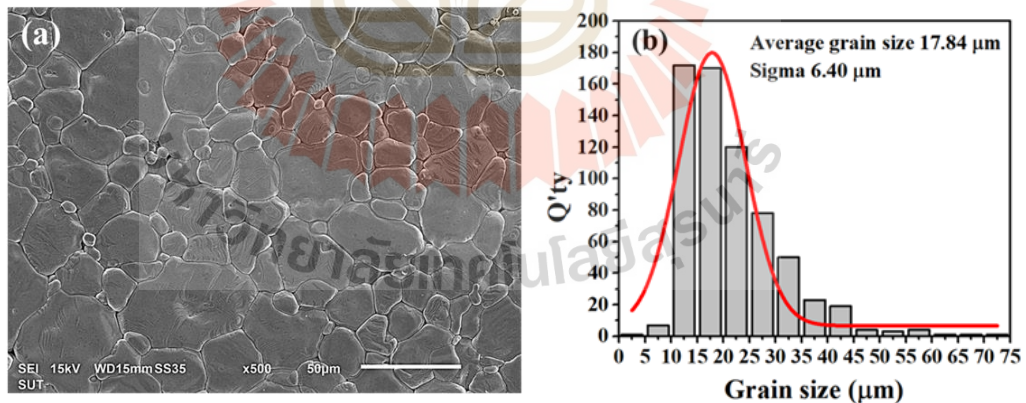


Figure 4.3 (a) SEM surface micrograph and (b) the average grain size of a sintered BCZT ceramics.

Hysteresis loops of polarization versus electric field (P - E) and stains versus electric field (S - E) are shown in Figure 4.4. The estimated value of P_r and E_c for unpoled conditions are $\pm 4 \mu\text{C}/\text{cm}^2$ and $\pm 3 \text{kV}/\text{cm}$, respectively. The P - E and S - E loops

exhibit the symmetric nature of unpoled BCZT ceramics. The measured piezoelectric constant (d_{33}) is 517 pC/N, and the calculated piezoelectric strain coefficient (d_{33}^*) (from the slope of S - E loop) is 138 pm/V. The measured piezoelectric constant of the BCZT ceramics is comparable to that of PZT ceramics.

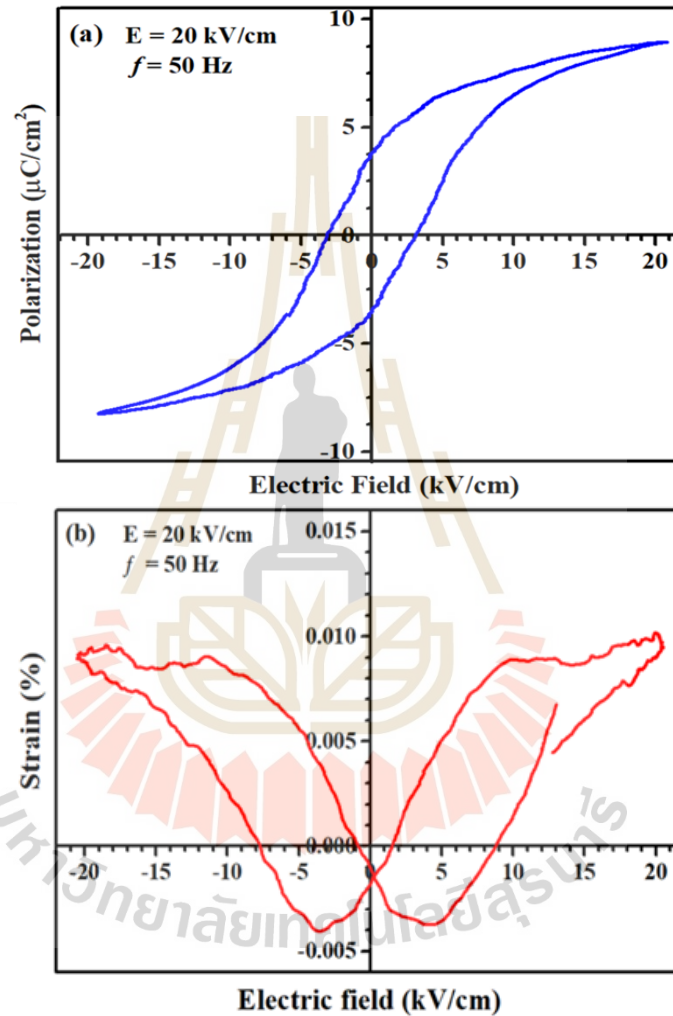


Figure 4.4 (a) P - E and (b) S - E loops of BCZT ceramics (unpoled) at 50 Hz frequency under ± 20 kV/cm electric field.

The piezoelectric voltage constant (g_{33}), electromechanical coupling factors (k_p), mechanical quality factor (Q_m), and figure of merit (FOM) were calculated using the following equations (4.2 – 4.5) (Li, Xu, Liu, & Gao, 2018; Mason & Jaffe, 1954):

$$g_{33} = \frac{d_{33}}{\epsilon_0 \epsilon_r} \quad (4.2)$$

$$k_p^2 = 2.51 \left(\frac{f_a^2 - f_r^2}{f_r^2} \right) + 0.038 \quad (4.3)$$

$$Q_m = \frac{1}{2\pi f_r Z_m C_0} \left(\frac{f_a^2}{f_a^2 f_r^2} \right) \quad (4.4)$$

$$FOM = d_{33} \times g_{33} \quad (4.5)$$

Here, d_{33} is the piezoelectric constant, ϵ_0 is the dielectric constant of vacuum, ϵ_r is the relative dielectric constant, f_r and f_a are the resonance and antiresonance frequencies, Z_m is the impedance value at f_r , and C_0 is static capacitance. Based on these equations, the calculated values of g_{33} , k_p , Q_m , and FOM of BCZT ceramics are 19×10^{-3} Vm/N, 0.33, 176, and $9,823 \times 10^{-15}$ m²/N, respectively. Table 4.1 provides a comparison of the piezoelectric properties of BCZT ceramics with other piezoelectric materials. As discussed, BCZT ceramics exhibit better piezoelectric properties than BaTiO₃ and are equivalent to PZT ceramics. Therefore, the prepared BCZT ceramics can convert mechanical energy to electrical energy and can be used as a piezoelectric energy harvester (PEH). The energy harvesting performance of BCZT ceramics under mechanical load is investigated in the following sections.

Table 4.1 Piezoelectric properties of BCZT ceramics compared with other piezoelectric materials.

Materials/ Properties	(Ba,Ca) (Zr,Ti)O ₃	BaTiO ₃	PZT-4	PZT-5A	PZT-5H	PZT-8	BCZT
d_{33} (pC/N)	546	149	289	374	593	225	517
g_{33} (10 ⁻³ Vm/N)	15.3	14.1	26.1	24.8	19.7	25.4	19
k_{33}, k_p	0.65	0.48	0.7	0.71	0.75	0.64	0.33
Mechanical Q_M		300	500	75	65	1,000	176
Dielectric loss			0.4 %		2 %	0.4 %	1 %
Curie Temp (°C)	94	115	328	365	193	300	90
FOM ($d_{33} * g_{33}$) (10 ⁻¹⁵ m ² /N)	8,354	2,100	7,543	9,275	11,682	5,715	9,823
Ref.	(Rödel et al., 2015)	(Yang, Zhou, Zu, & Inman, 2018)					This work

4.3.2 Energy harvesting under various compressive loads

In Figure 4.1(a), the top and bottom electrodes were attached to the BCZT ceramics to conduct electricity from polarized and rearrangement dipoles. The Cu plate electrode was connected to the pneumatic actuator machine base and diode bridge rectifier, as shown in Figure 4.1(b). The diode bridge rectifier converts the AC signal to a DC signal, and a 0.1 μ F capacitor smooths the signal by charge-discharge mechanism (Al-Ashtari, 2013). The DC electrical output responses, i.e., voltage (V), current (I), and power (P), were measured at various external load resistance (R_L), as shown in Figure 4.1(c). The DC electrical outputs were measured at R_L ranging from 100 k Ω to 20 M Ω when the pneumatic actuator machine applied compressive loads of 50 to 200 N to the ceramics at varies intervals and at an operating frequency of \sim 0.3 Hz. For instance, when the compressive load was 50 N and the electrical load resistance was varied between 100 k Ω to 20 M Ω . The output voltage is increased and output

current decreased continuously with an increasing load resistance, as shown in Figure 4.5(a). The output power initially increased but then reduced with increasing load resistance. The BCZT energy harvesting device exhibited a maximum output power value of $2.86 \mu\text{W}$ ($V_{\text{DC}} \sim 2.01 \text{ V}$, $I_{\text{DC}} \sim 1.42 \mu\text{A}$) at $1 \text{ M}\Omega$ load resistance, as shown in Figure 4.5(b).

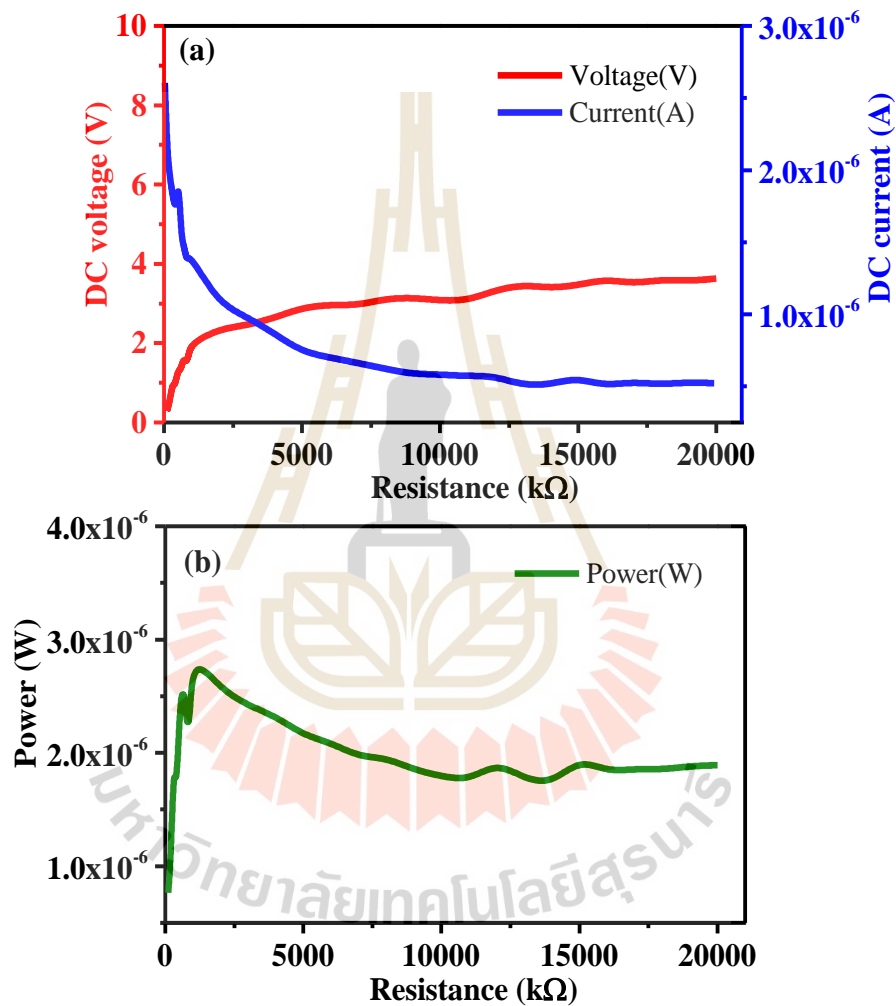


Figure 4.5 The output performance of BCZT ceramics at a range of resistance from $100 \text{ k}\Omega$ - $20 \text{ M}\Omega$ under compressive load 50 N at 0.3 Hz of frequency : (a) DC voltage and DC current, and (b) Power.

This result corresponds to the internal load resistance of the BCZT energy harvesting device with an impedance matching concept, according to the maximum power transfer theory (Alexander & Sadiku, 2017). Therefore, the external load resistance was fixed at 1 M Ω , and the compressive loads were varied from 50 to 200 N to optimize the output (V , I , P). The applied stress on the BCZT ceramics was calculated using equation (4.6):

$$\sigma = \frac{P}{A} \quad (4.6)$$

where σ is stress (N/m²), P is compressive force (N), and A is the cross-sectional area of the sample (m²). The dielectric displacement of the BCZT ceramics was estimated using equation (4.7):

$$D = \frac{Q}{A} = d\sigma \quad (4.7)$$

where D is dielectric displacement, Q is the electrical charge (C), A is the electrode area of the sample (m²), d is the piezoelectric constant (C/N), and σ is the stress (N/m²).

The compressive stress values applied to the BCZT ceramics are calculated to be 0.08 N/m², 0.16 N/m², 0.24 N/m², and 0.32 N/m². As depicted in Figure 4.6(a), an increase in the compressive stress values leads to a corresponding increase in the dielectric displacement values of the BCZT ceramics. Specifically, at applied loads of 50, 100, 150, and 200 N, the dielectric displacement values are observed to be 41.36 pC/m², 82.72 pC/m², 124.08 pC/m², and 165.44 pC/m², respectively. This increase is due to the electrical charge stored in the BCZT ceramics. The corresponding output values (V , I , and P) of the BCZT harvester as a function of compressive load were averaged and are presented in Figure 4.6(b) and Figure 4.6(c).

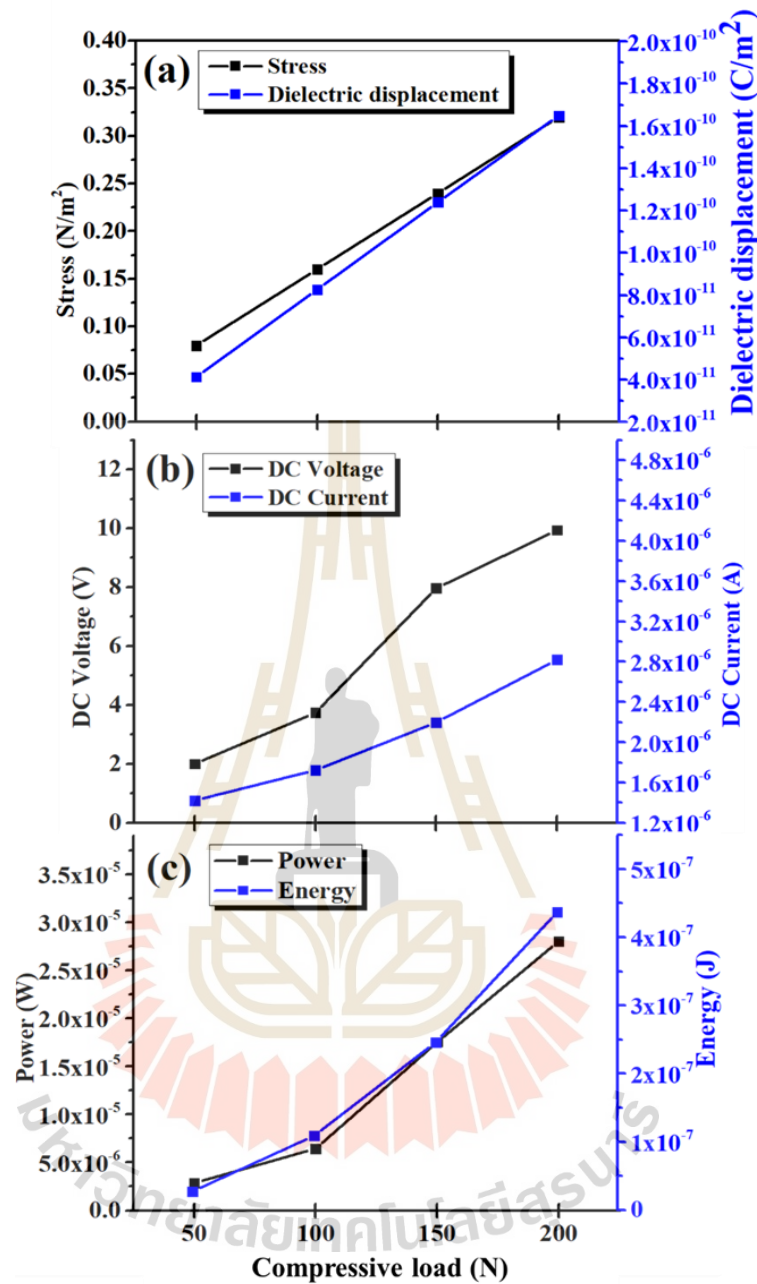


Figure 4.6 The physical and electrical properties of BCZT ceramics across $1 \text{ M}\Omega$ resistance under compressive loads 50 N, 100 N, 150 N, and 200 N at 0.3 Hz of frequency : (a) stress and dielectric displacement, (b) the output performance on DC voltage and DC current, (c) power and energy.

The DC voltage, current, and power values were measured to be 2.01, 3.74, 7.97, and 9.94 V, 1.42, 1.72, 2.20, and 2.82 μA , and 2.86, 6.45, 17.52, and 28.03 μW , respectively for loads of 50, 100, 150, and 200 N. As the load increases from 50 to 200 N, the output voltage, current, and power values also increase continuously. The energy generated by the BCZT harvester from d_{33} -effect mode can be calculated using equation (4.8) (Ji, Yoon, & Koh, 2021):

$$E_{max} = \frac{1}{2}(d_{33} \times g_{33})\frac{t}{s}F^2 \quad (4.8)$$

where d_{33} is the piezoelectric charge coefficient, g_{33} is the piezoelectric voltage coefficient, t is the thickness (m), s is the area (m^2), and F is the force (N). The calculated energy values are 27.3×10^{-8} , 1.09×10^{-7} , 2.46×10^{-7} , and 4.37×10^{-7} J for loads of 50, 100, 150, and 200 N, respectively, as shown in Figure 4.6(c). These results indicate that the output performance of the BCZT harvester is directly proportional to the force acting on the material. The maximum electrical output performance of the BCZT harvester was achieved at a compressive load of 200 N without any damage. To test the reliability of the BCZT energy harvester, a reliability test was conducted at a load of 200 N for 200 cycles at 0.3 Hz, and the results are shown in Figure 4.7. After 200 cycles, the device was found to be reliable with consistent values. However, the output power decreased slightly after 200 cycles, and the average output values were measured to be 11 V, 2 μA , and 22 μW for output voltage, current, and power, respectively. An optimized power and power density value of 28 μW and $0.1 \mu\text{W}/\text{mm}^3$, respectively, were obtained at a load resistance of 1 $\text{M}\Omega$. Table 4.2 provides a comparative study of power and power density with other work and this work. Obtained results in this work suggest that the BCZT ceramics are potentially viable for energy harvesting at low frequencies compared to other lead-based bulk piezoelectric ceramics and some cantilever piezoelectric energy harvesters at high frequencies.

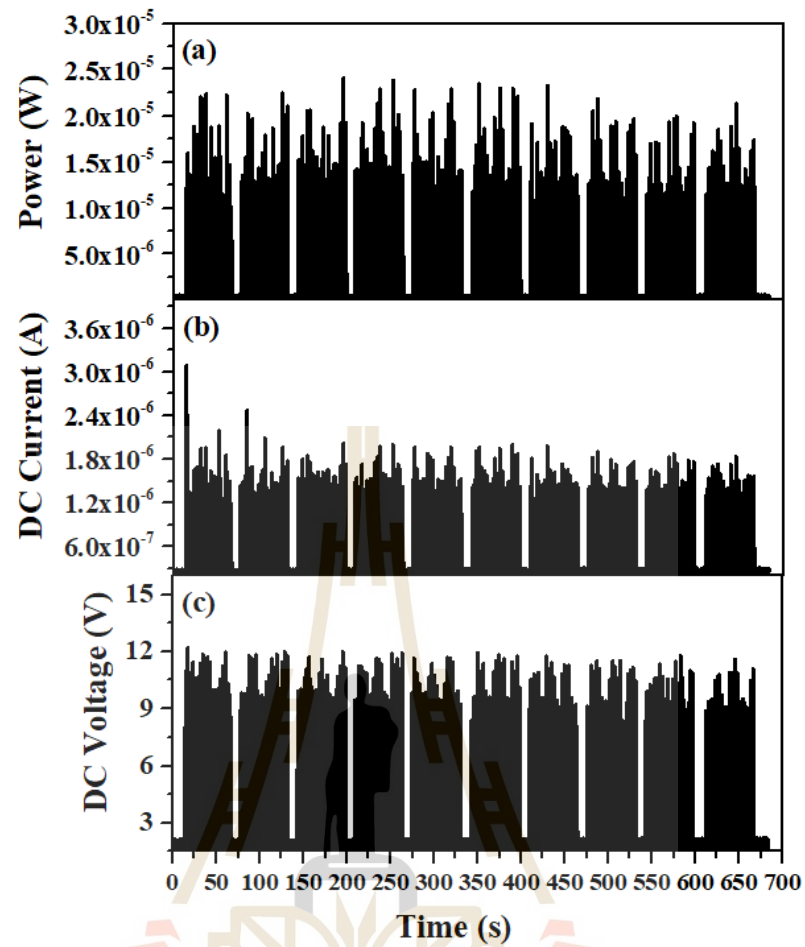


Figure 4.7 Output performance and reliability of BCZT ceramic energy harvester across $1 \text{ M}\Omega$ of resistance, at compressive load 200 N and 0.3 Hz of frequency: (a) Power, (b) DC current, and (c) DC voltage.

Table 4.2 Comparison of piezoelectric energy harvesters in terms of output performance.

Materials	Structure	Acceleration (m/s ²)	Frequency (Hz)	Compressive Load (N)	Power (μW)	Power density (μW/mm ³)	Energy density (J/m ³)	References
PZT	Cantilever	1	99.9	-	1.6	0.6	-	(Janphuang et al., 2014)
BS-PT	Cantilever	10	40	-	13	0.1	-	(Wu et al., 2016)
BMZ-PT	Bulk ceramic	-	0.18	350	21	0.14	101	(Ji et al., 2021)
BNZ-PT	Bulk ceramic	-	0.18	350	12	0.23	167	(Ji et al., 2021)
NBT-KBT-BT	Cantilever	9.8	80	-	7.44	0.37	-	(Zhang et al., 2020)
KNNS	Cantilever	-	70	-	0.84	0.008	-	(Oh et al., 2011)
Mn-KNN	Cantilever	10	90	-	16	0.32	-	(Zheng et al., 2017)
BCZT	Cantilever	10	90	-	70	1.4	-	(Yan et al., 2017)
BCZT	Cantilever	10	92	-	99	1.7	-	(Yan et al., 2018)
BCZT	Bulk ceramic	-	0.3	200	28	0.1	417	This work

4.3.3 Stored voltage and energy density in capacitors

Figure 4.1(c) shows a schematic circuit diagram of the piezoelectric energy harvester, which converts AC to DC and analyzes the stored energy in capacitors. Figure 4.8(a) illustrates the charging behavior of capacitors when a compressive load of 200 N was applied at a frequency of 0.3 Hz, and the output voltage was measured continuously for 300 s (equivalent to 900 load cycles). The four-diodes bridge rectifier with different capacitors of 1, 2.2, 4.7, and 22 μF showed output voltages of 3.96, 3.76, 3.32, and 4.13 V, respectively. The stored output energy can be estimated using equation (4.9) (Ji et al., 2021; Shin & Koh, 2017):

$$E = \frac{1}{2} CV^2 \quad (4.9)$$

where C is the capacitance of the capacitor, and V is the measured output voltage across the capacitor. The stored energy density can be estimated by dividing the volume of the sample. Figure 4.8(b) shows the calculated energy density of the capacitors from charging by the BCZT ceramics. The calculated energy densities were approximately 17, 35, 58, and 417 J/m^3 for capacitors of 1, 2.2, 4.7, and 22 μF , respectively. The optimized stored energy density was obtained from the 22 μF capacitor, which showed the maximum stored voltage. A comparison of the energy density of our BCZT material with other energy harvesting materials is presented in Table 4.2. These results indicate that the energy density of bulk BCZT ceramic obtained at a capacitor of 22 μF is approximately two to four times higher than that of lead-based bulk piezoelectric ceramics (i.e., BMZ-PT, and BNZ-PT) under compressive load at low frequencies. Therefore, bulk BCZT ceramics are excellent alternatives for energy harvesting applications.

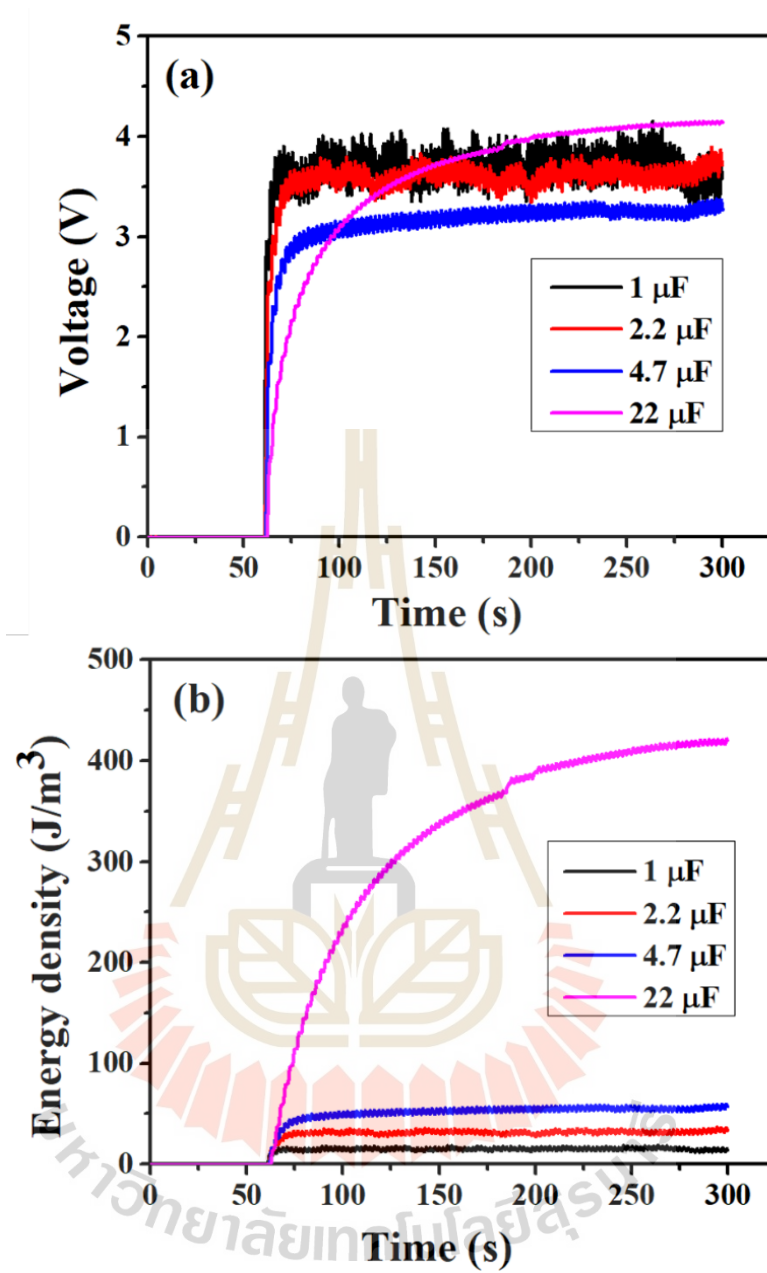


Figure 4.8 (a) Stored voltage and (b) energy density of BCZT ceramics at different capacitances. (The number of compressive cyclic mechanical loads are 900 cycles).

4.4 Chapter Summary

This study presents the performance of lead-free piezoelectric ceramics ($\text{Ba}_{0.85}\text{Ca}_{0.15}\text{Zr}_{0.1}\text{Ti}_{0.9}\text{O}_3$) for energy harvesting applications under compressive load at low frequency. X-ray diffraction analysis showed a pure perovskite structure with a mixture of rhombohedral and tetragonal phases. The average grain size was found to be $17.84 \pm 6.40 \mu\text{m}$, and the relative density was around 98-99 % with respect to the average bulk density of approximately 5.607 g/cm^3 . The BCZT ceramics demonstrated excellent piezoelectric properties, including d_{33} of 517 pC/N, g_{33} of $19 \times 10^{-3} \text{ Vm/N}$, and a figure of merit (*FOM*) of $9823 \times 10^{-15} \text{ m}^2/\text{N}$, making them suitable for mechanical to electrical energy harvesting. The optimized output performance was observed at a compressive load of 200 N ($\sim 0.3 \text{ Hz}$) without damage, yielding a DC voltage of 9.94 V, a DC current of 2.82 μA , a power of 28.03 μW , and an energy of $4.37 \times 10^{-7} \text{ J}$. The energy stored in the optimized capacitor of 22 μF was approximately 417 J/m^3 with an output voltage of approximately 4.13 V. These results demonstrate that bulk BCZT ceramics can be used as viable alternatives to lead-containing piezoelectric ceramics for piezoelectric microgenerator or sensor applications under mechanical compressive loads at low frequencies.



4.5 References

- Al-Ashtari, W. (2013). *Model Based Enhancement of an Autonomous System with a Piezoelectric Harvester*.
- Alexander, C. K., & Sadiku, M. N. O. (2017). *Fundamentals of Electric Circuits*: McGraw-hill Education.
- Buatip, N., Munthala, D., Amonpattaratkit, P., Pomyai, P., Sonklin, T., Reichmann, K., Pojprapai, S. (2020). Comparison of conventional and reactive sintering techniques for Lead-Free BCZT ferroelectric ceramics. *Radiation Physics and Chemistry*, 172, 108770. doi:10.1016/j.radphyschem.2020.108770
- Buatip, N., Promsawat, N., Pisitpipathsin, N., Namsar, O., Pawasri, P., Ounsung, K., Projprapai, S. (2018). Investigation on electrical properties of BCZT ferroelectric ceramics prepared at various sintering conditions. *Integrated Ferroelectrics*, 187(1), 45-52. doi:10.1080/10584587.2018.1445395
- GARVIE, R. C., & NICHOLSON, P. S. (1972). Phase Analysis in Zirconia Systems. *Journal of the American Ceramic Society*, 55(6), 303-305. doi:10.1111/j.1151-2916.1972.tb11290.x
- Janphuang, P., Lockhart, R., Uffer, N., Briand, D., & Rooij, N. F. (2014). Vibrational piezoelectric energy harvesters based on thinned bulk PZT sheets fabricated at the wafer level. *Sensors and Actuators A: Physical*, 210. doi:10.1016/j.sna.2014.01.032
- Ji, J.-H., Yoon, S., & Koh, J.-H. (2021). Comparative study of the Bi(Ni_{0.5}Zr_{0.5})O₃-PbTiO₃ and Bi(Mg_{0.5}Zr_{0.5})O₃-PbTiO₃ piezoelectric materials for energy harvesters. *Journal of Asian Ceramic Societies*, 9(1), 75-84. doi:10.1080/21870764.2020.1847428
- Li, L., Xu, J., Liu, J., & Gao, F. (2018). Recent progress on piezoelectric energy harvesting: structures and materials. *Advanced Composites and Hybrid Materials*, 1(3), 478-505. doi:10.1007/s42114-018-0046-1

- Mason, W. P., & Jaffe, H. v. (1954). Methods for Measuring Piezoelectric, Elastic, and Dielectric Coefficients of Crystals and Ceramics. *Proceedings of the IRE*, 42, 921-930.
- Munthala, D., Sonklin, T., Buatip, N., Pomyai, P., Amonpattaratkit, P., Klysubun, W., & Pojprapai, S. (2020). Angle dependent synchrotron X-ray absorption spectroscopic structural studies on Ba_{0.85}Ca_{0.15}Zr_{0.1}Ti_{0.9}O₃ ferroelectric ceramics. *Scripta Materialia*, 188, 249-253. doi:10.1016/j.scriptamat.2020.07.021
- Munthala, D., Sonklin, T., Pomyai, P., Luo, Z., Crawley, F., Buatip, N., Pojprapai, S. (2021). In-situ X-ray Absorption Spectroscopy (XAS) Studies of Electrical Field Induced Domain Switching in BCZT Ceramics. *Ceramics International*, 47. doi:10.1016/j.ceramint.2021.05.201
- Oh, Y., Noh, J., Yoo, J., Kang, J., Hwang, L., & Hong, J. (2011). Dielectric and piezoelectric properties of CeO₂-added nonstoichiometric (Na_{0.5}K_{0.5})_{0.97}(Nb_{0.96}Sb_{0.04})O₃ ceramics for piezoelectric energy harvesting device applications. *IEEE Trans Ultrason Ferroelectr Freq Control*, 58(9), 1860-1866. doi:10.1109/tuffc.2011.2024
- Rödel, J., Webber, K. G., Dittmer, R., Jo, W., Kimura, M., & Damjanovic, D. (2015). Transferring lead-free piezoelectric ceramics into application. *Journal of the European Ceramic Society*, 35(6), 1659-1681. doi:https://doi.org/10.1016/j.jeurceramsoc.2014.12.013
- Shin, D.-J., & Koh, J.-H. (2017). Comparative study on storing energy for (Ba,Zr)TiO₃ and CuO-(Ba,Zr)TiO₃ ceramics for piezoelectric energy harvesting applications. *Ceramics International*, 43. doi:10.1016/j.ceramint.2017.05.240
- Wang, P., Li, Y., & Lu, Y. (2011). Enhanced piezoelectric properties of (Ba_{0.85}Ca_{0.15})(Ti_{0.9}Zr_{0.1})O₃ lead-free ceramics by optimizing calcination and sintering temperature. *Journal of the European Ceramic Society*, 31(11), 2005-2012. doi:https://doi.org/10.1016/j.jeurceramsoc.2011.04.023

- Wu, J., Shi, H., Zhao, T., Yu, Y., & Dong, S. (2016). High Temperature BiScO₃ PbTiO₃ Piezoelectric Vibration Energy Harvester. *Advanced Functional Materials*, 26, 7186-7194.
- Yan, X., Zheng, M., Hou, Y., & Zhu, M. (2017). Composition-driven phase boundary and its energy harvesting performance of BCZT lead-free piezoelectric ceramic. *Journal of the European Ceramic Society*, 37(7), 2583-2589. doi:<https://doi.org/10.1016/j.jeurceramsoc.2017.02.049>
- Yan, X., Zheng, M., Sun, S., Zhu, M., & Hou, Y. (2018). Boosting energy harvesting performance in (Ba,Ca)(Ti,Zr)O₃ lead-free perovskites through artificial control of intermediate grain size. *Dalton Transactions*, 47(28), 9257-9266. doi:10.1039/C8DT01628C
- Yang, Z., Zhou, S., Zu, J., & Inman, D. (2018). High-Performance Piezoelectric Energy Harvesters and Their Applications. *Joule*, 2(4), 642-697. doi:<https://doi.org/10.1016/j.joule.2018.03.011>
- Zhang, Y., Liu, X., Wang, G., Li, Y., Zhang, S., Wang, D., & Sun, H. (2020). Enhanced mechanical energy harvesting capability in sodium bismuth titanate based lead-free piezoelectric. *Journal of Alloys and Compounds*, 825, 154020. doi:<https://doi.org/10.1016/j.jallcom.2020.154020>
- Zheng, M., Hou, Y., Yan, X., Zhang, L., & Zhu, M. (2017). High Dense Structure Boosts Energy Harvesting and Cycling Reliabilities of High-Performance Lead-Free Energy Harvester. *J. Mater. Chem. C*, 5. doi:10.1039/C7TC00914C

CHAPTER 5

PIEZO-TRIBOELECTRIC NANOGENERATOR BASED ON BCZT/MCNTs/PDMS COMPOSITE FOR COMPRESSIVE ENERGY HARVESTING

5.1 Introduction

In this chapter, the energy harvesting performance of $\text{Ba}_{0.85}\text{Ca}_{0.15}\text{Zr}_{0.1}\text{Ti}_{0.9}\text{O}_3$ (BCZT) microparticles at various weight ratios and multi-walled carbon nanotubes (MCNTs) mixed with polydimethylsiloxane (PDMS) composites was investigated to optimize the piezo-triboelectric nanogenerator combination. The primary goal was to improve the power output for compressive energy harvesting devices. The physical properties, including phase, microstructure, and cross-linking density, were characterized, along with the mechanical properties, such as static and dynamic behavior. The electrical properties, such as conductivity, resistivity, and dielectric properties, were also analyzed. Furthermore, the electrical output performance, energy harvesting capability, charging ability, and stability of the piezo-triboelectric nanogenerator (P-TENG) device based on the piezoelectric composite were reported.

This chapter is divided into multiple sections. Section 5.2 outlines the experimental procedures employed in this study, comprising sections 5.2.1 on materials, 5.2.2 on BCZT microparticle synthesis, 5.2.3 on preparation of the piezoelectric composite, 5.2.4 on the piezo-triboelectric nanogenerator (P-TENG) device fabrication, 5.2.5 on characterization of the piezoelectric composite, and 5.2.6 on energy harvesting testing of the P-TENG device. Section 5.3 presents the results and discussion, encompassing section 5.3.1 on the physical and chemical properties of the piezoelectric composite, section 5.3.2 on the mechanical properties of the piezoelectric composite, section 5.3.3 on the electrical properties of the piezoelectric composite, section 5.3.4 on the dielectric properties of the piezoelectric composite, and section 5.3.5 on the electrical output performance of the P-TENG device. Finally, section 5.4 concludes the chapter.

5.2 Experimental Procedure

5.2.1 Materials

Barium carbonate (BaCO_3 , Sigma Aldrich; 99.0 %), calcium carbonate (CaCO_3 , Eleps; 99.9 %), zirconium dioxide (ZrO_2 , Eleps; 99.5 %) and titanium dioxide (TiO_2 , 99.8 %; Aldrich chemistry) powders were used to prepare the $\text{Ba}_{0.85}\text{Ca}_{0.15}\text{Zr}_{0.1}\text{Ti}_{0.9}\text{O}_3$ (BCZT) piezoelectric ceramic. Polydimethylsiloxane (PDMS) (Sylgard® 184 Silicone Elastomer, Dow Corning Co., Ltd.) was used as a polymer matrix to create the flexible composite. Multi-walled carbon nanotubes (MCNTs, Nano generation Co., Ltd. Thailand; 99.9 %) powder was used as the electrically conducting filler. Conductive epoxy (EPO-TEK H2OE, Electron Microscopy Sciences, Hatfield, PA) was used to bond the composite and electrodes.

5.2.2 Synthesis of BCZT microparticles

The process for preparing the BCZT microparticles involved several steps. First, the BaCO_3 , CaCO_3 , ZrO_2 , and TiO_2 powders were mixed in appropriate ratios using ball milling in ethanol for 24 hrs. The resulting BCZT powder was dried at 120 °C to remove the ethanol, and then calcined at 1300 °C for 2 hrs. The calcined BCZT powder was then ball milled in ethanol for 6 hrs, dried at 120 °C for 24 hrs, and mixed with 3 wt% polyvinyl alcohol (PVA) binder. The mixture was then pressed into a pellet using a uniaxial press, and sintered at 1540 °C for 2 hrs with a heating and cooling rate of 5 °C/min. Here, the manufacture of the BCZT pellet was undertaken to achieve a particular phase and composition of the composite. Then the sintered BCZT pellets were cleaned in ethanol using an ultrasonic cleaner and then ground using a mini vibration milling method at 50 Hz frequency for 4 hrs to produce BCZT microparticles. Finally, the BCZT microparticles were annealed at 500 °C for 3 hrs in air at a heating and cooling rate of 5 °C/min before being used to form the composite.

5.2.3 Preparation of the piezoelectric composites

The BCZT/MCNTs/PDMS piezoelectric composite was fabricated using 3 wt% of MCNTs, and a range of BCZT microparticle weight fractions (40, 50, 60 wt%) within PDMS polymer matrix. To form the composites, the BCZT filler and MCNTs were initially stirred in 30 ml of ethanol solution for 30 minutes and then dried in an oven

at 90 °C for 24 hrs. Approximately 20-30 drops of toluene were mixed with the precursor to disperse the particles before loading them into the PDMS matrix material. A viscous PDMS polymer matrix was prepared separately by mixing a liquid phase PDMS with an elastic curing agent in a 10:1 (8 g : 0.8 g) weight ratio and stirred for 5 minutes. Subsequently, the viscous PDMS matrix and different weight percentages of BCZT/MCNTs in toluene solutions were mixed and blended by stirring for 30 minutes. Finally, the well-mixed composites were poured into a square aluminium mold (50 × 50 × 3 mm³). The formed composites were degassed in a vacuum machine at room temperature for 1 hr and cured at 70 °C for 2 hrs in a vacuum heat drying oven. The well-cured composites were then peeled from the mold and trimmed down to a dimension of 40 × 40 × 3 mm³ for characterization and energy harvesting assessment. The complete composition fabrication procedure is schematically shown in Figure 5.1.



Figure 5.1 The fabrication procedure of the piezoelectric composite (BCZT/MCNTs /PDMS).

5.2.4 Fabrication of the piezo-triboelectric nanogenerator (P-TENG) device

The basic structure of the P-TENG device and manufacturing process is shown in Figure 5.2(b). All the BCZT/MCNTs/PDMS piezoelectric composites were painted with conductive epoxy and attached to a copper plate with dimensions of 5 cm × 5 cm × 0.5 mm, which acts as a bottom electrode. To manufacture the P-TENG device, a 3D-printed thermoplastic polyurethane (TPU) layer was fitted in an arch-shaped stainless-steel cage (type-304 and 0.4 mm thick), and the piezoelectric composite was fixed to the bottom of the P-TENG device. Here, the bottom electrode of the composite was in contact with the device and the top electrode is separated by a 5 mm gap. An aluminium plate with the same dimensions (5 cm × 5 cm × 0.3 mm) was attached to an upper TPU to act as a top electrode, as shown in Figure 5.2(b). Then, the top and bottom electrodes were soldered and connected to an external circuit for signal measurement during energy harvesting.

5.2.5 Piezoelectric composites characterization

5.2.5.1 Physical and Chemical properties

The BCZT powder and the composites were characterized using X-ray Diffractometer (XRD, Bruker Phaser DII) for phase analysis. The particle size distribution of the BCZT was determined using a laser scattering particle size distribution analyzer (HORIBA, LA-950). The surface morphology and cross-sectional view of the composites were examined using an optical microscope (OM), while a Field Emission Scanning Electron Microscope (FE-SEM, Zeiss AURIGA, FE-SEM/EDX) was used for high-resolution electron microscopy. The dispersion of the BCZT particles in the PDMS matrix was studied using a full-field X-ray fluorescence imaging (FXI) technique with a synchrotron X-ray source with 10 keV energy and Ge (220) double crystal monochromator at the BL8: XAS/FXI at Synchrotron Light Research Institute (SLRI), Thailand. A dedicated MATLAB program was used for elemental mapping.

Synchrotron Radiation X-ray Tomographic Microscopy (SR-XTM) was performed at Beamline 1.2W, which operated at 1.2 GeV and 150 mA. Before installation on the goniometer stage, the sample was secured with Kapton tape to prevent movement during scanning. To minimize ring artefacts, the 350-micron-thick

aluminium foil was attenuated, and the mean energy was set at 11.5 keV. The X-ray radiographs were collected using an sCMOS camera (pco. edge 5.5, 2560 × 2160 pixels, 16 bits) and a lens-coupled X-ray microscope (Optique Peter, France) with a thickness of 200 microns. The radiographs were taken from 0 to 180 degrees with a 0.1-degree angular increment. The data was pre-processed, background-normalized, and CT-reconstructed using the Octopus Reconstruction program from TESCAN, Gent, Belgium (Vlassenbroeck et al., 2006). Sample reconstruction images were then created using Drishti software for 3D tomographic reconstruction (Limaye, 2006).

The density was measured using METTLER TOLEDO's analytical balances (ME204). According to the Flory-Rehner hypothesis, the crosslinking density of samples was measured using an equilibrium swelling method (Cai, Huang, Chen, & Wang, 2022). First, the composites were soaked in toluene for 7 days, where the toluene was changed once a day. After soaking for 7 days, when the samples reached the swelling equilibrium, they were carefully removed with tweezers, gently wiped off with tissue paper, and quickly weighed, and the swelling weight as M_1 was recorded. Then the samples were dried in a fume hood at room temperature for 10 days to remove the toluene. Then, the samples were weighed, and the initial weight as M_0 was recorded. Later, the cross-linking density was calculated using the following equation (Arends, Huinink, & Pel, 2019; Cai et al., 2022):

$$D = \frac{-[\ln(1 - \varphi) + \varphi + \chi\varphi^2]}{V_1\varphi^{1/3}} \quad (5.1)$$

$$\chi = 0.459 + 0.134\varphi + 0.59\varphi^2 \quad (5.2)$$

$$\varphi = \frac{\frac{M_0}{\rho_2}}{\frac{M_1}{\rho_1} + M_0\left(\frac{1}{\rho_2} - \frac{1}{\rho_1}\right)} \quad (5.3)$$

where D is the crosslinking density (mol/m^3), V_1 is the molar volume of the solvent toluene ($106.27 \text{ ml}/\text{mol}$) (Wemyss et al., 2022), ϕ is the volume fraction of the polymer in the swelling matrix, χ is the Flory–Huggins parameter, M_0 is the mass before swelling, M_1 is the mass after swelling, ρ_1 is the solvent density (toluene, $0.865 \text{ g}/\text{cm}^3$) (Wemyss et al., 2022), and ρ_2 is the polymer density (PDMS, $0.965 \text{ g}/\text{cm}^3$) (Izdihar et al., 2021).

5.2.5.2 Mechanical properties

To study the dynamic behavior of the composites, a rectangular sample with a cross-section of approximately $10 \times 3.5 \times 2.5 \text{ mm}^3$ was used for dynamic mechanical thermal analysis (DMTA) in tension mode. The behaviour was conducted with a frequency range of 1 Hz to 10 Hz, an amplitude of 0.03 mm, and a rate of $3 \text{ }^\circ\text{C}/\text{min}$ between $-140 \text{ }^\circ\text{C}$ and $140 \text{ }^\circ\text{C}$.

5.2.5.3 Electrical properties

The electrical conductivity and resistivity of the composites were measured using the four-point probe method with an Ossila instrument. In addition, the dielectric properties such as AC conductivity, phase angle, relative permittivity, and $\tan \delta$ were measured using a Solatron 1260 and 1296 Dielectric Interface. The composites were poled at $0.33 \text{ kV}/\text{mm}$ of DC electric field for 24 hrs in a silicone oil bath using Matsusada AU-30*40 instruments.

5.2.6 Energy harvesting testing of the P-TENG device

The electrical output performance of the P-TENG device was evaluated by applying an external mechanical force from a custom-built energy harvester testing machine at $70 \pm 5 \%$ relative humidity and at room temperature conditions of approximately $30 \text{ }^\circ\text{C}$; this is shown in Figure 5.2(a). Energy harvesting output parameters were collected while an alternating external mechanical load of 500 N was applied at a frequency of 1 Hz. Initially, the AC output voltage was collected during the mechanical loading using an oscilloscope (Tektronix, TDS2002C) with an internal impedance of $1 \text{ M}\Omega$. The output current was measured using a digital multimeter (Keysight, 34465A) with a load resistance of $10 \text{ k}\Omega$. Next, the sample was placed in a sample holder and connected to the load variable resistance box through a voltmeter

and an ammeter (Keysight, 34465A, Digital Multimeter). The energy harvested output DC parameters, which included the voltage (V), current (I), and power (P), were then recorded by Suraphinit software. The DC signal of the P-TENG device was collected during external mechanical loading with a force of 500 N at frequencies of 1 Hz and 3 Hz. Finally, the AC to DC conversion of the P-TENG energy harvester under compressive loading (500 N at 3 Hz) was measured by charging a variety of storage capacitors (0.33, 0.47, 2.2, 22 μ F, and 0.1 F) and long-term stability testing. The output performance was measured using an energy harvesting system diagram, as shown in Figure 5.14(a).

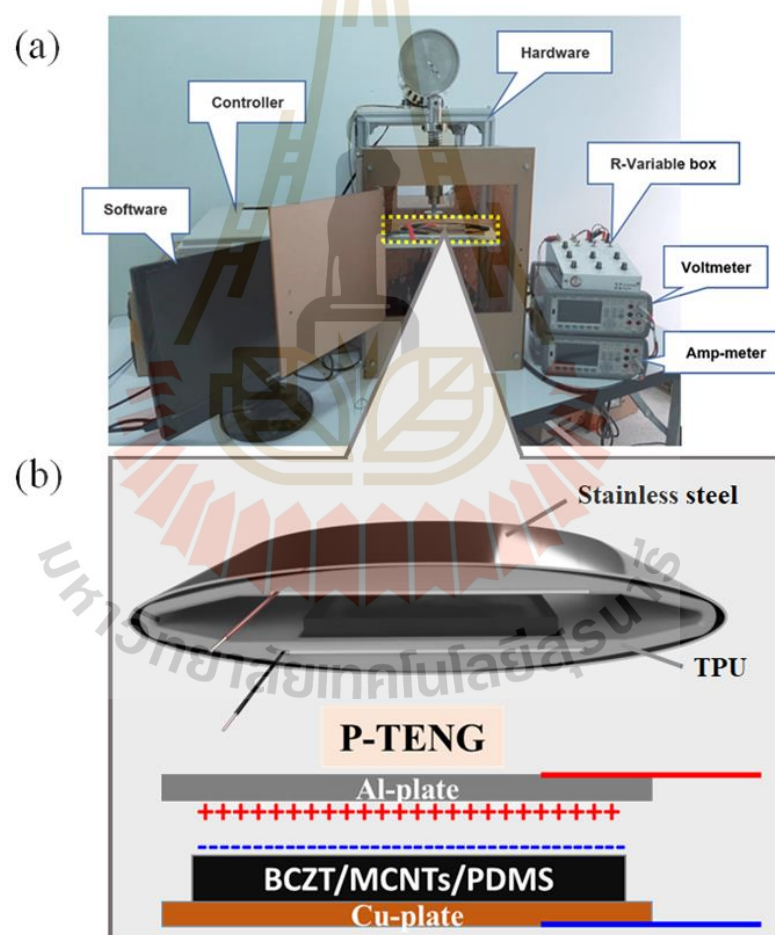


Figure 5.2 (a) Energy harvesting test machine and (b) schematic of triboelectric nanogenerator-based piezoelectric composite (P-TENG device).

5.3 Results and Discussion

5.3.1 Physical and chemical properties of the piezoelectric composites

Phase identification of BCZT powders and composites was investigated using the XRD method, as shown in Figure 5.3. The scan range of XRD patterns was measured from 20 to 70° of 2θ . The pure BCZT particles exhibited a pure perovskite structure, which is a combination of both orthorhombic (PDF 04-019-9410) and tetragonal (PDF 00-065-0109) phases, as shown in Figure 5.3(a). This result is in agreement with previous work by Wang *et al.* (Wang, Li, & Lu, 2011). The pure MCNTs/PDMS composite exhibited an amorphous nature, as shown in Figure 5.3(b). The mixed phase might be due to the morphotropic phase boundary (MPB) structure, which has already been discussed in our previous publications (Buatip *et al.*, 2020; Munthala *et al.*, 2020; Munthala *et al.*, 2021). The XRD pattern intensity increased with BCZT particle weight percent ratios, as shown in Figure 5.3(c, d, e).

Microstructural images of the BCZT particles, pure MCNTs/PDMS composite, and BCZT/MCNTs/PDMS composites were examined using FE-SEM, and their corresponding images are shown in Figure 5.4. The pure BCZT particles exhibited an average particle size of $2.73 \pm 1.40 \mu\text{m}$, as shown in Figure 5.4(a), and a particle size distribution histogram is shown in Figure 5.4(b). Similarly, the pure multi-walled carbon nanotubes (MCNTs) are well-distributed within the PDMS matrix, with an average size of each MCNTs approximately 10-50 nm, and corresponding images are shown in Figure 5.4(c, d).

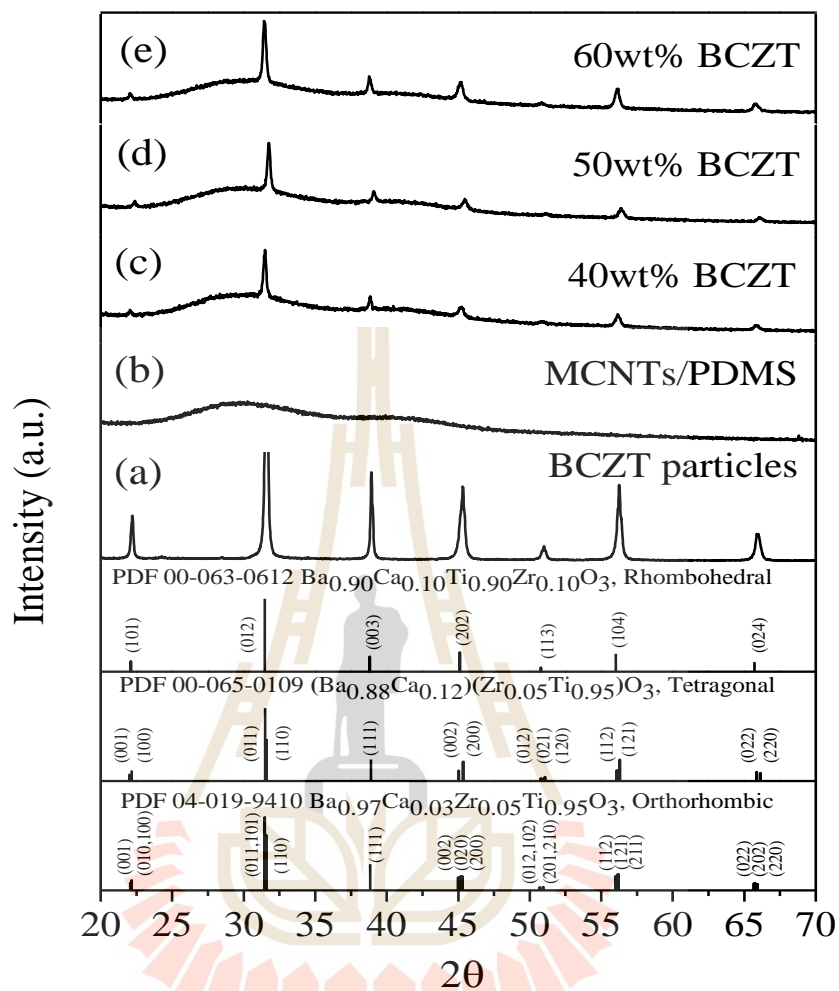


Figure 5.3 Phase structure of the piezoelectric composite : XRD patterns of (a) BCZT particles, (b) MCNTs/PDMS composite, the piezoelectric composites at different weight ratios of BCZT (c) 40 wt% BCZT, (d) 50 wt% BCZT, and (e) 60 wt% BCZT.

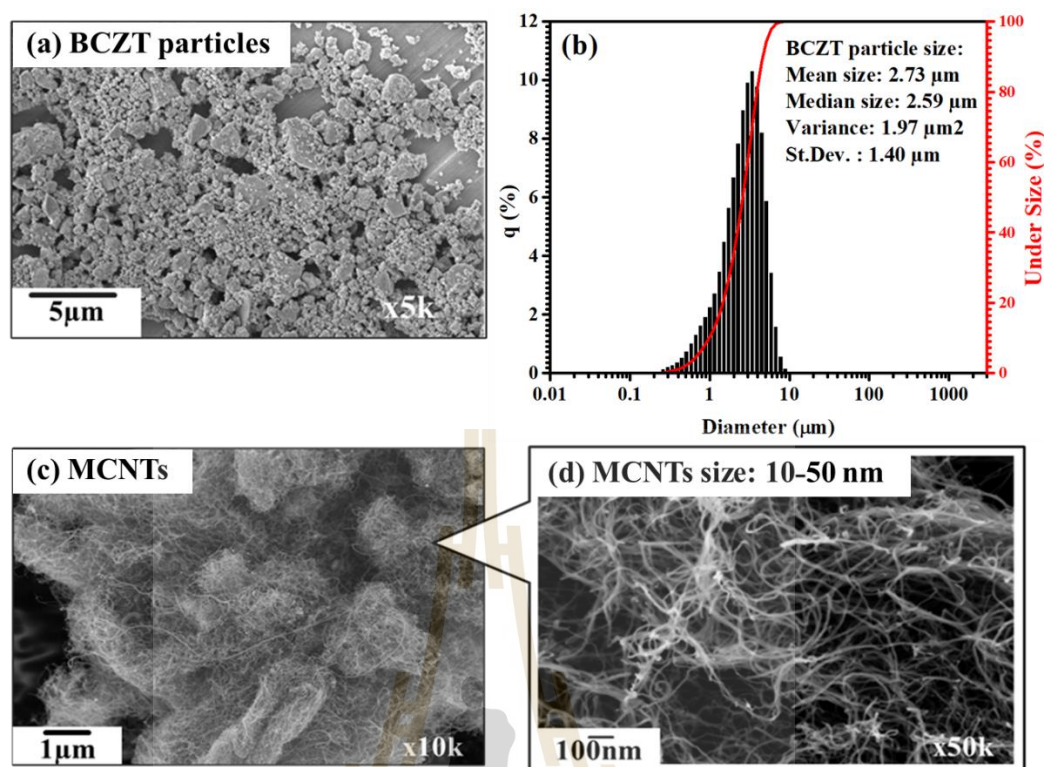


Figure 5.4 Physical properties of the piezoelectric composite : FE-SEM micrographs of (a) BCZT particles, (b) BCZT particle size distribution, (c) pure MCNTs, and (d) high-resolution images of MCNTs.

Figure 5.5 shows cross-sectional morphologies of BCZT/MCNTs/PDMS composites with various BCZT weight percentages (40, 50, and 60 wt%). These composites were examined using optical microscopy and FE-SEM measurements. Figure 5.5(a-d) shows the optical microscope images, which demonstrate that both MCNTs and BCZT particles are well mixed and distributed within the PDMS matrix. The dark area represents MCNTs, while the bright area represents BCZT particles dispersed within the PDMS matrix. High-resolution FE-SEM images confirm that the BCZT particles are evenly dispersed within the PDMS matrix and the MCNTs are bridged between the particles, as indicated by the red arrow in Figure 5.5(e-h). As the BCZT particle weight percentage increases, the degree of particle-to-particle separation decreases, and this can also be observed in the optical microscope images, as shown in Figure 5.5(a-d).

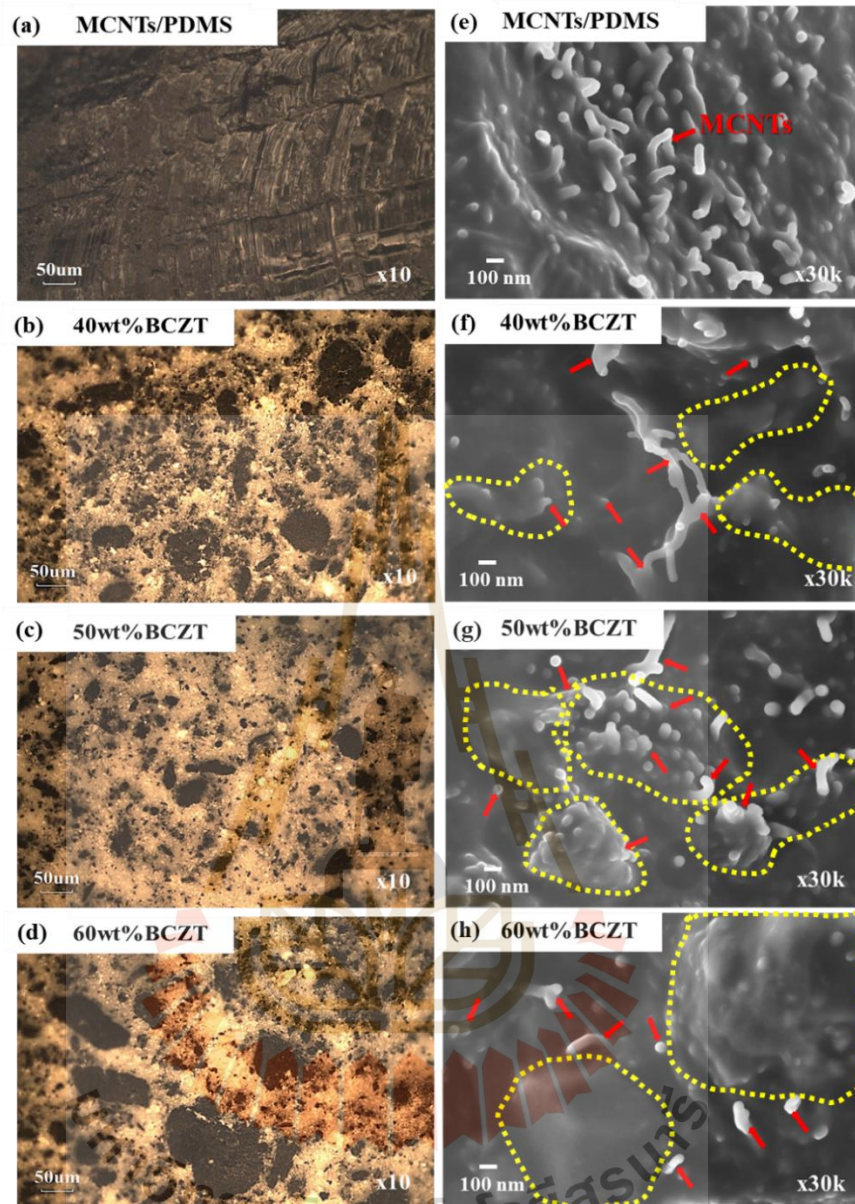


Figure 5.5 Physical properties of the piezoelectric composite: (a-d) Cross-sectional optical microscope images and (e-h) cross-sectional FE-SEM micrographs of the piezoelectric composites at different weight ratios of BCZT.

Figure 5.6 shows synchrotron based FXI images that confirm the trace level elemental distribution in the composites for different weight ratios of BCZT particles. The FXI measurement conducted at SLRI, Thailand is only capable of mapping the Ba, Ca, and Ti elements (De Samber et al., 2019; Walter et al., 2019) in

the composites. Figure 5.6(a) depicts a regular image of the composites without element mapping. Different contrast and brightness levels are employed to quantify the concentration of elements dispersed in the BCZT particles. The bright red region indicates a high concentration of the respective element in the figures, as shown in Figure 5.6(b, c, d). The Ba, Ca, or Ti elements are well dispersed in the PDMS polymer matrix.

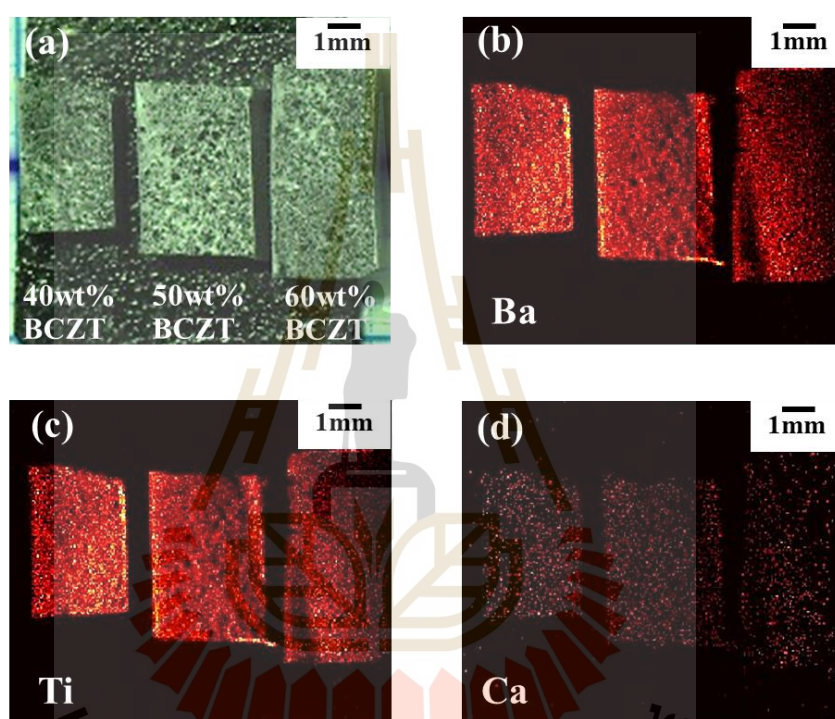


Figure 5.6 Chemical properties of the piezoelectric composite : FXI images of cross-sectional piezoelectric composites at different weight ratios of BCZT ; (a) regular image, (b) Ba element mapping, (c) Ti element mapping, and (d) Ca element mapping.

Furthermore, synchrotron based XTM images enable the observation of the dispersion of BCZT particles in the composite. Figure 5.7(a, b, c) shows SR-XTM images of the composite and the distribution of BCZT particles in a MCNTs/PDMS matrix with different concentrations of BCZT particles at 40, 50, and 60 wt%, respectively. It is evident that the appearance of the 50 wt% BCZT dispersion is better than that of the other concentrations, and at 40 and 60 wt% of BCZT, there is evidence of an

uneven particle distribution within the matrix. However, the micro-tomography beamline resolution cannot differentiate the MCNTs in the PDMS matrix since features less than a micrometer in scale are not visible.

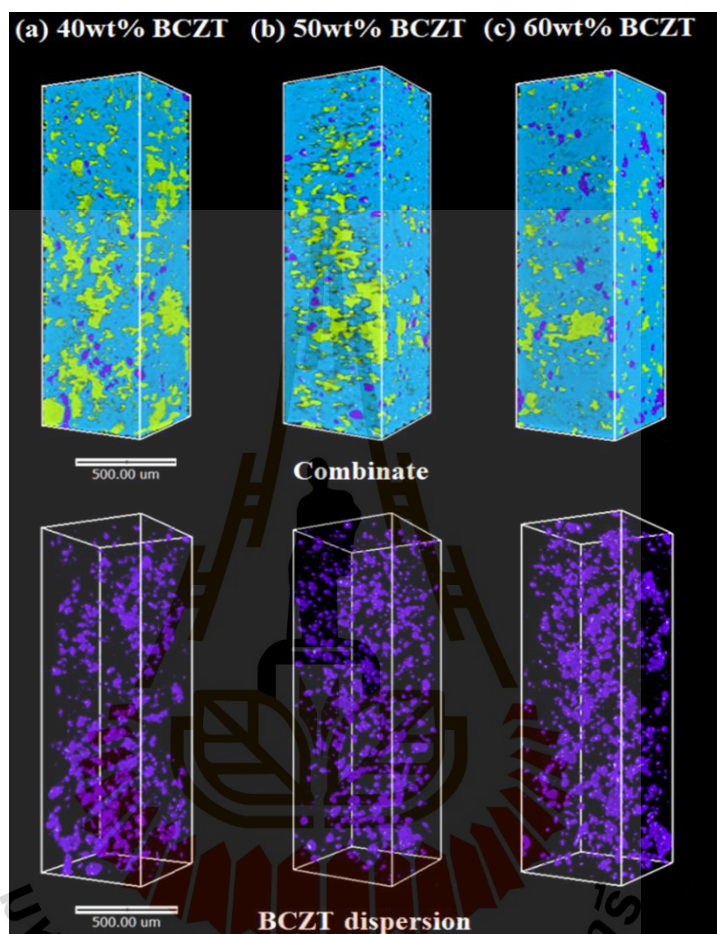


Figure 5.7 Physical properties of the piezoelectric composite : SR-XTM images of the piezoelectric composites at different weight ratios of BCZT ; (a) 40 wt% BCZT, (b) 50 wt% BCZT, and (c) 60 wt% BCZT.

5.3.2 Mechanical properties of the piezoelectric composites

Dynamic mechanical thermal analysis (DMTA) was used to accurately evaluate the physical characteristics and Figure 5.8 shows the data of the MCNTs/PDMS composite with different BCZT weight fractions. The mechanical properties, storage modulus (E') and loss factor ($\tan \delta$) were measured under tensile mode with an

oscillating load of 1 and 10 Hz frequency over a broad temperature range of -140 °C to 140 °C, as shown in Figure 5.8(a) and Figure 5.8(b). It was observed that the storage modulus of the composites differed, demonstrating the effect of BCZT weight ratios on the composite's glass transition temperature (T_g). The T_g of the 0, 40, 50, and 60 wt% of BCZT, which was determined from the characteristic peaks in the $\tan \delta$ curves of samples, is -114, -116, -118, and -115 °C at 1 Hz and -112, -113, -115, -112 °C at 10 Hz, respectively (Figure 5.8(c)). At the glass transition, the segments of the PDMS in the composite moved from being frozen (below the T_g) to being free to move (above the T_g), as the material changed from being in a glassy state to an elastic state. In this case, the crosslinking density decreased the composite's glass transition temperature by restricting the chains' molecular mobility. In addition, it is noted that the composites under different weight ratios of BCZT had a second relaxation peak that appeared at approximately -80 to -40 °C, and the $\tan \delta$ shifted lower in magnitude, while the relaxation peak was at a higher temperature. This can be explained by the fact that the complete crosslinking network is relaxed for the relaxation peak to appear (Cai et al., 2022; Hagen, Salmén, & Stenberg, 1996). The mechanical loss factor ($\tan \delta$) of all composites is less than 0.45, and the 50 wt% BCZT composite exhibits the lowest loss curve because as a result of its homogenous composition and increase in crosslinking density, which improves the stiffness and decreasing the degree of friction between molecular segments, which helps lower the $\tan \delta$ value. For the 0, 40, 50, and 60 wt% BCZT based composites, the $\tan \delta$ at room temperature and 1 Hz, is 0.087, 0.069, 0.095, 0.093, and 10 Hz is 0.121, 0.109, 0.133, 0.135, respectively. The storage modulus (E') and loss modulus (E'') analyzed from DMTA at room temperature of the composites with different BCZT weight ratios are illustrated in Figure 5.8(d). For the 0, 40, 50, 60 wt% BCZT composites, the E' is 2.909, 1.931, 4.195, 2.577 MPa, and the E'' is 0.253, 0.1343, 0.398, 0.239 MPa at 1 Hz, while at 10 Hz, the E' is 3.343, 2.170, 4.886, 2.980 MPa, and the E'' is 0.404, 0.237, 0.648, 0.401 MPa, respectively.

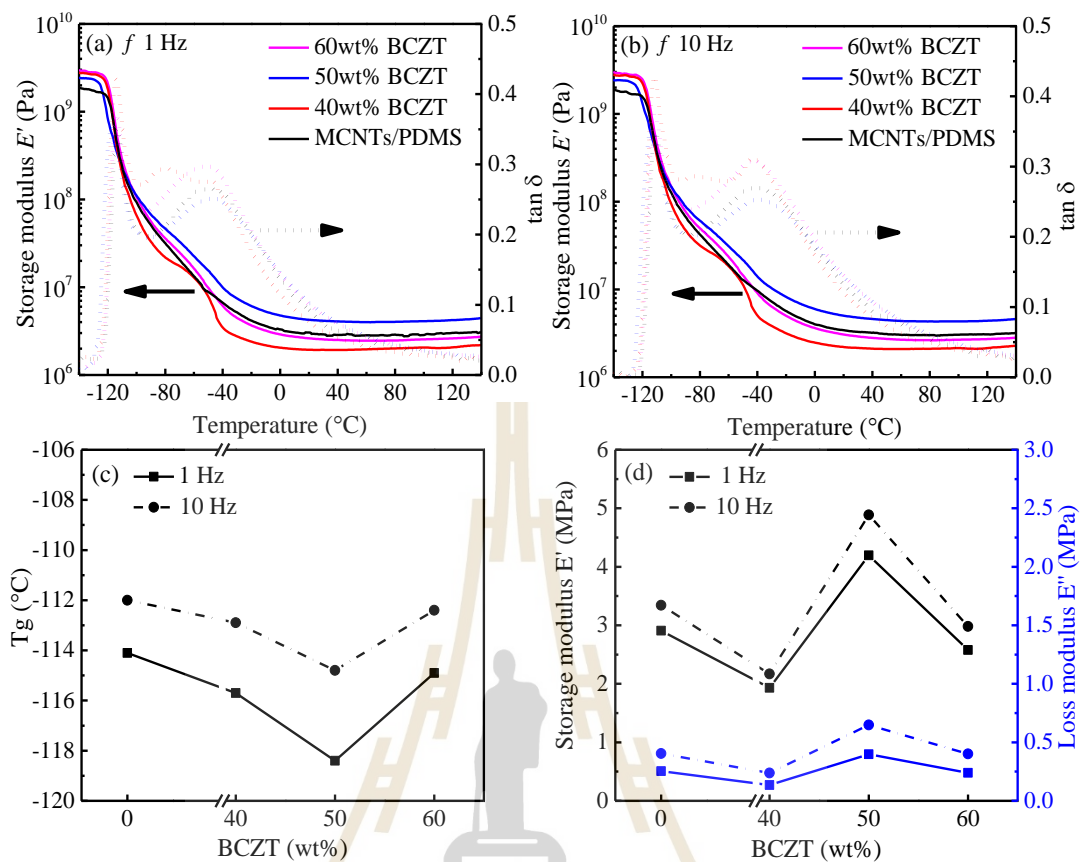


Figure 5.8 Mechanical properties of the piezoelectric composites : Dynamic behavior of composites with different BCZT particles weight ratios on storage modulus (E') and $\tan \delta$ versus temperature at (a) 1 Hz and (b) 10 Hz measured by DMTA method using a heating rate of 5 $^{\circ}\text{C}/\text{min}$. And (c) the glass transition temperature (T_g), (d) the storage modulus (E') and loss modulus (E'') at room temperature for 1 Hz and 10 Hz.

These results show that the E' and E'' of all composites are higher at the frequency of 10 Hz than at 1 Hz, which is a common observed for polymers and their composites (Babu & de With, 2014). This pattern is observed since under high-frequency cyclic loading the polymer molecules have insufficient time to undergo significant deformation, which increases both the magnitude of E' and E'' , and this tendency increases with increasing frequency. At room temperature, all composites exhibit a degree of elasticity and a rubbery state. The 50 wt% BCZT composite exhibits the highest E' and E'' and has a higher stiffness compared with composites with other BCZT filler contents, and this is related to the highest crosslink density of the 50 wt% BCZT composites.

5.3.3 Electrical properties of the piezoelectric composites

The effect of BCZT filler content on the electrical conductivity and resistivity of the composites was measured. To verify the formation of an electrical network in the composite structure, the corresponding images are shown in Figure 5.9(a). The pure MCNTs/PDMS composite exhibited a conductivity of 56.8 mS/m, and when BCZT particles were added to the MCNTs/PDMS composite, the conductivity decreased to 2.2, 0.9, and 0.4 mS/m for 40, 50, and 60 wt% addition of BCZT, respectively. Clearly, the resistivity inversely followed the conductivity, as shown in Figure 5.9(a). The pure MCNTs/PDMS composite exhibited a DC resistivity of 18 Ωm and increased to 449, 1017, and 2629 Ωm when the BCZT particle weight percentage increased to 40, 50, and 60 wt%, respectively. The increase in resistivity with BCZT concentration is due to the higher percentage of agglomeration of the electrically insulating BCZT particles, which affected the percolation of the delicate chains of MCNTs in the composite structure and decreased the connectivity of the conductive MCNTs chains, as shown in FE-SEM images (Figure 5.5(e-h)). For additions of 0, 40, 50, and 60 wt%, the calculated average values of density are 1.024, 1.281, 1.373, and 1.266 g/cm^3 , and the crosslink density values are 5.184, 7.510, 8.790, and 6.713 ($\times 10^{-4}$) mol/cm^3 , respectively. This indicates that the density increased with an increase of BCZT weight fractions due to the high concentration of ceramic filler (Babu & de With, 2014), as shown in Figure 5.9(b). The presence of BCZT particles in the MCNTs/PDMS matrix initially increased the density and crosslink density. However, the density and

crosslink density values decreased for the 60 wt% BCZT composite, since the high filler concentration affected the high viscosity of the matrix and led to poor dispersion of the fillers during solution casting. In this case, the 50 wt% BCZT composite exhibits the highest crosslink density among the other composite compositions. The higher crosslinking density leads to more constrained composite molecular chains, where the stiffness and crosslinking density of the material exhibit a strong correlation (Cai et al., 2022).

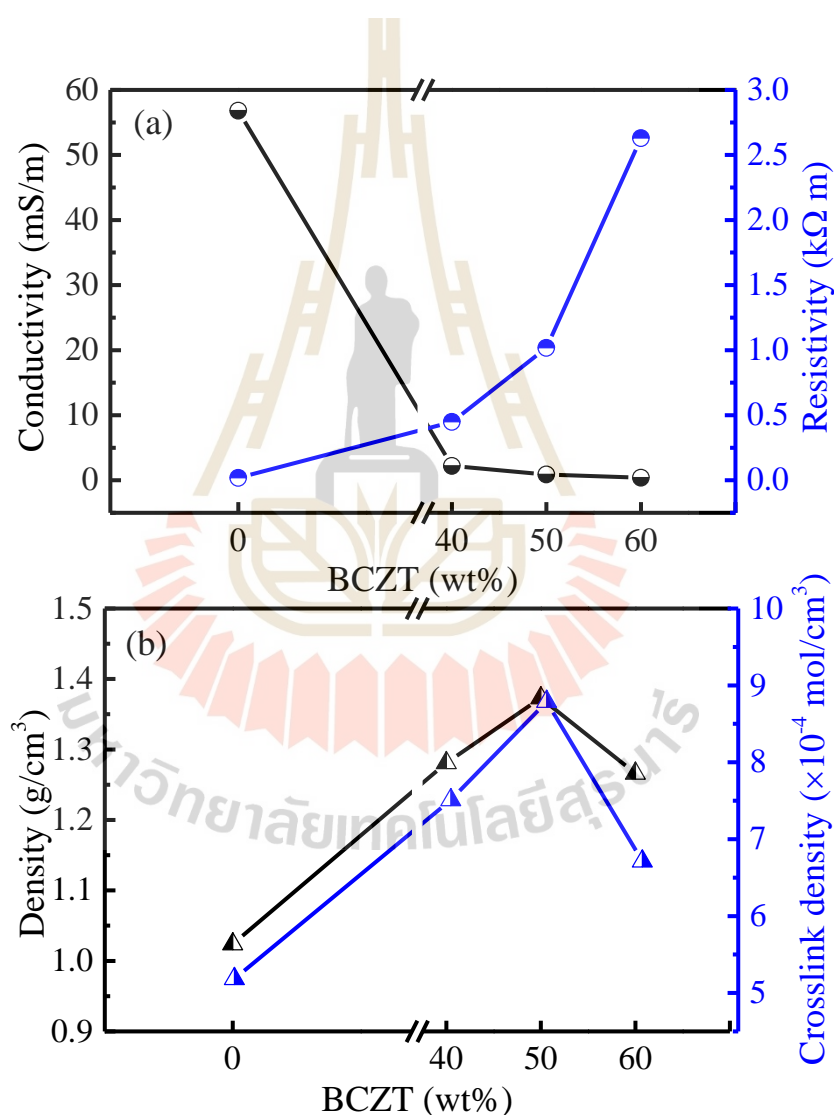


Figure 5.9 (a) Electrical conductivity and resistivity, (b) density and crosslink density of the piezoelectric composites at different weight ratios of BCZT.

5.3.4 Dielectric properties of the piezoelectric composites

The frequency-dependent AC conductivity, relative permittivity, $\tan \delta$, and phase angle of the piezoelectric composites were measured over a frequency range of 0.1 Hz to 1 MHz, as illustrated in Figure 5.10. Figure 5.10(a) shows that the frequency dependency of the AC conductivity of the MCNTs/PDMS composite (3 wt% MCNTs) is a function of the weight percentage of BCZT particles (40, 50, and 60 wt%). The AC conductivity of the MCNTs/PDMS is approximately 10^{-4} S/m and is relatively frequency independent from 10^{-1} to 10^4 Hz. This indicates that the composite behaves as a conductor in this frequency range, which is also illustrated by a phase angle of approximately 0° , as shown in Figure 5.10(b), since current and voltage are in phase for a conductor. At higher frequencies ($> 10^4$ Hz), the AC current begins to flow in the dielectric polymer phase, and this leads to a more frequency-dependent conductivity, this can also be seen in Figure 5.10(b) shows the decrease in the phase angle at higher frequencies. For the BCZT/MCNTs/PDMS composites the AC conductivity decreased by approximately six orders of magnitude compared to the pure MCNTs/PDMS at low frequency (~ 10 Hz); see Figure 5.10(a). In addition, the AC conductivity increased linearly with increasing frequency at frequencies above 10Hz. This indicates that the composite behaves as a capacitor in this frequency range, and this is also illustrated by a phase angle of approximately -90° for the BCZT/MCNTs/PDMS composites across the whole frequency range. The relative permittivity decreased gradually with increasing frequency for all the piezoelectric composites, as shown in Figure 5.10(c). The electrical $\tan \delta$ for the BCZT/MCNTs/PDMS composites is relatively low and initially decreased and then eventually increased with increasing frequency, as shown in Figure 5.10(d), while the conductive nature of the MCNTs/PDMS composites leads to a very high $\tan \delta$, particularly at low frequencies where AC currents flow through the conductive nanotubes. This behavior results from a polarization mechanism, where at higher frequencies charge mobility and reorientation is not being fast enough which decreases the dielectric permittivity (Buatip et al., 2018; Promsawat et al., 2018); as indicated by the reduction in permittivity at high frequencies in Figure 5.10(c). The relative permittivity of the piezoelectric composites increased as the BCZT particles increased from 40 wt% to 50 wt% in the MCNTs/PDMS composite, see Figure 5.10(c).

Then, the relative permittivity decreased as the BCZT particles was further increased to 60 wt%, which is possibly due to the interfaces and porosity produced from BCZT particles agglomeration in the composite with a high weight ratios of BCZT particles (Choi et al., 2013; Zhang, Xie, Roscow, & Bowen, 2019).

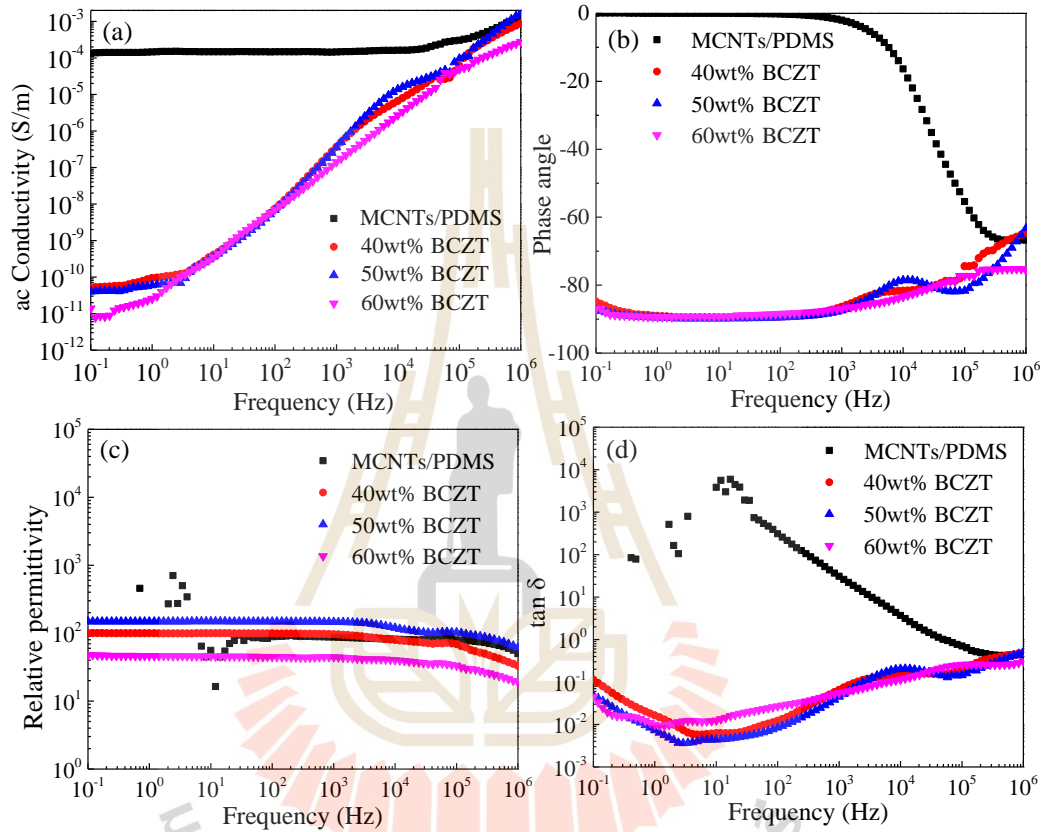


Figure 5.10 Electrical properties of the piezoelectric composites : (a) ac conductivity, (b) phase angle, (c) relative permittivity, and (d) $\tan \delta$ as a function of frequency, at different weight ratios of BCZT. (unpoled)

5.3.5 Electrical output performance of P-TENG devices

To enhance the performance of the P-TENG device, the ferroelectric dipoles in BCZT particles should align in their poled direction (Danish, Bin, Xiaochao, Hao, & Meifang, 2017; Fuentes-Fernandez, Gnade, Quevedo-Lopez, Shah, & Alshareef, 2015; Park et al., 2014). This condition refers to the optimized percolation threshold of the MCNTs/PDMS composite reported by Jian Du *et al.* (Du et al., 2020) and Hur *et al.* (Hur, Ha, & Park, 2020). In this study, the composite was poled by applying a 0.33 kV/mm DC electric field for 24 hrs in a silicone oil bath at room temperature. During the poling process, the ferroelectric dipoles in BCZT particles can orient in a common direction in response to the applied electric field, leading to an increase in charge density on the surface of the composite (Danish et al., 2017; Fuentes-Fernandez et al., 2015; Park et al., 2014). Figure 5.13 presents a schematic diagram of the internal structure of both the unpoled composites (left side) and poled composites (right side). Figure 5.13(a-d) shown the internal structure of the MCNTs/PDMS composite (Figure 5.13(a)) and the composite containing varying weight fractions (40, 50, and 60 wt%) of BCZT particles; Figure 5.13(b-d). It is thought that a high filler content leads to agglomeration of BCZT filler and formation of interfacial pores, Figure 5.13(d). Meanwhile, Figure 5.13(e-h) illustrates the impact of the electrical poling process, where for the MCNTs/PDMS composite, Figure 5.13(e), percolation of the MCNTs leads to current flow. The addition of the piezoelectric BCZT filler, Figure 5.13(f-h), disrupts the percolation of the MCNTs with a resulting polarization of the composite as domains rotate in the direction of the applied electric field. This leads to the accumulation of screening charges on the upper and lower surfaces of the composites.

The custom-built energy harvester testing machine in Figure 5.2(a) was utilized to investigate the electrical output performance of the P-TENG devices, and Figure 5.2(b) shows the structure of the P-TENG device based on the piezoelectric composite. In addition, Figure 5.11 provides a more detailed stepwise operating mechanism for analyzing the combined effect of piezoelectricity and triboelectricity in the P-TENG. The BCZT/MCNTs/PDMS composite was placed on a Cu plate electrode, with its upper surface facing a typically separated Al plate electrode, so that the device operated in a straightforward vertical contact/releasing mode (Figure 5.2(b) and Figure

5.11(a)). As a result of the stark contrast in the electron affinities between the upper Al plate and the lower composite layer, electrons were transported from the Al plate to the surface of the composite when both the composite and Al electrode surfaces made contact due to the application of an external force (Figure 5.11(b)). In the meantime, opposing charges were induced on the composite's reverse, leading to a net current flow from the Al to the Cu electrode plate in the contacting step. This is known as a triboelectric current pulse (I_T). Next, the composite was compressed, thereby creating a piezoelectric polarization in the pressing stage, (Figure 5.11(c)), resulting in an additional current pulse when the external force persisted (I_P).

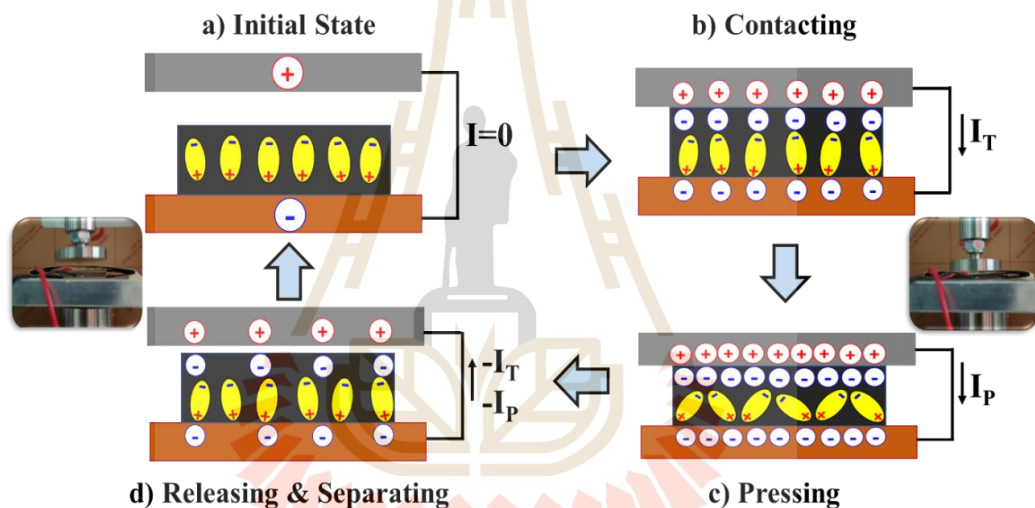


Figure 5.11 Stepwise operation mechanism of P-TENG device : (a) initial state, (b) contacting, (c) pressing, and (d) releasing and separating for the energy harvesting investigation.

The ferroelectric poling direction determines the polarization direction, and has the potential to augment or inhibit the total current flow, where $I_{total} = I_T + I_P$. Following the release of the compressive strain due to the removal of the external force, the piezoelectric polarization vanished in the release and separation step (Figure 5.11(d)). Reverse current pulses ($-I_P$ and $-I_T$) were therefore produced due to the recovery of the piezoelectric and triboelectric-induced charge. The triboelectric-induced charge then flowed back as the composite returned to its separating condition

from the Al electrode. Eventually, the charges generated flow to an external load until electrical potential balancing (equilibrium state) occurs at the initial state when the cycle is complete (Figure 5.11(a)). These phenomena occurred due to piezoelectric and triboelectric dual effects (Suo et al., 2016), and when an action force is repeatedly applied, electrical output is produced.

To quantitatively describe the operational performance of P-TENG devices based on BCZT/MCNTs/PDMS composites, the electrical output, open-circuit voltage (V_{OC}), and short-circuit current (I_{SC}) were investigated. The electrical output of a device was tested when subjected to a 500 N external compressive load at approximately 1 Hz frequency. A sample area of $4 \times 4 \text{ cm}^2$ and a thickness of 3 mm were employed for all devices. Due to the more substantial piezoelectric charge generation, the electrical output, V_{OC} and I_{SC} , increased with the amount of BCZT weight fraction up to 50 wt%; where the output results are summarized in Figure 5.12(a,b,c,d). However, both V_{OC} and I_{SC} reduced as the weight percentage exceeded 50 wt%. This may be due to the aggregation and uneven distribution of BCZT and MCNTs fillers inside the PDMS matrix. Figure 5.12(e) shows a trend representing the peak-to-peak power values extracted from each condition (the output power, calculated from V^2/R for $R = 10 \text{ k}\Omega$ external load resistance) for each condition. Therefore, the ideal condition in this work is BCZT at 50 wt%, which demonstrated the maximum electrical output of $V_{OC} \sim 39.7 \text{ V}$, $I_{SC} \sim 1.9 \mu\text{A}$, and a peak to peak ($P-P$) power of $\sim 157.7 \text{ uW}$. Compared to the composite with no BCZT (pure MCNTs/PDMS), it was demonstrated that the output performance of the P-TENG device with 50 wt% BCZT increased approximately 3.5, 1.7, and 11.8 times in terms of V_{OC} , I_{SC} , and $P-P$ power, respectively. It was determined that for the 50 wt% BCZT composite, the poled composite attained its maximum power output. At this condition, the high degree of alignment of ferroelectric dipoles towards the applied electric field and polarized surface charges is assumed, as shown in Figure 5.13(g). However, a further increase in the addition of BCZT particles to 60 wt% reduced the output performance, and this is thought to be due to increased particle porosity and decreased crosslink density as a result of the aggregation of BCZT particles at higher weight fractions (60 wt%), as shown in Figure 5.13(h).

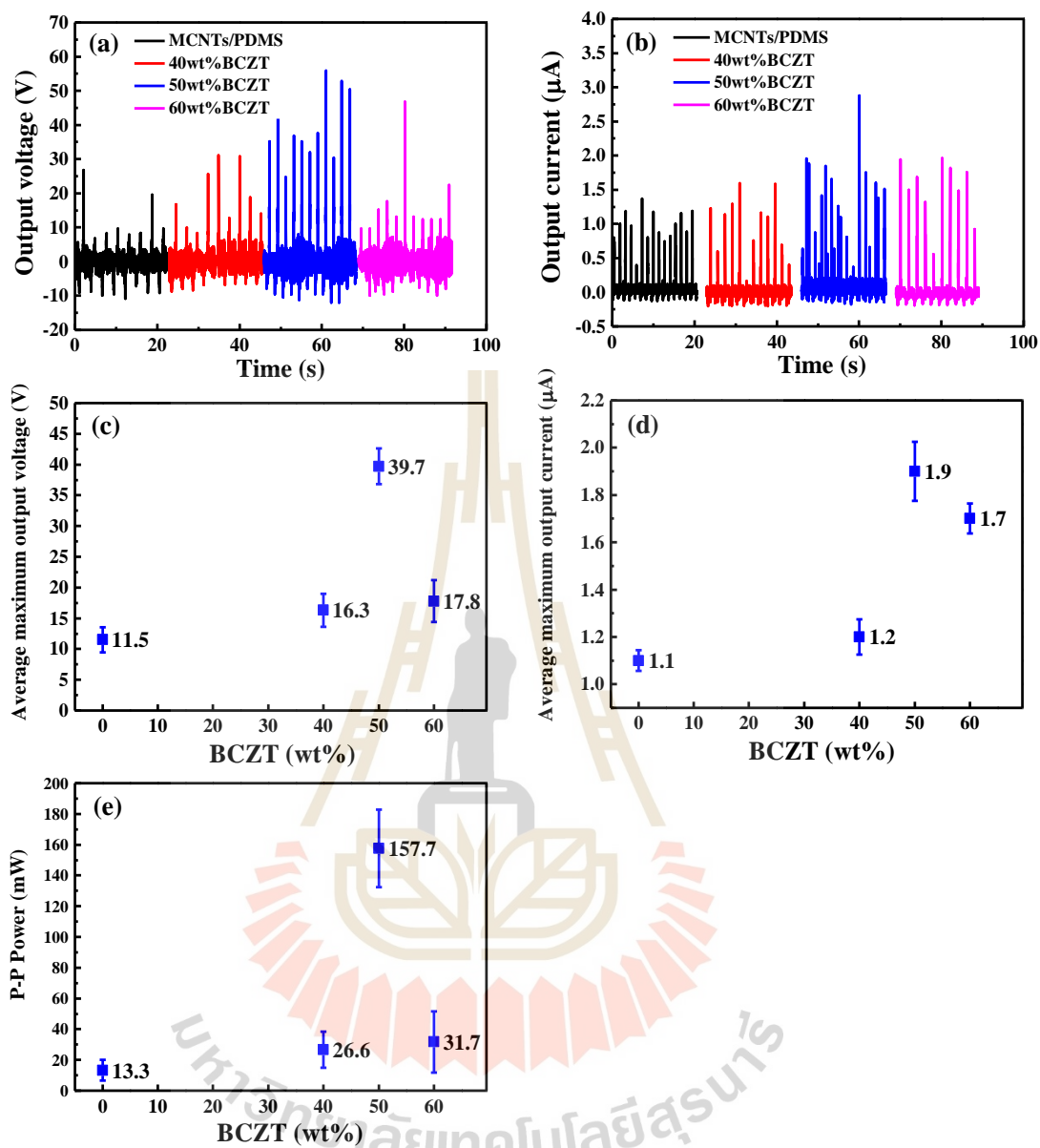


Figure 5.12 Electrical output performance of the P-TENG device (various weight ratios of BCZT) : (a) output voltage, (b) output current, (c) average maximum output voltage, (d) average maximum output current, and (e) peak to peak output power at $R = 10 \text{ k}\Omega$. The devices are operated under 500 N compressive mechanical load and $\sim 1 \text{ Hz}$ frequency.

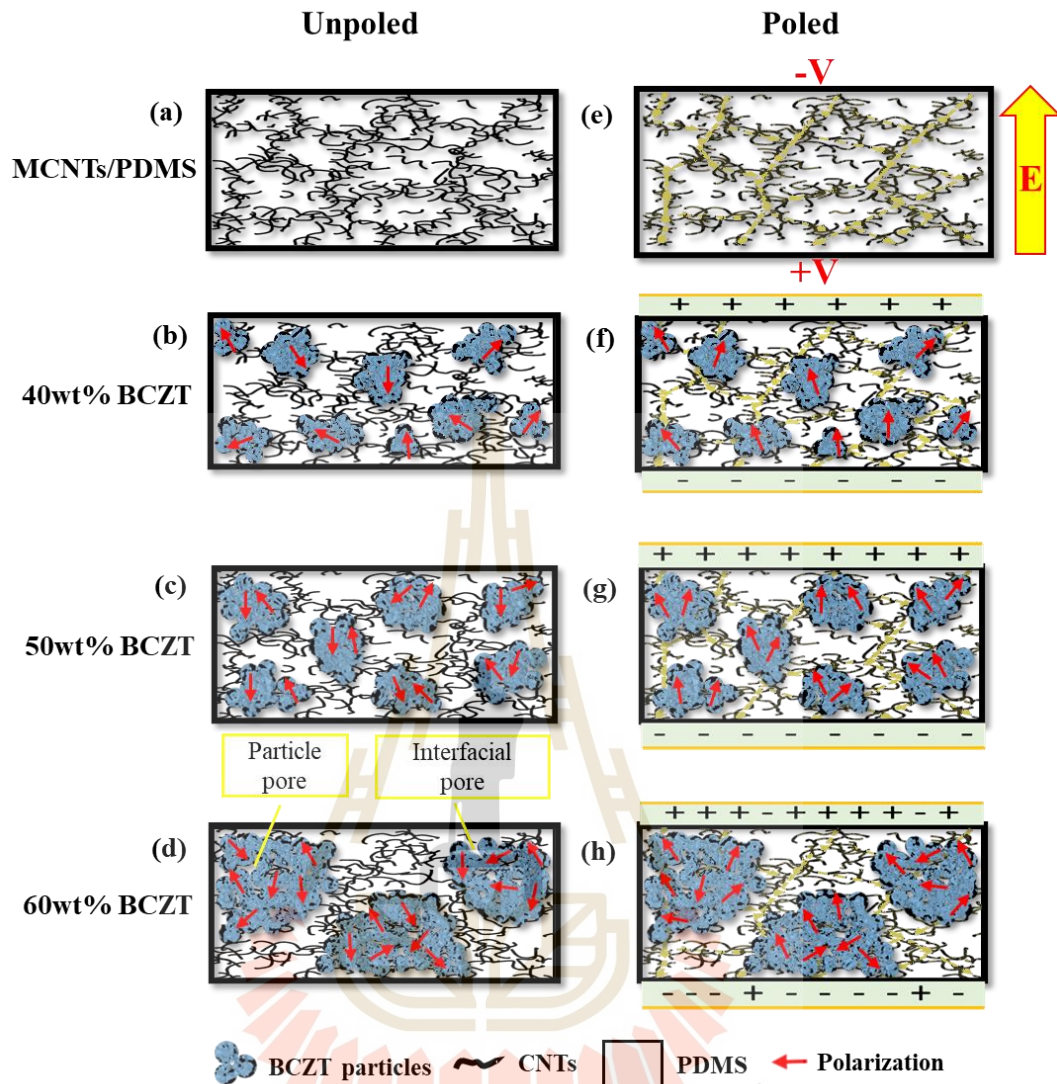


Figure 5.13 Schematic of the piezoelectric composites : microstructure diagram with various weight ratios of BCZT : (a-d) unpoled samples and (e-h) poled samples.

A 50 wt% BCZT of P-TENG device was selected to examine the instantaneous output power by various load resistance analyses, the charge ability into capacitors for energy storage, and the stability test to show long term reliability. The traditional four-diode bridge rectifier for converting AC to DC signals is shown in Figure 5.14(a). External load resistances ($10^4 - 10^6 \Omega$) were used to drive the output voltage (V_{DC}) and current (I_{DC}). Figure 5.14(b) and Figure 5.14(c) show the relationship between V_{DC} , I_{DC} , and the power of P-TENG generated under a compressive load force of 500 N with frequencies of 1 and 3 Hz, which are comparable to walking and running situations. As the load resistance increased, the V_{DC} of the P-TENG device also increased, while I_{DC} decreased, as predicted by Ohm's law. At 1 and 3 Hz frequencies, the output power (P) derived from $P = V \cdot I$ exhibited a maximum value of 35 μW (at 50 k Ω) and 47 μW (at 80 k Ω), respectively. This value corresponds to the preferred matching of internal load resistance for this P-TENG device. These results show that the P-TENG device outputs more power when loaded with 500 N at 3 Hz than at 1 Hz. Due to the device's deformation, the P-TENG's contact area between the Al plate and the composite's surface was expanded. The triboelectric effect separated charges generated by friction between the two materials, thereby increasing the electrical output. The output power increased because higher frequencies improved material contact and separation efficiency. Therefore, the device can produce more electrical charge at higher frequencies than at lower frequencies, leading to the observed 3 Hz difference in performance. As a result, a 3 Hz frequency was used to test the ability to charge energy into storage capacitors, which was examined using a range of capacitors (0.33, 0.47, 2.2, and 22 μF). The charging diagram and behavior are shown in Figure 5.14(d), where the signal analysis was gathered over around 600 s using a digital multimeter (Keysight, 34465A). The results showed that the P-TENG device quickly and efficiently charges the 0.33 and 0.47 μF capacitors to 6 V in less than 150 s, gradually raising the voltage to the 2.2 and 22 μF capacitors by 5.7 and 5.5 V within 300 and 600 s, respectively. In addition, the ability of this P-TENG to charge the supercapacitor (0.1 F) was also examined, where the results demonstrated that within 600 s, the P-TENG device could steadily raise the voltage from 0 to 40 mV, as shown in Figure 5.14(e).

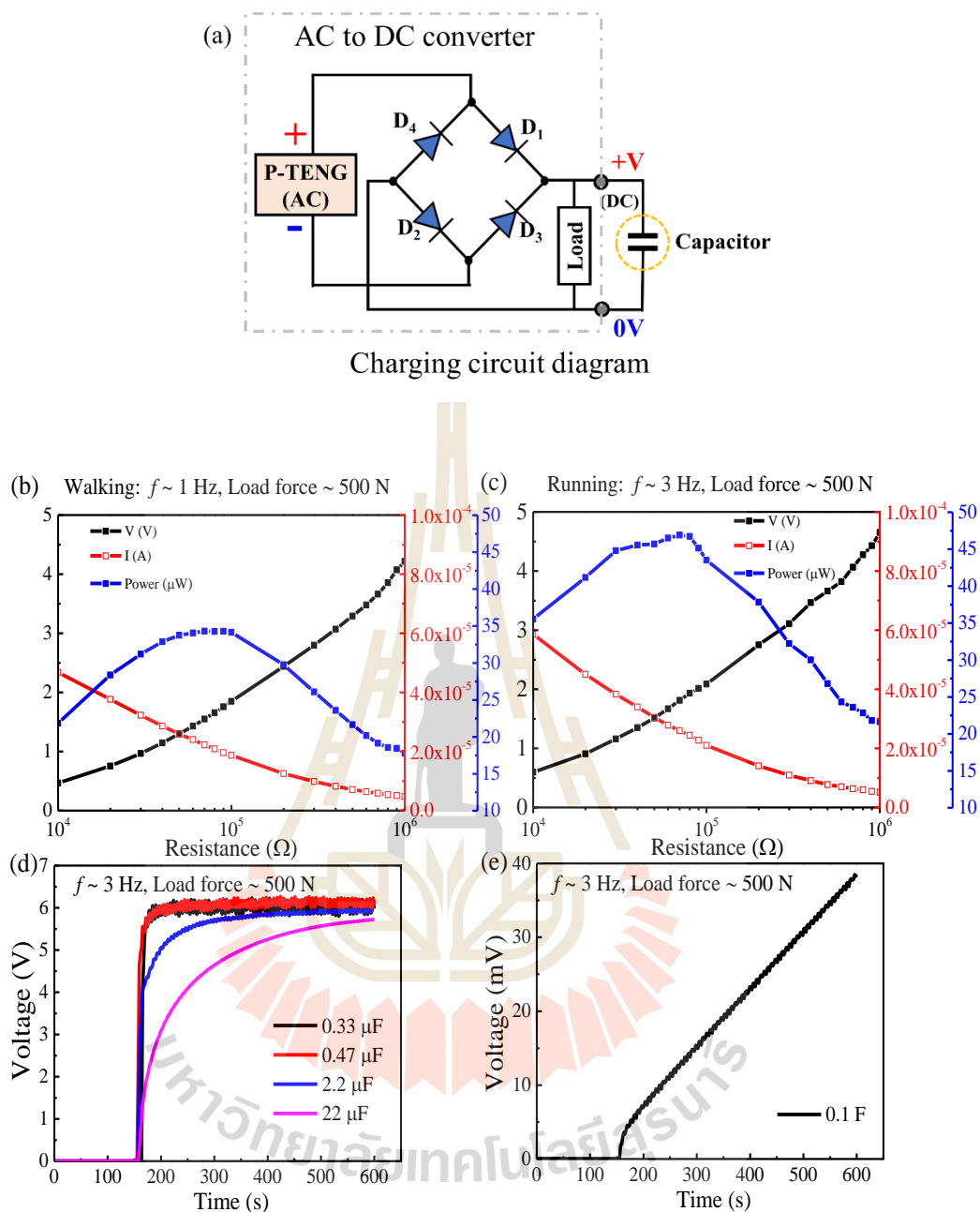


Figure 5.14 Electrical output performance of P-TENG device (50 wt% BCZT) : (a) block diagram of conventional diode bridge rectifier (AC to DC) and charging circuit diagram, the DC output voltage, output current, and output power of various load resistances under compressive loading 500 N at frequency 1 Hz (b) and 3 Hz (c), (d) and (e) charge ability into capacitors.

Finally, a stability test was performed on P-TENG device with 50 wt% BCZT under 500 N of compressive load force at 3 Hz of frequency for 6900 cycles, as shown in Figure 5.15. The results demonstrated that consistency in electrical output (V_{DC} , I_{DC} , and output power) with no noticeable degradation through the experiment. These results indicate that high durability of P-TENG for energy harvesting applications, and the P-TENG device at 50 wt% BCZT exhibited better electrical output performance compared to other composites. At this stage, the BCZT particles and MCNTs were well-distributed in the PDMS matrix, resulting in better charge transfer within the piezoelectric composite. This work therefore demonstrates the potential improvement in electrical output performance of lead-free piezoelectric composites for P-TENG device at an optimal 50 wt% BCZT particles with 3 wt% MCNTs after poling at 0.33 kV/mm. This investigation highlights that the P-TENG device has the potential for self-powered energy harvesting systems.

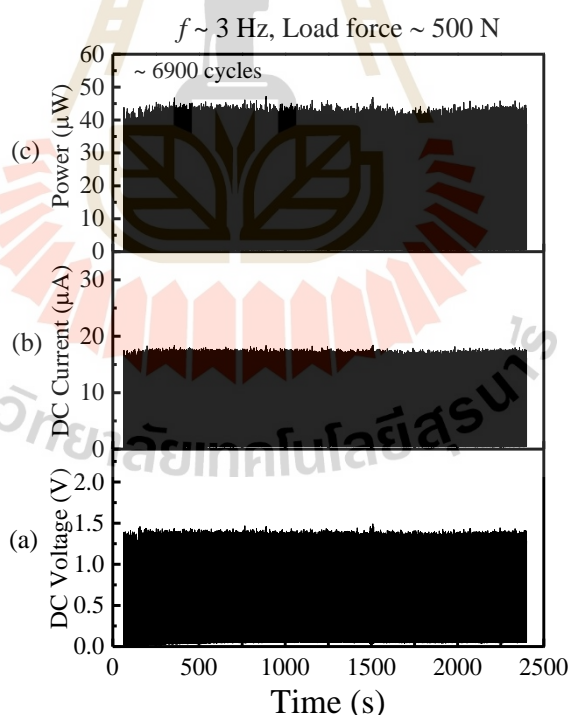


Figure 5.15 Electrical output performance of P-TENG device (50 wt% BCZT) : Stability test of DC output, (a) output voltage, (b) output current, and (c) output power under 6900 compressive loading cycles.

5.4 Chapter Summary

This study investigates a novel arch-shaped P-TENG based on a BCZT/MCNTs/PDMS composite with different weight fractions of BCZT (up to 60 wt%) for compressive energy harvesting at low frequencies. A detailed analysis of the physical and chemical properties (XRD, OM, FE-SEM, FIX, SR-XTM) of the piezoelectric composites revealed a homogeneous dispersion and distribution of 50 wt% piezoelectric BCZT particles in the polymer matrix. The 50 wt% BCZT showed the highest density (1.373 g/cm^3) and crosslinking density ($8.790 \times 10^{-4} \text{ mol/cm}^3$). Furthermore, the electrical properties (conductivity $\sim 0.9 \text{ mS/m}$, resistivity $\sim 1 \text{ k}\Omega\text{m}$) and mechanical properties ($T_g \sim -118 \text{ }^\circ\text{C}$, storage modulus $E' \sim 4.195 \text{ MPa}$, loss modulus $E'' \sim 0.398 \text{ MPa}$, $\tan \delta \sim 0.095$) were measured at room temperature. The P-TENG device based on the 50 wt% BCZT/MCNTs/PDMS composite generated the highest electrical output performance with a $V_{OC} \sim 39.7 \text{ V}$, $I_{SC} \sim 1.9 \text{ }\mu\text{A}$, and $P-P$ power of $\sim 157.7 \text{ }\mu\text{W}$ during application of a 500 N compressive load at 1 Hz. In addition, the device produced $V_{DC} \sim 1.9 \text{ V}$, $I_{DC} \sim 24.4 \text{ }\mu\text{A}$, and maximum output power of $\sim 46.7 \text{ }\mu\text{W}$ at 80 k Ω of external load resistance from impedance matching (under $F = 500 \text{ N}$, $f = 3 \text{ Hz}$). The P-TENG device demonstrated stability under cycle loading of approximately 6900 cycles and was able to charge several capacitors. These attractive mechanical and energy harvesting properties suggest that the P-TENG device based on the 50 wt% BCZT/MCNTs/PDMS composite has the potential for alternative and additional solutions in nanogenerator applications under high compressive loading at low frequency.

5.5 References

- Arends, T., Huinink, H. P., & Pel, L. (2019). Dynamics of heterogeneous crosslinking in room temperature vulcanizing poly(dimethyl siloxane) and its dependence on moisture supply. *Polymer*, *164*, 8-16. doi:<https://doi.org/10.1016/j.polymer.2018.12.059>
- Babu, I., & de With, G. (2014). Highly flexible piezoelectric 0–3 PZT–PDMS composites with high filler content. *Composites Science and Technology*, *91*, 91-97. doi:<https://doi.org/10.1016/j.compscitech.2013.11.027>
- Bowen, C. R., Buschhorn, S., & Adamaki, V. (2014). Manufacture and characterization of conductor-insulator composites based on carbon nanotubes and thermally reduced graphene oxide. *Pure and Applied Chemistry*, *86*(5), 765-774.
- Buatip, N., Dhanunjaya, M., Amonpattaratkit, P., Pomyai, P., Sonklin, T., Reichmann, K., Pojprapai, S. (2020). Comparison of conventional and reactive sintering techniques for Lead-Free BCZT ferroelectric ceramics. *Radiation Physics and Chemistry*, *172*, 108770. doi:<https://doi.org/10.1016/j.radphyschem.2020.108770>
- Buatip, N., Promsawat, N., Pisitpipathsin, N., Namsar, O., Pawasri, P., Ounsung, K., Projprapai, S. (2018). Investigation on electrical properties of BCZT ferroelectric ceramics prepared at various sintering conditions. *Integrated Ferroelectrics*, *187*(1), 45-52. doi:[10.1080/10584587.2018.1445395](https://doi.org/10.1080/10584587.2018.1445395)
- Cai, J. H., Huang, M. L., Chen, X. D., & Wang, M. (2022). Controllable construction of cross-linking network for regulating on the mechanical properties of polydimethylsiloxane and polydimethylsiloxane/carbon nanotubes composites. *Journal of Applied Polymer Science*, *139*(19), 52113.
- Choi, Y. J., Yoo, M.-J., Kang, H.-W., Lee, H.-G., Han, S. H., & Nahm, S. (2013). Dielectric and piezoelectric properties of ceramic-polymer composites with 0–3 connectivity type. *Journal of Electroceramics*, *30*(1), 30-35. doi:[10.1007/s10832-012-9706-7](https://doi.org/10.1007/s10832-012-9706-7)

- Danish, A., Bin, Y., Xiaochao, D., Hao, Y., & Meifang, Z. (2017). Enhancement of output performance through post-poling technique on BaTiO₃ /PDMS-based triboelectric nanogenerator. *Nanotechnology*, *28*(7), 075203. doi:<https://doi.org/10.1088/1361-6528/aa52b7>
- De Samber, B., Scharf, O., Buzanich, G., Garrevoet, J., Tack, P., Radtke, M., Vincze, L. (2019). Three-dimensional X-ray fluorescence imaging modes for biological specimens using a full-field energy dispersive CCD camera. *Journal of Analytical Atomic Spectrometry*, *34*(10), 2083-2093. doi:10.1039/C9JA00198K
- Du, J., Wang, L., Shi, Y., Zhang, F., Hu, S., Liu, P., Chen, J. (2020). Optimized CNT-PDMS Flexible Composite for Attachable Health-Care Device. *Sensors (Basel, Switzerland)*, *20*(16), 4523. doi:<https://doi.org/10.3390/s20164523>
- Fuentes-Fernandez, E. M. A., Gnade, B. E., Quevedo-Lopez, M. A., Shah, P., & Alshareef, H. N. (2015). The effect of poling conditions on the performance of piezoelectric energy harvesters fabricated by wet chemistry. *Journal of Materials Chemistry A*, *3*(18), 9837-9842. doi:10.1039/C5TA00447K
- Hagen, R., Salmén, L., & Stenberg, B. (1996). Effects of the type of crosslink on viscoelastic properties of natural rubber. *Journal of Polymer Science Part B: Polymer Physics*, *34*(12), 1997-2006.
- Hur, O.-N., Ha, J.-H., & Park, S.-H. (2020). Strain-Sensing Properties of Multi-Walled Carbon Nanotube/Polydimethylsiloxane Composites with Different Aspect Ratio and Filler Contents. *Materials*, *13*(11), 2431. doi:<https://doi.org/10.3390/ma13112431>
- Izdihar, K., Abdul Razak, H. R., Supion, N., Karim, M. K. A., Osman, N. H., & Norkhairunnisa, M. (2021). Structural, Mechanical, and Dielectric Properties of Polydimethylsiloxane and Silicone Elastomer for the Fabrication of Clinical-Grade Kidney Phantom. *Applied Sciences*, *11*(3), 1172. Retrieved from <https://www.mdpi.com/2076-3417/11/3/1172>

- Limaye, A. (2006). A volume exploration and presentation tool. *Developments in X-Ray Tomography VIII*, 17.
- Munthala, D., Sonklin, T., Buatip, N., Pomyai, P., Amonpattaratkit, P., Klysubun, W., & Pojprapai, S. (2020). Angle dependent synchrotron X-ray absorption spectroscopic structural studies on Ba_{0.85}Ca_{0.15}Zr_{0.1}Ti_{0.9}O₃ ferroelectric ceramics. *Scripta Materialia*, 188, 249-253. doi:10.1016/j.scriptamat.2020.07.021
- Munthala, D., Sonklin, T., Pomyai, P., Luo, Z., Crawley, F., Buatip, N., Pojprapai, S. (2021). In-situ X-ray Absorption Spectroscopy (XAS) Studies of Electrical Field Induced Domain Switching in BCZT Ceramics. *Ceramics International*, 47. doi:10.1016/j.ceramint.2021.05.201
- Park, K.-I., Bae, S. B., Yang, S. H., Lee, H. I., Lee, K., & Lee, S. J. (2014). Lead-free BaTiO₃ nanowires-based flexible nanocomposite generator. *Nanoscale*, 6(15), 8962-8968. doi:10.1039/C4NR02246G
- Promsawat, N., Promsawat, M., Janphuang, P., Luo, Z., Beeby, S., Rojviriyaya, C., Pojprapai, S. (2018). CNTs-added PMNT/PDMS flexible piezoelectric nanocomposite for energy harvesting application. *Integrated Ferroelectrics*, 187(1), 70-79. doi:10.1080/10584587.2018.1445684
- Suo, G., Yu, Y., Zhang, Z., Wang, S., Zhao, P., Li, J., & Wang, X. (2016). Piezoelectric and Triboelectric Dual Effects in Mechanical-Energy Harvesting Using BaTiO₃/Polydimethylsiloxane Composite Film. *ACS Applied Materials & Interfaces*, 8(50), 34335-34341. doi:10.1021/acsami.6b11108
- Vlassenbroeck, J., Masschaele, B., Cnudde, V., Dierick, M., Pieters, K., Van Hoorebeke, L., & Jacobs, P. (2006). Octopus 8: A High Performance Tomographic Reconstruction Package for X-ray Tube and Synchrotron micro-CT. *Advances in X-ray Tomography for Geomaterials*, 167-173.

- Walter, P., Sarrazin, P., Gailhanou, M., Hérouard, D., Verney, A., & Blake, D. (2019). Full-field XRF instrument for cultural heritage: Application to the study of a Caillebotte painting. *X-Ray Spectrometry*, *48*(4), 274-281. doi:<https://doi.org/10.1002/xrs.2841>
- Wang, P., Li, Y., & Lu, Y. (2011). Enhanced piezoelectric properties of $(\text{Ba}_{0.85}\text{Ca}_{0.15})(\text{Ti}_{0.9}\text{Zr}_{0.1})\text{O}_3$ lead-free ceramics by optimizing calcination and sintering temperature. *Journal of the European Ceramic Society*, *31*(11), 2005-2012. doi:<https://doi.org/10.1016/j.jeurceramsoc.2011.04.023>
- Wemyss, A. M., Marathianos, A., Heeley, E. L., Ekeocha, J., Morishita, Y., di Ronza, R., Wan, C. (2022). Oligomeric Curing Activators Enable Conventional Sulfur-Vulcanized Rubbers to Self-Heal. *ACS Applied Polymer Materials*, *4*(10), 7868-7877. doi:10.1021/acscapm.2c01398
- Zhang, Y., Xie, M., Roscow, J., & Bowen, C. (2019). Dielectric and piezoelectric properties of porous lead-free $0.5\text{Ba}(\text{Ca}_{0.8}\text{Zr}_{0.2})\text{O}_3-0.5(\text{Ba}_{0.7}\text{Ca}_{0.3})\text{TiO}_3$ ceramics. *Materials Research Bulletin*, *112*, 426-431. doi:<https://doi.org/10.1016/j.materresbull.2018.08.031>

CHAPTER 6

CONCLUSION AND FUTURE PERSPECTIVES

This chapter is the conclusion of the dissertation. Additionally, it offers perspectives for potential future work. Based on the studies outlined in the previous three chapters, this report summarizes the influence of fabrication and sintering techniques on the phase, grain size, density, and electrical, dielectric, and piezoelectric properties of BCZT ceramics. Additionally, it examines how the weight ratios of BCZT affect the physical, mechanical, dielectric, and electrical properties of composite materials. The study also explores how piezo-triboelectric hybridization can enhance the energy-harvesting ability of BCZT/MCNTs/PDMS piezoelectric composites under compressive loading when compared to BCZT piezoelectric ceramics. Lastly, the implications of these results are discussed.

6.1 General Conclusions

This section is based on the preliminary hypotheses for this investigation. They are as follows:

1. By employing a suitable sintering technique, the piezoelectric properties of BCZT ceramic could be improved, which could influence the phase, grain size, density, dielectric, piezoelectric, and electrical properties of the material. The improvement of piezoelectric properties for energy harvesting purposes can be gauged by assessing the piezoelectric charge coefficient (d_{33}) and piezoelectric voltage coefficient (g_{33}).
2. The physical, mechanical, dielectric, electrical properties, and electrical output performance of BCZT/MCNTs/PDMS composites, used for energy harvesting applications, could be affected by the weight percentage ratios of BCZT particles present in them.
3. The energy harvesting performance of BCZT/MCNTs/PDMS piezoelectric composite could be further enhanced by utilizing piezo-triboelectric hybridization.

Additionally, it could provide better mechanical endurance under compressive loading when compared to BCZT piezoelectric ceramic.

6.1.1 A comparison between conventional and reactive sintering techniques for BCZT ceramic fabrication

The preliminary results from Chapter 3 confirm Hypothesis 1. In this chapter, the fabrication techniques of BCZT ceramics using CS and RS methods were outlined, and their suitability for sintering, including dwelling times, was investigated to improve the phase, microstructure, electrical characteristics, and oxidation state of BCZT ferroelectric ceramics.

Using X-ray diffraction (XRD), it was observed that BCZT ceramics sintered at 1540 °C with varied dwell times (2, 3, and 4 hrs) exhibited pure perovskite and tetragonal-orthorhombic mixed phase structures under all conditions. The optimum characteristics were observed in BCZT ceramics (CS and RS) sintered at 1540 °C for 2 hrs of dwell time. The scanning electron microscopy (SEM) results revealed that the CS-BCZT ceramic exhibited a grain size of $14.42 \pm 6.02 \mu\text{m}$, while the RS-BCZT ceramic exhibited a grain size of $13.24 \pm 4.46 \mu\text{m}$. The relative density of both BCZT ceramics was found to be 96 %. After sputtering to coat electrodes on BCZT ceramics, the electrical properties (T_c , $\epsilon_{r,\text{max}}$, $\tan \delta$, P_r , E_c , and d_{33}) were investigated. The CS-BCZT ceramic exhibited 67 °C of T_c , 10610 of $\epsilon_{r,\text{max}}$, 0.02 of $\tan \delta$, $5.01 \mu\text{C}/\text{cm}^2$ of P_r , 2.53 kV/cm of E_c , and 284 pC/N of d_{33} , while the RS-BCZT ceramic exhibited 63 °C of T_c , 9628 of $\epsilon_{r,\text{max}}$, 0.02 of $\tan \delta$, $5.56 \mu\text{C}/\text{cm}^2$ of P_r , 3.26 kV/cm of E_c , and 288 pC/N of d_{33} . It was found that RS-BCZT ceramic (without calcining and re-grinding BCZT calcined powder process) exhibited physical and electrical properties similar to CS-BCZT ceramic, and at the same sintering temperature and dwelling time, the Ti *K*-edge and Zr *L*₃-edge XANES spectra matched the 4+ oxidation states of Ti and Zr atoms in both (CS and RS) BCZT ceramics. These characteristics were explained using X-ray absorption spectroscopy (XAS).

These results demonstrate the potential of reactive sintering to synthesize and fabricate BCZT ceramics more simply and economically than CS. However, the drawback of this technique is its inability to enhance the electrical

properties of BCZT ceramics suitable for energy harvesting applications. Thus, the next section (6.1.2) presents methods to improve the electrical and piezoelectric properties of these BCZT ceramics.

6.1.2 The energy harvesting performance of BCZT piezoelectric ceramic under low frequency

The observations and analysis presented in Chapter 4 confirm the validity of Hypothesis 1. The fabrication process of bulk piezoelectric ceramic was optimized by utilizing solid-state reaction and sintering processes, which resulted in achieving a high piezoelectric coefficient ($d_{33} \sim 350\text{--}650$ pC/N, $g_{33} \sim 12\text{--}20$ (10^{-3} Vm/N)) for BCZT ceramics.

X-ray diffraction examination showed a pure perovskite structure with a combination of rhombohedral and tetragonal phases, while SEM data revealed an average grain size of 17.84 ± 6.40 μm and a relative density of roughly 98-99 % compared to the average bulk density of 5.607 g/cm^3 . The results indicate that bulk BCZT ceramics fabricated through the solid-state reaction sintering technique, using a cold isostatic pressing machine (CIP), exhibit remarkable piezoelectric properties, including a d_{33} value of 517 pC/N, g_{33} of 19×10^{-3} Vm/N, and FOM of 9823×10^{-15} m^2/N , making them suitable for mechanical to electrical energy harvesting. An increase in the grain size, bulk density, and dimensions of ceramic enhances the electrical and piezoelectric properties of bulk BCZT ceramics. Therefore, the study evaluated the probability of BCZT piezoelectric ceramics for energy harvesting applications under a compressive load of 200 N (0.3 Hz) without damage. The optimized output performance yielded a DC voltage (V_{DC}) of 9.94 V, a DC current (I_{DC}) of 2.82 μA , a power of 28.03 μW , and an energy of 4.37×10^{-7} J.

These results demonstrate that bulk BCZT ceramics can be utilized as lead-free piezoelectric microgenerators or sensor alternatives under mechanical compressive load at low frequency. However, the drawback of bulk BCZT ceramics for compressive energy harvesting is their inability to sustain high loads. Thus, Section 6.1.3 reports on composite materials and piezo-triboelectric devices that enhance mechanical endurance under compressive loading when compared to BCZT ceramics.

6.1.3 Piezo-Triboelectric nanogenerator based BCZT/MCNTs/PDMS composite for compressive energy harvesting

This chapter confirms Hypotheses 2 and 3, as supported by the findings presented in Chapter 5. The research study examined the influence of weight ratios of barium calcium zirconate titanate (BCZT) particles on the energy harvesting performance of BCZT/multi-walled carbon nanotubes (MCNTs)/polydimethylsiloxane (PDMS) composites and piezo-triboelectric hybrid devices. The outcomes of the investigation showed that the BCZT weight percentage had a significant impact on the energy harvesting performance of these devices under compressive loading force and frequency. Additionally, the study analyzed the effect of external load resistance on impedance matching. Finally, the study evaluated the mechanical endurance of the devices under compressive loading.

X-ray diffraction (XRD) analysis showed that the pattern intensity increased with increasing BCZT particles weight percentage. A comprehensive examination of the microstructure of the piezoelectric composites, using optical microscopy (OM), field-emission scanning electron microscopy (FE-SEM), focused ion beams cross-sectioning (FIB), and synchrotron radiation X-ray tomographic microscopy (SR-XTM), demonstrated a homogeneous dispersion and distribution of BCZT particles in the polymer matrix. Increasing the weight percentage of BCZT particles in the MCNTs/PDMS composite from 40 wt% to 50 wt% improved the electrical output performance of the piezoelectric composites. However, increasing the BCZT weight percentage to 60 wt% reduced the output performance of the piezoelectric composites, possibly due to the formation of interfaces and porosity resulting from BCZT particle agglomeration. These findings are consistent with the observation that the composite containing 50 wt% BCZT had the maximum density and crosslink density, as well as the optimal mechanical and electrical properties, compared to other weight percentages studied.

The improvement in the piezo-triboelectric hybridization based on BCZT/MCNTs/PDMS composites provides further support for the hypothesis that these materials can enhance the energy harvesting ability of the devices. Under a compressive load force of 500 N and a frequency of 1 Hz, the piezo-triboelectric nanogenerator (P-TENG) device based on the BCZT/MCNTs/PDMS composite exhibited remarkable electrical output performance, with a voltage open-circuit (V_{OC}) of approximately 39.7 V, a short-circuit current (I_{SC}) of roughly 1.9 μ A, and a peak-to-peak power ($P-P$) of around 157.7 μ W. The maximum output power was 46.7 μ W at 80 kHz when the impedance was matched ($F = 500$ N, $f = 3$ Hz), with a DC voltage (V_{DC}) of approximately 1.9 V and a DC current (I_{DC}) of about 24.4 μ A. Furthermore, the device was able to charge several capacitors and exhibited stability under cyclic loading of around 6900 cycles, suggesting its potential for use in nanogenerator applications.

Overall, the results indicate that the P-TENG device based on the BCZT/MCNTs/PDMS composite exhibits better mechanical endurance under compressive loading up to 500 N without damage, compared to BCZT piezoelectric ceramic (which can sustain up to 200 N). These findings suggest that these devices have potential for use in energy harvesting applications under compressive load force and mechanical cyclic loading.

6.2 Recommendations for Future Work

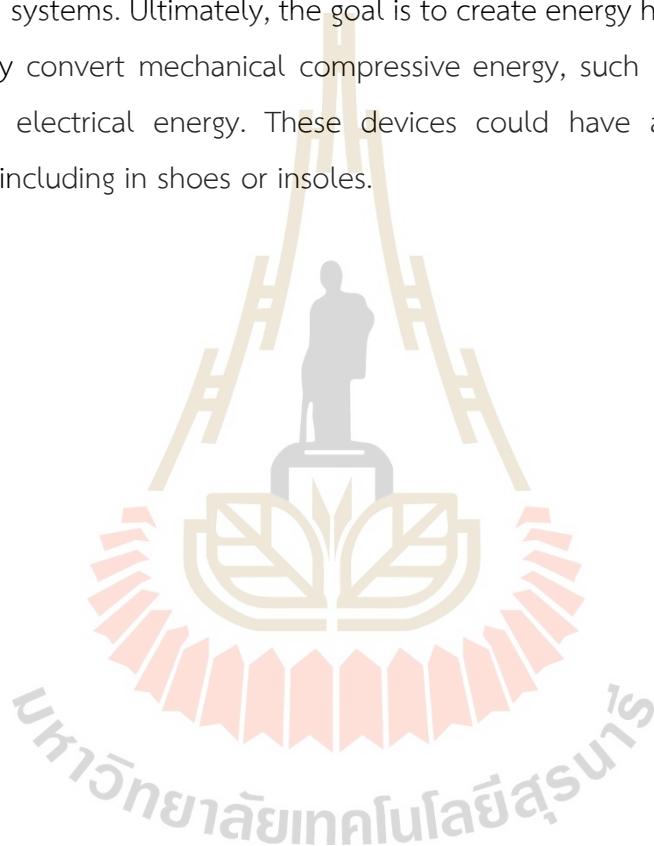
The piezo-triboelectric hybrid based on BCZT/MCNTs/PDMS has a significant potential for various applications. Here are some recommendations for future work in this area:

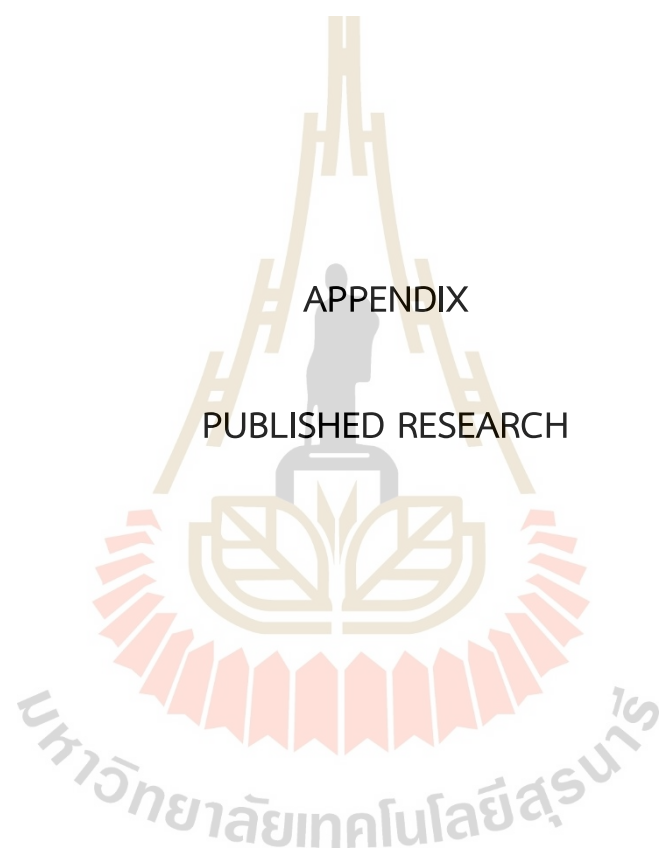
6.2.1 Investigation of the hybrid system's energy conversion efficiency : The energy conversion efficiency of the piezo-triboelectric hybrid system based on BCZT/MCNTs/PDMS can be investigated to determine its suitability for different energy harvesting applications. Future research could focus on studying the hybrid system's energy conversion efficiency under different environmental conditions, such as temperature and humidity, including heat or energy losses of the system.

6.2.2 Development of new hybrid structures : Future research could focus on developing new hybrid structures that incorporate other functional materials, such as graphene, silver nanowires, BCZT nanoparticles or other piezoelectric or triboelectric materials, to enhance the hybrid system's performance.

6.2.3 Investigation of the hybrid system's durability : The durability of the piezo-triboelectric hybrid system based on BCZT/MCNTs/PDMS is critical for its practical applications. Future research could focus on investigating the hybrid system's durability under different mechanical loads, frequencies, and environmental conditions.

Finally, the author hopes that the research presented in this study will lead to advances in the development of high-performance energy harvesting devices based on the piezo-triboelectric effect. In particular, the knowledge gained on the physical, chemical, mechanical, dielectric, piezoelectric, electrical, and energy harvesting properties of lead-free BCZT piezoelectric ceramic, BCZT/MCNTs/PDMS piezoelectric composite, and the piezo-triboelectric hybrid system based on BCZT/MCNTs/PDMS will help in the synthesis, fabrication, characterization, optimization, and study of these materials and systems. Ultimately, the goal is to create energy harvesting devices that can efficiently convert mechanical compressive energy, such as that generated by walking, into electrical energy. These devices could have a range of potential applications, including in shoes or insoles.

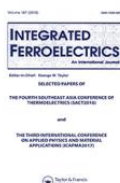




List of Publications

Buatip, N., Promsawat, N., Pisitpipathsin, N., Namsar, O., Pawasri, P., Ounsung, K., Phabsimma, K., Rattanachan, S. T., Janphuang, P. & Projprapai, S. (2018). Investigation on electrical properties of BCZT ferroelectric ceramics prepared at various sintering conditions. *Integrated Ferroelectrics*, 187(1), 45-52. <https://doi.org/10.1080/10584587.2018.1445395>

Buatip, N., Dhanunjaya, M., Amonpattaratkit, P., Pomyai, P., Sonklin, T., Reichmann, K., Janphaung, P., & Pojprapai, S. (2020). Comparison of conventional and reactive sintering techniques for Lead-Free BCZT ferroelectric ceramics. *Radiation Physics and Chemistry*, 172, 108770. <https://doi.org/10.1016/j.radphyschem.2020.108770>



Integrated Ferroelectrics

An International Journal



ISSN: 1058-4587 (Print) 1607-8489 (Online) Journal homepage: <http://www.tandfonline.com/loi/ginf20>

Investigation on electrical properties of BCZT ferroelectric ceramics prepared at various sintering conditions

N. Buatip, N. Promsawat, N. Pisitpipathsin, O. Namsar, P. Pawasri, K. Ounsung, K. Phabsimma, S. T. Rattanachan, P. Janphuang & S. Projprapai

To cite this article: N. Buatip, N. Promsawat, N. Pisitpipathsin, O. Namsar, P. Pawasri, K. Ounsung, K. Phabsimma, S. T. Rattanachan, P. Janphuang & S. Projprapai (2018) Investigation on electrical properties of BCZT ferroelectric ceramics prepared at various sintering conditions, *Integrated Ferroelectrics*, 187:1, 45-52

To link to this article: <https://doi.org/10.1080/10584587.2018.1445395>

 Published online: 05 Apr 2018.

 Submit your article to this journal [↗](#)

 View related articles [↗](#)

 View Crossmark data [↗](#)

มหาวิทยาลัยเทคโนโลยีสุรนารี

Full Terms & Conditions of access and use can be found at
<http://www.tandfonline.com/action/journalInformation?journalCode=ginf20>



Investigation on electrical properties of BCZT ferroelectric ceramics prepared at various sintering conditions

N. Buatip^a, N. Promsawat^a, N. Pisitpipathsin^b, O. Namsar^a, P. Pawasri^a, K. Ounsung^a, K. Phabsimma^a, S. T. Rattanachan^a, P. Janphuang^c, and S. Projprapai^a

^aSchool of Ceramic Engineering, Suranaree University of Technology, Nakhon Ratchasima, Thailand;

^bDepartment of Applied Physics, Faculty of Sciences and Liberal Arts, Rajamangala University of Technology Isan, Nakhon Ratchasima, Thailand; ^cSynchrotron Light Research Institute, Nakhon Ratchasima, Thailand

ABSTRACT

The influence of sintering conditions on phase formation, density, microstructure and electrical properties of BCZT ceramics were investigated. The BCZT ($\text{Ba}_{0.85}\text{Ca}_{0.075}\text{Zr}_{0.1}\text{Ti}_{0.9}\text{O}_3$) ceramics were fabricated by a mixed oxide synthetic route of BaCO_3 , CaCO_3 , ZrO_2 and TiO_2 precursors and then sintered at 1250, 1300 and 1350°C for 2 and 4 hrs. Phase formation, densification, microstructure surfaces, dielectric properties, ferroelectric and piezoelectric properties were analyzed by using X-ray diffraction (XRD), Archimedes method, Scanning Electron Microscopy (SEM), LCR Meter, P - E hysteresis and d_{33} meter, respectively. In processes of sintering, the results show that BCZT structures are perovskite with pseudocubic phase. Sintering condition at 1300°C for 4 hrs exhibits optimum density, grain size and higher electrical properties: density 5.62 g/cm^3 (~98% of theoretical density), average grain size = $2.19 \pm 0.87 \text{ }\mu\text{m}$, dielectric constant (ϵ_r) = 2840, dielectric loss ($\tan \delta$) = 0.10, remanent polarization (P_r) = $5.84 \text{ }\mu\text{C/cm}^2$ and $d_{33} = 167 \text{ pC/N}$.

ARTICLE HISTORY

Received 15 December 2016
Accepted 31 July 2017

KEYWORDS

BCZT; lead free ferroelectric; sintering condition; grain size and density; electrical properties

1. Introduction

Ferroelectric materials possess piezoelectric properties, which can convert kinetic energy to electrical energy and vice versa. Therefore, these materials are widely used in various applications such as generators, sensors, actuators, transducers, etc [1]. Lead Zirconate Titanate (PZT) based ferroelectric ceramics have dominated the commercial market and devices more than half a century in worldwide due to their excellent piezoelectric properties [2]. However, the lead-based ferroelectric ceramics direction from global requirement are restricted due to their toxicity [3]. Over the last decades, many research groups have developed the new materials which could be replaced Lead (Pb) in ferroelectric ceramics using non-toxic alternatives [4]. One possibility reason is a legislative activity of the European Union that

CONTACT S. Projprapai  soodkhet@g.sut.ac.th

Color versions of one or more of the figures in this article can be found online at www.tandfonline.com/ginf.

© 2018 Taylor & Francis Group, LLC

purposes to eliminate toxic substances from electronic and electrical device for decrease the effect on environment and health [4]. The lead-free piezoelectric materials in competition with PZT are BaTiO_3 (BT), $(\text{Bi}_{0.5}\text{Na}_{0.5})\text{TiO}_3$ - BaTiO_3 (BNT-BT), $(\text{K}_{0.5}\text{Na}_{0.5})\text{NbO}_3$ (KNN) and $\text{Ba}_{1-x}\text{Ca}_x\text{Ti}_{1-y}\text{Zr}_y\text{O}_3$ (BCZT) [4–5]. Among of these materials, barium calcium zirconate titanate $(\text{Ba,Ca})(\text{Zr,Ti})\text{O}_3$, BCZT) exhibits excellent dielectric, ferroelectric and piezoelectric properties which can be applied to multilayer ceramic capacitors (MLCC), piezoelectric actuators and positive temperature coefficient resistors (PTCR) [6]. Previously, the dielectric constant values as high as ~ 18000 have been achieved form BCZT ceramics [7]. Tian et al. [5,8] reported about the lead free $\text{Ba}_{1-x}\text{Ca}_x\text{Ti}_{0.9}\text{Zr}_{0.1}\text{O}_3$ ($0.00 \leq x \leq 0.20$) ceramics fabricated by a solid-state method exhibited piezoelectric coefficient (d_{33}) of about 160–550 pC/N (d_{33} of PZT = 500–600 pC/N). In addition, Villafuerte-Castrejón et al. [5] illustrated that the sintering parameters such as temperature and dwelling time are important factors that affect the phase formation, physical properties and electrical properties of BCZT ceramics. Nevertheless, there is a lack of knowledge of the fabrication process of BCZT ceramics. Such basic knowledge can be used to improve the piezoelectric properties of BCZT ceramics. Therefore, this research aims to investigate the influence and the optimum of sintering conditions on phase formation, density, microstructure and electrical properties of BCZT ($\text{Ba}_{0.85}\text{Ca}_{0.075}\text{Zr}_{0.1}\text{Ti}_{0.9}\text{O}_3$) ceramics. In this work, BCZT ceramics were investigated in the sintering conditions range from 1250°C to 1350°C for 2 and 4 hrs. These conditions were chosen because there is a lack of understand and very few research report on the effect of sintering temperature and dwelling time on microstructure and electrical properties.

2. Experimental details

The BCZT ($\text{Ba}_{0.85}\text{Ca}_{0.075}\text{Zr}_{0.1}\text{Ti}_{0.9}\text{O}_3$) ceramics were fabricated using the conventional solid-state reaction technique. The oxide or carbonate powders of BaCO_3 (99.0%, Sigma Aldrich), CaCO_3 (99.0%, Loba Chemie), ZrO_2 (99.0%, Carlo Erba) and TiO_2 (99.0–100.9%), Riedel-deHaën) were used as initialize materials. The starting powders were mixed by ball milling with ethanol for 24 hrs. The slurries were dried at 110°C for 24 hrs, then they were pestled and calcined at 1200°C for 2 hrs with a heating/cooling rate of 5°C/min in a covered alumina crucible. The powders were pressed into 10 mm diameter pellets with 0.5 g: 3 wt% polyvinyl alcohol (PVA) as a binder and then sintered at 1250°C to 1350°C for 2 and 4 hrs in air with a heating/cooling rate of 5°C/min, respectively.

The phase structure of these ceramics was analyzed using X-ray diffractometer (XRD, Bruker Phaser DII). Density of the ceramics was determined by Archimedes' principle (ASTM C 378–88). Microstructure was observed using a scanning electron microscope (SEM, JEOL JSM-6010LV). The average grain size was determined by a linear intercept method [9] from SEM images. The parallel surfaces of each sample were polished sequentially using 320, 400 and 600 grit SiC paper. Before measuring the dielectric and piezoelectric properties, both faces of the ceramic were coated with silver paint as electrodes. The dielectric properties were measured

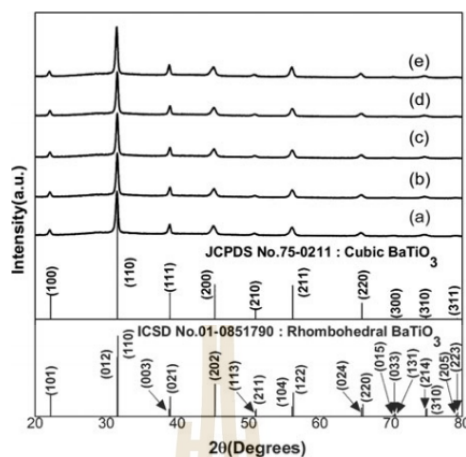


Figure 1. XRD patterns of BCZT ceramics sintered at (a) 1250°C/2 hrs, (b) 1250°C/4 hrs, (c) 1300°C/2 hrs, (d) 1300°C/4 hrs and (e) 1350°C/2 hrs.

by a LCR meter (GW INSTRON LCR-821) at room temperature and frequency of 12 Hz-100 kHz. Ferroelectric hysteresis loop was measured by *P-E* hysteresis (TREK, Model 20/20C) at room temperature and frequency at 50 Hz under an electric field ± 25 kV/cm. These ceramics were poled in a silicon oil bath under 3.0 kV/mm DC field at 50°C for 30 min (Matusada, AU-30*40). The piezoelectric constant d_{33} was measured by d_{33} meter (International Ltd., APC-S5865).

3. Results and discussion

The XRD diffraction patterns of BCZT ($\text{Ba}_{0.85}\text{Ca}_{0.075}\text{Zr}_{0.1}\text{Ti}_{0.9}\text{O}_3$) ferroelectric ceramics sintered at various conditions are illustrated in Figure 1. All XRD patterns at $2\theta \approx 20\text{--}80^\circ$ of BCZT ceramics demonstrated pure phase with perovskite structure pseudo-cubic phase (ICSD file No.01-0851790). In contrast with BaTiO_3 , a slight shift to the left of XRD patterns was also observed. This indicates that the substitution of Ca^{2+} to A-site and Zr^{4+} to B-site are accomplished by a solid-phase reaction. This result is in agreement with the previous research that was done by Ju et al [10]. It is indicated that sintering conditions at 1250°C to 1350°C for 2 and 4 hrs have no effect on the phase formation of BCZT ceramics. However, it is found that microstructures, including grain size and density, are vary with sintering conditions.

The microstructures of BCZT ceramics at various sintering conditions are shown in Figure 2. SEM patterns of sintered surfaces of BCZT ceramics that were sintered at 1200°C, 1300°C and 1350°C for 2 hrs exhibited a small grain boundary and amount of pores in their ceramics. This could be because there is not enough sintering kinetics energy for the grain growth and densifying mechanism

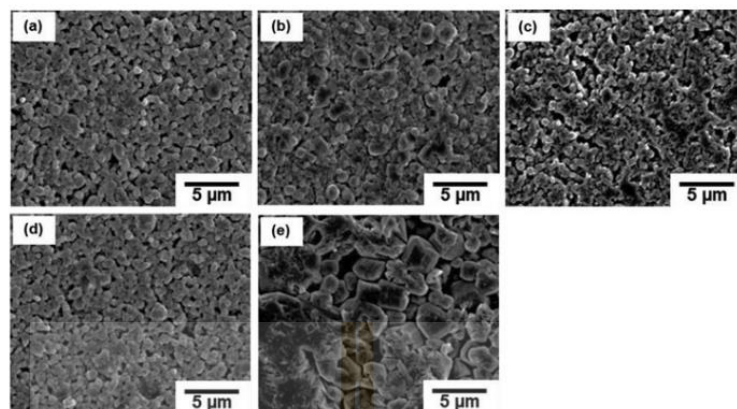


Figure 2. SEM micrographs of BCZT ceramics sintered at (a) 1250°C/2 h, (b) 1300°C/2 h, (c) 1350°C/2 h, (d) 1250°C/4 h and (e) 1300°C/4 h.

of BCZT ceramics [5,11,12,15]. On the other hand, the grain size and the density drop at 1350°C. This may be because the sintering stage was inhibited during vapor transportation and grain boundary diffusion. This leads to increment of intergrain pore [15]. Remarkably, the sintering at 1300°C shows the maximum density. At this condition, the grain size is bigger for longer dwelling time while density does not significantly change. As shown in Figure 2(e), an inhomogeneous grain-size distribution has been developed by sintering BCZT at 1300°C for 4 hrs because at longer dwelling time, atoms at grain boundary diffused into adjoining grains. It leads to grain growth and increasing of density of BCZT ceramics. [2,11–12]. The average grain size and density as a function of sintering temperature and dwelling time are reported in Table 1. The average grain size with various sintering conditions are about 0.69–2.19 μm . The BCZT ceramics were sintered and considerably dense with densities in the range of 5.37–5.69 g/cm^3 (equivalent to 94–99% of theoretical density). It shows that the temperature and time have an influence on grain size and density of BCZT ceramics. The grain size and the density tend to increase when the sintering temperature and dwelling time increase because of greater diffusion mechanisms that lead to densifying mechanisms of ceramics.

The effects of various sintering conditions on dielectric constant (ϵ_r) and dielectric loss ($\tan \delta$) were measured at room temperature using various frequencies from 12 Hz to 100 kHz as shown in Figure 3(a)–3(b). The ϵ_r and $\tan \delta$ values of all sintering conditions tend to decrease with increasing frequency (>100 Hz). This could be because the polarization mechanism does not completely response at the higher frequency.

Table 1 shows the average grain size and density with ϵ_r and $\tan \delta$ values of BCZT ceramics, measured at 50 Hz. The ϵ_r value increases from 1320 to 2840 with increase sintering temperature and dwelling time from 1250°C for 2 and 4 hrs and 1300°C for 2 and 4 hrs, respectively. $\tan \delta$ values are in the range of 0.09–0.73. It is known

Table 1. Physical and electrical properties of BCZT ceramics sintered at various conditions.

Sintering conditions	Physical properties				Electrical properties			
	Density (g/cm ³)	Relative density (%)	Grain size (μm)	ϵ_r (at 50 Hz)	$\tan \delta$ (at 50 Hz)	Remanent polarization, P_r ($\mu\text{C}/\text{cm}^2$)	Coercive field, E_c (kV/cm)	d_{33} (pC/N)
1250°C/2 h	5.37 \pm 0.06	94	0.69 \pm 0.29	1316 \pm 349	0.521 \pm 0.212	1.00	3.34	10
1300°C/2 h	5.69 \pm 0.04	99	1.03 \pm 0.46	1958 \pm 352	0.307 \pm 0.017	1.29	8.15	17
1350°C/2 h	5.52 \pm 0.08	97	0.68 \pm 0.19	1674 \pm 129	0.516 \pm 0.167	1.43	4.32	16
1250°C/4 h	5.48 \pm 0.08	96	0.86 \pm 0.41	1375 \pm 412	0.732 \pm 0.150	1.70	5.13	14
1300°C/4 h	5.62 \pm 0.02	98	2.19 \pm 0.87	2844 \pm 586	0.092 \pm 0.019	5.84	4.22	167

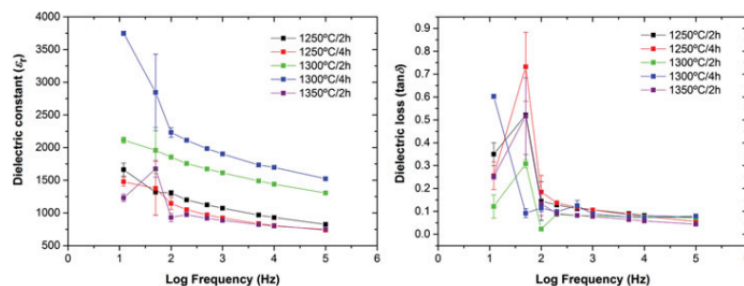


Figure 3. (a) Dielectric constant (ϵ_r) and (b) dielectric loss ($\tan \delta$) with various sintering conditions as a function of frequencies in room temperature.

that the switchability of domains in a large grain is greater than that in a small grain. The smaller grain size and intergrain pores lead to increasing in the surface area of charge layer causing an accumulating in the number of space charge and could lead to a lower dielectric constant [14]. The BCZT ceramics sintered at 1300°C for 4 hrs shows the maximum $\epsilon_r = 2840$ and minimum $\tan \delta = 0.10$ due to the larger grain size compared to other sintering conditions. In case of the sintered at 1350°C for 2 hrs, the ϵ_r value reduced because the grain size and the density decreased due to smaller grain growth as previously mentioned.

The Polarization-Electric field (P - E) hysteresis loop of BCZT ceramics was measured. The influence of sintering conditions on P - E loops is reported in Figure 4. The BCZT ceramics present the slim shape of P - E loops and low P_r . The P_r value of BCZT ceramics increases while raising sintering temperature from 1250°C to 1350°C and dwelling time from 2 and 4 hrs. However, The BCZT ceramics that were sintered at 1300°C for 4 hrs exhibits wider shape of P - E loop and provided the maximum P_r ($5.84 \mu\text{C}/\text{cm}^2$). The relatively remarkable ferroelectric properties could be attributed to grain size and density (i.e. BCZT at a such sintering

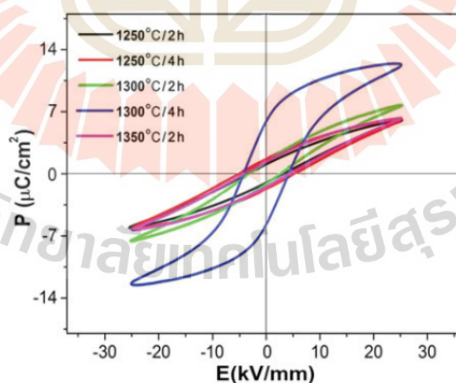


Figure 4. P - E hysteresis loops of BCZT ceramics sintered in various conditions at frequencies 50 Hz under an electric field $\pm 25 \text{ kV}/\text{cm}$.

condition has maximum grain size (average $2.19 \pm 0.87 \mu\text{m}$) and optimum density (5.62 g/cm^3 , $\sim 98\%$ of theoretical density). According to the previous discussion, the grain size and density, which can be varied by different sintering conditions, have strong effects on dielectric and ferroelectric properties of BCZT. To explain the relationship between grain size and ferroelectric properties, the theory of D - E hysteresis loop based on the Kolmogorov-Avrami model (K-A model) is applied. The modified K-A model reported by Orihara is expressed as a following equation [13].

$$f = f_0[1 - \exp(-G_a d^3/kT)], \quad (1)$$

where f is ferroelectric properties reflecting polarization or domain switchability, f_0 is the initial polarization or domain of ferroelectric materials, G_a is a constant that represents grain anisotropy energy density, d is a grain size, k is a rate constant, and T is temperature. From the equation, " f " is directly proportional to grain size. Therefore, the increase in size of grains enhances the domain switchability that improves the ferroelectric properties [13–14].

In addition to P - E loops, the piezoelectric coefficient (d_{33}) of BCZT sintered ceramics at different temperatures and dwelling times were measured as shown in Table 1. The d_{33} value is higher with larger grain size due to an increasing in the sintering temperature and dwelling time of 1250°C for 2 and 4 hrs and 1300°C for 2 and 4 hrs, respectively. In addition, it is lower at 1350°C for 2 hrs due to a smaller grain size. The larger grain size of BCZT ceramics enhance d_{33} value because the domains can be easier aligned in the same direction compared with the domains in a smaller grain size. These results are in agreement with the change of P - E loop and P_r as a function of grain size, and density affected by sintering conditions.

4. Conclusion

The BCZT ($\text{Ba}_{0.85}\text{Ca}_{0.075}\text{Zr}_{0.1}\text{Ti}_{0.9}\text{O}_3$) lead-free ferroelectric ceramics were prepared by a solid state and sintered with a heating/cooling rate of $5^\circ\text{C}/\text{min}$. The XRD patterns show that BCZT ceramic structures are perovskite with pseudo-cubic phase in all sintering conditions. The grain size and the density tend to increase with sintering temperature and dwelling time at sintered 1250°C to 1300°C for 2 and 4 hrs, except 1350°C for 2 hrs. The sintering conditions affect the physical and electrical properties of BCZT ceramics because density and grain size effect to the domain switchability and alignment. The BCZT ceramics sintered at 1300°C for 4 hrs exhibit an optimum density (5.62 g/cm^3 , $\sim 98\%$ of theoretical density), grain size (average $2.19 \pm 0.87 \mu\text{m}$) and electrical properties ($\epsilon_r = 2840$, $\tan \delta = 0.10$, $P_r = 5.84 \mu\text{C}/\text{cm}^2$ and $d_{33} = 167 \text{ pC/N}$).

Acknowledgments

This work is supported by Suranaree University of Technology (SUT) and Office of the Higher Education Commission under NRU Project of Thailand. N. Buatip would like to thank the Royal

Golden Jubilee (RGJ) Ph.D. Programme and Synchrotron Light Research Institute (Public Organization) for the support with appreciation. The authors also would like to acknowledge Newton Fund (UK) and the Higher Education Commission (Thailand) to support this project under Industry Academia Partnership Programme - THAILAND (IAPPT).

Funding

Suranee University of Technology; Light Research Institute; Royal Golden Jubilee Programme; Office of the Higher Education Commission; Newton Fund (UK); the Higher Education Commission (Thailand) under Industry Academia Partnership Programme - THAILAND (IAPPT).

References

1. P. K. Panda and B. Sahoo, PZT to Lead Free Piezo Ceramics: A Review, *Ferroelectrics* **474**, 128–143 (2015).
2. P. Wang, Y. X. Li, and Y. Q. Lu, Enhanced piezoelectric properties of $(\text{Ba}_{0.85}\text{Ca}_{0.15})(\text{Ti}_{0.9}\text{Zr}_{0.1})\text{O}_3$ lead-free ceramics by optimizing calcination and sintering temperature, *J Eur Ceram Soc.* **31**, 2005–2012 (2011).
3. S. D. Chavan and D. J. Salunkhe, Ferroelectric Relaxation Behavior of Lead free BCZT Ceramics, *Int. J. Sci. Rec.* **3**, 1557–1561 (2014).
4. J. Rödel, K. G. Webber, R. Dittmer, W. Jo, M. Kimura, and D. Damjanovic, Transferring lead-free piezoelectric ceramics into application, *J Eur Ceram Soc.* **35**, 1659–1681 (2015).
5. M. E. Villafuerte-Castrejón, E. Morán, A. Reyes-Montero, R. Vivar-Ocampo, J. A. Peña-Jiménez, S. O. Rea-López, and L. Pardo, Towards Lead-Free Piezoceramics: Facing a Synthesis Challenge, *Materials* **9** (21), 1–27 (2016).
6. A. Frattini, A. D. Loreto, O. D. Sanctis, and E. R. Benavidez, BCZT ceramics prepared from activated powders, *Procedia Materials Science* **1**, 359–365 (2012).
7. P. Hansen, D. Henning, and H. Schreinemacher, High-K Dielectric Ceramics From Donor/Acceptor-Codoped $(\text{Ba}_{1-x}\text{Ca}_x)(\text{Ti}_{1-y}\text{Zr}_y)\text{O}_3$ (BCTZ), *J. Am. Ceram. Soc.* **81**, 1369–1373 (1998).
8. Y. Tian, L. Wei, X. Chao, Z. Liu, and Z. Yang, Phase transition behavior and large piezoelectricity near the morphotropic phase boundary of lead-free $(\text{Ba}_{0.85}\text{Ca}_{0.15})(\text{Zr}_{0.1}\text{Ti}_{0.9})\text{O}_3$ ceramics, *J. Am. Ceram. Soc.* **96**, 496–502 (2013).
9. J. C. Wurst and J. A. Nelson, Lineal Intercept Technique for Measuring Grain Size in Two-Phase Polycrystalline Ceramics, *J. Amer. Ceram. Soc.* **109** (1972).
10. S. G. Ju, X. G. Tang, J. B. Wu, Y. P. Jiang, and Q. X. Liue, Dielectric relaxation in $(\text{Ba}_{0.7}\text{Ca}_{0.3})\text{TiO}_3$ - $\text{Ba}(\text{Zr}_{0.2}\text{Ti}_{0.8})\text{O}_3$ ceramics, *AMR* **287–290**, 503–508 (2011).
11. J. Wu, D. Xiao, B. Wu, W. Wu, J. Zhu, Z. Yang, and J. Wang, Sintering temperature-induced electrical properties of $(\text{Ba}_{0.90}\text{Ca}_{0.10})(\text{Ti}_{0.85}\text{Zr}_{0.15})\text{O}_3$ lead-free ceramics, *Mater. Res. Bull.* **47**, 1281–1284 (2012).
12. J. Wu, D. Xiao, W. Wu, J. Zhu, and J. Wang, Effect of dwell time during sintering on piezoelectric properties of $(\text{Ba}_{0.85}\text{Ca}_{0.15})(\text{Ti}_{0.90}\text{Zr}_{0.10})\text{O}_3$ lead-free ceramics, *J. Alloys Compd.* **509**, L359–L361 (2011).
13. H. Orihara, S. Hashimoto, and Y. Ishibashi, A Theory of D-E Hysteresis Loop Based on the Avrami Model, *J. Phys. Soc. Jpn.* **63**, 1031–1035 (1994).
14. P. Bharathi and K. B. R. Varma, Grain and the concomitant ferroelectric domain size dependent physical properties of $\text{Ba}_{0.85}\text{Ca}_{0.15}\text{Zr}_{0.1}\text{Ti}_{0.9}\text{O}_3$ ceramics fabricated using powders derived from oxalate precursor route, *J. Appl. Phys.* **116**, 164107-0-164107-10 (2014).
15. C. L. D. Jonghe and M. N. Rahaman, *Handbook of Advanced Ceramics*, edited by S. Somiya et al. (2003), pp. 187–264.



Contents lists available at ScienceDirect

Radiation Physics and Chemistry

journal homepage: www.elsevier.com/locate/radphyschem

Comparison of conventional and reactive sintering techniques for Lead-Free BCZT ferroelectric ceramics



N. Buatip^a, M. Dhanunjaya^a, P. Amonpattaratkit^b, P. Pomyai^a, T. Sonklin^a, K. Reichmann^c, P. Janphaung^b, S. Pojprapai^{a,*}

^a School of Ceramic Engineering, Suranaree University of Technology, Nakhon Ratchasima, 30000, Thailand

^b Synchrotron Light Research Institute, Nakhon Ratchasima, 30000, Thailand

^c Institute of Chemistry and Technology of Materials, Graz University of Technology, Stremayrgasse 9, 8010, Graz, Austria

ARTICLE INFO

Keywords:

BCZT
Lead-free piezoelectric
Reactive sintering
Electrical properties
XANES

ABSTRACT

Piezoelectric, dielectric and ferroelectric properties of a ceramic material greatly influenced by the synthesis technique and prepared condition. In this work, the efforts have been made to prepare barium calcium zirconium titanate (BCZT) ceramics and used to study the effectiveness of conventional sintering (CS) and reactive sintering (RS) methods. Specific composition of BCZT ceramic ($\text{Ba}_{0.85}\text{Ca}_{0.15}\text{Zr}_{0.1}\text{Ti}_{0.9}\text{O}_3$) was achieved by suitable and verified sintering condition. Phase and structure of ceramics identified by using X-ray Diffraction (XRD). The result confirms the existence of pure perovskite structure and mixture phase of orthorhombic and tetragonal in both CS and RS sintering techniques. Surface morphology and grain size variations for different dwell times were studied using Scanning Electron Microscopy (SEM). In both CS and RS techniques, the optimal sintering condition (1540 °C and 2 h of dwell time) possess gives relatively high density, better electric and piezoelectric properties. RS technique emerged as an alternative for CS technique. The implementation of sintering conditions, driven effects and their role on the above-mentioned properties were discussed. Pre-edge fine structure (PEFS) and X-Ray absorption near edge spectroscopy (XANES) is employed to elucidate the variation and oxidation state of 4+ of Ti and Zr in BCZT ceramics.

1. Introduction

Lead-based (like PZT) piezoelectric materials have widely studied for the last 5 decades due to their eminent properties and enriched piezoelectric, ferroelectric, sensor, transducer and actuator applications (Rödel et al., 2015; Kang et al., 2016). However, owing to serious environmental issues with Lead-based materials, many research groups put their efforts to invent new lead-free alternative ferroelectric materials like BaTiO_3 (BT) (Acosta et al., 2017), $(\text{K}_{0.5}\text{Na}_{0.5})\text{NbO}_3$ (KNN) (Izzuddin et al., 2019), $(\text{Bi}_{0.5}\text{Na}_{0.5})\text{TiO}_3$ (BNT) (Zhou et al., 2019), $(\text{Bi}_{0.5}\text{K}_{0.5})\text{TiO}_3$ (BKT) (Khanal et al., 2019), $(\text{Bi}_{0.5}\text{Na}_{0.5})\text{TiO}_3$ - BaTiO_3 (BNT-BT) (Hajra et al., 2018) and $(\text{Ba,Ca})(\text{Zr,Ti})\text{O}_3$ or BCZT (Wang et al., 2011; Wu et al., 2011). Among all the above lead-free materials, barium calcium zirconium titanate (BCZT) exhibits great piezoelectric and ferroelectric properties which are almost equal to PZT materials (Rödel et al., 2015). There are many publications on BCZT ceramics prepared by solid-state reactive (SSR) technique (Wang et al., 2011; Wu et al., 2011), hydrothermal technique (Liu et al., 2014; Lu et al., 2017), and sol-gel technique (Bharathi and Varma, 2014; Praveen et al., 2015).

It is well known that various synthesis techniques and different preparation conditions affect the physical, chemical and electrical properties of a material (Villafuerte-Castrejón et al., 2016; Coondoo et al., 2018). BCZT ceramics that are synthesized by SSR technique shown excellent piezoelectric coefficient (d_{33}) about 140–620 pC/N (Villafuerte-Castrejón et al., 2016) and this value is greater than or equal to the PZT ($d_{33} \sim 225$ –593 pC/N) (Yang et al., 2018). BCZT ceramics prepared by a conventional sintering (CS) technique requires high calcination temperature (~ 1200 – 1350 °C), high sintering temperature (~ 1300 – 1500 °C) and long dwelling time (~ 2 – 6 h) (Villafuerte-Castrejón et al., 2016). Reactive sintering (RS) technique is an optional method to fabricate the piezoelectric ceramics, in which the constituent phases react with each other and lead to the formation of new phase at high sintering temperature without need of calcination process (Loiu, 2015). Many materials such as PZT (Kong and Ma, 2001), KNN (Farooq et al., 2016), $(\text{K}_{0.5}\text{Bi}_{0.5})\text{TiO}_3$ - BiFeO_3 (Fisher et al., 2015) and $0.94\text{Bi}_{0.5}\text{Na}_{0.5}\text{TiO}_3$ - 0.06BaTiO_3 (Kawashima and Suzuki, 2016) have been reported by RS technique. The advantages of RS technique is its simple procedure to improve the density of ceramics, cost-effective,

* Corresponding author.

E-mail address: soodkhet@g.sut.ac.th (S. Pojprapai).

<https://doi.org/10.1016/j.radphyschem.2020.108770>

Received 9 November 2019; Received in revised form 15 January 2020; Accepted 8 February 2020

Available online 09 February 2020

0969-806X/© 2020 Elsevier Ltd. All rights reserved.

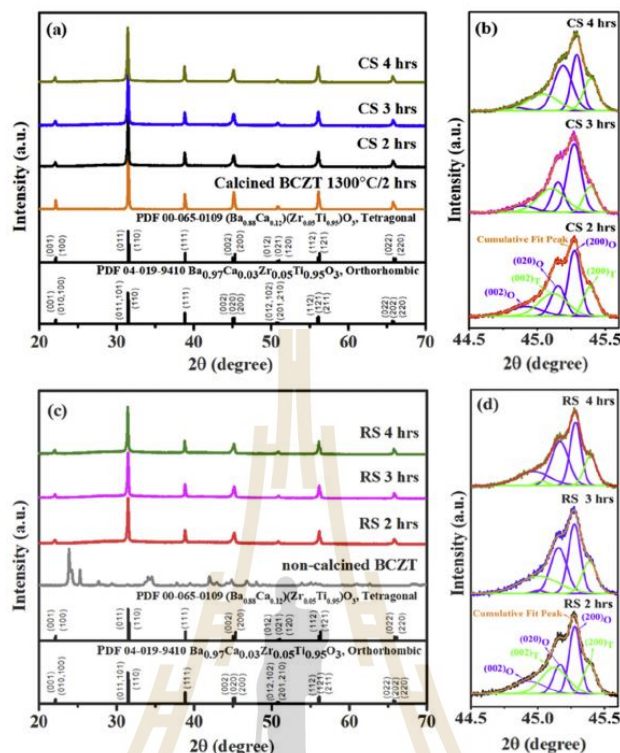


Fig. 1. XRD patterns of BCZT ceramics: (a, b) CS and (c, d) RS techniques.

less preparation time, can avoid contamination during the re-grinding process and suitable for the preparation of electronic ceramic materials (Loiu, 2015). Wang et al. (2011) reported that the specific composition of BCZT ($\text{Ba}_{0.85}\text{Ca}_{0.15}\text{Zr}_{0.1}\text{Ti}_{0.9}\text{O}_3$) ceramics can be achieved by sintered at 1540 °C for 2 h of dwelling time using CS method. Therefore, we would like to adapt the same composition and sintering condition to prepare the BCZT ceramics by RS technique, and compare this result with the CS technique prepared ceramics to investigate the effect of various sintering dwell times.

In general, characterization techniques like Scanning Electron Microscope (SEM) and X-Ray Diffraction (XRD) methods are used to investigate microstructure and phase formation in ferroelectric materials (Bharathi and Varma, 2014). However, SEM and XRD cannot provide the information of oxidation state and electronic transitions in a material (Kempet et al., 2016). In this experiment, the X-ray Absorption Spectroscopy (XAS) was employed to investigate the oxidation state, electronic transitions, neighboring atoms, coordination number and local structure of a material (Ray et al., 2011; Kempet et al., 2016; Bootchanont et al., 2014; Mastelaro et al., 2015; Leitzke et al., 2018). This work aims to compare the microstructure, phase, electrical, ferroelectric and piezoelectric properties of BCZT ceramics fabricated by RS and CS techniques. We believe that this work will be useful to understand the effect of sintering techniques to prepare the BCZT

ceramics.

2. Experimental details

Specific composition of BCZT ($\text{Ba}_{0.85}\text{Ca}_{0.15}\text{Zr}_{0.1}\text{Ti}_{0.9}\text{O}_3$) ceramics were fabricated by using both CS and RS sintering techniques. Commercially purchased BaCO_3 (99.0%, Sigma Aldrich), CaCO_3 (99.0%, Loba Chemie), ZrO_2 (99.5%, Eleps) and TiO_2 (99.8%, Aldrich) powders were used as an initial material. A 30.0951 g of BaCO_3 powder, 12.8965 g of TiO_2 powder, 2.6936 g of CaCO_3 and 2.2109 g of ZrO_2 powders were mixed by ball milling process in ethanol for 24 h. Then, the ball-milled powders dried at 120 °C for 24 h to remove the ethanol content. For RS technique, 0.5 g of compositionally mixed powders (without calcine) was prepared as pellets with 1 cm of diameter by uniaxial press 1.25 ton. Then the pellets were sintered at 1540 °C for 2, 3 and 4 h of dwell time. For CS technique, the compositionally mixed powders were dried and calcined at 1300 °C in an alumina crucible for 2 h (as mentioned condition by Wang et al. (2011)), then were re-grinded the calcined powders and formed as pellets with 1 cm diameter by uniaxial press 1.25 ton. After that, pellets were sintered at 1540 °C for 2, 3 and 4 h of dwell time. Both sintering and calcination processes, heating and cooling rates were maintained at 5 °C/min. The key differences between RS and CS techniques that were

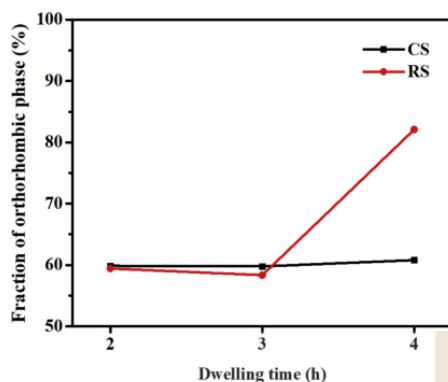


Fig. 2. Fraction of orthorhombic phase of BCZT ceramics were sintered at 1540 °C for 2, 3 and 4 h by CS and RS.

used in this manuscript are shown in Table-4.

BCZT ceramics prepared by both CS and RS methods characterized by using X-Ray Diffractometer (XRD, Bruker Phaser DII). Dwell time driven surface morphology and grain size were measured using a Scanning Electron Microscope (SEM, JEOL JSM-6010LV). The average grain size was estimated by using ImageJ software. Each of the pellet was polished on both side and thinned down to 1 mm by using SiC paper (this process was done sequentially by decreasing the roughness of SiC paper). The density of the pellets was estimated by using Archimedes' principle (ASTM C 378–88) (Kireš, 2007). Both faces of each pellet were coated with gold (Au) of thickness around 100 nm as a top and bottom electrode using radio frequency (RF) sputtering technique. The dielectric properties of pellets were measured at 100 Hz frequency by using aixPES piezoelectric evaluation system from aix-ACCT Systems GmbH, Aachen, Germany. Ferroelectric hysteresis loop (P - E) was measured by P - E hysteresis (TREK, Model 20/20C) at room temperature under 50 Hz frequency by applying ± 10 kV/cm electric field. Then, some of the ceramics were dipped in silicon oil bath (in order to avoid the high voltage spark) and poled under 2.0 kV/mm DC field for 30 min at room temperature. The piezoelectric constant (d_{33}) was measured from the poled ceramics by using d_{33} m (International Ltd., APC-S5865).

XAS measurement was performed on BCZT ceramics at Beam Line 8 (BL-8), Siam Photon Laboratory, Synchrotron Light Research Institute (SLRI), Thailand. 1.2 GeV energetic electron beam and 60–150 mA beam current was utilized to get the energetic polarized X-ray beam. A double crystal monochromator (a pair of Ge (220) and InSb (111) crystals) were used to collect the fluorescent X-ray beam with energy steps of 0.2 eV. Ti K-edge (4966 eV) and Zr L₂-edge (2223 eV) absorption spectra were recorded to analyze the structural parameters. Before the actual experiment, the photon energy was calibrated by measuring Ti and Zr foils absorption edges respectively. Finally, data was analyzed by using ATHENA program (Ravel and Newville, 2006) to extract the structural parameters.

3. Result and discussion

XRD patterns of BCZT ceramics prepared by CS and RS techniques at 1540 °C for 2, 3 and 4 h dwell time are shown in Fig. 1. Here we have included XRD patterns of calcined and non-calcined powders as a reference. For all the samples, XRD measurement was performed from 20° to 70° of 2θ . Fig. 1(a) and (b) represents the CS technique prepared

samples and Fig. 1(c) and (d) represents the RS technique prepared samples. Initial observation suggests that the XRD pattern of both (RS and CS) techniques exhibit a pure perovskite structure without any secondary phase. This considers that Ca²⁺ diffuses into Ba²⁺ A-site and Zr⁴⁺ diffuses into Ti⁴⁺ at B-site, and Ca and Zr have completely diffused into the BaTiO₃ lattice (Wang et al., 2011; Buatip et al., 2018). All BCZT ceramics resemble mixture phase structures of tetragonal and orthorhombic. Even though prepared BCZT ceramics from both RS and CS techniques exhibit the same phase, the CS-BCZT ceramics shown greater XRD peak intensities than RS-BCZT ceramics. This might be because CS-BCZT pellet was prepared from pure phase calcined BCZT powder before sintering. The XRD peak pattern at 44°–46° of 2θ indicates multiple phase formation in the both of CS-BCZT and RS-BCZT ceramics. The peak deconvolution is shown in Fig. 1(b) and (d). The deconvoluted peaks at 44.91°, 45.15° and 45.27° of 2θ belong to the orthorhombic phase of (002), (020) and (200) crystal planes. These peaks are well matched with the JCPDS file (PDF# 04-019-9410). Similarly, the peaks at 45.12° and 45.39° belong to the tetragonal phase of (002) and (200) crystal planes. The same tetragonal phase peaks are well-matched with the JCPDS file (PDF# 00-064-0109). This trend was same in both CS and RS techniques prepared samples. The mixture phase of orthorhombic and tetragonal peak intensities was studied with respect to the various sintering dwell times to understand the phase evaluation. A fraction of orthorhombic phase is calculated by applying Garvie and Nicholson (Garvie and Nicholson, 1972) equation as given below

$$C_o = \frac{I_o(002) + I_o(020) + I_o(200)}{I_o(002) + I_t(002) + I_o(020) + I_o(200) + I_t(200)} \quad (1)$$

where ' C_o ' is the compositional weight of orthorhombic phase, ' I_o ' and ' I_t ' are integral areas of the orthorhombic and tetragonal phases (or intensities of corresponding peaks). The fraction of orthorhombic phase increased with an increase of dwell time. The calculated fractional orthorhombic phase with respect to dwell time in both (CS and RS) techniques are shown in Fig. 2. An increase in the fraction of orthorhombic phase was observed with increasing dwell time. However, fraction of orthogonality is less in RS technique compare to CS technique at 2, 3 h of dwell time and higher than CS technique at 4 h of dwell time. Along with that, tetragonality (c/a ratio) of BCZT samples (from both techniques) were calculated; they equal to 1.006, 1.006, 1.008 for CS and 1.006, 1.008, 1.008 for RS, at 2, 3 and 4 h of dwell time respectively (shown as Fig. 6(a)). These values are consistent with the standard XRD pattern of the tetragonal BCZT JCPDS file (PDF#00-064-0109) which is around 1.006.

SEM micrographs of BCZT ceramics prepared by RS and CS techniques are shown in Fig. 3 (inset shows the corresponding histograms). RS-BCZT ceramics sintered within 2, 3 and 4 h dwell time possess the average grain size of $13.24 \pm 4.46 \mu\text{m}$, $7.82 \pm 2.38 \mu\text{m}$, and $12.56 \pm 6.58 \mu\text{m}$, respectively. By comparison with RS-BCZT, CS-BCZT ceramics exhibit $14.42 \pm 6.02 \mu\text{m}$, $11.84 \pm 4.20 \mu\text{m}$, and $12.38 \pm 4.04 \mu\text{m}$ for 2, 3 and 4 h of dwell time, respectively. In RS technique, average grain size decreased significantly for 3 h dwell time and increased further. Inhomogeneous grain size was observed for 4 h of dwell time. The decrease and increase in grain sizes could be because of strain/stress relaxation induced grain fragmentation and/or agglomeration (Wu et al., 2011; Cheng et al., 2013). CS-BCZT ceramics do not shown much variations in their grain sizes. This can be taken account of pre-calcination effect. Therefore, we can conclude that long dwell time can cause abnormal grain growth and inhomogeneous microstructure. The average grain size and relative density of BCZT ceramics fabricated from both sintering techniques are plotted in Fig. 3(b) and (c). The grain size of RS-BCZT ceramics are smaller than CS-BCZT ceramics, this could be because particles of non-calcined BCZT powder do not aggregate as same as the calcined BCZT powder in the process of high-temperature sintering does. However, density of RS-BCZT ceramics, 96–97%, are comparable to the theoretical density.

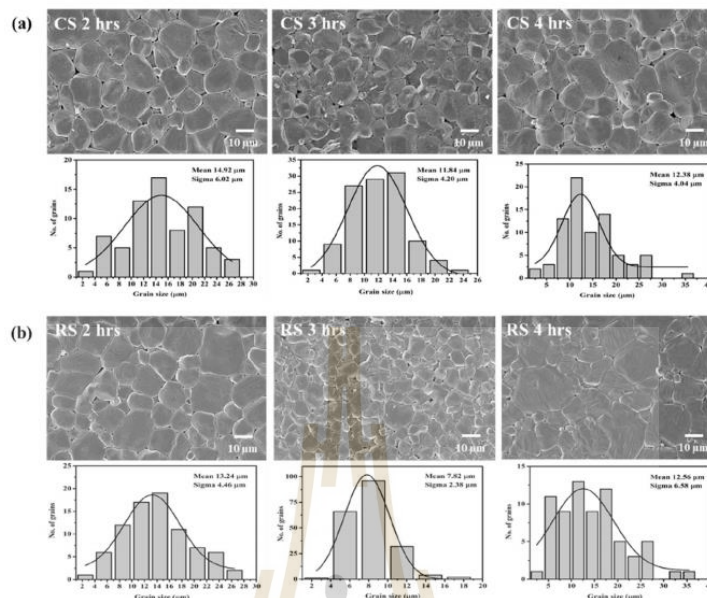


Fig. 3. SEM micrograph of surface of BCZT ceramics were sintered at 1540 °C for 2, 3 and 4 h by CS (a) and RS (b).

At 2 h dwell time, RS-BCZT and CS-BCZT ceramic densities are equal. However, for further increase of dwell time to 3 h and 4 h, RS-BCZT ceramics showed higher density than that of CS-BCZT ceramics. In overall comparison, RS-BCZT ceramics shown better densification similar to the PZT and KNN ferroelectric ceramics reported by L.B. Kong and J. Ma (Kong and Ma, 2001), and M. U. Farooq et al. (2016). Moreover, all the RS-BCZT ceramics exhibited 24% shrinkage ratio, which is higher than the CS-BCZT ceramics shrinkage ratio (9%) under the same sintering condition. This is the effect of non-aggregation of BCZT powder with and without the calcination process.

The hysteresis loop of BCZT ceramics are shown in Fig. 4. In overall, the ferroelectric properties (E_c , P_s , P_r) of BCZT ceramics slightly decreased with an increase of dwell time. The coercive fields (E_c), the saturation polarization (P_s) and the remnant polarization (P_r) values of RS-BCZT and CS-BCZT ceramics are tabulated in Table 1. The E_c of RS-BCZT ceramics decreased from 3.26 to 1.80 kV/cm with an increase of dwell time. E_c of CS-BCZT ceramics initially decreased but increased further with respect to increased dwell time. For saturation polarization, P_s , RS-BCZT ceramics decreased from 9.32 to 3.34 $\mu\text{C}/\text{cm}^2$, and CS-BCZT ceramics decreased from 9.68 to 5.31 $\mu\text{C}/\text{cm}^2$ with respect to the increase of dwell time. It can be seen clearly that in both techniques (CS and RS), P_s and P_r values decreased with an increase of dwell time. Similarly, for piezoelectric coefficient (d_{33}), the maximum d_{33} value of RS-BCZT ceramics is approximately 288 pC/N comparing to CS-BCZT ceramics which is 284 pC/N. It decreased with an increase of dwell time in both sintering techniques and exhibit maximum values at 2 h dwell time. The piezoelectric constant (d_{33}) of both RS-BCZT and CS-BCZT ceramics are rather low, this could be the consequence of inhomogeneous grain size and porosity inside the microstructure. It affects the domain orientation in the aligned electric field direction. The reduction of porosity inside microstructure can improve the packing

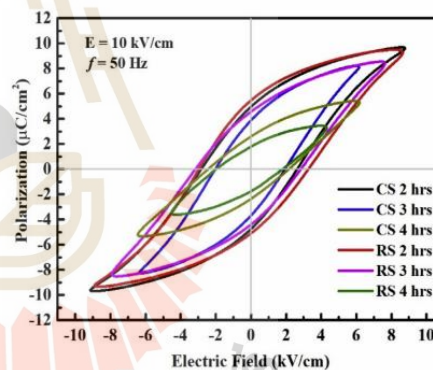


Fig. 4. P-E hysteresis loops of BCZT ceramics were sintered by CS and RS at 1540 °C for 2, 3 and 4 h at frequencies 50 Hz under an electric field $\pm 10 \text{ kV/cm}$.

density and bulk density and this can be achieved by adding a binder and apply the Cold Isostatic Pressing (CIP) method to enhance d_{33} of BCZT ceramics. The temperature dependent dielectric constant (ϵ_r) and dielectric loss ($\tan \delta$) of BCZT ceramics measured at 100 Hz frequency from 20 °C to 160 °C were illustrated in Fig. 5. The BCZT ceramics transformed from tetragonal phase to cubic phase with increasing

Table-1
Electrical properties of BCZT ceramics sintered at 1540 °C for 2, 3 and 4 h by CS, RS techniques.

Sintering condition		Electrical properties					
Techniques	Dwell time (hrs.)	$\epsilon_{r,max}$	Tan δ_{max}	Saturation polarization; P_s ($\mu\text{C}/\text{cm}^2$)	Remanent polarization; P_r ($\mu\text{C}/\text{cm}^2$)	Coercive field; E_c (kV/cm)	d_{33} (pC/N)
CS	2	10610	0.02	9.68	5.01	2.53	284 ± 6.97
	3	7035	0.03	8.13	3.98	1.91	230 ± 11.09
	4	8232	0.09	5.31	2.60	2.11	236 ± 9.65
RS	2	9628	0.02	9.32	5.56	3.26	288 ± 13.27
	3	8295	0.02	8.54	4.63	2.80	246 ± 8.02
	4	9807	0.02	3.34	1.82	1.80	226 ± 10.93

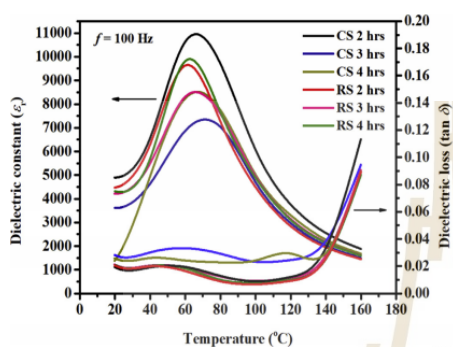


Fig. 5. Temperature dependent dielectric constant (ϵ_r) and dielectric loss ($\tan \delta$) at 100 Hz of BCZT ceramics prepared by CS and RS techniques.

temperature. The Curie temperature (T_c) of RS-BCZT and CS-BCZT ceramics was noticed in the ranges of 63–67 °C and 67–73 °C, respectively. Similar kind of results was reported by M. Villafuerte-Castrejón et al. (2016) ($T_c \approx 60$ –120 °C). The T_c of RS-BCZT ceramics is slightly

lower than CS-BCZT ceramics. It is believed that inhomogeneous grain formation, domain wall motion, internal stress/strain are responsible for the change in transition temperature (Martirena and Burfoot, 1974; Buessem et al., 2006). The relative maximum permittivity ($\epsilon_{r,max}$) of BCZT ceramics showed maximum value at 2 h of dwell time and these values 9628 and 10610 respectively for RS and CS-BCZT. The noticed dielectric loss ($\tan \delta$) was approximately 0.02 and it is well below 2% in both techniques. The polarization curves also give enough evidence that leakage current density of both CS and RS samples are low.

Ti K -edge and Zr L_{3-2} -edge X-ray absorption spectra of BCZT ceramics prepared by CS and RS sintering techniques are shown in Fig. 7. Fig. 7(a) refers to the Ti K -edge XANES spectra and Fig. 7(b) refers to the Zr L_{3-2} -edge XANES spectra, respectively. XANES spectra of Ti foil, Zr foil, Ti_2O_3 , TiO_2 (Anatase) and ZrO_2 used for reference purpose (shown in Fig. 7(a) and (b)). The main absorption peak located at 4980 eV in XANES spectra (i.e. mainly due to Ti 1s to 4p dipole transitions) obtained from all sintering conditions is the same. A small hump at 4969 eV labeled as A_1 represents 1s to 3d quadrupolar transition. This peak is prominent in perovskite ferroelectric structures with a twisted TiO_6 octahedral site (Vedriniskii et al., 1998; Ray et al., 2011; Mastelaro et al., 2015). The second peak labeled as ' A_2 ' at 4970 eV is mainly related to the hybridization effect of 3d and 4p orbitals under the neighboring oxygen atoms. This peak also indirectly related to the Ti off-center distortion in TiO_6 octahedron perovskite ferroelectrics (Vedriniskii et al., 1998; Bootchanont et al., 2014; Mastelaro et al., 2015).

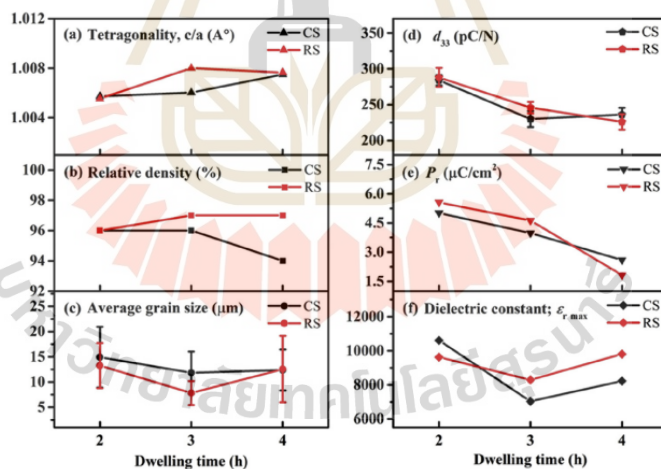


Fig. 6. Physical properties (a, b, c) and piezoelectric properties (d, e, f) of BCZT ceramics at 1540 °C by different sintering techniques (CS and RS) and dwelling times.

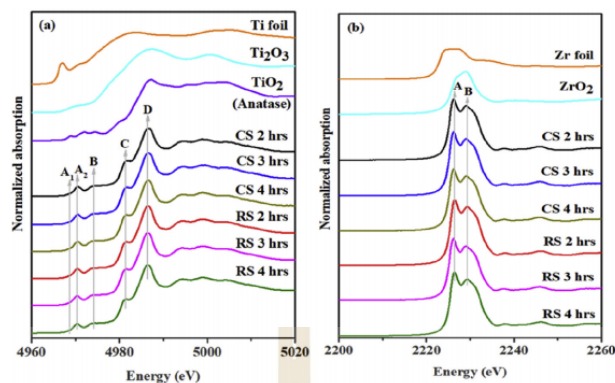


Fig. 7. Normalized XANES spectra of BCZT ceramics prepared by CS and RS techniques: (a) Ti K-edge spectra and (b) Zr L_3 -edge spectra.

Table-2

Edge position of Ti K-edge and Zr L_3 -edge of BCZT ceramics sintered at 1540 °C for 2, 3 and 4 h by CS, RS techniques and reference samples.

Sample Name	Dwell time (hrs.)	Edge position (eV)	
		Ti K-edge (± 0.3 eV)	Zr L_3 -edge (± 0.2 eV)
Ti foil	-	4966.0	-
Ti ₂ O ₃	-	4976.6	-
TiO ₂ (Anatase)	-	4979.2	-
Zr foil	-	-	2222.9
ZrO ₂	-	-	2225.9
CS-BCZT	2	4980.3	2225.3
CS-BCZT	3	4980.3	2225.4
CS-BCZT	4	4980.2	2225.3
RS-BCZT	2	4980.2	2225.3
RS-BCZT	3	4980.2	2225.4
RS-BCZT	4	4980.2	2225.4

Table-3

The area under the corresponding peaks at the PEFS of XANES Ti K-edge of BCZT ceramics sintered at 1540 °C for 2, 3 and 4 h by CS, RS techniques.

Sample Name	Dwell time (hrs.)	Area under a corresponding peak at the PEFS (eV)				
		Peak A Total (A ₁ + A ₂)	Peak A ₁	% increase/decrease (-)	Peak A ₂	% increase/decrease (-)
CS-BCZT	2	0.21	0.03	-	0.18	-
	3	0.22	0.03	-19.44	0.19	3.69
	4	0.22	0.03	-10.37	0.19	4.68
RS-BCZT	2	0.21	0.04	-	0.17	-
	3	0.21	0.05	20.81	0.16	-5.94
	4	0.20	0.03	-34.53	0.17	8.31

The peak was deconvoluted into 'A₁' and 'A₂' and analyzed the variation of peak intensity with different sintering conditions (see Table-3). RS-BCZT ceramics exhibit an increase or decrease of the area under a corresponding peak at the PEFS more than CS-BCZT ceramics. The peak labeled as 'B' at 4974 eV related to the Ti 1s electron transition to unoccupied 3d states of the neighboring atom such Zr (Vedriniskii et al., 1998; Ray et al., 2011; Mastelaro et al., 2015). In addition, the features of peak labeled as 'C' and 'D' show the higher energies of 4981 eV and 4986 eV. This is also attributed to the ratio of

Table-4

The difference between RS and CS techniques.

Process/Method	RS	CS
Weighing substrate i.e. BaCO ₃ , CaCO ₃ , ZrO ₂ , TiO ₂	●	●
Mixing substrate of BCZT by ball mill in ethanol for 24 h	●	●
Drying mixed BCZT at 120 °C for 24 h in Oven	●	●
Calcining BCZT powder at 1300 °C for 2 h	●	●
Re-grinding BCZT calcined powder by ball mill in ethanol for 6 h	●	●
Drying calcined BCZT at 120 °C for 24 h in Oven	●	●
Dry Pressing BCZT powders into pellets (Ø ~10 mm, t ~2 mm)	●	●
Sintering at 1540 °C for 2, 3 and 4 h of dwell time	●	●

Zr/Ti in the 3rd shell and the change in the local structure around main absorbed atom (Ti), respectively (Boothanont et al., 2014). These results show that RS-BCZT ceramics in each dwell time exhibited the features of peaks labeled as A, B, C and D from XANES spectra which are comparable to CS-BCZT ceramics. The oxidation state of the Ti atoms was studied in each sintered BCZT ceramics, as well as compared with the three reference samples that were shown in Fig. 7(a). Table-2 shows the Ti K-edge absorption positions of RS-BCZT, CS-BCZT and the reference samples. The pure Ti foil absorption edge position showed at 4966.1 eV which is related to Ti⁰ oxidation state. Ti K-edge position for Ti₂O₃ powder showed at 4976.6 eV which is related to the Ti³⁺ oxidation state and TiO₂ (Anatase) at 4979.2 eV related to Ti⁴⁺ oxidation state. These results are in agreement with the report done by Waychunas and Lin et al. (Waychunas, 1987; Lin et al., 2012). The absorption edge positions of RS-BCZT and CS-BCZT ceramics are at 4980 eV and these positions are very much close to the TiO₂ (Anatase) with Ti⁴⁺ oxidation state. This implies that BCZT ceramics prepared in both techniques were showed octahedrally coordinated TiO₆ structure and this coordination does not affect by various dwell times.

The Zr L_3 -edge XAS spectra of BCZT ceramics prepared by CS and RS techniques at different dwell times are shown in Fig. 7(b). Two dominant peaks labeled as 'A' at 2226 eV and 'B' at 2229 eV are composed to the $2p \rightarrow e_g$ and $2p \rightarrow t_{2g}$ transitions, respectively. Zr foil L_3 absorption edge at 2222.9 eV correspond to the Zr⁰ oxidation state and ZrO₂ L_3 absorption edge at 2225.9 eV correspond to the Zr⁴⁺ oxidation state respectively. In our case, Zr L_3 -edge of all BCZT ceramics showed at 2225 eV, which is very close to the Zr⁴⁺ oxidation state. The intensity ratio of peak 'A' to 'B' gives the information of the coordination number around Zr (i.e. absorbent atom) (Ikeno et al., 2013). Peak A and B are originated from Zr 4d orbitals due to ligand field splitting effect into e_g

and t_{2g} states within the ZrO_6 octahedral. This results are also consistent with the existing results in perovskite PZT system (Ray et al. (2011)). Similar kind of results in ferroelectric perovskite BCZT were reported by V.R. Mastelaro et al. (2015) $Ba(Ti,Zr)O_3$ (Bootchanont et al., 2014) and PZT compounds (Ray et al., 2011).

4. Conclusion

The effect of CS and RS sintering techniques on the phase formation, microstructure, electrical properties and oxidation state of BCZT ferroelectric ceramics have been studied in detail. The proposed composition of BCZT ($Ba_{0.85}Ca_{0.15}Zr_{0.1}Ti_{0.9}O_3$) was achieved by sintering at 1540 °C with different dwell times. All BCZT ceramics appear a pure perovskite phase and mixture phase structures of tetragonal and orthorhombic. The both (CS and RS) BCZT ceramics prepared at 1540 °C for 2 h of dwell time exhibit optimal properties. RS-BCZT ceramic exhibits $13.24 \pm 4.46 \mu m$ of grain size, 96% of relative density, $63 \text{ }^\circ C$ of T_c , $5.56 \mu C/cm^2$ of P_r , 3.26 kV/cm of E_c , 9628 of $\epsilon_{r,max}$, 0.02 of $\tan \delta$ and 288 pC/n of d_{33} . In CS-BCZT ceramic exhibits $14.42 \pm 6.02 \mu m$ of grain size, 96% of relative density, $67 \text{ }^\circ C$ of T_c , $5.01 \mu C/cm^2$ of P_r , 2.53 kV/cm of E_c , 10610 of $\epsilon_{r,max}$, 0.02 of $\tan \delta$ and 284 pC/n of d_{33} . The Ti K-edge and Zr L₃-edge XANES spectra resembles the 4+ oxidation state for Ti and Zr atoms of both (CS and RS) BCZT ceramics. Thus, the current study demonstrates that RS technique is a simple procedure and cost&time effective to prepare the BCZT ceramics than CS method.

CRedit authorship contribution statement

N. Buatip: Conceptualization, Methodology, Validation, Formal analysis, Investigation, Resources, Writing - original draft, Visualization, Project administration, Data curation, Supervision, Writing - review & editing. **M. Dhanunjaya:** Validation, Formal analysis, Data curation, Supervision, Writing - review & editing. **P. Amonpattarakit:** Methodology, Validation, Formal analysis, Investigation, Resources, Data curation, Supervision, Writing - review & editing. **P. Pomyai:** Investigation, Resources. **T. Sonklin:** Investigation, Resources. **K. Reichmann:** Investigation, Resources, Writing - review & editing. **P. Janphaung:** Supervision, Writing - review & editing. **S. Pojprapai:** Conceptualization, Methodology, Validation, Formal analysis, Investigation, Resources, Data curation, Writing - original draft, Writing - review & editing, Visualization, Supervision, Project administration, Funding acquisition.

Declaration of competing interest

The authors declare that they have no known competing financial interests or personal relationships that could have appeared to influence the work reported in this paper.

Acknowledgments

This work is supported by Suranaree University of Technology (SUT), Thailand. N. Buatip would like to thank the Royal Golden Jubilee (RGJ) Ph.D. Program and Synchrotron Light Research Institute (SLRI) Public Organization, Thailand for financially support. The authors also acknowledging the BLS: XAS scientists and technicians for their help throughout the experiment.

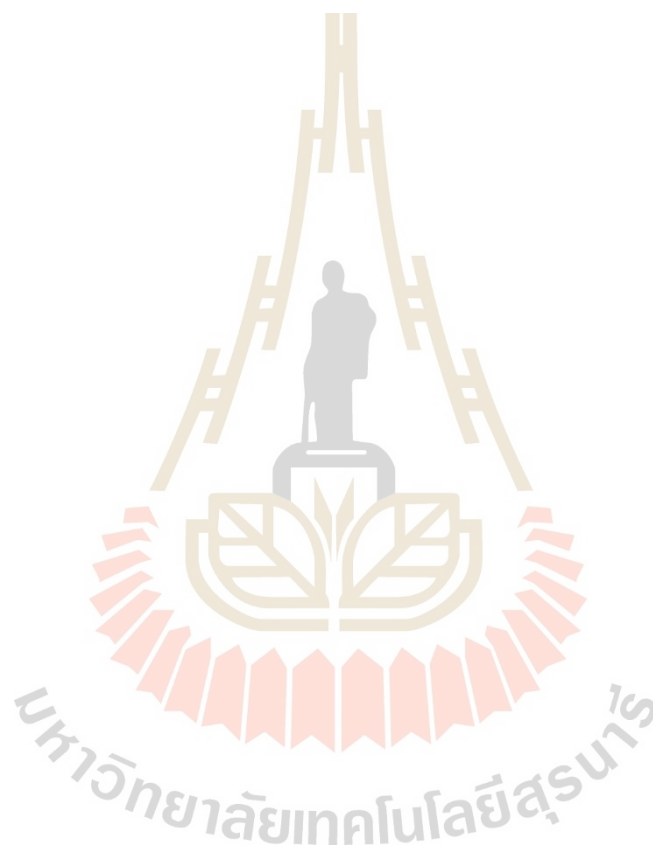
References

- Acosta, M., Novak, N., Rojas, V., Patel, S., Vaish, R., Koruza, J., Rossetti, G.A., Ridel, J., 2017. BaTiO₃-based piezoelectrics: fundamentals, current status, and perspectives. *Appl. Phys. Rev.* 4, 041305. <https://doi.org/10.1063/1.4990046>.
- Bharathi, P., Varma, K.B.R., 2014. Grain and the concomitant ferroelectric domain size dependent physical properties of Ba_{0.85}Ca_{0.15}Zr_{0.1}Ti_{0.9}O₃ ceramics fabricated using powders derived from oxalate precursor route. *J. Appl. Phys.* 116, 164107.

<https://doi.org/10.1063/1.4990046>.

- Bootchanont, A., Jutimosik, J., Chandarak, S., Unruan, M., Kidkhunthod, P., Klysubun, W., Rujirawat, S., Yimnirun, R., Guo, R., Bhalla, A., 2014. Synchrotron X-ray absorption spectroscopy study of local structure transformation behavior in perovskite Ba(Ti,Zr)O₃ system. *J. Alloys Compd.* 616, 430–435. <https://doi.org/10.1016/j.jallcom.2014.07.175>.
- Buatip, N., Promsawat, N., Pisitipathsin, N., Namsar, O., Pawasri, P., Ounsung, K., Phabsinma, K., Rattanachan, S.T., Janphaung, P., Projprapai, S., 2018. Investigation on electrical properties of BCZT ferroelectric ceramics prepared at various sintering conditions. *Integrated Ferroelectrics* 187, 45–52. <https://doi.org/10.1080/10584587.2018.1445395>.
- Buessem, R., Cross, W.E., Goswami, L.A.K., 2006. Phenomenological theory of high permittivity in fine-grained BaTiO₃. *J. Am. Ceram. Soc.* 49, 33–36. <https://doi.org/10.1111/j.1151-2916.1966.tb13144.x>.
- Cheng, H.-J., Zhou, W.-c., Du, H.-L., Luo, F., Zhu, D.-m., 2013. Effects of dwell time during sintering on electrical properties of 0.98(K_{0.5}Na_{0.5})NbO₃-0.02LaFeO₃ ceramics. *Trans. Nonferr. Metal. Soc.* 23, 2984–2988. [https://doi.org/10.1016/S1003-6326\(13\)62824-1](https://doi.org/10.1016/S1003-6326(13)62824-1).
- Coondoo, I., Panwar, N., Alikin, D., Bdkin, I., Islam, S.S., Turygin, A., Shur, V.Y., Kholkin, A.L., 2018. A comparative study of structural and electrical properties in lead-free BCZT ceramics: influence of the synthesis method. *Acta Mater.* 155, 331–342. <https://doi.org/10.1016/j.actamat.2018.05.029>.
- Farooq, M.U., Fisher, J., Kim, J.-H., Kim, D., Shin, E.-C., Kim, Y.-H., Kim, J.-H., Moon, S.-H., Lee, J.-S., Lin, X., Zhang, D., 2016. Reactive sintering of lead-free piezoelectric (K_{0.5}Na_{0.5})NbO₃ ceramics. *J. Ceram. Process. Res.* 17, 304–312.
- Fisher, J.G., Kim, M.-G., Kim, D., Cha, S.-J., Yu, H.V., Nguyen, D., Kim, Y.-H., Moon, S.-H., Lee, J.-S., Hussain, A., Kim, M.-H., 2015. Reactive sintering of (K_{0.5}Na_{0.5})TiO₃-BiFeO₃ lead-free piezoelectric ceramics. *J. Kor. Phys. Soc.* 66, 1426–1438. <https://doi.org/10.3938/jkps.66.1426>.
- Garvie, R.C., Nicholson, P.S., 1972. Phase Analysis in zirconia systems. *J. Am. Ceram. Soc.* 55, 303–305. <https://doi.org/10.1111/j.1151-2916.1972.tb11290.x>.
- Hajra, S., Sahoo, S., Das, R., Choudhary, R.N.P., 2018. Structural, dielectric and impedance characteristics of (Bi_{0.5}Na_{0.5})TiO₃-BaTiO₃ electronic system. *J. Alloys Compd.* 750, 507–514. <https://doi.org/10.1016/j.jallcom.2018.04.010>.
- Ikeno, H., Krause, M., Hoche, T., Patzig, C., Hu, Y., Gawronski, A., Tanaka, I., Rüssel, C., 2013. Variation of Zr-L_{2,3}XANES in tetraivalent zirconium oxides. *J. Phys. Condens. Mat.* 25, 165505. <https://doi.org/10.1088/0953-8984/25/16/165505>.
- Izzuddin, I., Hj Jumal, M.H., Zainuddin, Z., Janil, N.H., 2019. Piezoelectric enhancements in K_{0.5}Na_{0.5}NbO₃-based ceramics via structural evolutions. *Ceram. Int.* 45, 17204–17209. <https://doi.org/10.1016/j.ceramint.2019.05.275>.
- Kang, M.-G., Jung, W.-S., Kang, C.-Y., Yoon, S.-J., 2016. Recent progress on PZT based piezoelectric energy harvesting technologies. *Actuators* 5, 5.
- Kawashima, T., Suzuki, Y., 2016. Reactive sintering and piezoelectric properties of 0.94Bi_{0.5}Na_{0.5}TiO₃-0.06BaTiO₃ ceramics with ZnO additive. *J. Ceram. Soc. Jpn.* 124, 911–914. <https://doi.org/10.2109/jcersj2.16051>.
- Kempet, W., Marangsi, B., Yimnirun, R., Klysubun, W., Pojprapai, S., 2016. Investigation of the unit cell distortion in PZT ceramic via in-situ XAS technique. *Ferroelectrics* 492, 35–42. <https://doi.org/10.1080/00150193.2013.842138>.
- Khanal, G.P., Fujii, I., Kim, S., Ueno, S., Suzuki, T.S., Wada, S., 2019. Optimization of preparation conditions of highly textured piezoelectric (Bi_{0.5}K_{0.5})TiO₃ ceramics. *J. Ceram. Soc. Jpn.* 127, 362–368. <https://doi.org/10.2109/jcersj2.19009>.
- Kireš, M., 2007. Archimedes' principle in action. *Phys. Educ.* 42, 484–487. <https://doi.org/10.1088/0031-9120/42/5/006>.
- Kong, L.B., Ma, J., 2001. PZT ceramics formed directly from oxides via reactive sintering. *Mater. Lett.* 51, 95–100. [https://doi.org/10.1016/S0167-577X\(01\)00272-5](https://doi.org/10.1016/S0167-577X(01)00272-5).
- Leitzke, F., Fonseca, R., Goettlicher, J., Steininger, R., Jahn, S., Prescher, C., Lagos, M., 2018. Ti K-edge XANES study on the coordination number and oxidation state of Titanium in pyroxene, olivine, armalcolite, ilmenite, and silicate glass during mare basalt petrogenesis. *Contrib. Mineral. Petrol.* 173. <https://doi.org/10.1007/s00410-018-1533-7>.
- Lin, K.-S., Mai, Y.-J., Chiu, S.-W., Yang, J.-H., Chan, S.L.I., 2012. Synthesis and characterization of metal hydride/carbon aerogel composites for hydrogen storage. *J. Nanomater.* 2012, 9. <https://doi.org/10.1155/2012/201584>.
- Liu, Y., Pu, Y., Sun, Z., 2014. Enhanced relaxor ferroelectric behavior of BCZT lead-free ceramics prepared by hydrothermal method. *Mater. Lett.* 137, 128–131. <https://doi.org/10.1016/j.matlet.2014.08.138>.
- Loitu, Y.-C., 2015. Reaction-sintering process for preparing electronic ceramics. *Recent. Pat. Mater.* 8, 225–238.
- Lu, X., Fang, B., Zhang, S., Yuan, N., Ding, J., Zhao, X., Wang, F., Tang, Y., Shi, W., Xu, H., Luo, H., 2017. Decreasing sintering temperature for BCZT lead-free ceramics prepared via hydrothermal route. *Funct. Mater. Lett.* 10, 1750046. <https://doi.org/10.1142/17936617500461>.
- Martirena, H.T., Burfoot, J.C., 1974. Grain-size effects on properties of some ferroelectric ceramics. *J. Phys. C Solid State* 7, 3182–3192. <https://doi.org/10.1088/0022-3719/7/17/024>.
- Mastelaro, V.R., Favarim, H.R., Mesquita, A., Michalowicz, A., Moscovici, J., Eiras, J.A., 2015. Local structure and hybridization states in Ba_{0.9}Ca_{0.1}Ti_{1-x}Zr_xO₃ ceramic compounds: correlation with a normal or relaxor ferroelectric character. *Acta Mater.* 84, 164–171. <https://doi.org/10.1016/j.actamat.2014.10.059>.
- Praveen, J.P., Karthik, T., James, A.R., Chandrakala, E., Ashana, S., Das, D., 2015. Effect of sintering process on piezoelectric properties of sol-gel derived BZT-BCT ceramics. *J. Eur. Ceram. Soc.* 35, 1785–1798. <https://doi.org/10.1016/j.jeurceramsoc.2014.12.010>.
- Ravel, B., Newville, M., 2006. Ravel, B. & Newville, M. ATHENA and ARTEMIS: interactive graphical data analysis using IFFFIT. *Phys. Scripta* 115, 1007–1010.
- Ray, S.C., Hsueh, H.C., Wu, C.H., Pao, C.W., Asokan, K., Liu, M.T., Tsai, H.M., Chuang,

- C.H. Pong, W.F. Chiou, J.W. Tsai, M.H. Lee, J.M. Jang, L.Y. Chen, J.M. Lee, J.F., 2011. Local atomic and electronic structures and ferroelectric properties of $\text{PbZr}_{0.52}\text{Ti}_{0.48}\text{O}_3$: an x-ray absorption study. *Appl. Phys. Lett.* 99, 042909. <https://doi.org/10.1063/1.3607475>.
- Rödel, J., Webber, K.G., Dittmer, R., Jo, W., Kimura, M., Damjanovic, D., 2015. Transferring lead-free piezoelectric ceramics into application. *J. Eur. Ceram. Soc.* 35, 1659–1681. <https://doi.org/10.1016/j.jeurceramsoc.2014.12.013>.
- Vedinskii, R.V., Kratizman, V.L., Novakovich, A.A., Demekhin, P.V., Urazhdin, S.V., 1998. Pre-edge fine structure of the 3d atom K x-ray absorption spectra and quantitative atomic structure determinations for ferroelectric perovskite structure crystals. *J. Phys. Condens. Mat.* 10, 9561–9580. <https://doi.org/10.1088/0953-8984/10/42/021>.
- Villafuerte-Castrejón, M., Morán, E., Reyes-Montero, A., Vivar-Ocampo, R., Peña-Jiménez, J.-A., Rea-López, S.-O., Pardo, L., 2016. Towards lead-free piezoceramics facing a synthesis challenge. *Materials* 9, 21.
- Wang, P., Li, Y., Lu, Y., 2011. Enhanced piezoelectric properties of $(\text{Ba}_{0.85}\text{Ca}_{0.15})$ $(\text{Ti}_{0.9}\text{Zr}_{0.1})\text{O}_3$ lead-free ceramics by optimizing calcination and sintering temperature. *J. Eur. Ceram. Soc.* 31, 2005–2012. <https://doi.org/10.1016/j.jeurceramsoc.2011.04.023>.
- Waychunas, G., 1987. Synchrotron radiation XANES spectroscopy of Ti in minerals: effects of Ti bonding distances, Ti valence, and site geometry on absorption edge structure. *Am. Mineral.* 72.
- Wu, J., Xiao, D., Wu, W., Zhu, J., Wang, J., 2011. Effect of dwell time during sintering on piezoelectric properties of $(\text{Ba}_{0.85}\text{Ca}_{0.15})(\text{Ti}_{0.9}\text{Zr}_{0.1})\text{O}_3$ lead-free ceramics. *J. Alloys Compd.* 509, L359–L361. <https://doi.org/10.1016/j.jallcom.2011.08.024>.
- Yang, Z., Zhou, S., Zu, J., Inman, D., 2018. High-performance piezoelectric energy harvesters and their applications. *Joule* 2, 642–697. <https://doi.org/10.1016/j.joule.2018.03.011>.
- Zhou, X., Qi, H., Yan, Z., Xue, G., Luo, H., Zhang, D., 2019. Large energy density with excellent stability in fine-grained $(\text{Bi}_{0.5}\text{Na}_{0.5})\text{TiO}_3$ -based lead-free ceramics. *J. Eur. Ceram. Soc.* 39, 4053–4059. <https://doi.org/10.1016/j.jeurceramsoc.2019.05.056>.



BIOGRAPHY

Natthawadi Buatip was born in Chiang Mai, Thailand on November 20, 1988. She graduated with a bachelor's degree in Materials Science (First Class Honors) from the Physics and Materials Department, Faculty of Science, Chiang Mai University, Thailand in 2011. After graduation, she started working in the engineering section at Murata Electronics (Thailand) Ltd. Lamphun plants, Thailand (2011-2016). While working, she also worked at Murata Manufacturing Co., Ltd. Yokaichi plants, Japan in 2013. Subsequently, Natthawadi decided to continue her studies and became a Ph.D. candidate in the Materials Engineering Program at the Institute of Engineering, Suranaree University of Technology in 2016. Her Ph.D. was funded by the Royal Golden Jubilee (RGJ) Ph.D. Program through the National Research Council of Thailand (NRCT), Thailand Research Fund (TRF), and Synchrotron Light Research Institute (SLRI) Public Organization Thailand. While studying, she participated in an international research exchange program at the School of Electronics and Computer Science, University of Southampton, United Kingdom (2018). She also conducted research at the International Institute for Nanocomposites Manufacturing (IINM), University of Warwick, and Mechanical Engineering, University of Bath, United Kingdom (2022). Natthawadi completed her Doctoral degree in 2023 and her research interests include lead-free piezoelectric, ceramic-polymer composites, piezo-triboelectric hybrid for nanogenerators, and energy harvesters.